A Direct Shape Design Method For Thermo-Fluid Engineering Problems

by

Ali Ashrafizadeh

A thesis
presented to the University of Waterloo
in fulfilment of the
thesis requirement for the degree of
Doctor of Philosophy
in
Mechanical Engineering

Waterloo, Ontario, Canada, 2000

The University of Waterloo requires the signatures of all persons using or photocopying this thesis. Please sign below, and give address and date.

Abstract

A design method for thermo-fluid engineering problems is proposed in which the desired distribution of pressure, for example, is specified on the boundary, and the dependent variables in the equations of motion are the boundary coordinates that define the boundary shape, and the field variables (e.g. pressure and velocity). When the surface (boundary) shape is unknown, the problem is called a shape design problem. The final discretized form of the governing equations, obtained by the proposed method and called the unified formulation, can be used for solving both analysis and shape design problems.

The method, at its current stage of development, is applied to some steady two-dimensional thermal and fluid flow problems. Shape design problems in the context of inviscid, irrotational flow in ducts (formulated with the secondary variables) and conduction heat transfer problems are directly solved to achieve a prescribed pressure or heat flux distribution along the boundaries.

An integral boundary layer analysis method is modified and used together with the proposed direct shape design method to design short ducts. Short ducts are defined as ducts in which the flow is hydrodynamically developing and the boundary viscous layers remain thin along the duct.

A simple one dimensional flow model which uses primitive variables (pressure and velocity) is used to discuss some new ideas regarding the pressure-velocity coupling and advection modeling and also to implement the proposed direct shape design method in the context of primitive variable formulation.

Acknowledgements

First and foremost, I would like to express my sincere appreciation to my supervisor, Professor G.D. Raithby and my co-supervisor, Professor G.D. Stubley, for their continuous support and guidance throughout this study. I had no, or very little, background in the computational fluid dynamics when I started my graduate studies four years ago. During these four years, I had the wonderful privilege to meet professor Raithby on a regular weekly basis. These weekly meetings made my graduate years at the University of Waterloo extremely enjoyable and unforgettable. Professor Raithby is not only a great teacher and advisor, with a wealth of insight and intelligence in his field of expertise, but also is a very considerate person. He was always concerned, when he was in my office, to not interrupt my office mates. In spite of his busy schedule, he always took care of his responsibilities as a super-supervisor very well. Without his support, patience and encouragement, particularly during the final corrections of this thesis, this work would have never been finished as it is.

Brief, but very useful comments and questions of Professor Stubley, and his co-supervision, when Professor Raithby was not available, are also much appreciated.

Regarding my teachers in Waterloo, I had the opportunity to study Professor Raithby's notes for ME780 (on the control volume method) and also to attend very well organized ME780 lectures of Professor Stubley. AM741 lectures of Professor Forsyth (on numerical solution of partial differential equations), ME664 lectures of Professor Strong (on turbulence) and CS770 lectures of Professor Simpson (on mesh generation) provided me the required background in the field. I also attended and enjoyed lectures of Professor Yovanovich (on conduction), Professor Mallinson (on computer graphics) and Professor Calamai (on optimization). Occasional short discussions with Professors R.A. Fraser and M. Renksizbulut, on classical thermody-

namics and heat transfer were useful and enjoyable.

I wish to take this opportunity to thank my dear brother Mahmud, for his assistance as the computer system administrator of the thermal group and for introducing me the Bezier curves. Without his help I could not settle down in Canada easily and have the privilege of working with Professor Raithby. I also owe thanks to my friends Dr. P. Zwart, for enjoyable conversations, to D. Yin for the Latex template file and enjoyable conversations, and to Stephen Reuss for friendly talks and always knowing what to do when I needed assistance or the computer system misbehaved.

The scholarship that I received from the Ministry of Culture and Higher Education of Iran and the financial support of the Natural Science and Engineering Research Council of Canada are gratefully acknowledged.

My love, respect and appreciation is extended to my dear parents for being my first teachers and for their continuous support throughout my entire life.

Finally, I would like to heartily appreciate my wife, Fahime. Without her sacrifices throughout our common life and in particular during our stay in Canada, I would have not been able to focus on and accomplish my work and achieve my goals. This thesis, in fact, is largely the outcome of her loving support and is dedicated, with love and respect, to her.

Contents

List of Figures

List of Tables

Nomenclature

Latin Letters

A, a	cross sectional area
$\tilde{A}_\Theta$	matrix of coefficients (discretized system of equations for Θ)
$\vec{A}_n, \vec{A}_{ni}$	normal vector whose magnitude is equal to the area
AR	duct area ratio (W_2/W_1)
$\tilde{B}_\Theta$	right hand side vector (discretized system of equations for Θ)
$B_i^\Theta, B_i^x, B_i^y, B^{xy\Theta}$	coefficients in Eq. 3.60
C_F	coefficient of friction
C^{im}	parameter defined in Eq. 3.31
C_{ij}	coefficients in Eq. 6.43
C_0, C_1, C_2	coefficients of the Das correlation
$C_i^\Theta, C_i^{RL}, C_i^{RU}, C^{R\Theta}$	coefficients in Eq. 3.64
$C_R^{LPE}, C_C^{LPE}, D^{LPE}$	coefficients in Eq. 4.5
$C_L^{LPW}, C_C^{LPW}, D^{LPW}$	coefficients in Eq. 4.6
D^i	parameter defined in Eq. 3.63
$\mathcal{F}_{\Theta i}$	diffusion flow of Θ at the integration point i
$\vec{F}_\Theta^D, \vec{F}_\Theta, \vec{F}_{\Theta i}$	diffusion flux of Θ
$\vec{F}_\Phi^C$	convective flux of Φ
$\vec{F}_\Phi^D$	diffusion flux of Φ
$\vec{g}, g_i$	the gravitational acceleration vector and its components
H	boundary layer shape factor
$\vec{i}$	Cartesian unit vector

$\vec{j}$	Cartesian unit vector
J	the determinant of the Jacobian of local-global transformation
K	thermal conductivity
k	turbulent kinetic energy, Karman constant
L	wall length, characteristic length
L_i^m	coefficients in Eq. 8.21
L_i^u	coefficients in Eq. 8.22
$L_{PW}, L_{PE}, L_{PS}, L_{PN}$	boundary line segments
M_i	coefficients in Eq. 6.42
$\vec{n}$	outward unit vector
N_i	shape function for node i, coefficients in Eq. 6.42
P	thermodynamic pressure
$\tilde{P}$	modified pressure
P_d	hydrodynamic pressure
P_e	pressure at the edge of the boundary layer
P_i	coefficients in Eq. 6.42
q	fluid speed, surface heat flux
Q	heat transfer rate
Q_i	coefficients in Eq. 6.42
R	spine coordinate
$\mathcal{R}^m, \mathcal{R}^u$	coefficients in Eq. 8.21 and 8.22
Re_θ	Reynolds number based on the momentum thickness
S	conduction shape factor, source term
s	element local coordinate, body fitted coordinate
s^*	normalized body fitted coordinate
T	temperature
t	element local coordinate
U	characteristic velocity
u_e	velocity at the edge of the boundary layer
u_i	velocity components (Cartesian)
u_τ	shear velocity
$\vec{V}$	velocity vector
V_1	inlet uniform velocity
W	width
x, X	x coordinate in a Cartesian reference frame

x_i	Cartesian coordinates
x_i^*	x coordinate of the spine i reference point
y, Y	y coordinate in a Cartesian reference frame
y_i^*	y coordinate of the spine i reference point

Greek Letters

α_p	defined in Eq. 3.25
β	Clauser equilibrium parameter
γ_{ij}	defined in Eq. 3.48
Γ	boundary of the computational domain
Γ_ϕ	a diffusion coefficient
Γ_{cv}	boundary surface of a discrete volume
δ	arbitrary perturbation in a quantity. boundary layer thickness
δ^*	boundary layer displacement thickness
δ_{ij}	Kronecker delta
Δ	offset. length of a one-dimensional control volume
Δ_1, Δ_2	duct size variables
Δ_{1C}, Δ_{2C}	critical (minimum) size variables
$\Delta x, \Delta y, \Delta \vec{r}, \Delta s, \Delta t$	line segments
η	stream function. ratio y^+/δ^+
θ	streamline angle. duct turning angle
θ	momentum thickness. non-dimensional temperature
θ^i	angle of the spine i
Θ	a generic scalar
λ_m	defined in Eq. 3.50
μ_{eff}	effective (dynamic+turbulent eddy) viscosity
ν, ν_t, ν_{eff}	laminar. turbulent and effective kinematic viscosity
$\vec{\xi}$	vorticity vector
Π	wake parameter
ρ	density
$\tilde{\tau}, \tilde{\tau_{ij}}$	total stress tensor
τ_W	wall shear stress
ϕ	scalar potential
Φ	a generic scalar
ψ	stream function

$\bar{\Psi}$	vector potential
Ω_{cv}	discrete volume
Ω	computational domain

Subscripts

a	ambient
e	east integration point
E	east node
ip	an arbitrary integration point
i	dummy variable
j	dummy variable
m	dummy variable
n	dummy variable
p	dummy variable
P	node under consideration
S	surface
W	wall. west node
w	west integration point
1	duct inlet
2	duct outlet

Superscripts

i	associated with node i (summation rule is not applied)
L	related to the lower surface
m	related to the mass equation. related to the internal node m
mA	coefficients of A in the discretized mass equation (Eq. 8.39)
mP	coefficients of P in the discretized mass equation (Eq. 8.39)
mU	coefficients of U in the discretized mass equation (Eq. 8.39)
u	related to the u-momentum equation
U	related to the upper surface
uA	coefficients of A in the discretized momentum equation (Eq. 8.40)
uP	coefficients of P in the discretized momentum equation (Eq. 8.40)
uU	coefficients of U in the discretized momentum equation (Eq. 8.40)
0	old or lagged value

$+$	normalized with the inner variable scales
$'$	fluctuating component
$*$	non-dimensional quantity. reference coordinate for a spine

Acronyms

CDS	Central Difference Scheme
CFD	Computational Fluid Dynamics
EB-FVM	Element-Based Finite Volume Method
FDM	Finite Difference Method
FEM	Finite Element Method
FVM	Finite Volume Method
PDE	Partial Differential Equation
SCV	Sub-Control Volume
SSD	Surface Shape Design
TPD	Target Pressure Distribution
TVD	Target Velocity Distribution

Chapter 1

Introduction

1.1 Motivation

The challenge of designing hardware involving fluid flow or heat transfer such as intake manifolds, duct reducers, fins, etc. is one of determining the shapes of the solid elements so that the flow or heat transfer rate is optimal in some sense. In these optimal shape design problems, an optimum flow or heat transfer condition is defined as the design objective and the shape which provides that particular condition is sought. Calculation of the optimum shape requires a computational algorithm which inevitably includes the flow field calculations. Often it is necessary to use numerical methods to be able to solve for the flow field. Therefore, both the Computational Fluid Dynamics (**CFD**) and design algorithms are involved in solving optimal shape design problems. Due to the complexity of the fluid flow calculations, in general, and the limitations and computational cost of the design techniques, these are challenging problems for the computational technology available at the present time.

In shape design problems, the shape of the flow field boundaries is unknown (or partially unknown) and therefore extra information in the flow domain or along the boundaries has to be specified to make the problem mathematically well-posed. In the most common form of optimal shape design problems, the pressure distribution along the boundaries of the domain is specified as the required extra information. This surface pressure distribution is called the target pressure distribution and the associated design problem is called a Surface Shape Design (**SSD**) problem. In surface shape design in the context of heat transfer problems, a target surface heat flux is often specified as the design objective.

There are basically two different algorithms for solving **SSD** problems: "direct"

and "iterative" techniques. Iterative design methods solve a sequence of "analysis" problems and iteratively correct the shape until the target pressure is approached. An analysis problem is defined as one in which the governing equations are solved for a prescribed geometry. Direct design methods relate the surface shape to dependent variables in the governing equations and provide an alternative form of the governing equations so that the solution to these equations directly gives the shape. For example, boundary coordinates could appear as unknowns in the alternative form of the governing equations.

Iterative methods, such as optimization techniques, have been by far the most widely used for solving practical **SSD** problems. However, these methods are computationally expensive. On the other hand, the available direct design methods are inherently limited to some simple (e.g. potential) flow models. Engineering would greatly benefit from improved direct design methods which are applicable for solving different flow or thermal problems and are less expensive computationally than iterative methods.

1.2 Objective

The objective of the current work is to develop a new direct design method for solving **SSD** problems. This method should apply to internal and external flows, should be applicable whether the full Navier-Stokes equations or a simplified set (e.g. potential flow) is applied as the flow model, and should be comparable or cheaper than iterative methods in terms of computational cost. In this thesis the basic idea is developed and implemented for some simple shape design problems.

The primary objective of the thesis, as just explained, is to propose a new direct solution technique for **SSD** problems. As is usual, and reasonable, the new proposal is applied to simple test cases. This provides insight into the possible implementation difficulties for more complex problems.

The following are considered as sub-objectives in this thesis:

- Develop a unified formulation of governing equations and computational algorithm which can be used in solving both the analysis and corresponding shape design problem.
- Apply the proposed method to design two-dimensional potential flow ducts.
- Apply the proposed method to design flow passages which have large potential cores and thin viscous wall layers (here called *short ducts*).

- Apply the method to design the shape of conducting materials , governed by the Laplace equation, to achieve a given target heat flux along the boundaries.
- Since much of the proof of concept work for the above sub-objectives is done with the Laplace equation as the flow model, there is a need to establish that the method is applicable to velocity-pressure formulations.

1.3 Outline

The thesis is divided into nine chapters, of which this is the first.

Chapter 2 reviews the relevant background and literature and briefly explains the basic idea behind the proposed method as compared to the available shape design methods.

Chapters 3 and 4 explain, in detail, how a unified formulation, as the discretized mathematical model of the Laplace equation, is obtained and the proposed direct design approach is implemented for the design of two-dimensional ducts in which the fluid motion is treated as potential flow. This simplified problem has challenged researchers for years. It is believed that the proposed method has distinct advantages compared to earlier methods, especially when it is implemented in the three-dimensional context.

In Chapter 5 the validation of the proposed potential flow duct design method is discussed. In real flows the effect of viscosity cannot be neglected throughout the flow field. For high Reynolds number flow in sufficiently short ducts, there is a potential core surrounded by a thin viscous layer all along the duct. The proposed direct shape design method for potential flows can be used in short duct design if an appropriate turbulent boundary layer analysis technique is also used. Therefore, in Chapter 6, turbulent boundary layer analysis and prediction of separation are discussed and a generalized integral boundary layer approach, based on the well known integral inner variable theory, is developed.

Chapter 7 is devoted to some engineering applications of the method at its current stage of development. In this chapter first some practically important *short ducts* are categorized into three general families of shapes and then design of these shapes is discussed. Afterwards, two families of shapes are introduced for two-dimensional heat conductors and a number of conduction shape design problems are solved. The ease of implementation of the method for solving different flow and thermal design problems, which have been solved separately and with different approaches during the years, is emphasized. Problems which are solved in this chapter are sufficient proof that the

proposed method is robust and has the ability of solving shape design problems with different levels of geometrical complexities.

Successful solution of the conduction and potential flow duct design problems confirms mainly the geometrical capability of the new method. There are many other difficulties that appear when the potential flow equation of motion is replaced by more complete equations expressed in terms of primitive variables. These issues arise for analysis problems, and persist for shape design problems as well. Chapter 8 may be considered as an introduction to those issues. In this chapter one-dimensional ideal flow in a duct is considered as the flow model. Even though this simple flow model is used to clarify the idea of the unified governing equations in the context of primitive variable formulation and implement the direct design method, the issues of pressure-velocity coupling and convection modeling are also discussed in some detail and some new ideas are introduced.

Areas of research which remain untouched in the current work will be addressed in a closure chapter. Chapter 9 wraps up the thesis with some final conclusions and discussions and proposes some topics for further research.

Chapter 2

Background

2.1 Introduction

This chapter is devoted to some of the required theoretical background and the relevant literature survey. The background material, and the survey, is presented in four sections.

In Section 2, engineering analysis and design problems are more precisely defined and categorized. Surface Shape Design (**SSD**) problems are then introduced as one of the sub-categories of engineering design problems.

In Section 3, alternatives for mathematically modeling fluid flow problems are addressed. Some of these alternatives are used to model the flow problems discussed in this thesis.

Noting that the mathematical models are often in the form of some Partial Differential Equations (**PDE**'s), the basic concepts related to the discretization and numerical solution of **PDE**'s, in the context of **CFD**, are discussed in Section 4. Some important features of the discretization technique used in the proposed direct design method are highlighted in this section.

Section 5 reviews two general families of algorithms for solving design problems, i.e. direct and iterative approaches. In Section 6 a direct shape design method, which is one of the contributions of this research work, is conceptually described and compared to the available design algorithms.

The chapter ends with a summary section.

2.2 Analysis and Design Problems in Engineering

Mathematical models for engineering problems are symbolic statements of some physical laws and models. These physical laws and models are obtained either directly from experiments or indirectly from many observations. The mathematical models are often in the form of some **PDE**'s which are called the governing equations. The governing equations for fluid flow problems, which are the main focus here, when written in the Eulerian form, specify how unknown quantities (dependent variables) vary with respect to time and space (independent variables). The physical-based mathematical models are not always well posed. Well posedness is defined based on the definition given by Hadamard [1]. A mathematical problem is well posed if its solution exists, is unique and is stable. Stability here means continuous and smooth dependency of the solution (output) on the given information (input).

Analysis problems in engineering may be defined as those well-posed problems in which the governing **PDE**'s, the solution domain Ω bounded by the boundary Γ, and a set of *appropriate* boundary and initial conditions (hereafter called the *formal* conditions) are known. The distribution of the dependent variables inside the solution domain and along its boundary is the result or output of the analysis.

In contrast, in engineering *design problems* some extra information (hereafter called the *extra* conditions) is provided and because of this over-specification of the input data, compared to the corresponding analysis problems, more unknowns can be found (designed).

There is no universally accepted categorization for different engineering design problems, to the knowledge of the author, in the context of thermo-fluid problems. However, it is beneficial to classify them in terms of the knowns and unknowns. Based on what has appeared in the literature [2–8], it seems logical to define four types of thermo-fluid design problems. In the proposed categorization, the first descriptor (*field* or *surface*) refers to the location where extra information, compared to the analysis formulation, is provided. The second descriptor (*value* or *shape*) refers to whether additional solution variables must be calculated or the shape must be found. Here, for the sake of simplicity, only steady problems are taken into the consideration. The four types of design problems are:

- field value design problems,
- surface value design problems,
- field shape design problems,

- surface shape design problems.

In the field value design problems, the shape of the solution domain (Γ), part of the boundary conditions and some extra information in Ω are given and the field dependent variables as well as missing boundary conditions are sought. In the surface value design problems, the extra information is provided at the boundary (Γ) and to render the problem well posed, some unknown sources or sinks have to be determined in the domain Ω.

Correspondingly, in field shape design problems, boundary conditions and some extra information in the solution domain are given and the field dependent variables as well as the shape of the missing part of the boundary (Γ) are sought. In the surface shape design problems, the extra information is provided at the boundary whose shape is unknown.

Note that the proposed categorization can be extended to unsteady problems as well.

Optimal shape design problems, which were briefly introduced in the previous chapter, are now described as one of the sub-categories in Surface Shape Design (**SSD**) problems. In aerodynamic or hydrodynamic **SSD** problems, a Target Pressure Distribution (**TPD**) is specified as the extra given information. The pressure distribution, specified at the domain boundary, is directly related to many important engineering phenomena such as lift, drag, separation, cavitation, frictional losses and shock waves. Therefore, the **TPD** may be specified to achieve objectives such as lift maximization, drag minimization or other design objectives. It should be noted that the solution of a **SSD** problem is not generally an optimum solution in a mathematical sense. The optimality, in many of the applications, is not studied rigorously in this type of the design problem; it just means that the solution satisfies a **TPD** which resembles a nearly optimum performance. In other words, it is assumed that an optimized **TPD** is known as the objective and the solution of the corresponding surface shape design problem is considered, then, as the optimum.

In heat transfer **SSD** problems, a target surface heat flux is specified as the extra information.

2.3 Formulation of the Flow Governing Equations

In both analysis and design problems, the equations governing the relevant physical phenomena have to be known. The phenomenon of steady incompressible flow of a Newtonian fluid inside a duct is considered in this thesis. The governing equations for

these types of flow problems are the conservation statements for mass and momentum. The issue of the formulation of the required governing equations is considered in this section.

2.3.1 Primitive Variable Formulation

When pressure P and velocity $\vec{V}$ are considered as the field variables, the mass and momentum constraints for a steady incompressible flow are written as follows [9]:

$$\vec{\nabla} \cdot \vec{V} = 0. \tag{2.1}$$

$$\rho \vec{V} \cdot \vec{\nabla} \vec{V} = \rho \vec{g} + \vec{\nabla} \cdot \tilde{\tau}. \tag{2.2}$$

This form of the governing equations is independent of the coordinate system and the theorems and techniques of vector calculus can be easily applied to obtain alternative forms of the governing equations. In a Cartesian reference frame, which is more convenient for discretizing the equations and used here to mathematically model the problems, the mass constraint is[1]:

$$\frac{\partial u_i}{\partial x_i} = 0. \tag{2.3}$$

The i component of the momentum equation is:

$$\frac{\partial (\rho u_j u_i)}{\partial x_j} = \rho g_i + \frac{\partial (\tilde{\tau_{ij}})}{\partial x_j}. \tag{2.4}$$

In these equations all the dependent quantities are time averaged so that the equations are valid for both laminar and turbulent flows. $\vec{V}$ is the velocity with components u_i , $\vec{g}$ is the gravitational acceleration vector with components g_i and $\tilde{\tau}$ is the total (laminar + turbulent) stress tensor with components $\tilde{\tau}_{ij}$. The Stokes viscosity law gives the constitutive equations, which specify the relationship between stress and the rate of deformation for the laminar flow of a Newtonian fluid. Based on the Stokes postulates, equations for the normal and shear stresses in laminar flows are obtained.

A common modified form of the Stokes law combined with the eddy viscosity assumption is often used in turbulence modeling when the time-averaged form of the

1. Einstein summation is assumed.

equations are used [10, 11]. The modified form is introduced here as follows[2]:

$$\tilde{\tau_{ij}} = \delta_{ij}\left[-P - \frac{2}{3}\rho k\right] + \mu_{eff}\left(\frac{\partial u_i}{\partial x_j} + \frac{\partial u_j}{\partial x_i}\right). \tag{2.5}$$

In this equation, P is the thermodynamic pressure of the fluid, μ_{eff}, is the sum of the dynamic viscosity, μ, which is a fluid property, and the turbulent eddy viscosity, μ_t, which is a flow property and k is the turbulent kinetic energy.

The pressure gradient, which is part of the $\vec{\nabla} \cdot \tilde{\tau}$ term in Eq. 2.2, arises from both the hydrostatic effect which depends on $\vec{g}$ and a "hydrodynamic" component which depends on the fluid motion. The hydrostatic pressure gradient is defined as equal and opposite to the $\rho\vec{g}$ term so these terms cancel out of the momentum equation. This cancelation makes sense because, for example, the velocity field around a moving fish is the same regardless of the depth of the water (considered truly incompressible). Therefore, combining the turbulent kinetic energy term, which is a scalar quantity, with the hydrodynamic pressure, the momentum conservation can be written as follows:

$$\frac{\partial(\rho u_j u_i)}{\partial x_j} = -\frac{\partial P_d}{\partial x_i} + \frac{\partial}{\partial x_j}\left[\mu_{eff}(\frac{\partial u_i}{\partial x_j} + \frac{\partial u_j}{\partial x_i})\right]. \tag{2.6}$$

Knowing that density variations are negligible in incompressible isothermal flows, this constant quantity can also be cancelled to get another simplified version of the momentum equation:

$$\frac{\partial(u_j u_i)}{\partial x_j} = -\frac{\partial \tilde{P}}{\partial x_i} + \frac{\partial}{\partial x_j}\left[\nu_{eff}\left(\frac{\partial u_i}{\partial x_j} + \frac{\partial u_j}{\partial x_i}\right)\right]. \tag{2.7}$$

In this equation, $\tilde{P}$ stands for P_d/ρ and $\nu_{eff} \equiv \nu + \nu_t$ is the effective kinematic viscosity.

It is clear that the mass and momentum constraints provide four equations for the four unknowns in a general three-dimensional steady incompressible flow, i.e the velocity components and the (modified) pressure. In turbulent flows a set of equations, provided by the turbulence model, should be solved for the unknown ν_t. In spite of the fact that there are enough independent equations for finding the unknowns from the mathematical point of view, a problem arises in the numerical solution of the set because the pressure does not appear in the continuity equation. The

2. In most of the references the Reynolds stresses are written and then modeled. The final result will be similar to the modified form of the Stokes law as is introduced here.

strategy for solving these coupled set of equations has been, and still remains, a matter of debate. The momentum equations can always be solved for arbitrarily specified pressure fields. In other words there is a multiplicity of flow fields that satisfy the momentum equations. The correct pressure field is the one that results in a velocity field which also satisfies continuity equation. The formulation that allows pressure to play this role in the satisfaction of continuity in **CFD** solutions of these equations is called the pressure-velocity coupling algorithm. Pressure-velocity coupling is discussed in the eighth chapter of this thesis and some new ideas in that regard will be introduced then.

Pressure and velocity are measurable quantities and appear naturally in the governing equations when the conservation principles are formulated mathematically. Therefore, the above formulation is called the primitive-variable formulation. If the effect of the viscosity is negligible, the inviscid flow assumption can be used and the momentum equation simplifies to the following:

$$\frac{\partial (u_j u_i)}{\partial x_j} = -\frac{\partial \tilde{P}}{\partial x_i}. \tag{2.8}$$

This form of the momentum equation simply states a balance between pressure and momentum change. The governing equations of inviscid flows are known as the Euler equations. The following forms of the momentum constraint in the Eulerian flows can be obtained by using the concepts and identities of vector calculus [12]:

$$\vec{\nabla} \cdot \vec{V}\vec{V} = -\vec{\nabla}\tilde{P}. \tag{2.9}$$

$$\vec{V} \cdot \vec{\nabla}\vec{V} = -\vec{\nabla}\tilde{P}. \tag{2.10}$$

$$\vec{\xi} \times \vec{V} + \vec{\nabla}\left(\frac{1}{2}q^2\right) = -\vec{\nabla}\tilde{P}. \tag{2.11}$$

In these equations, $\vec{\xi}$ stands for the vorticity ($\vec{\xi} = \vec{\nabla} \times \vec{V}$), q is the fluid speed ($q = |\vec{V}|$) and $\vec{V}\vec{V}$ is the dyadic product for the velocity vector.

The equations of motion for both viscous and inviscid flows can be manipulated into different forms with alternative dependent variables [13]. Some of the formulations for inviscid flows are reviewed in the next section.

2.3.2 Secondary Variable Formulation

One well known idea is to eliminate the pressure from the equations. While there are some benefits in eliminating pressure, new difficulties arise. One obvious difficulty is that extra work is required to calculate the pressure field separately. Also, the physical-based primitive variable formulation is replaced by a set of mathematically obtained equations and one should be very careful to not lose physical clarity in favor of mathematical beauty!

The pressure is eliminated from momentum by taking the curl of Eq. 2.11:

$$\vec{\nabla} \times \vec{\xi} \times \vec{V} = 0. \tag{2.12}$$

Now, Eq. 2.1 and 2.12 are the governing equations for the steady inviscid incompressible flows. Equation 2.1 constrains the incompressible velocity fields to be divergence-free (solenoidal). If the velocity field is defined as the curl of another vector field, it will be solenoidal and continuity is automatically and unconditionally satisfied. Therefore, assuming $\vec{V} = \vec{\nabla} \times \vec{\Psi}$, renders the following governing equations:

$$\vec{\nabla} \times \left[\vec{\nabla} \times \left(\vec{\nabla} \times \vec{\Psi}\right)\right] \times \left(\vec{\nabla} \times \vec{\Psi}\right) = 0. \tag{2.13}$$

The vector quantity $\vec{\Psi}$ is known as the vector potential in calculus [12] and stream vector in fluid mechanics [14]. The stream function (ψ) is often considered as the two-dimensional counterpart of $\vec{\Psi}$, although it is not strictly true from the mathematical and physical point of view. It is important to note that the field variable in the $\vec{\Psi}$ formulation is still a vector quantity whose physical interpretation in three-dimensional flows is not an easy task.

Another idea for automatically satisfying the mass constraint and defining a solenoidal velocity field, is to use a pair of stream functions (ψ, η) and defining the velocity field as $\vec{V} = \vec{\nabla}\psi \times \vec{\nabla}\eta$ for a general three-dimensional flow. In this case the governing equations are obtained from the following vector equation:

$$\vec{\nabla} \times \left[\vec{\nabla} \times \left(\vec{\nabla}\psi \times \vec{\nabla}\eta\right)\right] \times \left(\vec{\nabla}\psi \times \vec{\nabla}\eta\right) = 0. \tag{2.14}$$

The mathematical structure of this equation looks horrible and in fact it is. However, better physical interpretation of the stream functions, compared to the vector potential, is the benefit.

If the flow is assumed to be irrotational as well ($\vec{\xi} = 0$), then Eq. 2.13 and 2.14

respectively simplify to:

$$\vec{\nabla} \times \left(\vec{\nabla} \times \vec{\Psi} \right) = 0. \tag{2.15}$$

$$\vec{\nabla} \times \left(\vec{\nabla}\psi \times \vec{\nabla}\eta \right) = 0. \tag{2.16}$$

For incompressible irrotational (ideal) flow applications, another formulation (ϕ formulation) has been proposed in which just one scalar parameter (the scalar potential or ϕ) is required. For potential flows, the velocity is defined as $\vec{V} = \vec{\nabla}\phi$. This definition automatically satisfies the irrotationality condition, which replaces the momentum equations, and renders the mass constraint as below:

$$\vec{\nabla} \cdot \left(\vec{\nabla}\phi \right) = \nabla^2\phi = 0. \tag{2.17}$$

Although the application of this idea is limited to ideal flows, the flow field is described by just one scalar quantity, no matter how many spatial dimensions are involved. The unknown scalar potential is given by the Laplace equation (Eq. 2.17). This equation is probably the most well known equation in mathematical physics and all the mathematicians, physicists and engineers would love it!

Having appropriate mathematical models for the flow problem, the question now is how to solve the equations. The next section discusses this issue.

2.4 Numerical Solution of the Governing Equations

In the past few decades **CFD** has advanced tremendously. The basic idea of **CFD** is to replace the governing differential equations (including the initial and boundary conditions) with algebraic equations. **CFD**, as a technology, depends heavily on computer hardware and software. Due to the amazing development in computer technology, **CFD** has become an indispensable tool in thermo-fluid analysis and design. From the implementation point of view, the issues of pre-processing, processing and post-processing are the major subdivisions in **CFD**. The evolving picture of **CFD**, from the point of view of the discretization and solution techniques, has been reviewed comprehensively by some of the experts in the field over recent years [15–25].

Traditionally, in the context of the analysis problems and assuming that the governing equations are appropriately formulated, the following issues are discussed separately in **CFD**:

- issues related to the discretization:
  - discretization of the solution domain (grid generation),
  - discretization of the governing equations (interpolation schemes),
- issues related to the numerical solution of discrete equations:
  - solver technology and performance.

These issues are now briefly explained in the following sub-sections.

2.4.1 Discretization of the Solution Domain

The issue of the solution domain discretization, or grid generation, is an important part of **CFD**. The accuracy of the numerical solution, and the solver performance, depend strongly on the quality of the grid. Commonly, time and space are discretized separately but discretization of the time-space domain has also been investigated by some researchers [26]. Time is usually discretized by simply defining some time steps. Regarding the discretization of space there are, at least conceptually, two basic discretization approaches.

In the first spatial discretization approach, one may directly define a number of points in the solution domain (nodes or grid points) on which the unknowns are approximately calculated. This type of the grid for a simple rectangular domain is shown in Figure 2.1. For lack of a better name, it is referred to here as a finite-difference type grid [1].

Another approach, more popular in solid mechanics, is to approximate the solution domain by some sub-domains, called finite elements. In the latter type of the grid, nodes are defined at different locations on or inside the elements, but usually at the element vertices. Figure 2.2 shows a finite element type grid in a rectangular domain with the nodes defined at the element vertices.

In fluid flow problems, as will be explained in the next section, it is beneficial to associate with each node a specified region in the domain, called a control volume. In conventional finite volume methods, control volumes are associated with each node as is shown in Figure 2.3 [27]. One may first define the nodes and then specify the control volumes (vertex-centered mesh in which each control surface is located midway between two neighbor nodes) or first define the control volumes and then specify the

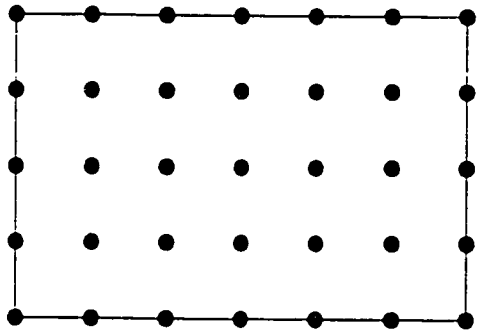

Figure 2.1: A finite difference type grid.

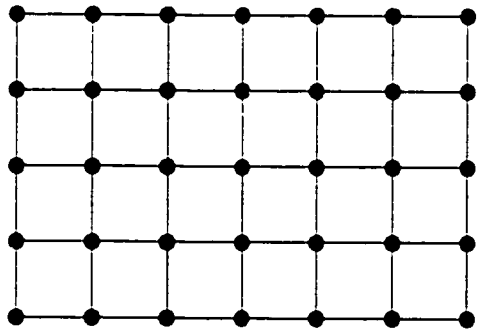

Figure 2.2: A finite element type grid.

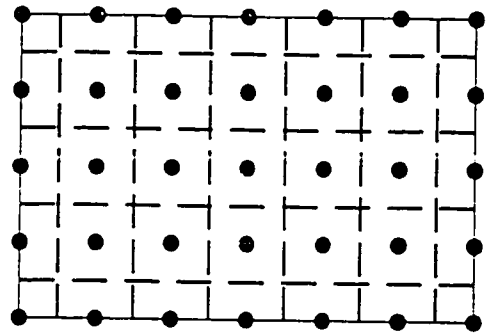

Figure 2.3: Control volumes defined in a finite difference type grid.

nodes (cell-centered mesh in which the nodes are located in the centers of the control volumes).

More recently another interesting space discretization technique has been used by researchers [28–30] and in some commercial codes [11][3]. It has been common to first define the elements (solid lines in Figure 2.4) and then the control volumes (dashed lines). Considering the fact that the grid points are often defined at the element vertices, the nodes are not necessarily in the center of the control volumes and the grid is basically vertex-centered . In [11] the discretization of the space using both finite elements and control volumes has been described in detail for three-dimensional Cartesian domains. Figure 2.4 shows a two-dimensional rectangular domain discretized by finite elements and control volumes. In this thesis, both finite elements and control volumes are used and further details about this form of the grid will be discussed in the next chapter.

There are other categorizations for computational grids among which the followings are particularly important:

- orthogonal or non-orthogonal.

3. Baliga and Patankar were the first researchers who acknowledged the benefits of using both finite elements and control volumes in the context of **CFD** [28]. They preferred to call schemes which use both finite elements and control volumes, *control-volume-based finite element methods.*

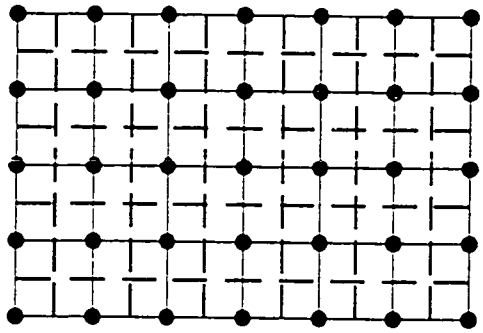

Figure 2.4: A finite element-based control volume grid.

- structured or unstructured.

Non-orthogonal computational grids allow more flexibility in the placement of nodes with a very modest increase in complexity compared to orthogonal grids. Unstructured meshes provide still greater flexibility but with considerable added complexity. The ability to change the shape and the resolution of the grid is important in solving geometrically complex problems. Having an unstructured mesh that automatically adapts to provide an optimized solution is something that **CFD** experts are eagerly looking for.

In this thesis, domains are discretized using structured non-orthogonal grids. These grids provide sufficient flexibility for the geometries encountered without increasing the complexity associated with unstructured meshes.

2.4.2 Discretization of the Governing Equations

Discretization methods for the flow governing equations can be divided into three major groups, at least from a historical point of view.

The Finite Difference Method (**FDM**) is the oldest method used to solve differential equations. Various schemes in the **FDM** give point-wise approximations of the actual solution. In fact the method is based on the difference approximation of the derivatives obtained from truncated Taylor series.

The Finite Element Method (**FEM**) was first developed for stress analysis in

solid mechanics and later was used in thermo-fluid problems as well. In this method, the solution is approximated by some profiles in a piecewise manner. Shape functions are used in the assumed profiles.

The Finite Volume Method (**FVM**) was specifically designed to retain and guarantee the conservation properties over the finite volume associated with each node during the numerical modeling. The **FVM** originally used finite difference type grids and discretization techniques and because of that may be called the difference-based finite volume method. Another version of **FVM** which is called the Element-Based Finite Volume Method (**EB-FVM**) preserves the traditional conservation philosophy of **FVM**, but uses the geometrical as well as the algorithmic advances in the **FEM**. In other words **FVM** is a conservative numerical approach which may use point or piece-wise approximations to numerically model the problem.

While many consider the **FVM** to be very close to **FDM**, it has been explained in some references (e.g. [31]) that in fact **FEM** and **FVM** are both members of one family, called the method of weighted residuals. This issue has been studied by some researchers [28, 32] and it is now believed that the distinction between the methods is not always clear. Of course the philosophies of the methods are different and because of that, they are introduced here as different approaches.

While more detailed explanations about the **FVM** are given in Chapter 3, where the method is used for the numerical solution of a specific flow problem, here one important feature of successful **FVM** schemes, i.e. correct modeling of the transportive properties of the flow field, is emphasized. As is explained in [31], the **FVM** needs exact integral conservation equations as the starting point. These integral expressions may be obtained by directly expressing the conservation laws for a chosen finite volume or by integrating the divergence form of the differential conservation laws. The divergence form of the transport (conservation) equation for the generic scalar Φ, defined per unit mass, in the presence of a known velocity field is [27]:

$$\frac{\partial(\rho\Phi)}{\partial t} + \vec{\nabla}\cdot(\vec{F}_\Phi^C) + \vec{\nabla}\cdot(\vec{F}_\Phi^D) = \dot{S}_\Phi. \tag{2.18}$$

The generic terms, which are all per unit volume, are as follow:

- rate of storage of Φ.
- convective flux of Φ: $\vec{F}_\Phi^C = \rho\vec{V}\Phi$.
- diffusive flux of Φ (Γ_Φ represents a diffusion coefficient): $\vec{F}_\Phi^D = -\Gamma_\Phi\vec{\nabla}\Phi$.
- rate of generation (or dissipation) of Φ.

Equation 2.18 represents the differential form of mass conservation ($\Phi = 1$), momentum conservation (Φ represents the Cartesian velocity components), energy conservation (Φ is internal energy), etc. The starting point in the **FVM** is the integral of the above equation over the discrete volume Ω_{cv} with surface Γ_{cv} and outward unit normal vector $\hat{n}$:

$$\frac{d}{dt}\int_{\Omega_{cv}}(\rho\Phi)d\Omega + \int_{\Gamma_{cv}}\vec{F}_{\Phi}^{C}\cdot\hat{n}d\Gamma + \int_{\Gamma_{cv}}\vec{F}_{\Phi}^{D}\cdot\hat{n}d\Gamma = \int_{\Omega_{cv}}\dot{S}_{\Phi}\,d\Omega. \tag{2.19}$$

The surface integrals in Eq. 2.19 are usually approximated by discretizing the surface into discrete panels, and evaluating Φ at an integration point on each panel from values of Φ at neighboring nodes. These interpolated values should be both "accurate" and have correct "transportive properties". Accuracy requires that the interpolated value lies on an accurate profile spanning the neighbor points, so that the value is reasonable and the error diminishes quickly with grid refinement. Correct transportive properties requires some kind of upwinding, so that the influence of the surrounding nodes on the interpolated value at the integration point is physically correct. Stubley *et.al.* [33] show how "profile" and "operator" errors propagate to produce the solution error. It is shown, for example, how a higher order scheme (which is accurate) can lead to a large solution error if the transportive properties of the approximation are incorrect (i.e. there is large operator error).

Ferziger and Peric [34] point out that successful application of **CFD** requires background in both fluid mechanics and numerical analysis. Accordingly, the discretization methods used in **CFD** should be flexible enough to satisfy both physical and mathematical requirements. The **FVM** is capable and adaptive enough to take care of both and therefore it is often the chosen approach in **CFD**.

The issue of obtaining robust and accurate discretization schemes for the convective and diffusive fluxes, in particular, has been (and is) one of the most important issues in **FVM**. In fact discretization schemes in **FVM** are different mainly because they provide different computational molecules for the diffusion and advection fluxes [35]. Generally speaking, the diffusion phenomenon is not as complicated as convection. For that reason much of the efforts in **CFD** have been devoted to convection modeling [36, 37].

Considering all these factors, in this thesis, **EB-FVM** is selected for the numerical modeling of the problems. Because only steady problems are considered here, the transient term of the generic governing equation will no longer be discussed.

The issues of robustness and accuracy of the numerical schemes are not only

important from the point of view of the analysis problems in **CFD**, but also have great impact on the numerical solution of the design problems. This point will be addressed later again when the new direct design method and the unified discrete formulation are discussed.

2.4.3 Solution of the Discretized Equations

The numerical solution of the discretized equations (the solver issue) is another important part of **CFD** technology. However, it is beyond the objectives of this thesis to consider this issue. Although iterative solvers are often chosen for solving complex problems with many thousands or millions of unknowns, here an appropriate direct sparse matrix solver [38] is used for solving the algebraic equations obtained as the result of the discretization of the governing equations. The formulation and solution of the discrete equations were treated as separate issues, and the focus here was on the formulation.

2.5 Surface Shape Design Algorithms

SSD problems can be solved by two families of methods, i.e. iterative and direct methods.

In the iterative methods for solving flow design problems, governing equations in their primitive or secondary variable forms are used, and a sequence of analysis problems are solved in which the surface shape is altered between iterations in such a way that the desired **TPD** is approached.

In the direct solution approach, an *alternative* formulation of the problem is used in which the surface coordinates appear (explicitly or implicitly) as dependent variables. In other words, direct methods tend to find the unknown part of the boundary and the flow field unknowns simultaneously in a (theoretically) *single-pass* or *one-shot* approach. In this section, available iterative and direct design methods are reviewed. The emphasis will be on the internal potential flows but the survey covers more general flow situations.

2.5.1 Iterative Design Algorithms

In Figure 2.5 a general iterative design flow chart is shown. All the iterative methods start with an initial guess, solve the corresponding analysis problem and then correct

the shape, and repeat until a convergence criterion (normally defined as the difference between the current surface pressure distribution and the **TPD**) is satisfied. The difference among the available iterative methods is how they correct an initial guess. The correction strategy is the most important part of an iterative design algorithm. In simple iterative techniques, the designer has to define special, problem dependent,

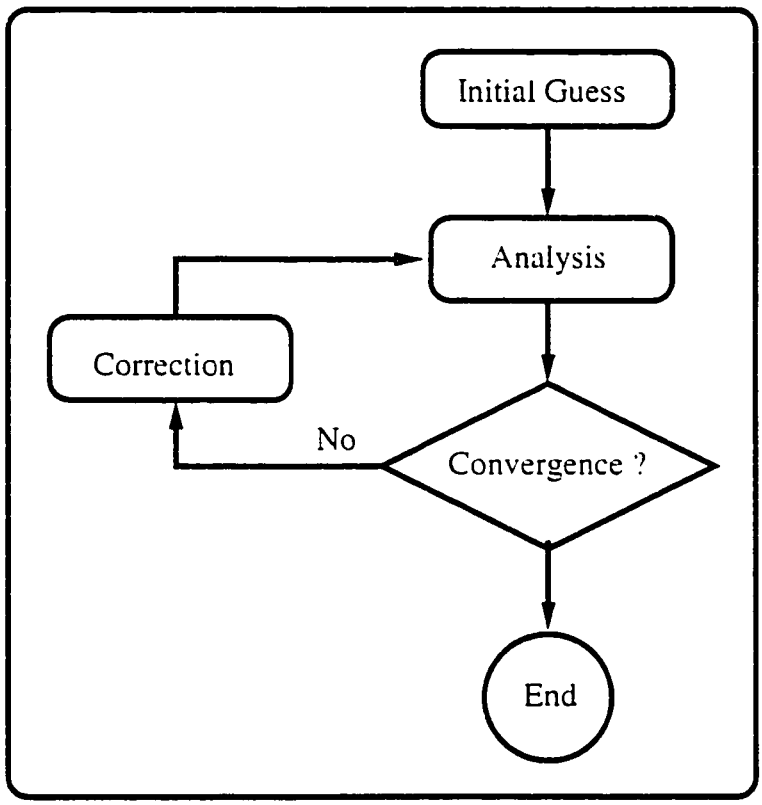

Figure 2.5: Iterative design algorithm.

correction rules. Obviously these methods lack generality. In [39], a simple iterative technique is proposed for solving two-dimensional internal potential flow design problems. In that reference the analysis problem is solved and the results of the analysis are used to calculate the Surface Tangential Velocity (**TVD**) distribution[4]. The calculated velocity at each boundary node is then compared to the **TVD** at that node.

4. Note that in ideal flows the pressure and velocity are related through the Bernoulli equation. Therefore one may use the surface velocity distribution instead of the pressure distribution.

The corrector, then, decides how to change the position of the nodal point to alter the velocity at that location. One obvious difficulty is that the relocation of each node is done independently and the effects of the neighbors are not taken into consideration. Consequently the convergence is often very slow in simple iterative techniques. If the initial guess is not good enough, the iterations will not converge at all.

Optimization techniques offer an automatic correction routine for solving **SSD** problems. This, in principle, makes the optimization methods problem independent. Ideally, a **CFD** code can be linked to an optimizer to get an optimization (iterative) algorithm. No special, problem dependent, policy is required and an automatic mathematical procedure is used in the optimizer. In terms of the common terminology in the optimization [40], an *objective function* has to be defined. The objective function in fluid flow **SSD** problems, which has to be minimized, is defined as a weighted difference between the current surface pressure distribution and the **TPD**. *Constraints* may also be defined. In each iteration the optimizer checks the objective function, determines the search direction and finally chooses a step size (magnitude of the change in the design variables which should be implemented in the search direction). Generally speaking, different optimizers use different logic to find the search direction and the step size in each iteration. In terms of the elements of the general iterative algorithm (shown in Figure 2.5) they use different correctors. Optimization methods have been used for solving many different **SSD** problems successfully, mostly in external flows [41–53]. In [54–56] examples of applications of optimization techniques in solving shape design problems in the context of heat transfer have been given.

In recent years the application of evolutionary and genetic algorithms, which may be considered as trained optimizers, has been an interesting research topic and some researchers have tried to use it in some applications [57–60]. The major shortcoming of the optimization methods, which has been the driving force for the development of the control theory-based approaches, is the huge computational cost in real practical design problems [61,62].

The control theory approach tries to reduce the computational cost in optimization techniques by offering a more efficient method for finding a search direction in each iteration. Instead of calculating the sensitivities, a set of equations, called the *adjoint equations*, are solved to find a search direction in each iteration [63,64]. It has been claimed that the control theory approach is more efficient than the optimization techniques, when the number of unknowns is very high [65].

2.5.2 Direct Design Algorithms

The idea of using an *alternative (inverse) formulation* for solving a design problem, just as using a *regular (direct) formulation* in an analysis problem, seems very attractive. However, there are many difficulties. It is well known, even from very basic algebra, that the inverse formulation of a well-posed problem is not going to work well in general [66]. The same thing happens for the mathematical models (governing equations) used in the flow problems. As a matter of fact the flow equations at the continuous level, are so complex that one cannot, in general, even find an inverse formulation for the problem. However, there are certain simplified flow situations in which the alternative (inverse) formulation idea works.

Stanitz [67], in a very remarkable study, noted that for potential flow **SSD** problems there is such an opportunity. He showed that an alternative formulation to the Laplace equation for steady ideal flows can be formulated in a transformed computational space. This alternative formulation for the two-dimensional case is:

$$\frac{\partial^2(\ln V)}{\partial\psi^2} + \frac{\partial^2(\ln V)}{\partial\phi^2} = 0. \tag{2.20}$$

Where ψ is the stream function and ϕ is the potential function. In the Stanitz shape design method, the **TVD** is required along the boundaries of the solution domain in the computational space. When Eq. 2.20 is solved with appropriate boundary conditions (Stanitz used the **FDM** to solve the equation), x and y coordinates of the stream and iso-potential lines and the distribution of the flow angles along them can be calculated through the following equations [68]:

$$\theta = \int_{\psi} \frac{\partial \ln V}{\partial\psi}\, d\phi. \tag{2.21}$$

$$\theta = -\int_{\phi} \frac{\partial \ln V}{\partial\phi}\, d\psi. \tag{2.22}$$

$$x = \int_{\psi} \frac{\cos\theta}{V} d\phi. \tag{2.23}$$

$$x = -\int_{\phi} \frac{\sin\theta}{V} d\psi. \tag{2.24}$$

$$y = \int_{\psi} \frac{\sin\theta}{V} d\phi. \tag{2.25}$$

$$y = \int_{\phi} \frac{\cos\theta}{V} d\psi. \tag{2.26}$$

In these equations θ stands for the direction of the streamlines at each point, and the duct geometry is obtained by knowing the stream function values of the boundary stream lines. This method needs special treatments at the stagnation points. Stanitz method has been used by many researchers for solving shape design problems in both internal and external flow problems [69].

About thirty years after the two-dimensional solution, Stanitz published the equally remarkable three-dimensional version of his method [70]. Stanitz solves the three-dimensional potential duct design problem in the $\phi - \psi - \eta$ computational space (ψ and η are pair of stream functions which make the stream tubes in the three-dimensional space). The simplified final working form of the (alternative) governing equation for the three-dimensional ideal flow shape design problems is as follows:

$$\begin{aligned}
&\frac{\partial^2}{\partial\phi^2}\left[\ln(V) + \ln(\sin\theta)\right] + B^2\frac{\partial^2}{\partial\psi^2}\left[\ln(V)\right] + A^2\frac{\partial^2}{\partial\eta^2}\left[\ln(V)\right] + \\
&B^2\left[\frac{\partial}{\partial\psi}(\ln B)\cdot\frac{\partial}{\partial\psi}(\ln V)\right] + A^2\left[\frac{\partial}{\partial\eta}(\ln A)\cdot\frac{\partial}{\partial\eta}(\ln V)\right] - \\
&\left[\frac{\partial}{\partial\phi}(\ln B)\cdot\frac{\partial}{\partial\phi}(\ln V) + \frac{\partial}{\partial\phi}(\ln B)\cdot\frac{\partial}{\partial\phi}(\ln B)\right] - \\
&\left[\frac{\partial}{\partial\phi}(\ln A)\cdot\frac{\partial}{\partial\phi}(\ln V) + \frac{\partial}{\partial\phi}(\ln A)\cdot\frac{\partial}{\partial\phi}(\ln A)\right] + \\
&B\left[\frac{\partial\hat{e_\psi}}{\partial\phi}\cdot\frac{\partial\hat{e_\phi}}{\partial\psi} - \frac{\partial\hat{e_\psi}}{\partial\psi}\cdot\frac{\partial\hat{e_\phi}}{\partial\phi}\right] + A\left[\frac{\partial\hat{e_\eta}}{\partial\phi}\cdot\frac{\partial\hat{e_\phi}}{\partial\eta} - \frac{\partial\hat{e_\eta}}{\partial\eta}\cdot\frac{\partial\hat{e_\phi}}{\partial\phi}\right] = 0.
\end{aligned} \tag{2.27}$$

In this equation $A \equiv (d\eta/d\psi)\sin\theta$, $B \equiv (dm/d\eta)\sin\theta$ and ds, dn and dm are differential path lengths in the directions $\hat{e_\phi}$, $\hat{e_\psi}$ and $\hat{e_\eta}$. Two stream surfaces ($\psi = const.$ and $\eta = const.$) intersect each other on potential surfaces with the angle θ ($0 \leq \theta \leq 180°$). Equation 2.27 should be solved in the $(\phi - \psi - \eta)$ space for the unknown $(\ln V)$. Auxiliary integral equations (like Eq. 2.21 to 2.26) then have to be solved for the duct shape. Note that the above formulation which is used to solve a three-dimensional ideal flow problem in the computational space is considerably more complicated than the Laplace equation.

It is interesting to note that Stanitz mentions an ill-posedness in three-dimensional potential duct design problems. He points out, however, that the ill-posedness is not serious and one can solve the problem using reasonably compatible prescribed upstream boundary shapes and prescribed velocity distributions on lateral boundaries [71]. Stanitz used his method for designing aerodynamically efficient ducts [72], showed how his method can be used for designing high solidity cascades and validated his numerical calculations experimentally [73].

In 1995, Chaviaropoulos *et.al* solved the three-dimensional potential duct design problem with another approach [74–78]. They proved that the problem was ill-posed (accepted multiple solutions) and showed how the multiplicity can be alleviated. Their method is again based on the potential-stream function formulation where the physical space is mapped onto a computational one via a body fitted coordinate transformation. Although the Chaviaropoulos *et.al* approach uses the same type of variables as the Stanitz method, they derive the final governing equations from differential geometry and generalized tensor analysis arguments. The final working equations in their approach are somewhat more complicated than in the Stanitz method.

The use of stream functions (ψ and η) or stream vector ($\vec{\Psi}$) in solving non-recirculating flow problems (both analysis and design), has been studied by many researchers. These are attractive because they are not limited to the inviscid and potential flow applications and do not have some of the difficulties of the primitive variable formulation.

Flow field calculations using the familiar concept of stream functions, has been studied by some researchers. Dulikravich [79], Greywall [80–82] and many others [83–90] have used the stream functions to solve flow problems. The problem with these approaches is the difficulties associated with the vorticity which appears in rotational inviscid and in viscous flows. When there are recirculation zones in the flow field, stream function-based methods face the difficulties associated with unbounded values of the stream functions. To the knowledge of the author, stream functions have not been used to solve design problems in the context of three-dimensional viscous flows.

The stream vector concept has failed to provide a general solution technique for complex flow problems, although there are many successful applications limited to certain flow situations [91–102]. The main difficulty is the implementation of the stream vector boundary conditions [103]. In fact, the application of the vector potential concept in three-dimensional problems with arbitrary geometries, even inviscid

flow type problems, has some difficulties which at the present time and to the knowledge of the author, have not been solved in a satisfactory manner. Lack of generality for solving analysis problems and difficulties in implementing the formal boundary conditions, prevent $\tilde{\Psi}$ from being used in shape design problems. This author is not aware of any design application of the stream vector concept.

Having a brief survey of the available iterative and direct design methods, the idea behind the proposed direct shape design method in this thesis is introduced in the next section.

2.6 The New Direct Design Method

In this section the ideas behind a new direct design technique for solving **SSD** problems is given very briefly. Implementation of the idea in the context of ideal flows will be given in Chapters 3 and 4.

Iterative design methods usually solve the design problem in physical space. There are also iterative design methods which do the calculations in transformed (computational) space (e.g. [54]). Obviously these methods suffer not only from time consuming design iterations, but also from the necessary operations involved in transforming the equations. In general the transformed equations are mathematically more complicated than the original equations.

In direct design methods, the difficulty in obtaining appropriate alternative (inverse) formulations is the major drawback. In most cases, an appropriate inverse formulation requires transformation of the equations into a space other than the physical space. This, as was just explained, complicates the governing equations.

A question arises here: is there any possibility to start with an initial guess in physical space and find the desired shape in a (theoretically) one shot (direct) procedure? Note that the generality of the method is important, i.e. it should not be inherently limited to certain applications, it should not rely on alternative formulations at the continuous level (which are not available for most of the flow problems and often require transformations), and it has to be direct (not iterative) from the algorithmic point of view. The last argument does not rule out the possibility of a few iterations, which may be required because of the nonlinearities involved or other similar reasons.

The answer to this question is **yes!** This thesis, in fact, addresses the ingredients and logical steps required in the implementation of such a direct shape design algorithm. To provide an overview of the method, consider potential flow in the straight

two-dimensional nozzle in Figure 2.6A. If one uses an appropriate discretization approach and solves an analysis problem corresponding to this potential flow nozzle, the surface pressure along the upper and lower walls can be obtained as shown in Figure 2.6B. Now suppose that another nozzle, as shown by the dashed lines in Figure 2.6C, is analyzed. The surface pressure distribution along the boundaries for this nozzle is shown with the dashed line in Figure 2.6D. Basically, two known geometries (nozzles

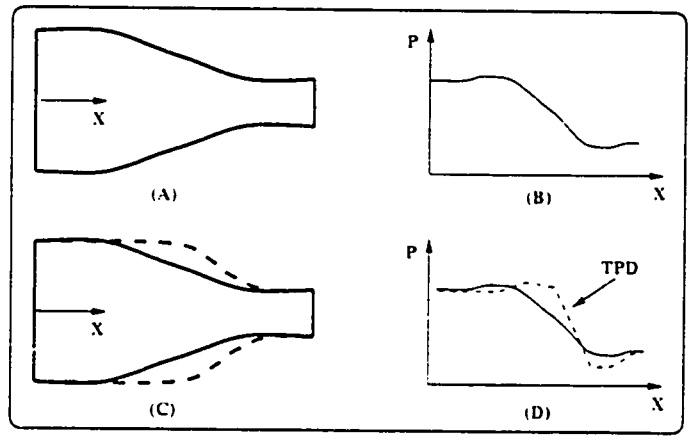

Figure 2.6: The proposed direct **SSD** method.

A and **C**) are given. The governing equations and boundary conditions are known and the surface pressure distributions for both cases are calculated.

However, one can look at the whole process from another point of view. One may equally assume that this whole process has been as follows:

- an *initial shape* is given (Figure 2.6A),
- the flow field in the initial shape is solved and consequently the surface pressure distribution is obtained (Figure 2.6B),
- a known *shape perturbation* is implemented (as shown by the dashed line in Figure 2.6C),
- the resulting *perturbed surface pressure distribution* is obtained (as shown by the dashed line in Figure 2.6D).

Of course in the direct form of the governing equations there is no perturbation terms for the geometry and the governing **PDE** in its continuous form does not allow such

an operation. However, one can define or interpret each boundary point of the new geometry in terms of its old position and a perturbation (correction) term.

Having this form of the interpretation for the two previous analysis problems in mind, the new direct shape design method looks to the corresponding **SSD** problem as follows:

- an *initial guess* is made for the nozzle (Figure 2.6A).
- the flow field in the initial shape is solved and consequently the *initial surface pressure distribution* is obtained (Figure 2.6B).
- a known *perturbed surface pressure distribution* (the **TPD**) is implemented (as shown by the dashed line in Figure 2.6D).
- the resulting *perturbed shape* is obtained (as shown by the dashed lines in Figure 2.6C).

The direct design approach needs the solution for the initial guess and the **TPD** as the input. The initial surface pressure distribution, shown in Figure 2.6B is not required as the input but considering the fact that the difference between the initial surface pressure distribution and the **TPD** is conceptually the driving force for the shape change, it is shown here for the purpose of comparison. Also, as will be explained later, the initial surface pressure distribution can be used to propose or modify the **TPD**. This very important point, which is one of the rewards of solving the shape design problem in the physical space, will be used in Chapter 7 where some design examples are presented.

It is obvious, from the above explanations, that the analysis and design problems are just different because of the difference between *inputs* and the *outputs*. Both type of problems are governed by the same physical laws. Mathematically, this means a unified formulation should exist which governs both the analysis and the corresponding shape design problem.

The concept of solving both analysis and design problems with just one formulation is a natural outcome of the direct design philosophy. The idea of using a unified formulation was proposed by Xu *et.al.* in the context of compliant-surface flows [104] and also Raithby *et.al.* in the context of free surface flows [105]. The computer code used in [105] could be applied to solve several types of free surface flow problems by simply changing the *inputs*. If the user provided the pressure at the free surface (which was simply the constant atmospheric pressure), the shape of the free surface

was calculated among the other dependent variables, and if the shape of the free surface was given, the corresponding surface pressure distribution could be calculated. That is to say that the work of Raithby *et.al.* and Xu *et.al.* triggered the idea behind the proposed direct duct design method in this thesis.

The intention of presenting this kind of interpretation for the analysis and design problems here is to provide a unified framework in which the difference between an analysis problem and its corresponding shape design problem appears only in the *inputs* and *outputs*. In other words, both the mentioned problems talk about one single physical phenomenon in two different ways. Mathematically, the flow governing equations can be formulated in a *unified discretized form* such that the designer simply switches between the required inputs (in the analysis and design problem) to solve either of the problems in the physical space.

While in conventional direct design methods, the *inversion of the formulation* takes place at the continuous level (the governing **PDE**'s are formulated in an alternative form), in the proposed direct design method a unified formulation is obtained at the discrete level which governs both the analysis and design problems. In other words the conventional direct design methods first do a kind of *inversion* and then *discretization* and the new direct design method first *discretize* the governing equations and then does the *inversion* as is required in shape design applications.

The final discretized working equations in the proposed direct design approach are obtained from the governing equations used in the corresponding analysis problem but can be used in solving both analysis and design problems. Because of this, the discretized governing equations, which are used in the direct shape design method, are here called *unified governing equations*. The unified governing equations can be used in solving both analysis and design problems with just changing the inputs.

2.7 Summary

In this chapter, engineering analysis and design problems were defined and categorized with particular attention to the thermo-fluid problems. Also the issue of numerical solution of the governing **PDE**'s in thermo-fluid problems was briefly reviewed and then iterative and direct design algorithms for solving **SSD** problems were introduced. Finally, the philosophy of a new direct design method, which is intended to be an efficient solution technique for **SSD** problems, was explained. In the next two chapters the details regarding to the implementation of the new method in a fairly simple flow situation (ideal flow) is discussed.

Chapter 3

Direct Design: Secondary Variable Formulation

3.1 Introduction

In this chapter the implementation of the proposed direct design method, introduced in Chapter 2, is discussed. To make the problem as simple as possible, a steady two-dimensional ideal (incompressible and irrotational) flow is considered. This simplified flow model leads to simple equations that can be solved with little computational effort; this, in turn, allows experience to be gained that will be invaluable when the same direct design method is applied using the full Navier-Stokes equations. The present direct design method applied to ideal two-dimensional flows also provides a simpler, and perhaps superior, method for solving problems previously solved by the Stanitz approach [71].

The first step in the proposed shape design method is to make an appropriate initial guess. The next section explains how an appropriate initial guess is made in the proposed design method. Then the issues of the formulation and discretization of the governing equations are discussed with the aim of providing a unified set of governing equations applicable in both analysis and shape design problems.

3.2 The Initial Guess Generator

The proposed direct design method starts the design process with an initial guess for the shape in the physical space. The designer will be able to make such a guess based on previous experience, or based on a few solutions to analysis problems in which

different geometries are prescribed.

In this thesis the required flexibility to quickly generate initial guesses is obtained by using a Bezier curve fitting technique[1]. According to the Bezier method, each point on a curve can be described by the following parametric function:

$$\vec{P}(u) = \sum_{i=0}^{n} \vec{P}_i f_i(u). \tag{3.1}$$

In this equation $\vec{P}_i$ presents a polygon with $(n+1)$ vertices which are called the control points. u is the parameter ($u \in [0,1]$) and $f_i(u)$ represents blending functions. Bezier chose a family of functions, called Bernstein polynomials, as the blending functions:

$$f_i(u) = B_{i,n}(u) = \frac{n!}{i!(n-i)!} u^i (1-u)^{n-i}. \tag{3.2}$$

For $(n+1)$ points, $B_{i,n}(u)$ determines a polynomial with degree n. Bezier curves are sensitive to local changes in control points and because the effects of these local changes are propagated along the curve, they are not appropriate for local fine tuning of the shape. B-splines use different blending functions and have a better ability to control the shape locally. However, For the initial guess, local fine tuning is not necessary and Bezier curves can provide the required shapes. Therefore, Bezier curves are used in this thesis. In a Bezier curve if the number of control points is low, one does not have a good ability to control the shape and if there are too many control points, it is difficult to figure out how the curve is affected by the control points. Here the Bezier curves are generated by 4 control points as is shown in Figure 3.1. Consequently, the parametric function for the Bezier curves would be as follow:

$$\vec{P}(u) = (1-u)^3 \vec{P}_0 + 3u(1-u)^2 \vec{P}_1 + 3u^2(1-u)\vec{P}_2 + u^3 \vec{P}_3. \tag{3.3}$$

$\vec{P}_0$ and $\vec{P}_3$ are the end points of the curve and $\vec{P}_1$ and $\vec{P}_2$ actually control the shape of the curve. For complex curves, one can use different pieces of curves and control the shape of each piece by simply playing with two internal control points.

3.3 Formulation of the Problem

It was shown that there were three possible secondary variable formulations for steady ideal flows: Equations 2.15, 2.16 and 2.17. For a two-dimensional problem all of the

1. Bezier invented this approximation method for the design of automobile bodies in 1960 [106].

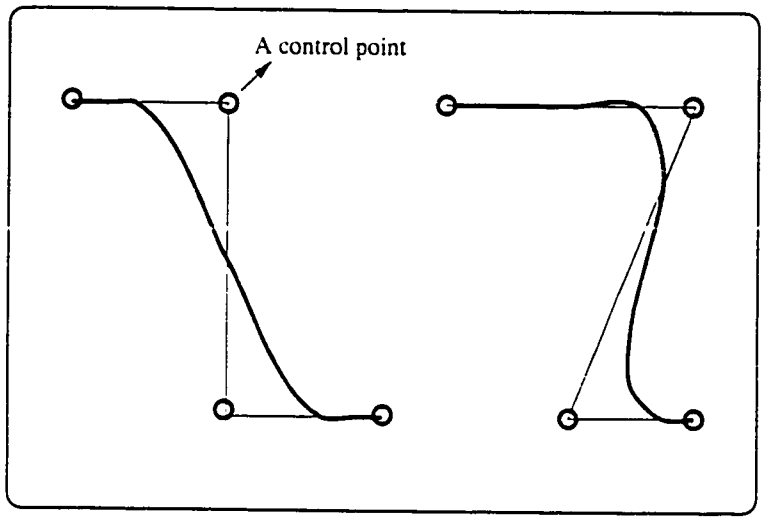

Figure 3.1: Creating Bezier curves with four control points.

above formulations simplify to the following general form:

$$\nabla^2\Theta = 0. \tag{3.4}$$

The scalar Θ stands for ϕ in the scalar potential formulation, ψ^* in the vector potential formulation, ψ in the stream function formulation[2] and T (the temperature) in conduction heat transfer problems. Two points are worthy of mention at this stage.

First, note that, for the particular flow model used here (i.e. the ideal flow), the ϕ formulation is the simplest and also the most convenient one. Even in three-dimensional problems the governing equation for ϕ is just the Laplace equation.

Another point is that the Laplace equation represents many equilibrium type phenomena in different branches of the physics and engineering. Solving a shape design problem for this linear operator (the Laplacian) is not just useful in the context of fluid flow. Steady heat conduction is a typical example and obviously electrical fields and other diffusion type transport phenomena can also be described by this mathematical model. To make the solution of the **SSD** problem as general as possible at this level, the solution procedure has to be able to handle different types of boundary conditions. This, indeed, has been considered and will be discussed in

2. ψ^* is used for the two-dimensional counterpart of the vector potential to differentiate it from the stream function (ψ).

Chapter 4.

Having described an appropriate initial guess generator and the flow governing equation, the following sections turn to the numerical simulation of the problem.

3.4 Discretization of the Solution Domain

A typical computational grid, as is required in **EB-FVM**, was shown in Chapter 2. Other relevant information about this type of grid in the context of two-dimensional potential flow duct design is explained in this section. Figure 3.2 shows a two-

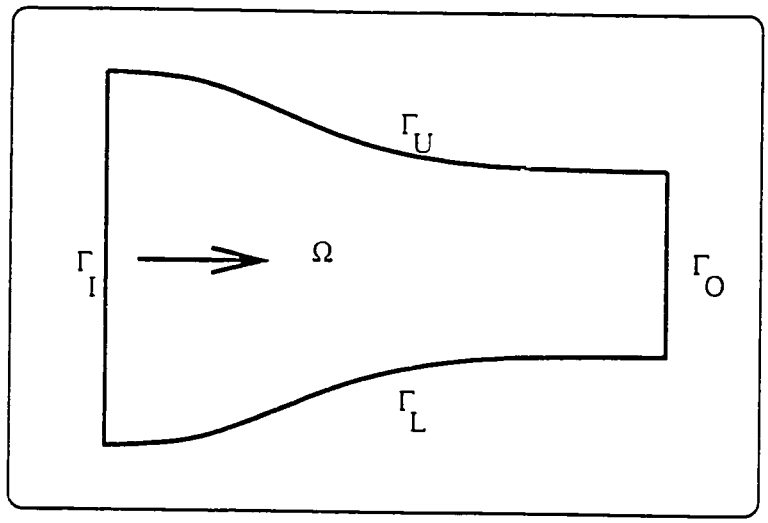

Figure 3.2: The solution domain.

dimensional duct, which may be considered as the initial guess for a typical design problem. The computational domain (Ω) is bounded by the exterior boundary surface Γ which is composed of the inlet boundary Γ_I, upper boundary Γ_U, outlet boundary Γ_O and lower boundary Γ_L[3]. This domain should be discretized to make a computational grid. The computational grid is known when the Cartesian coordinates (x and y) of all of the grid points (nodes) are known. The grid is structured so that each node

3. In this thesis, the inlet of the duct is always located at the left hand side and the flow is from the left (west) to the right (east). Therefore, the upper boundary is in the north and there is no ambiguity in defining the upper and lower surfaces.

is described by a pair of numbers (I, J) which shows its position in a two-dimensional data matrix. In general, the grid is also non-orthogonal.

3.4.1 Local and Global Coordinates

The construction of the grid in the direct design method, as is introduced here, starts with defining some reference points for a number of spines. Spines were introduced and used by S. F. Kistler and L.E. Scriven [107]. In [105] vertical spines were used in free surface flow computations. Each spine (e.g. spine i) is defined here by a reference point (x_i^*, y_i^*) and an angle (θ^i) as shown in Figure 3.3 for a straight two-dimensional nozzle. Note that all the spines are fixed vertical lines in this simple case, but this will not generally be the case. The intersection of the Bezier curves with the spines define

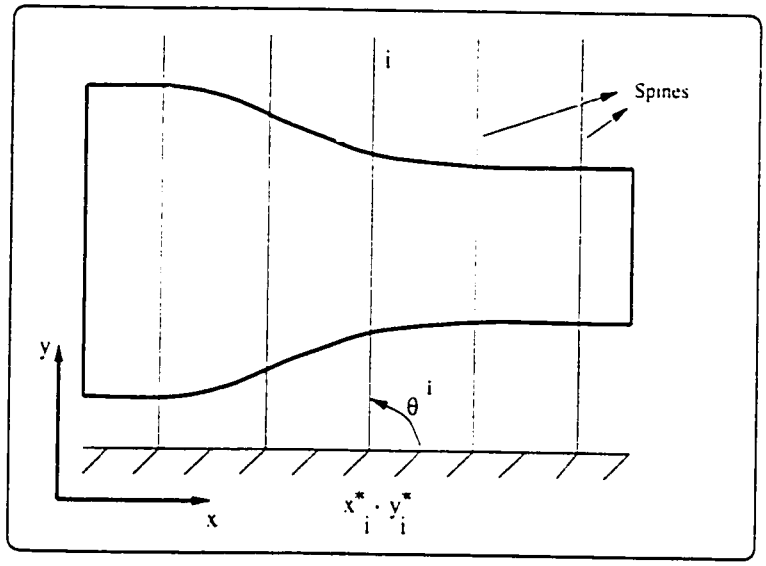

Figure 3.3: Semi-discretized domain and the spines.

nodes on the boundary. Interior nodes are distributed between the boundary nodes on each spine. The computational grid, and the approximation of the boundary, are obtained by joining nodes by straight lines to produce a mesh of quadrilaterals as shown in Figure 3.4.

To be able to describe all the geometrical properties of the domain in terms of the global coordinates of the grid points (x and y), the element local coordinate system

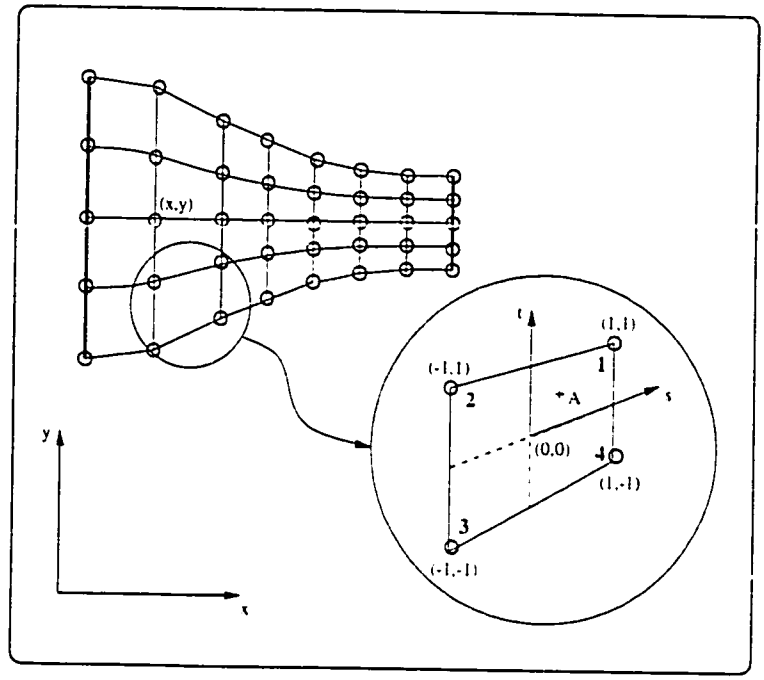

Figure 3.4: The finite element grid.

$(s\ .\ t)$ and the bi-linear shape functions (N_i) are introduced. In Figure 3.4 the local numbering system of the nodes within an element and their local coordinates are shown. The bi-linear shape functions for an arbitrary point A inside a quadrilateral element are defined as follows:

$$N_{1A} = \frac{1}{4}(1 + s_A s_1)(1 + t_A t_1) \tag{3.5}$$

$$N_{2A} = \frac{1}{4}(1 + s_A s_2)(1 + t_A t_2) \tag{3.6}$$

$$N_{3A} = \frac{1}{4}(1 + s_A s_3)(1 + t_A t_3) \tag{3.7}$$

$$N_{4A} = \frac{1}{4}(1 + s_A s_4)(1 + t_A t_4) \tag{3.8}$$

These shape functions can be used to determine global coordinates of an arbitrary

point A in an element in terms of the global coordinates of neighbor nodes:

$$x_A = \sum_{i=1}^{4} N_{iA} x_i. \tag{3.9}$$

$$y_A = \sum_{i=1}^{4} N_{iA} y_i. \tag{3.10}$$

Hereafter, the summation rule is used and it is not necessary to use the $\sum_{i=1}^{4}$ to denote summation. Therefore the global coordinates of any point can be expressed as follows:

$$x = N_i x_i. \tag{3.11}$$

$$y = N_i y_i. \tag{3.12}$$

The finite element grid (shown in Figure 3.4) is used to define the control volumes which are necessary for the implementation of the conservation law(s) in the discretized domain. Figure 3.5 shows the fully discretized space as required by **EB-FVM**. Note the following points regarding to the computational grid:

- internal control volumes have 8 internal integration points (*ip*'s),
- regular boundary control volumes have 4 internal and 2 boundary *ip*'s,
- corner control volumes have 2 internal and 2 boundary *ip*'s,
- in each element 4 Sub-Control Volumes (**SCV**'s) are defined,
- there are 4 integration points inside each element, numbered locally as shown in Figure 3.5.

Hereafter, nodes associated with the regular boundary control volumes will be called *regular boundary nodes* and those associated with corner control volumes are called *corner nodes*.

In **EB-FVM**, it is often required to calculate the length of a *directed* line segment $\Delta\vec{r}$ and its corresponding normal vector $\Delta\vec{n}$ as shown in Figure 3.6. From analytic geometry:

$$|\Delta\vec{r}| = \sqrt{(\Delta x)^2 + (\Delta y)^2}. \tag{3.13}$$

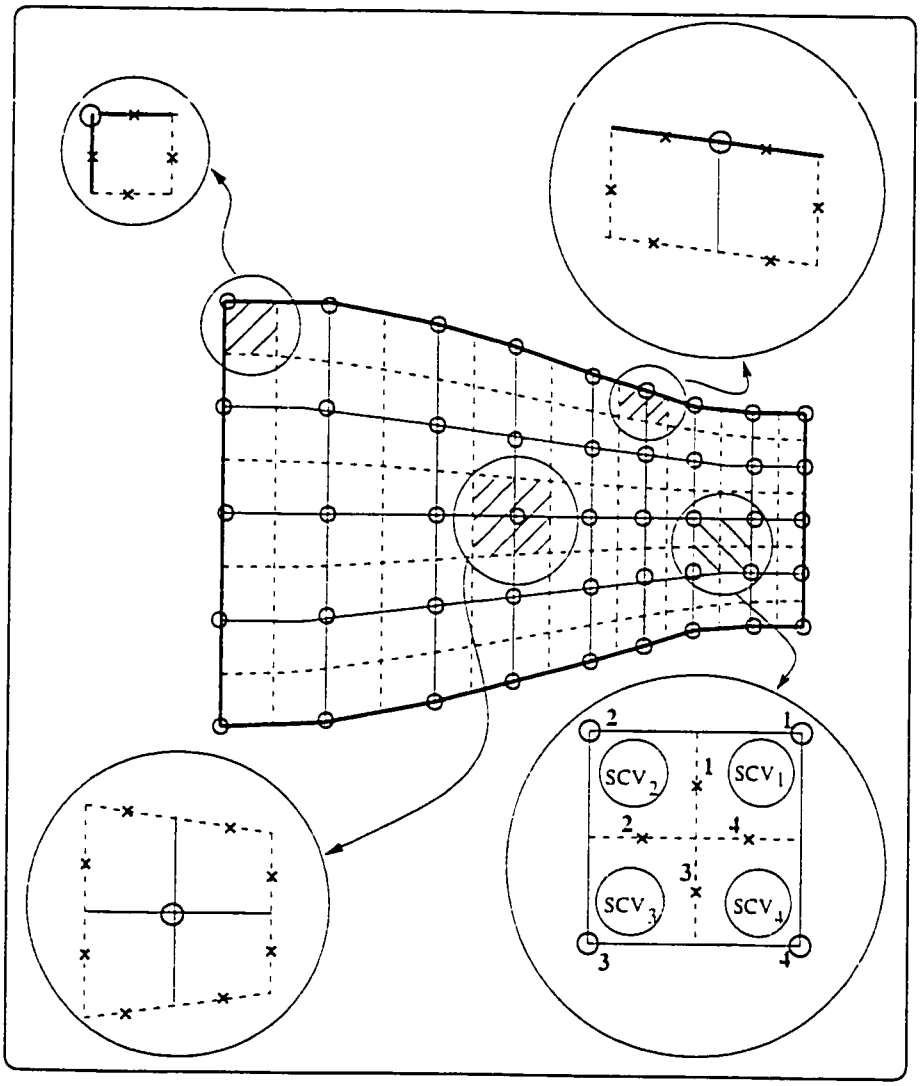

Figure 3.5: The computational grid as required in **EB-FVM**.

$$\Delta\vec{r} = (\Delta x)\vec{i} + (\Delta y)\vec{j}. \tag{3.14}$$

In these equations $\vec{i}$ and $\vec{j}$ are the Cartesian unit vectors and Δx and Δy can be calculated as below:

$$\Delta x = \int_a^b dx, \tag{3.15}$$

$$\Delta y = \int_a^b dy. \tag{3.16}$$

Using the chain rule in differentiation, one would obtain:

$$dx = \frac{\partial x}{\partial s}ds + \frac{\partial x}{\partial t}dt, \tag{3.17}$$

$$dy = \frac{\partial y}{\partial s}ds + \frac{\partial y}{\partial t}dt. \tag{3.18}$$

It is not difficult to show that [108]:

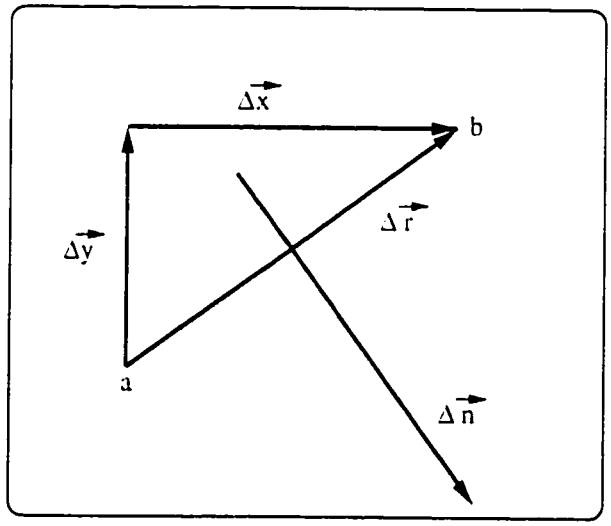

Figure 3.6: Definition of a directed-line segment and its normal.

$$\frac{\partial x}{\partial s} = (x_1 - x_2)\frac{\partial N_1}{\partial s} + (x_4 - x_3)\frac{\partial N_4}{\partial s}. \tag{3.19}$$

$$\frac{\partial x}{\partial t} = (x_1 - x_4)\frac{\partial N_1}{\partial t} + (x_2 - x_3)\frac{\partial N_2}{\partial t}. \tag{3.20}$$

$$\frac{\partial y}{\partial s} = (y_1 - y_2)\frac{\partial N_1}{\partial s} + (y_4 - y_3)\frac{\partial N_4}{\partial s}. \tag{3.21}$$

$$\frac{\partial y}{\partial t} = (y_1 - y_4)\frac{\partial N_1}{\partial t} + (y_2 - y_3)\frac{\partial N_2}{\partial t}. \tag{3.22}$$

One can use equations 3.15 to 3.22 to obtain the following equations for Δx and Δy (see Appendix A):

$$\Delta x = \alpha_p x_p. \tag{3.23}$$

$$\Delta y = \alpha_p y_p. \tag{3.24}$$

in these equations:

$$\alpha_p = \frac{\partial N_p}{\partial s}\Delta s + \frac{\partial N_p}{\partial t}\Delta t. \tag{3.25}$$

$$\Delta s = s_b - s_a. \tag{3.26}$$

$$\Delta t = t_b - t_a. \tag{3.27}$$

Note that the outward normal vector for the directed line segment $\Delta\vec{r}$ is defined according to Figure 3.6 and can be obtained by the following equation:

$$\Delta\vec{n} = (\Delta y)\vec{i} - (\Delta x)\vec{j}. \tag{3.28}$$

Calculation of finite surfaces in the domain (or volumes in three-dimensional problems) can also be done easily. However, in this thesis, the above mentioned geometrical relations are sufficient.

3.4.2 Spine Coordinates

As was mentioned in the previous section, all geometrical information in the domain can be obtained with the aid of the local co-ordinates once the computational grid (defined by the global positions of the nodes) is available. This section provides details on how the global co-ordinates of the nodes are computed from "spine coordinates".

Each grid point on a spine, for example node m on the spine i (Figure 3.7), can be located by just a single *variable* called the spine coordinate of that node (R_i^m).

Figure 3.7 shows that the position of point m on spine i can be described by either (x_i^m, y_i^m) or R_i^m when the spine i reference point coordinates (x_i^*, y_i^*) and θ^i are known. The following transformation relates the global coordinates of an arbitrary node m

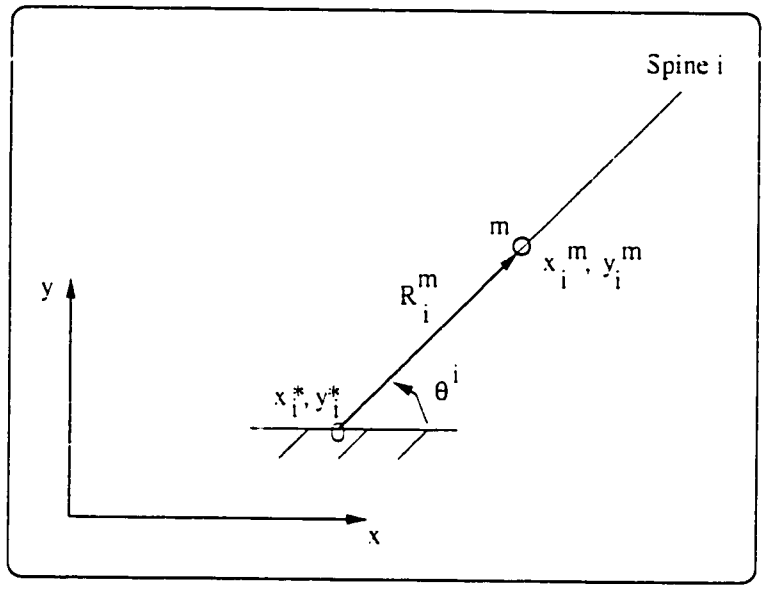

Figure 3.7: Spine coordinate of a grid point.

to its spine coordinate (the distance between nodal point m and the reference point along its associated spine):

$$x_i^m = x_i^* + R_i^m \cos\theta^i. \tag{3.29}$$

$$y_i^m = y_i^* + R_i^m \sin\theta^i. \tag{3.30}$$

Note that i is used as a superscript in θ^i to emphasize that the summation rule does not operate on θ^i. The fact that a grid point remains on a specified spine during the shape evolution in shape design problems, allows the designer to address the unknown position of each boundary node in a shape design problem with just one variable: its spine coordinate. This means that even in a three-dimensional shape design problem only one variable (unknown) appears in the discrete governing equations to represent the (unknown) location of each boundary node.

It is assumed that in shape design problems, the designer has chosen a *grid evolution strategy* which constrains the grid points to remain along their associated spines and relates the internal nodes to the boundary nodes. There are different strategies for relating interior and boundary nodes, but the simplest one would be to keep the relative positions of nodes along a spine fixed as is shown in Figure 3.8. In other words, the parameter C^{im} for the node m on the spine i, as defined below, remains fixed during the shape evolution:

$$C^{im} \equiv \frac{R_i^m - R_i^L}{R_i^U - R_i^L}. \tag{3.31}$$

In this definition, R_i^L and R_i^U are the spine coordinates of the boundary points and R_i^m is the spine coordinate of the internal node m along the spine i. Fixing C^{im} causes the internal nodes to be tied to the boundary nodes and to follow them during the shape evolution. This is the *boundary-connection rule* used here as part of the grid evolution policy. Each nodal point, in the global discretized space has its own C^{im}. When the local numbering system for the nodes in an element is used, each local node has its own position characteristic parameter C^m and m goes from 1 to 4. Note that one superscript is used to address nodes' C parameters when the element local numbering system is applied.

3.4.3 Boundary-Linked Computational Grids

In the previous section some concepts related to the computational grid were introduced: the *spine coordinate*, the *grid evolution policy* and the *boundary-connection rule*. There are different ways that one could manage the spines and the relative positions of the internal nodes to keep or modify the quality of the grid. The chosen strategy (fixed spines with fixed C parameters), as described in the previous section, is fairly appropriate for now and as the computational results will show, it works well at this level.

The purpose of choosing a grid evolution policy is to control and keep track of the computational grid during the shape evolution. Whatever strategy is used (whether the spines are straight or curved, or whether spines are used at all) there must be some boundary-connection rule. Therefore it is meaningful to call these types of computational grids *boundary-linked computational grids*. Boundary-linked computational grids deserve to be considered as one of the main ingredients of all the numerical simulation methods used in direct shape design algorithms. The whole

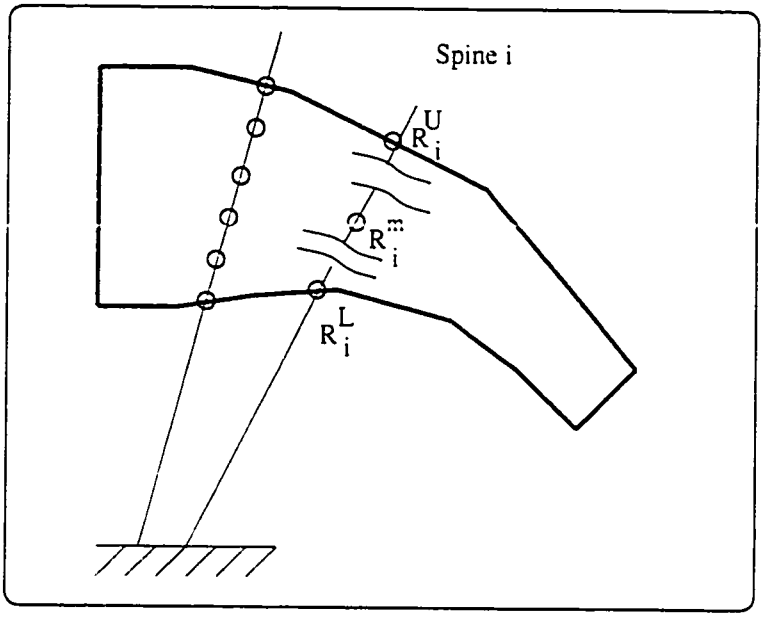

Figure 3.8: Nodes with equal distances along a spine.

purpose of a boundary-linked computational grid is to recover all the geometrical information in the solution domain based on the geometrical information provided at the boundary (the boundary shape). The idea is not only extremely useful in solving shape design problems, as will be shown later, but also can be very useful for the analysis problems as well.

Now that the domain is discretized, the discretization of the governing equation is in order. This is the subject of the next section.

3.5 Discretization of the Governing Equation

3.5.1 Level C Mathematical Model

Following the brief discussion in Chapter 2, regarding to the generic form of the field equations, the Laplace equation (Eq. 3.4) is now written in the following form:

$$\nabla^2\vec{\Theta} = \vec{\nabla}\cdot(\vec{\nabla}\Theta) = \vec{\nabla}\cdot\vec{F}_\Theta^D = 0. \tag{3.32}$$

This form of the Laplace equation is actually a balance equation and the quantity $\vec{F}_\Theta^D$ can be considered as a diffusion flux term. For the sake of simplicity, the superscript D will be dropped and $\vec{F}_\Theta$ represents this flux term hereafter.

The starting point in the **EB-FVM** would be the following integral equation for an arbitrary control volume:

$$\int\int\int_{\Omega_{cv}} \left(\vec{\nabla}\cdot\vec{F}_\Theta\right) d\Omega = 0. \tag{3.33}$$

Using the divergence theorem, the volume integral changes to a surface integral as follows:

$$\int\int_{\Gamma_{cv}} \vec{F}_\Theta \cdot d\vec{A}_n = 0. \tag{3.34}$$

Equation 3.34 is the governing equation for the problems governed by the Laplace equation at the continuous level as required by the **FVM**. The governing equation at this level is called here the level C (C for Continuous) mathematical model. In this equation $d\vec{A}_n$ is the differential outward normal vector with a magnitude equal to $\mid d\vec{A}_n \mid$.

3.5.2 Level D_0 Mathematical Model

Using the midpoint rule, the integral balance equation for an internal control volume is approximated by the following algebraic equation:

$$\sum_{i=1}^{8} \vec{F}_{\Theta i}\cdot\vec{A}_{ni} = 0. \tag{3.35}$$

Let's define the quantity $(\vec{F}_{\Theta i}\cdot\vec{A}_{ni})$ as the flow term $(\mathcal{F}_\Theta)$ and rewrite the above equation in the following form:

$$\sum_{i=1}^{8} \mathcal{F}_{\Theta i} = 0. \tag{3.36}$$

In Eq. 3.36 the integration point quantities (in this case diffusion flow terms) appear. This equation is a discretized form of Eq. 3.34 but is not the final working form which must only include the nodal quantities. Therefore, it is called the level D_0 (D for Discrete) mathematical model for the problems governed by the Laplace equation. According to Eq. 3.36, for the implementation of the conservation law over a control

volume it is only necessary to specify how the flow term ($\mathcal{F}_\Theta$) is estimated at an arbitrary integration point.

Eq. 3.36 is a balance equation written for an internal control volume. From the coding point of view, it is better to implement the constraint given by Eq. 3.36, in an element-wise manner. As was shown in Figure 3.5, each quadrilateral finite element is composed of four **SCV**'s. The flow terms can be calculated at the integration points in each element and the balance equation (Eq. 3.36) is actually satisfied after the elemental equations are assembled.

For the simple problem considered here, the flow term at an arbitrary integration point is equal to:

$$\left[\mathcal{F}_\Theta \equiv \vec{F}_\Theta \cdot \vec{A}_n = \vec{\nabla}\Theta \cdot \vec{A}_n\right]_{ip}. \tag{3.37}$$

Note that in a two-dimensional geometry (shown in Figure 3.5) the integration faces are represented by line segments. Therefore, using Eq. 3.28 ($\vec{A}_n$ is equal to $\Delta\vec{n}$ in this case), Eq. 3.37 can be written in the following form:

$$[\mathcal{F}_\Theta]_{ip} \equiv \left[\frac{\partial\Theta}{\partial x}\Delta y - \frac{\partial\Theta}{\partial y}\Delta x\right]_{ip} \tag{3.38}$$

Δx and Δy are the x and y components of the flux surface associated with $\vec{A}_n$.

3.5.3 Level *D* Mathematical Model

The level D mathematical model is the final working form of the governing equations in the **FVM**. In general, two major steps are required to obtain the level D mathematical model from the corresponding level D_0 model. The integration point quantities in the level D_0 mathematical model have to be related to nodal point quantities. An *appropriate interpolation scheme* is required to establish the relationships between the integration and nodal point quantities. Furthermore, often the algebraic equations have to be linearized. In this sub-section, both these issues are discussed. First, by using an appropriate interpolation scheme, a nonlinear discrete expression for the flow term at the Level D is derived. Then, linearization of the flow term expression and derivation of the final (linearized) discrete form of the flow term is discussed.

The issue of approximating the gradient terms at an integration point is the major issue here. The elements are assumed to be iso-parametric and therefore the

same bi-linear shape functions which were used for the geometrical modeling are used in the diffusion modeling. Therefore, the following approximations are used:

$$[\Theta]_{ip} = N_i \Theta_i, \tag{3.39}$$

$$\left[\frac{\partial \Theta}{\partial x}\right]_{ip} = \frac{\partial N_i}{\partial x}\Theta_i, \tag{3.40}$$

$$\left[\frac{\partial \Theta}{\partial y}\right]_{ip} = \frac{\partial N_i}{\partial y}\Theta_i. \tag{3.41}$$

In [108] it has been shown that:

$$\frac{\partial N_i}{\partial x} = \frac{1}{|J|}\left(\frac{\partial y}{\partial t}\frac{\partial N_i}{\partial s} - \frac{\partial y}{\partial s}\frac{\partial N_i}{\partial t}\right). \tag{3.42}$$

$$\frac{\partial N_i}{\partial y} = \frac{1}{|J|}\left(\frac{\partial x}{\partial s}\frac{\partial N_i}{\partial t} - \frac{\partial x}{\partial t}\frac{\partial N_i}{\partial s}\right). \tag{3.43}$$

$|J|$ is the determinant of the Jacobian of the local-global transformation and is equal to:

$$|J| = \frac{\partial x}{\partial s}\frac{\partial y}{\partial t} - \frac{\partial y}{\partial s}\frac{\partial x}{\partial t}. \tag{3.44}$$

For the sake of simplicity $|J|$ is represented by J hereafter and called the Jacobian.

It is useful, in shape design problems in the context of **EB-FVM**, to separate the quantities defined in terms of the local coordinates and the quantities defined in terms of the global coordinates. During the shape evolution, the local coordinates of a point (for example) in an element does not change, but its global coordinates might change. Therefore the above equations are re-written in the following forms (see Appendix A):

$$J = (\gamma_{pn})\,(x_p y_n - x_n y_p)\,. \tag{3.45}$$

$$\frac{\partial \Theta}{\partial x} = (\gamma_{mn} - \gamma_{nm})\left(\frac{y_n}{J}\right)\Theta_m. \tag{3.46}$$

$$\frac{\partial \Theta}{\partial y} = -(\gamma_{mn} - \gamma_{nm})\left(\frac{x_n}{J}\right)\Theta_m. \tag{3.47}$$

In these equations the summation rule is applied and dummy variables m, n and p take values 1 to 4 to account the effects of all the nodes surrounding an integration point. γ_{mn} is defined as:

$$\gamma_{mn} = (\frac{\partial N_m}{\partial s})(\frac{\partial N_n}{\partial t}). \tag{3.48}$$

Using equations 3.23, 3.24, 3.46 and 3.47 in Eq. 3.38, the flow term can be written in the following compact form:

$$[\mathcal{F}_\Theta]_{ip} = \frac{\lambda_m \Theta_m}{J}. \tag{3.49}$$

For simplicity, the subscript ip will not be used hereafter and $\mathcal{F}_\Theta$ represents the flow term associated with the quantity Θ from the integration point ip. In Eq. 3.49, λ_m is defined as below (see Appendix A):

$$\lambda_m \equiv \alpha_p \left(\gamma_{mn} - \gamma_{nm}\right)\left(x_p x_n + y_p y_n\right). \tag{3.50}$$

In analysis problems, in which the duct geometry is known, J and λ_m are known and $\mathcal{F}_\Theta$ is just a linear function of unknown Θ's at the nodes associated with the element which contains the integration point. These nodes are defined here as *neighbor nodes* for the integration point ip. Equation 3.49, in fact, provides the level D mathematical model of the diffusion flow term appropriate for solving analysis problems which are described by the Laplace equation.

The computational molecule, provided by the **EB-FVM** for the Laplace equation, models the physical influences of the neighbor nodes quite appropriately. In Figure 3.9 the diffusion computational molecules provided by different numerical schemes, when applied in a uniform Cartesian grid, are shown and compared. It is seen that the diffusion computational molecule provided by the **EB-FVM** is better than ones obtained by the Galerkin **FEM**. Note that the **FDM** computational molecule in this case would be similar to the computational molecule provided by the Galerkin method used with the triangular elements.

In shape design problems, in which the duct geometry is not known, $\mathcal{F}_\Theta$ is a function of both global co-ordinates and Θ's of neighbor nodes. The dependency of the flow term on the global coordinates of the neighbor nodes is through the parameters λ_m and J which are non-linear functions of the global co-ordinates of the neighbor nodes.

Looking back to the conceptual description of the new direct design method, given in Chapter 2, it makes sense to assume that if the initial (old) flow term at an

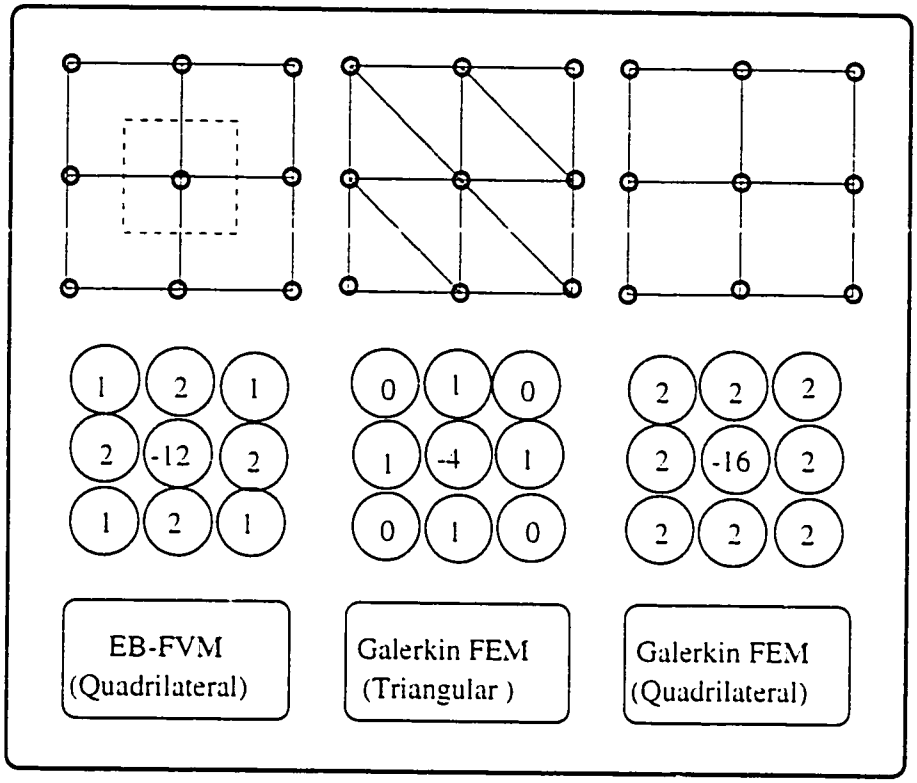

Figure 3.9: Comparison of some diffusion computational molecules.

arbitrary integration point is $\mathcal{F}_\Theta^0$. it will take a new (perturbed) quantity $\mathcal{F}_\Theta^{new}$ for the final (designed) shape. Mathematically. this can be written as follows:

$$\mathcal{F}_\Theta^{new} \equiv \mathcal{F}_\Theta = \mathcal{F}_\Theta^0 + \delta\mathcal{F}_\Theta. \tag{3.51}$$

Note that $\mathcal{F}_\Theta$ as expressed by Eq. 3.49 may be considered as a function of $\lambda_m . \theta_m . J$:

$$\mathcal{F}_\Theta = \mathcal{F}_\Theta \left(\lambda_m . \theta_m . J\right). \tag{3.52}$$

Therefore. $\delta\mathcal{F}_\Theta$ can be estimated as:

$$\delta\mathcal{F}_\Theta \approx \left(\frac{\partial\mathcal{F}_\Theta}{\partial\lambda_m}\right)^0 \left(\lambda_m - \lambda_m^0\right) + \left(\frac{\partial\mathcal{F}_\Theta}{\partial\Theta_m}\right)^0 \left(\Theta_m - \Theta_m^0\right) + \left(\frac{\partial\mathcal{F}_\Theta}{\partial J}\right)^0 \left(J - J^0\right). \tag{3.53}$$

Using Eq. 3.49 it is easy to obtain:

$$\left(\frac{\partial \mathcal{F}_\Theta}{\partial \lambda_m}\right)^0 = \left(\frac{\theta_m}{J}\right)^0 \tag{3.54}$$

$$\left(\frac{\partial \mathcal{F}_\Theta}{\partial \theta_m}\right)^0 = \left(\frac{\lambda_m}{J}\right)^0 \tag{3.55}$$

$$\left(\frac{\partial \mathcal{F}_\Theta}{\partial J}\right)^0 = -\left(\frac{\mathcal{F}_\Theta}{J}\right)^0 \tag{3.56}$$

Using Eq. 3.54 to 3.56 in Eq. 3.53 results in the following approximate expression for the perturbed (diffusion) flow term (as described in Eq. 3.51):

$$\mathcal{F}_\Theta \approx \left(\frac{\theta_m}{J}\right)^0 \lambda_m + \left(\frac{\lambda_m}{J}\right)^0 \theta_m - \left(\frac{\mathcal{F}_\Theta}{J}\right)^0 J. \tag{3.57}$$

Considering the fact that λ_m and J are nonlinear functions of the coordinates of the neighbor nodes of an arbitrary internal integration point, the above expression for the flow term should be linearized in shape design problems. To linearize Eq. 3.57, linearized forms of λ_m and J are substituted in this equation. Full Newton linearization of these terms results in:

$$\lambda_m \approx \alpha_p \left(\gamma_{mn} - \gamma_{nm}\right)\left(x_p^0 x_n + x_n^0 x_p + y_p^0 y_n + y_n^0 y_p\right) - \lambda_m^0. \tag{3.58}$$

$$J \approx \gamma_{pn}(x_p^0 y_n + y_n^0 x_p - x_n^0 y_p - y_p^0 x_n) - J^0. \tag{3.59}$$

Using the above linearized forms of λ_m and J in Eq. 3.57 and arranging terms, the following linear equation is obtained for the flow term at an arbitrary internal integration point:

$$\mathcal{F}_\Theta \approx \left[B_i^\Theta\right]\Theta_i + \left[B_i^x\right] x_i + \left[B_i^y\right] y_i + \left[B^{xy\Theta}\right]. \tag{3.60}$$

Coefficients B are just functions of old values of the geometry and the flow parameters and are reported in Appendix A.

It is important to note that Eq. 3.60 not only provides an appropriate expression for the flow term at the level D mathematical model for the shape design problems, but also can be used in modeling and solving analysis problems as well. The major step in obtaining the level D mathematical model from the corresponding level D_0 model (Eq. 3.36), as far as the **FVM** is concerned, was the profile assumption or

the interpolation scheme used to relate the integration point quantities to the nodal point quantities. The bi-linear assumption used in the elements, in fact, provides the required interpolations in the **EB-FVM** as used here. More precisely, the level D equation for the flow term was obtained after implementing the profile assumption and the linearization. These two logical steps may be distinguished by defining an intermediate step between the level D_0 and the level D. This, in fact, will be considered in Chapter 8.

For a boundary-linked grid, like the one used here, the coordinates of all the internal grid points can be expressed in terms of the boundary node coordinates. This is very beneficial in shape design problems in which the boundary shape is under consideration. For the proposed grid evolution policy in this thesis, spines are used and all the grid points are constrained to follow some fixed spines. Using Eq. 3.29, 3.30 and 3.31, which describe the linkage between the internal and boundary nodes and constrain the grid deformation, it is easy to show that:

$$x_i = x_i^* + \left(C^i \cos\theta^i\right) R_i^U + \left(D^i \cos\theta^i\right) R_i^L. \tag{3.61}$$

$$y_i = y_i^* + \left(C^i \sin\theta^i\right) R_i^U + \left(D^i \sin\theta^i\right) R_i^L. \tag{3.62}$$

In equations 3.61 and 3.62, D^i is defined as below:

$$D^i \equiv 1 - C^i. \tag{3.63}$$

Note that C^i and D^i here are attributed to nodes with local numbers 1 to 4 in an element. Introducing x_i and y_i, as defined by equations 3.61 and 3.62, in Eq. 3.60, results in an appropriate equation for the flow term ($\mathcal{F}_\Theta$) in terms of the problem unknowns (i.e. R^U, R^L and Θ):

$$\mathcal{F}_\Theta \approx \left[C_i^\Theta\right] \Theta_i + \left[C_i^{RU}\right] R_i^U + \left[C_i^{RL}\right] R_i^L + \left[C^{R\Theta}\right]. \tag{3.64}$$

Coefficients C in Eq. 3.64 are defined as:

$$C_i^\Theta \equiv B_i^\Theta \tag{3.65}$$

$$C_i^{RU} \equiv \left(B_i^x \cos\theta^i + B_i^y \sin\theta^i\right) C^i \tag{3.66}$$

$$C_i^{RL} \equiv \left(B_i^x \cos\theta^i + B_i^y \sin\theta^i\right) D^i \tag{3.67}$$

$$C_i^{R\Theta} \equiv B_i^x \left(x_i^* - x_i^0\right) + B_i^y \left(y_i^* - y_i^0\right) \tag{3.68}$$

Note that (x_i^r, y_i^r) represent the reference coordinates for the spine associated with the local node number i and (x_i^0, y_i^0) represent the old coordinates of a grid point with the local number i.

Figure 3.10 shows a typical internal integration point in an element and its associated neighbor and boundary neighbor nodes. The numerical model for the flow term at an internal integration point (Eq. 3.64), when applied in the balance equations, introduces the unknowns Θ and R^U and R^L into the element equation and finally (after assembling the elemental equations) into the global set of equations. This completes the numerical modeling of the problem inside the domain. It remains to apply the formal and extra boundary conditions and close the set of equations. This is the subject of the next chapter.

3.6 Summary

In this chapter a number of important issues regarding to the implementation of the proposed direct design approach was explained.

First, a simple robust initial guess generator was introduced.

Second, domain discretization was discussed in which the importance of the spines and boundary-linked computational grids was emphasized.

Third, the derivation of the discretized form of the governing equation in the context of **EB-FVM** was discussed. The equation proposed for calculating the diffusion flow term at an integration point (Eq. 3.64) may be considered as a unified expression for the estimation of the flow term, both in the analysis and shape design problems. However, if the computational grid is known (analysis problems), no linearization is required and Eq. 3.49 can be more easily used to estimate the flow term.

It remains to talk about the implementation of the formal and extra boundary conditions required to close the system of (linear) equations. This is the subject of the next chapter.

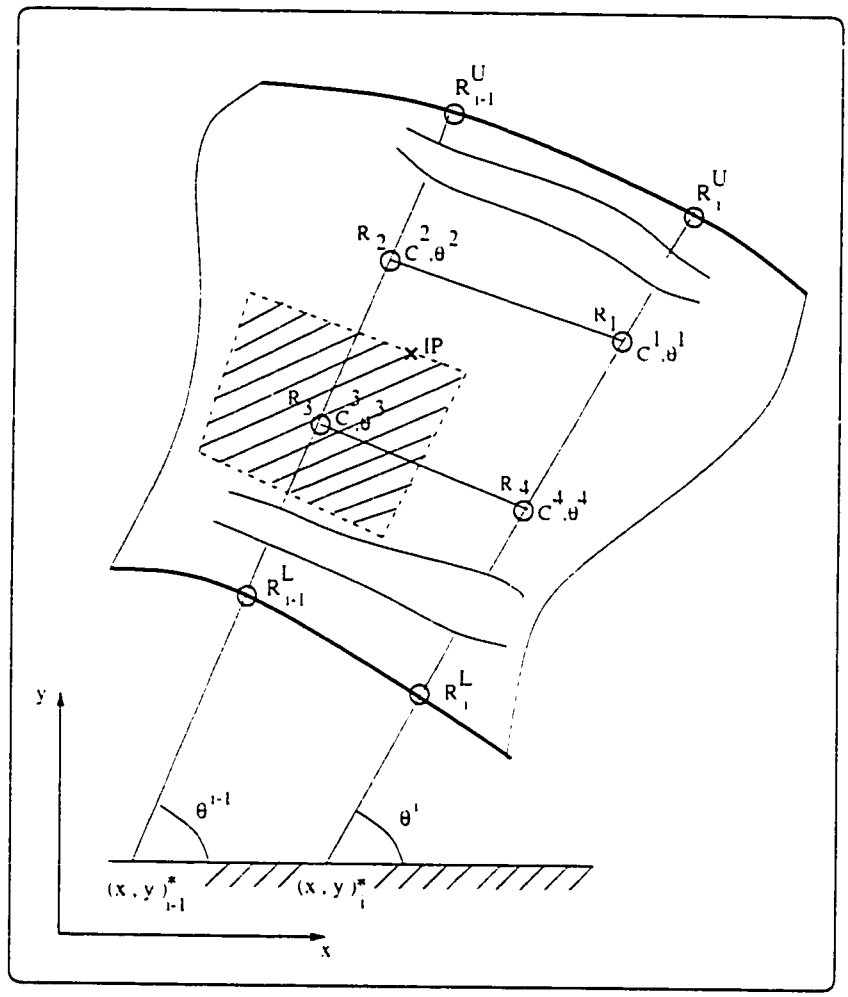

Figure 3.10: Neighbor and boundary neighbor nodes for an integration point.

Chapter 4

Direct Design: Boundary Condition Implementation

4.1 Introduction

In Chapter 3 an approximate expression for the flow term at an arbitrary internal integration point was obtained. It was shown how the flow term ($\mathcal{F}_\Theta$) could be modeled and approximately calculated at each integration point (control surface). After using that approximate expression at integration points, the element equations are assembled to form the conservation law (Eq. 3.36).

In this chapter the boundary conditions required to define a well-posed analysis problem (called *formal boundary conditions*) and the extra boundary conditions required in the corresponding shape design problem (called *extra boundary conditions* as compared to analysis problems) are also discretized and the complete unified numerical model of the problem is obtained. To do so, first some difficulties in the implementation of the extra boundary conditions required in **SSD** problems are discussed. Then formal and extra boundary conditions in two-dimensional internal ideal flows (for both ψ and ϕ formulations) and in heat conduction problems are implemented to close the system of equations in the discretized domain.

4.2 Extra Boundary Conditions

As was mentioned previously, in **SSD** problems the boundary coordinates are unknowns, to be constrained by the specified target surface distribution. In the context of heat conduction problems target heat flux distribution is assumed to be known

and in the context of the fluid flow problems the **TPD** is often specified. In potential flow shape design problems, the Target Velocity Distribution (**TVD**) can be specified along the boundary instead of the **TPD**. The boundary shape and length is unknown in shape design problems and a question that arises is how can one specify the pressure, velocity or the heat flux along an unknown boundary. Because of the similarity of the governing equations in the steady heat conduction and potential flow, only the latter is discussed here. Obviously, the arguments given in this section about the **TVD** are equally applicable when a target surface heat flux is specified.

In some applications it is possible to use a reference coordinate for specifying the **TVD**. For example it is quite usual to use the fixed chord length as the reference coordinate in airfoil shape design [109]. As an another example, in straight ducts one can use the axis of the duct (from the inlet to the outlet) as the reference length.

However, it is difficult to find an appropriate reference coordinate in general duct design problems. Therefore, in this thesis, a normalized body-fitted coordinate along the boundary is used for specifying the **TVD**. The body-fitted coordinate along the upper wall of a duct (s) is shown in Figure 4.1 and normalized as below:

$$s^* \equiv \frac{body - fitted\ coordinate\ (s)}{total\ length\ (L)} \tag{4.1}$$

Note that s^* is independent of the real length and takes values in the range $0 \leq s^* \leq 1$. When this normalized coordinate is used, the tangential velocities along the lower

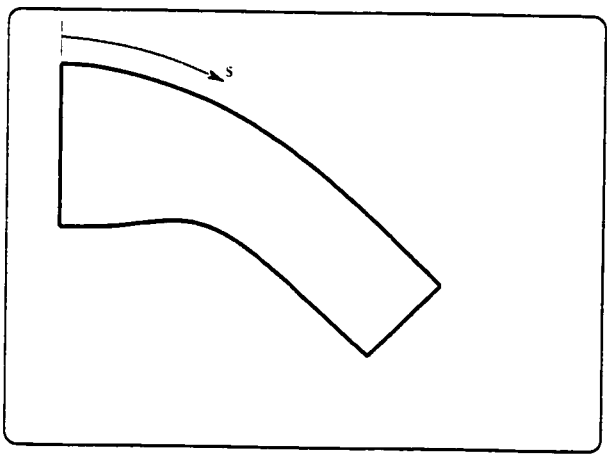

Figure 4.1: The body-fitted coordinate.

and upper walls can be represented on the same diagram with the same domain. Obviously two points at the upper and lower boundaries with the same s^* are not generally at the same distance from the inlet. Another important point about the normalized body-fitted coordinate is that the s^* positions of boundary nodal points in the initial guess would not remain fixed when the shape evolves and changes to a new one. Initially, the s^* positions of boundary nodes are known and the target velocity corresponding to each boundary node is also known. When the shape evolves, the s^* positions of boundary nodes change and therefore the target velocity for a particular boundary node is actually not known in advance.

Therefore two problems should be addressed: first, how to define the **TVD** such that it does not change when the shape evolves, and second, how to assign a target velocity to a boundary node whose final location is not known.

The remedy for the first problem, i.e. specification of the **TVD**, is to specify it with analytical functions in the range $0 \leq s^* \leq 1$. Even though simple mathematical functions can be used in some cases, they are not flexible enough to produce desirable **TVD**'s in general. To cope with this problem in this thesis, the **TVD** is specified using Bezier curves. This allows the designer to arbitrarily change the **TVD** without being worried about the mathematical expressions which actually govern the curve. Figure 4.2 shows a typical **TVD** produced by three Bezier curves.

For the second problem, the uncertainty about the final s^* position of the boundary nodes, it is assumed that the final s^* position of each boundary node is equal to its initial s^*. This assumption is obviously not realistic and means that a wrong target velocity has been assigned to the boundary node. Therefore, a few iterations are required to assign correct target velocities to boundary nodes. The number of iterations depends on the **TVD** and also the difference between the initial and final shape. If the **TVD** is uniform, for example when the shape is designed to achieve a constant boundary tangential velocity, no iteration for correcting the **TVD** is required. In general, if the difference between the **TVD** and the current boundary tangential velocity is considerable, it is better to define some *intermediate* or *temporary* **TVD**'s. In other words the design problem is solved when a sequence of sub-design problems, in each of which an intermediate boundary tangential velocity is used as the **TVD**, is solved. Therefore, the shape does not change drastically in each sub-design problem and the uncertainty about the final s^* position of the boundary nodes is not then a serious problem. It should be emphasized that the iterations just described, are actually the price that should be paid for not using a fixed reference coordinate in specifying the **TVD**. There are many shape design problems, for example airfoil design or design of

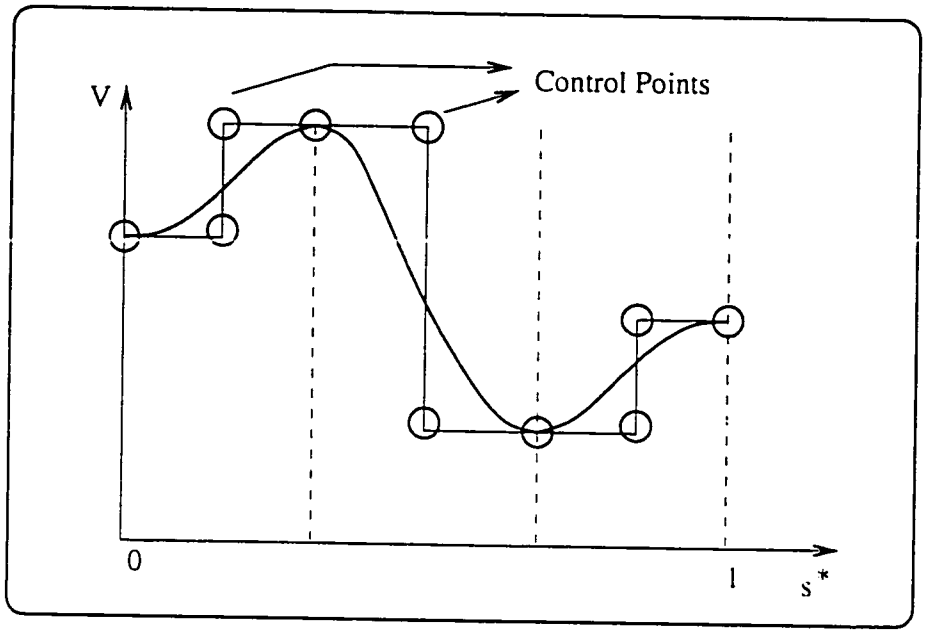

Figure 4.2: Specification of the TVD.

straight ducts, for which the designer can easily find an appropriate fixed reference to specify the **TVD** and no extra iterations, for correcting the assigned target velocities to the boundary points, are required.

4.3 Shape Design in Internal Potential Flow Problems

4.3.1 ψ Formulation

In the ψ formulation of the design problem, one may use the Dirichlet boundary condition at all boundary nodes as the formal boundary conditions (see Figure 4.3). The extra information at the upper and lower boundaries (the **TVD**) specifies the normal derivatives of the stream function on those boundaries. In this section the implementation of these constraints in the frame work of the **EB-FVM** will be discussed.

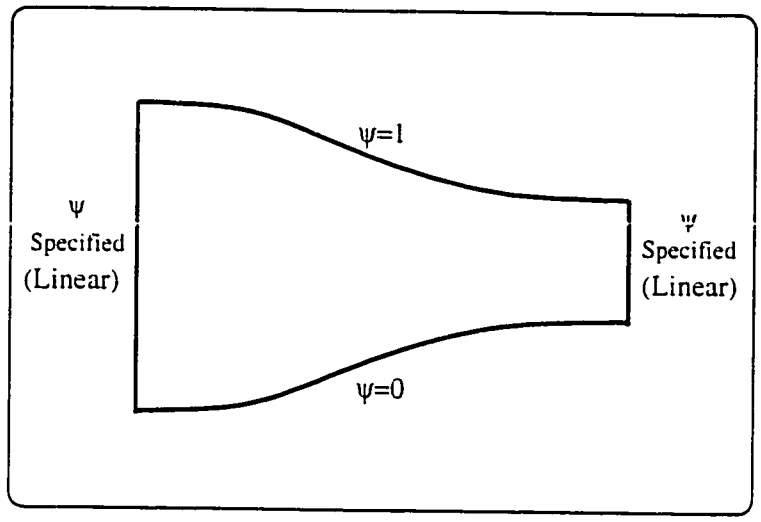

Figure 4.3: Formal boundary conditions in the ψ formulation.

4.3.1.1 Formal Boundary Conditions

Implementation of the Dirichlet boundary conditions poses no difficulty at all. In fact when the ψ values of the boundary nodes are known, no equation for the boundary $\psi's$ is required. The conservation law for a boundary control volume can be implemented, in analysis problems, to calculate the tangential velocity at the boundary. In design problems, as will be explained, the conservation law is implemented for each boundary control volume to obtain an equation for the unknown spine coordinate of the corresponding boundary node.

4.3.1.2 Extra Boundary Conditions

The stream-wise velocity at each point in a two-dimensional flow field is related to the cross-stream derivative of the stream function at that point as:

$$(\frac{\partial \psi}{\partial n})_P = V_P. \tag{4.2}$$

Therefore, in the discretized numerical model of the flow field, the flow term at the boundary integration point A (see Figure 4.4) can be calculated as:

$$\mathcal{F}_\psi \equiv \vec{\nabla}\psi \cdot \vec{A_n} = \frac{\partial \psi}{\partial n}\Big|_A \left(\frac{1}{2}L_{PW}\right) = V_A \left(\frac{1}{2}L_{PW}\right). \tag{4.3}$$

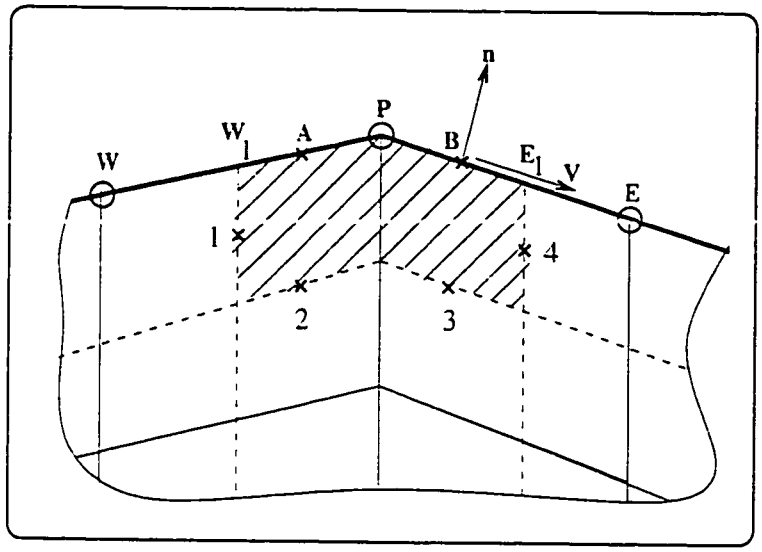

Figure 4.4: Extra boundary conditions in the ψ formulation.

Now, the conservation equation (Eq. 3.36) can be satisfied at a typical regular upper boundary control volume (see Figure 4.4) as:

$$\sum_{i=1}^{4} \mathcal{F}_{\psi i} + \left(\frac{1}{2} L_{PW}\right) V_A + \left(\frac{1}{2} L_{PE}\right) V_B = 0. \tag{4.4}$$

This can be easily done for the regular lower boundary control volumes as well. The above equation should provide an equation for the unknown R_P. To do so, L_{PW} and L_{PE} have to be written in terms of the spine coordinates of the neighbor nodes (R_P, R_W and R_E). The required equations are obtained as below (see Appendix A):

$$L_{PE} \approx (C_R^{L_{PE}}) R_E + (C_C^{L_{PE}}) R_P + (D^{L_{PE}}). \tag{4.5}$$

$$L_{PW} \approx (C_L^{L_{PW}}) R_W + (C_C^{L_{PW}}) R_P + (D^{L_{PW}}). \tag{4.6}$$

When equations 3.64, 4.5 and 4.6 are used in the conservation equation for the control volume around the boundary node P (Eq. 4.4), and the value $\psi_P = 1$ is inserted, an equation for the unknown R_P is obtained.

4.3.1.3 Final Working Equations

In the ψ formulation of the shape design problem, the stream function values of all the internal nodes and the spine coordinates of all the regular upper and lower boundary points are unknown. The required equations for the unknown stream functions were obtained in Chapter 3 and the equations for the unknown spine coordinates at lower and upper boundaries were obtained in the previous sub-section. After using all of the equations, which form a closed set of linear algebraic equations, and assembling the element equations to satisfy the conservation law for the control volumes, the following matrix equation is obtained:

$$\left[\tilde{A}_\psi\right] \left\{ \begin{array}{c} \{\psi\} \\ \{R^U\} \\ \{R^L\} \end{array} \right\} = \left\{\tilde{B}_\psi\right\}. \tag{4.7}$$

In this equation the elements of the coefficient matrix $\tilde{A}_\psi$ and vector $\tilde{B}_\psi$ are known. As was mentioned previously, this equation may be considered as a unified formulation for an analysis and its associated shape design problem. One can simply change the inputs (elements of $\tilde{A}_\psi$ and $\tilde{B}_\psi$) to switch from the analysis mode to the design mode and vice versa.

In Figure 4.5, an example of the application of the ψ formulation in **SSD** problems is shown. For the given (fixed) inlet and outlet, the initial straight nozzle shape is prescribed as shown in Figure 4.5A. The calculated initial surface tangential velocity distribution is shown in Figure 4.5B. The **TVD** (Figure 4.5D) is then used to (directly) design a new shape as shown in Figure 4.5C. Note that the duct length and width is non-dimensionalized by the inlet width (W_1) and the velocities are non-dimensionalized by the inlet (uniform) velocity (V_1).

4.3.2 ϕ Formulation

In the ϕ formulation of the ideal flow design problem, Neumann boundary conditions (ϕ_n or $\partial\phi/\partial n$, in which n is in the direction of the unit normal vector directed outward) are used as the formal boundary conditions as is shown in Figure 4.6. It is well known that an equilibrium problem with Neumann type boundary conditions is ill-posed because it accepts an infinite number of solutions. To define a level for ϕ and make the problem well-posed, the **EB-FVM** allows ϕ to be specified for one arbitrary nodal point and still satisfies the conservation principle everywhere. In other words the conservation law is not actually implemented for one control

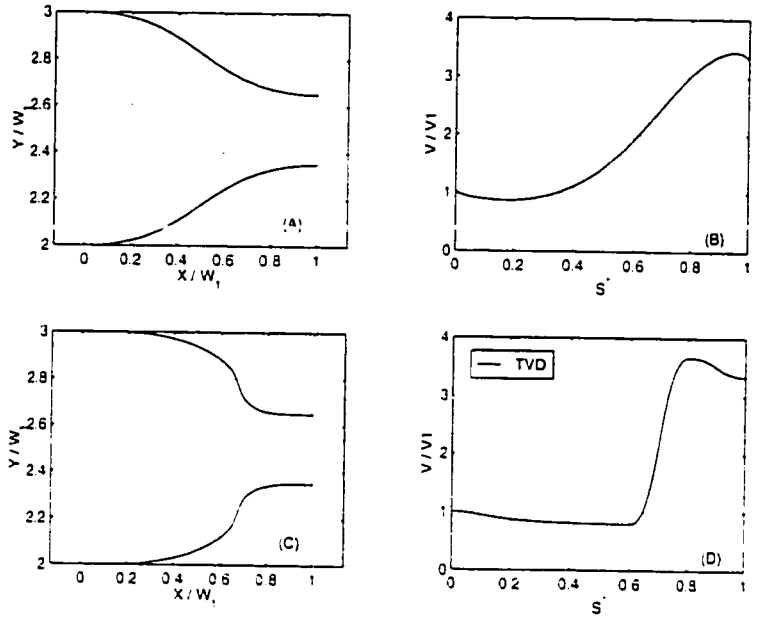

Figure 4.5: Design of a straight nozzle (ψ formulation).

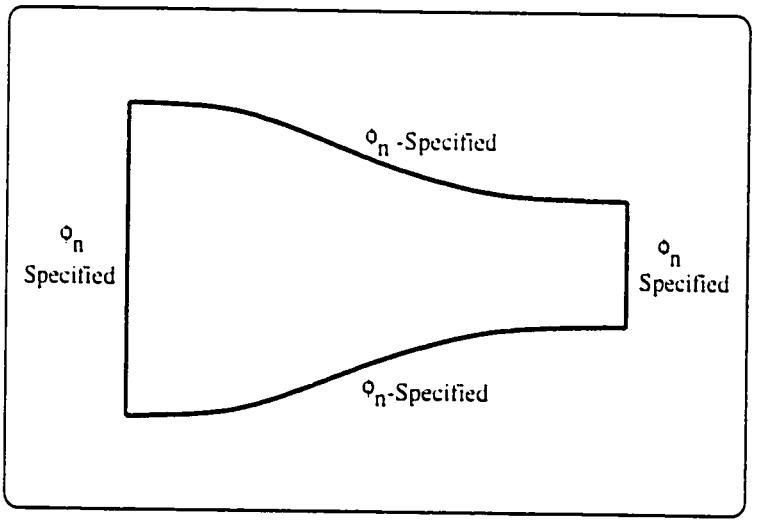

Figure 4.6: Formal boundary conditions in the ϕ formulation.

volume. But, considering the fact that the conservation principle is satisfied globally by the boundary conditions and locally for all control volumes except one, then the conservation property of the method is actually satisfied for all control volumes.

In this section, the implementation of the formal and extra boundary conditions for the ϕ formulation is discussed.

4.3.2.1 Formal Boundary Conditions

At the lower and upper boundaries, the fluid cannot cross the walls. This means that the Neumann boundary condition is applied at these boundaries as follows:

$$(\frac{\partial \phi}{\partial n}) = 0. \tag{4.8}$$

In other words for a regular lower or upper boundary control volume, $\mathcal{F}_{\phi A} = \mathcal{F}_{\phi B} = 0$ (see Figure 4.4). Therefore, the conservation law is implemented as:

$$\sum_{i=1}^{4} \mathcal{F}_{\phi i} = 0. \tag{4.9}$$

Equation 4.9 provides one equation for one unknown at each node located on the upper or lower boundaries. Considering the fact that in the ϕ formulation there are two unknowns at each upper or lower boundary node (R and ϕ), another equation is required at these points to close the system of equations. The extra boundary information (**TVD**) will be used to do so. This issue will be discussed in the next sub-section.

Inlet and outlet boundaries are known in the duct design problems considered in this thesis. In other words, the spine coordinates of the inlet and outlet boundary nodes are known and remain fixed during the shape design procedure. Therefore, only one equation is required to find the unknown ϕ at each node located at the inlet or outlet boundary. Neumann boundary conditions are used to provide the required equations. The implementation of the Neumann boundary condition at the inlet and outlet is as below:

$$(\frac{\partial \phi}{\partial n}) = \pm V. \tag{4.10}$$

The + sign is used at the outlet where the velocity is equal to V_2 and n is in the flow direction and the − sign is used at the inlet where the velocity is equal to V_1 and n is in the opposite flow direction. Therefore, the conservation law for a regular inlet

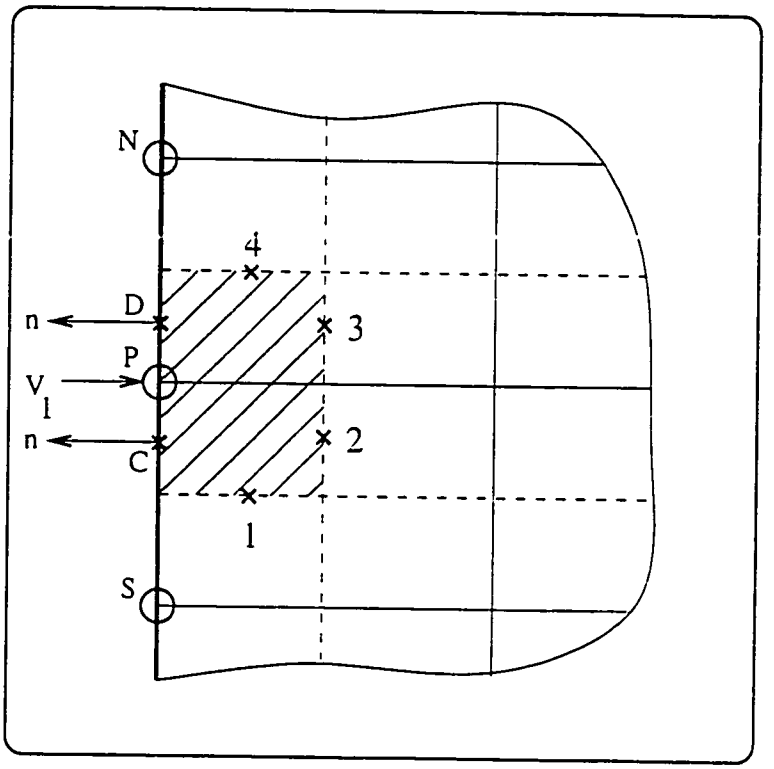

Figure 4.7: Implementation of the formal boundary conditions (ϕ formulation).

or outlet boundary control volume is as follows (see Figure 4.7):

$$\sum_{i=1}^{4} \mathcal{F}_{\phi i} \pm (\frac{1}{2}) L_{PS} V_C \pm (\frac{1}{2}) L_{PN} V_D = 0. \tag{4.11}$$

Note that $V_C = V_D = V_1$ in Figure 4.7. When equation 3.64 and the known values for the L_{PS}, L_{PN} and inlet and outlet velocities are used in the conservation equation for the control volume around the boundary node P, an equation is obtained for each unknown ϕ_P at the inlet and outlet boundaries.

4.3.2.2 Extra Boundary Conditions

The **TVD** which is specified as the required extra boundary information in potential flow shape design problems is related to the tangential derivative of ϕ as (see Figure

4.8):

$$(\frac{\partial \phi}{\partial s}) = V. \tag{4.12}$$

Application of Eq. 4.12 in the discretized domain raises a serious problem which

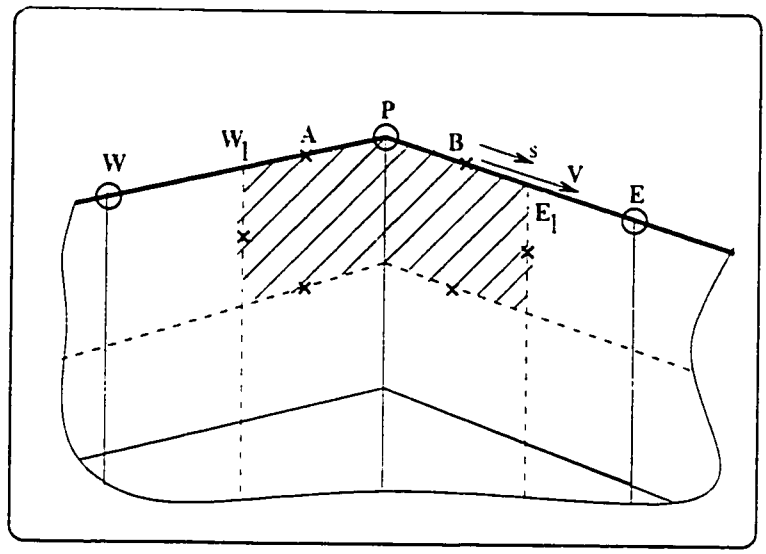

Figure 4.8: Implementation of the extra boundary conditions (ϕ formulation).

did not arise in the ψ formulation. If one attempts to discretize this equation using a Central Difference Scheme (**CDS**), the final (discretized) mathematical model will be ill-posed. As it is well known, **CDS** creates an unconstrained numerical oscillation accepting an infinite number of oscillatory solutions. Unconstrained modes are among the biggest problems in all numerical schemes and their removal is surprisingly complex.

To examine the undesirable properties of **CDS** approximations, different possible discretizations and their difficulties are first explored. The final proposed scheme, which is actually used in the ϕ formulation, is then described.

The first and most natural choice for the discretization of Eq. 4.12 would be the following **CDS** form (see Figure 4.8):

$$V_P = (\frac{\partial \phi}{\partial s})_P = \frac{\phi_E - \phi_W}{L_{PE} + L_{PW}}. \tag{4.13}$$

As is clear, ϕ_P has no role in this equation and is not constrained by this equation. If one uses this equation to apply the extra boundary conditions in the numerical scheme, the solution of the straight nozzle design problem (previously solved by the ψ formulation and showed in Figure 4.5) gives rise to the wiggly duct in Figure 4.9C. Note that an unacceptable shape is obtained for a smooth **TVD**. As a matter of fact the numerical model accepts oscillatory solutions with different amplitudes as the duct wall.

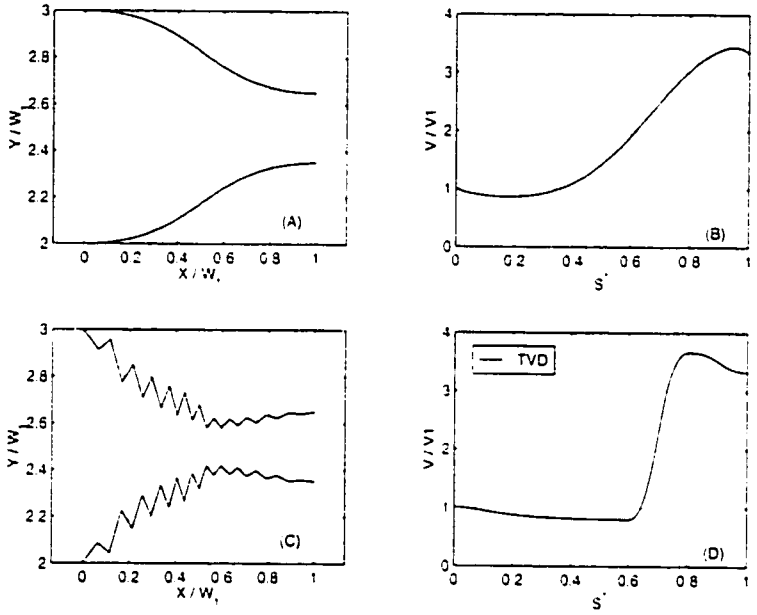

Figure 4.9: Implementation of Eq. 4.13 in the ϕ formulation.

Another **CDS** discretization for Eq. 4.12 is as follows:

$$\frac{\phi_P - \phi_W}{L_{PW}} = V_{W_1} = \frac{1}{2}(V_W + V_P). \tag{4.14}$$

The difficulty with this scheme is that the number of midpoints (like W_1) along each boundary is one more than the unknown nodes along that boundary. Therefore Eq. 4.14 can not be applied for the last boundary element and the ϕ value of the last node is not constrained. Consequently, wiggles triggered at the outlet, spread backward as is shown in Figure 4.10. However, it is interesting to note that this scheme works well near the inlet and in the middle part of the boundary.

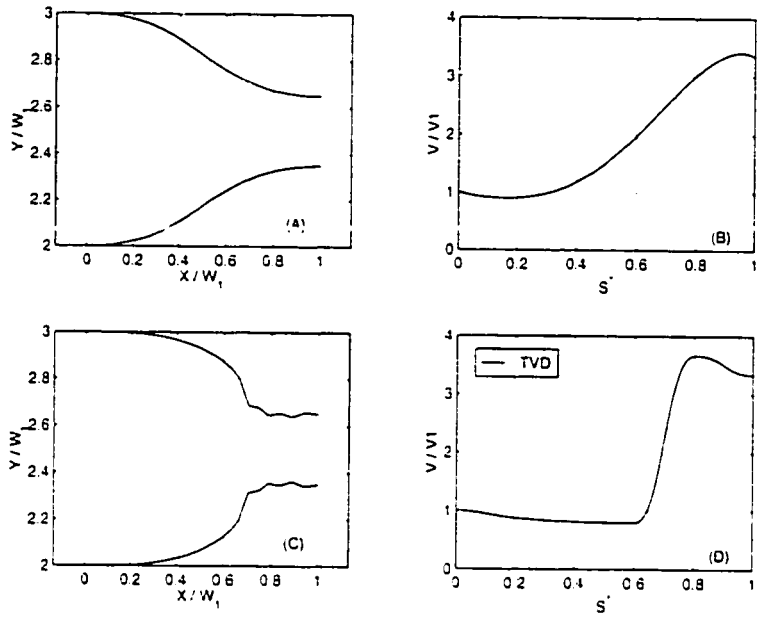

Figure 4.10: Implementation of Eq. 4.14 in the ϕ formulation.

To be able to fix the above mentioned problem, one possibility is to apply Eq. 4.14 at all midpoints along each boundary such that for each boundary node, one equation is obtained. In other words, at each boundary point P the following condition is satisfied:

$$\left[(\frac{\partial\phi}{\partial s})_{W_1} - V_{W_1}\right] + \left[(\frac{\partial\phi}{\partial s})_{E_1} - V_{E_1}\right] = 0. \tag{4.15}$$

The discretized form of this equation is as follows:

$$(-\frac{1}{V_{W_1}})\phi_W + (\frac{1}{V_{W_1}} - \frac{1}{V_{E_1}})\phi_P + (\frac{1}{V_{E_1}})\phi_E = L_{PW} + L_{PE}. \tag{4.16}$$

If this scheme is used in the discretized mathematical model of the design problem, the straight nozzle shown in Figure 4.11C will be obtained. Note that the scheme works well in regions for which $V_{E_1} \neq V_{W_1}$. In fact, as Eq. 4.16 shows, the coefficient of ϕ_P vanishes when $V_{E_1} = V_{W_1}$ and this allows the wiggles to appear.

The implementation of the extra boundary condition used in this thesis is now explained. It is a requirement that second order accuracy be maintained, which rules out the use of one-sided differences. Instead, a combination of the equations already

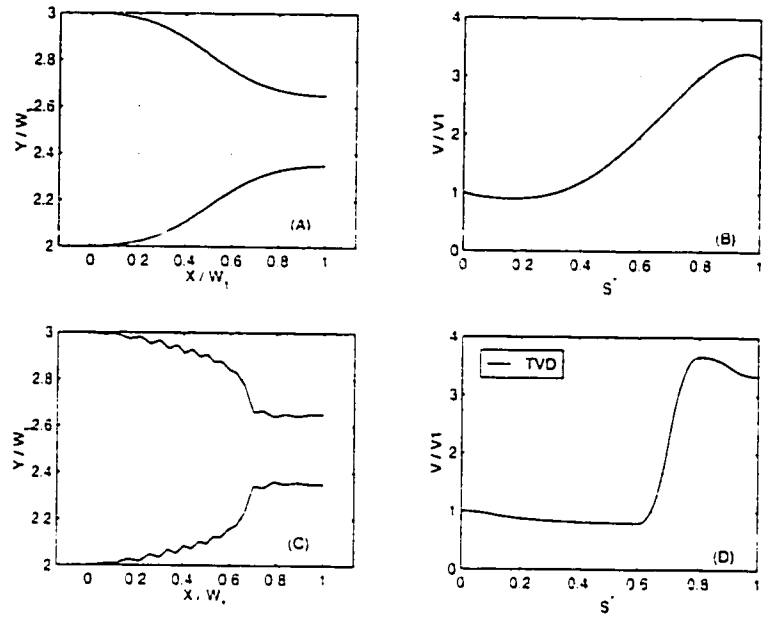

Figure 4.11: Implementation of Eq. 4.16 in the ϕ formulation.

presented is used: in regions where the **TVD** in the neighborhood of a boundary node is uniform, Eq. 4.14 is used: in regions where the **TVD** varies, Eq. 4.16 is used. Note that in the potential flow ducts, designed in this thesis, there is always uniform flow sections near the inlet and outlet. This means that Eq. 4.14 is always used for the discretization of the extra boundary conditions near the inlet and outlet.

Application of this algorithm results in a satisfactory solution of the nozzle problem as is shown in Figure 4.12C. This algorithm has been found to work very well except when the specified **TVD** has very sharp slopes and the grid is not fine enough.

4.3.2.3 Final Working Equations

In the ϕ formulation of the shape design problem, the potential function values at all nodes (except the one which determines the level) and the spine coordinates of all the regular upper and lower boundary points are unknown. Required equations were obtained in Chapter 3 and this section. Using all of the equations, which form

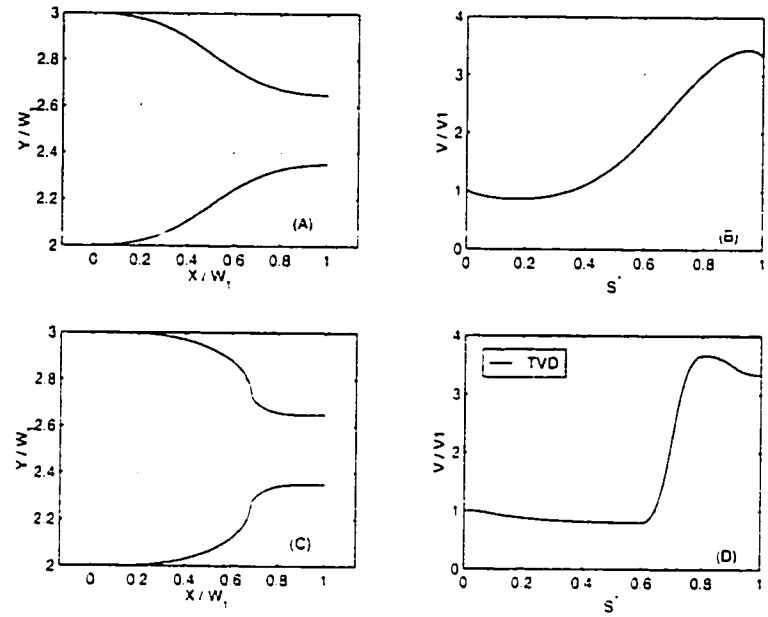

Figure 4.12: Implementation of the proposed policy in the ϕ formulation.

a closed set of linear algebraic equations, the following matrix equation is obtained:

$$\left[\tilde{A}_\phi\right] \left\{ \begin{array}{c} \{\phi\} \\ \{R^U\} \\ \{R^L\} \end{array} \right\} = \left\{\tilde{B}_\phi\right\}. \tag{4.17}$$

In this equation, the elements of the coefficient matrix $\tilde{A}_\phi$ and vector $\tilde{B}_\phi$ are known. Again, this equation may be considered as a unified formulation for an analysis and its associated shape design problem. One can simply change the inputs (elements of $\tilde{A}_\phi$ and $\tilde{B}_\phi$) to switch from the analysis mode to the design mode and vice versa.

4.4 Shape Design in Heat Conduction Problems

A two-dimensional domain can be tailored to conduct heat in an appropriate way. For steady two-dimensional conduction, the shape design method would be the same as described previously. Different (Dirichlet or Neumann) boundary conditions may be used at different boundaries but the mathematical treatment would not be different. The application of the method in shape design of heat conductors will be discussed

in Chapter 7.

4.5 Summary

In Chapter 3, an appropriate discretized form of the diffusion flow term at an arbitrary integration point was obtained. In this chapter the following were discussed to obtain a unified discretized formulation for the Laplace equation applicable in both analysis and shape design problems:

- how to specify the required extra boundary information,
- how to implement formal boundary conditions,
- how to implement extra boundary conditions.

The final matrix equation, which is a unified formulation for the Laplacian in a discrete domain applicable in solving both analysis and shape design problems, obtained as:

$$\left[\tilde{A}_\Theta\right] \left\{ \begin{array}{c} \{\Theta\} \\ \{R^U\} \\ \{R^L\} \end{array} \right\} = \left\{\tilde{B}_\Theta\right\}. \tag{4.18}$$

The scalar Θ can be the stream function ψ or the scalar potential ϕ in ideal flow problems or the temperature T in heat conduction problems.

Chapter 5

Direct Design: Validation

5.1 Introduction

In this chapter, the numerical technique, developed in Chapters 3 and 4, is validated. Special attention is devoted to the application of the ϕ formulation in solving ideal flow duct design problems.

In Section 2, the convergence criterion, required when the unified formulation is used to solve a **SSD** problem, is introduced.

In Section 3, a straight potential flow duct with constant cross sectional area is designed. Considering the fact that the **TVD** is a constant tangential velocity along the upper and lower boundaries and also the final shape (constant cross sectional area duct) is known, this is a good validation test and also a good test for the robustness of the method. Different initial guesses are given to see if the method converges to the expected solution independent of the initial guess.

Section 4 uses a bench-mark solution provided by Stanitz for a 90°-curved nozzle [71]. The **TVD**, as given in [71], is applied and the computational results are compared to the Stanitz solution.

Finally, it is shown that the unified formulation, which can be used in both analysis and design problems, and the direct discretized formulation, which can only be used in the analysis problems, are practically the same and produce similar results when applied to the same problem.

5.2 Convergence Criterion

One needs to set a convergence criterion for an iterative algorithm. Usually there are two levels of iterations: inner iterations, within which the linear equations are solved, and the outer iterations, that deal with the non-linearity and coupling of the equations [34].

The solver used in this research is a direct solver. It was shown that in the proposed direct shape design method, a nonlinear set of equations has to be solved even when the associated analysis problem is linear. Therefore, here only one level of iterations (outer iterations), is involved. The converged solution is actually the correct solution of the nonlinear equations, although it is arrived at by solving a sequence of linear equations.

If correct coefficients are used in the linearized discrete equations, which are conservation statements for the control volumes, the right and left hand sides of the equations will be the same and there are no residuals (non-physical or numerical sources or sinks) associated with the control volume balance equations. For a consistent set of discrete equations, when the residuals are small and the computational grid is fine enough, the numerical solution is close to the exact solution of the problem.

In this study absolute values of the residuals for all control volumes are calculated in each (outer) iteration and the largest residual is used as the measure of the convergence. It was observed that when this maximum value was less than 0.001, the changes in the dependent (unknown) variables (in particular the positions of the boundary nodes which describe the shape) were negligible. Therefore, this is used as the convergence criterion in this study.

5.3 A Trivial Test Case

The robustness of the proposed design method can be checked with a trivial test problem. Here the robustness of the design method is considered as the ability of the method to use different initial guesses and computational grids. An ideal robust method should work well regardless of the resolution of the computational grid and the initial guess.

To examine the robustness of the proposed potential flow design method, a 20×10 computational grid is used to design a straight duct with constant cross sectional area. The nice thing about this example is that both the **TVD** and its corresponding shape are exactly known in advance.

Let's start with an intentionally distorted shape (Figure 5.1A) as the initial guess and impose a constant tangential velocity as the **TVD** (Figure 5.1D). The boundary tangential velocity corresponding to the initial shape is shown in Figure 5.1B. In this case the deviation of the initial boundary tangential velocity distribution from the **TVD** is moderate and both ψ and ϕ formulations solve the design problem in 3 (outer) iterations and find the desired shape (Figure 5.1C).

Figure 5.2A shows another initial guess, whose corresponding boundary velocity distribution is shown in Figure 5.2B. For this problem the ψ formulation solves the problem in a single pass with 3 iterations. However, when the ϕ formulation was applied, convergence was not obtained. To obtain the solution, some intermediate **TVD**'s were defined and the shape design problem was replaced with some sub-design problems; for each of these the difference between its initial boundary velocity distribution and the corresponding **TVD** was less than the original problem. With five intermediate **TVD**'s, it takes 15 iterations for the ϕ formulation to converge to the solution shown in Figure 5.2C. Therefore, for this particular problem the ϕ formulation is not as robust as the ψ formulation. Numerical experiments also show that the ϕ formulation is sensitive to the grid resolution. In other words in some cases just changing the grid resolution can result in convergence rather than divergence.

Figure 5.3 shows another example. While the final result is obtained with 3 iterations and without any intermediate **TVD** when the ψ formulation is used, the ϕ formulation never converges to the solution regardless of the number of intermediate **TVD**'s used. If the designer chooses a finer grid, the ϕ formulation will converge to a solution. Therefore, for the given grid, the initial guess shown in Figure 5.3A may be considered as a bad initial guess for the ϕ formulation.

Even though the ψ formulation is more robust than the ϕ formulation for the given trivial test cases, it has its own limitations. For example if the duct shown in Figure 5.4A is used as the initial guess, none of the formulations will work, regardless of the number of intermediate **TVD**'s used. Of course the initial guess in this example is too far from the expected result and the initial grid is so much distorted. Therefore the proposed design method shares one of the limitations of the iterative methods, i.e. the need for a relatively good initial guess. However, as was shown in the test cases, the method is fairly robust in this regard.

5.4 Comparison to Stanitz' Results

In Chapter 2 Stanitz' shape design method was briefly described. The Stanitz 90°-elbow example, with area ratio equal to 0.5[1] not only was validated by the experimental results [71], but also was reproduced by many others, e.g. [69,110]. A 65×15 computational grid was used in the Stanitz calculations. This solution is used here as a bench mark solution to validate the present method.

The **TVD** used by Stanitz is shown in Figure 5.5B, and his corresponding elbow shape appears in Figure 5.5A. When the **EB-FVM** is used to solve the potential flow inside the Stanitz elbow in Figure 5.5A (solving the analysis problem), the tangential velocity distribution at the boundary is obtained. The present predictions are compared with the Stanitz results in Figure 5.5B. It is seen that the computational results match very well with the Stanitz results.

In Figure 5.6 the Stanitz **TVD** (Figure 5.6D) is used to design a 90°-elbow with the proposed shape design method. The initial guess and its associated surface velocity distribution are shown in Figure 5.6A and 5.6B and the designed duct is shown in Figure 5.6C. Only one intermediate **TVD** was used and it took the ϕ-formulation 7 iterations to converge to the solution. The Stanitz duct is shown by dashed lines in Figure 5.6C which are not distinguishable from the solid lines (computational results).The results indicate that the design approach works very well.

Figure 5.7 shows the results obtained for the Stanitz elbow problem when a 20×4 computational grid is used. It is seen that the designed shape is nearly the same as the Stanitz duct, even for this extremely coarse grid.

5.5 Comparison Test For the Unified Formulation

As explained previously, the final discretized equations in the proposed method may be considered as a unified formulation applicable for solving both analysis and design problems. However, one should note that different approximations are used for the estimation of the flow term in the direct formulation (used in the analysis problems) and in the unified formulation (used in the design problems). As a matter of fact, $(\mathcal{F}_\Theta)_{design}$ (Eq. 3.64) is a linearized form of the $(\mathcal{F}_\Theta)_{analysis}$ (Eq. 3.49). Therefore, when $(\mathcal{F}_\Theta)_{design}$ is used in an analysis problem, a sequence of linear problems have to be solved to approach the solution which is obtained when the $(\mathcal{F}_\Theta)_{analysis}$ is used as

1. The area ratio for a duct is defined as the outlet area divided by the inlet area.

the flow term in the same problem.

In other words when $(\mathcal{F}_\Theta)_{design}$ is used in an analysis problem, iterations are required to correct the initially guessed Θ^0 (see the coefficients of Eq. 3.64, fully defined in the Appendix A). This usually takes very few iterations.

Even though the unified formulation was validated in the previous sections, here the results obtained from $(\mathcal{F}_\Theta)_{design}$ are compared to the results obtained from $(\mathcal{F}_\Theta)_{analysis}$ when both applied to the same problem and the initial guess or **TVD** is reproduced in a two-step calculation procedure. This numerical test, which is now described, was proposed in [74] to check the accumulated numerical errors and was called the reproduction test.

In Figure 5.8 the ψ formulation is used to design a straight nozzle[2]. The computational grid is (65 × 15). Figure 5.8A shows the designed potential flow duct corresponding to the **TVD** shown in Figure 5.8B. $(\mathcal{F}_\Theta)_{design}$ was used in the numerical model in this calculation. The potential flow in the designed duct, shown again in Figure 5.8C, is now analyzed with the direct formulation (this time $(\mathcal{F}_\Theta)_{analysis}$ is used in the numerical model) and the boundary tangential velocity is calculated afterward. As Figure 5.8D shows, the calculated velocity at the boundary is practically the same as the **TVD**. One could first solve an analysis problem and calculate the surface tangential velocity and then use the calculated surface velocity as the **TVD** to solve a design problem and reproduce the initial shape. The real value of these reproduction test cases becomes more evident in three-dimensional problems in which the number of the numerical calculations is huge and these solutions form a hard test for the accuracy of both the inverse (design) and direct solver since the numerical errors tend to accumulate within the two-step validation procedure. Here, the concept of reproduction test, as proposed in [74], was used to check the accumulated numerical errors and the equivalence of $(\mathcal{F}_\Theta)_{design}$ and $(\mathcal{F}_\Theta)_{analysis}$.

5.6 Summary

In this chapter the application of the **EB-FVM** in the analysis and shape design problems, in the context of potential flows, was validated.

First, the convergence criterion, used to terminate the (outer) iterations in the numerical solution, was introduced.

Second, the design of a two-dimensional straight constant cross-sectional area

2. Similar results were obtained when the ϕ formulation was used.

duct was considered. This trivial test case was used to examine the flexibility and robustness of the method. The results showed that the method was robust and converged to the right solution after few iterations. In some cases it was necessary to use intermediate **TVD**'s to obtain the convergence.

Third, the Stanitz computational results were used to validate the proposed shape design method. Results obtained from both analysis and unified formulations were in excellent agreement with the Stanitz data.

Finally, The **TVD** used to design a potential duct was reproduced by analyzing the potential flow in the designed duct. This reproduction test case was also used to confirm the equivalence of the $(\mathcal{F}_\Theta)_{analysis}$ (Eq. 3.49) and $(\mathcal{F}_\Theta)_{design}$ (Eq. 3.64), when both are applicable.

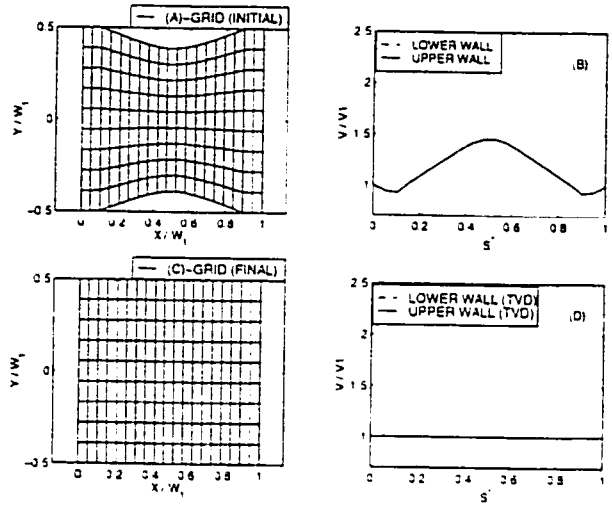

Figure 5.1: The trivial test case: a good initial guess.

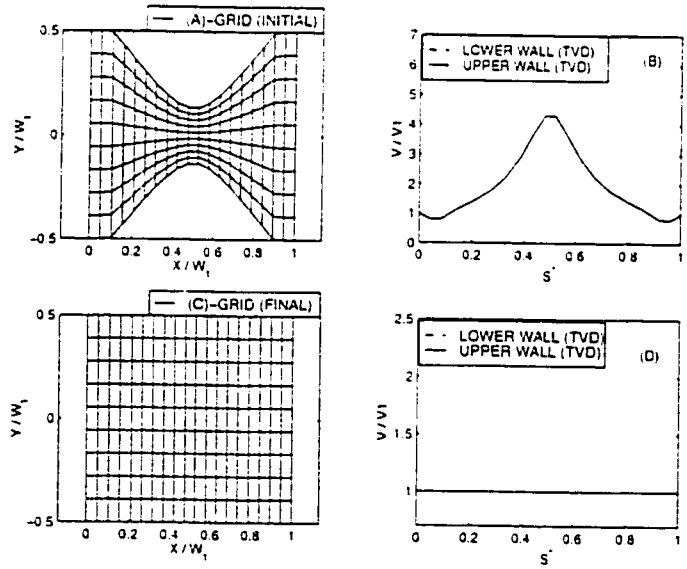

Figure 5.2: The trivial test case: a tolerable initial guess.

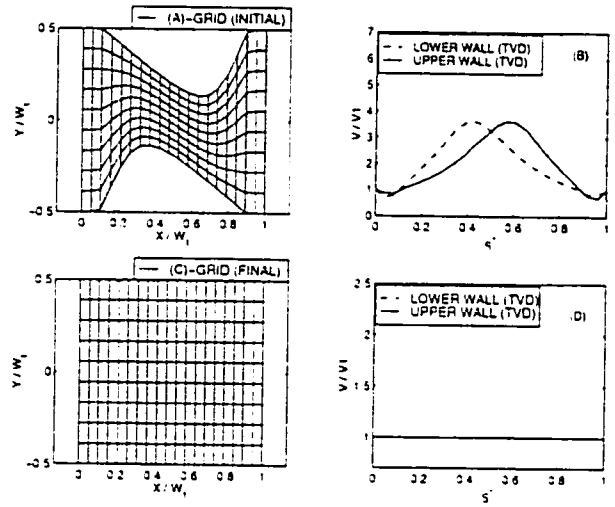

Figure 5.3: The trivial test case: a bad initial guess for the ϕ formulation.

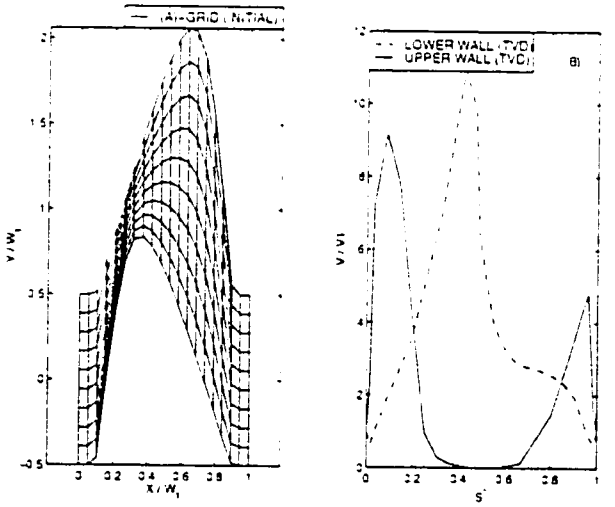

Figure 5.4: The trivial test case: an absolutely bad initial guess.

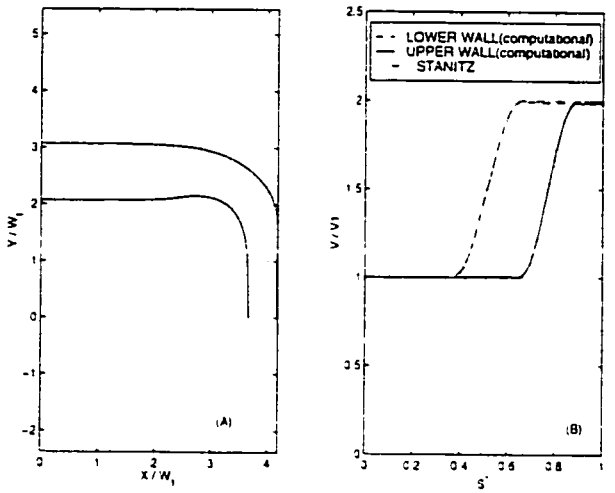

Figure 5.5: Comparison with the Stanitz results (ϕ-formulation, analysis mode, grid=65 $\times$ 15).

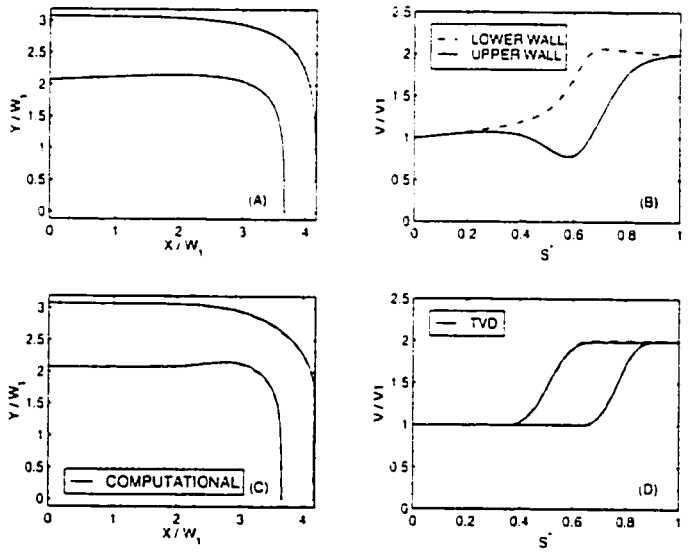

Figure 5.6: Comparison with the Stanitz results (ϕ-formulation, design mode, grid=65 $\times$ 15).

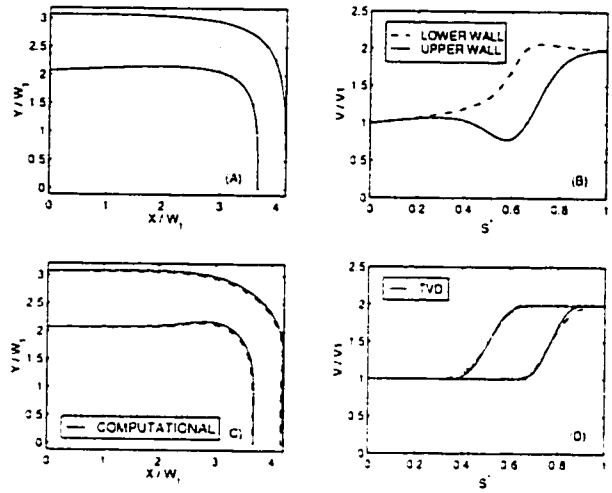

Figure 5.7: Comparison with the Stanitz results (ϕ-formulation. design mode. grid=20 $\times$ 4).

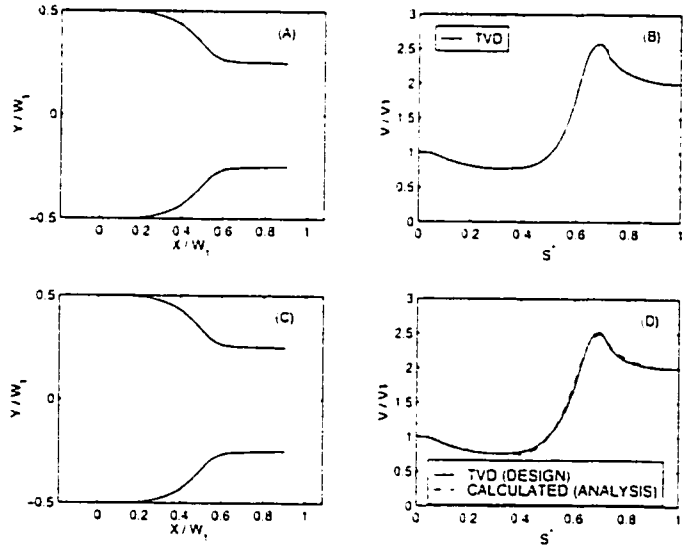

Figure 5.8: A reproduction test case (ψ-formulation. grid=65 $\times$ 15).

Chapter 6

Turbulent Boundary Layer Analysis And Separation

6.1 Introduction

Having a validated direct design method for phenomena governed by Laplace's equation, this chapter provides additional computational tools necessary for applying the direct shape design method to solve some engineering problems.

First, efficient short ducts are introduced. Then, two major related subjects, i.e. turbulent boundary layer analysis under arbitrary pressure gradients and prediction of separation, will be addressed. Both of these issues are, in fact, very difficult to cope with and at the present time there is no any accurate, robust and handy computational tool appropriate for predicting the separation and turbulent boundary layer evolution in a general design problem. Available integral turbulent boundary layer analysis methods are reviewed and categorized and a generalized integral turbulent boundary layer analysis method, based on the inner variable theory [9], is proposed.

Discussions are limited to steady, two-dimensional turbulent boundary layer flows.

6.2 Efficient Short Ducts

There are many engineering applications in which high Reynolds number flow occurs in a relatively short duct. As Figure 6.1 shows, in such cases a potential core exists all along the duct. If the boundary layers remain attached and thin, the pressure distribution at the edge of the potential core is almost the same as the pressure dis-

tribution along the walls. As was explained previously, the pressure and tangential velocity (V_t) at the edge of the potential core are related through the Bernoulli equation and one can use the **TVD** to design the potential core. The flow in a duct like

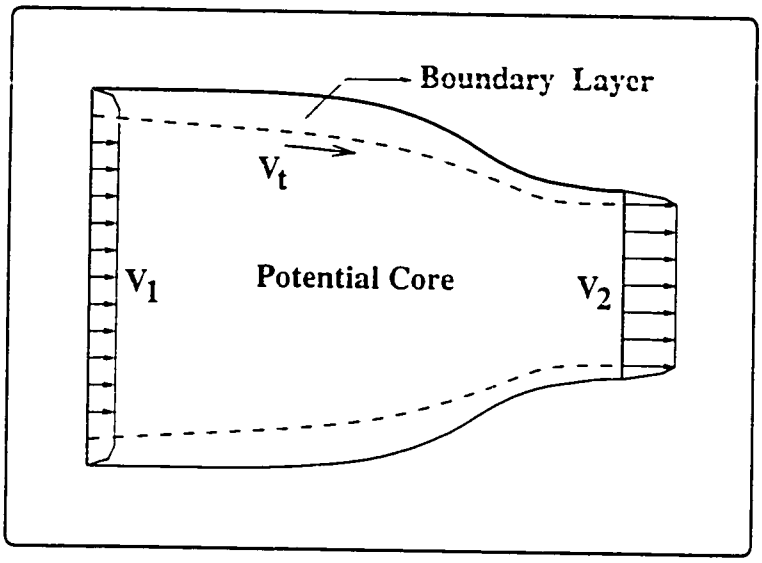

Figure 6.1: A short duct.

the one shown in Figure 6.1 is, in fact, hydrodynamically developing and boundary layer theory can be used to analyze the viscous layers near the walls. Such a duct is called here a *short duct*. To design a short duct, one may first design the potential core and then calculate and add the displacement thickness to the potential core to obtain the actual duct shape.

Depending on the inlet flow and the required turning and acceleration or deceleration, there is a minimum length for which the boundary layers can remain attached. A short duct with such a minimum length and attached flow is called here an *efficient short duct*. Design of efficient short ducts, in the context of incompressible turbulent flows, is practically important in low speed aerodynamics. The duct designer, in this case, needs to be able to predict the separation (to determine the minimum required length) and calculate the displacement thickness of the attached turbulent boundary layer (to correct the potential core shape for the viscous effects).

The complexity of attached turbulent boundary layer analysis is, to large extent, a function of the external pressure field imposed on the boundary layer. The pressure

distribution at the edge of thin viscous layers in short ducts is determined mainly by the duct shape. Therefore, turbulent boundary layer analysis and prediction of separation are necessary tools in efficient short duct design and are discussed in the following sections.

6.3 Turbulent Boundary Layer Analysis

A boundary layer is developed whenever a fluid stream meets a solid surface. The flow near the wall (in the boundary layer) is first laminar, but enters a transitional state and finally becomes turbulent. If the flow Reynolds number is sufficiently high, the transition to turbulent boundary layer flow occurs in a short distance and one may treat the entire boundary layer flow as turbulent. A turbulent boundary layer, as is known from many observations, is a three layer structure consisting of a laminar sub-layer, a buffer (transition) layer and a turbulent core (layer) [9]. The turbulence is represented by the appearance of eddies which provide bulk circulatory fluid motions. Eddies carry mass, momentum and energy and therefore affect the transport phenomena in the flow field. It is very common to neglect the buffer layer and assume that the turbulent boundary layer is composed of just two, inner and outer, layers. This two-layer model of turbulent boundary layers seems to be very useful, and more or less realistic, as will be discussed later. It is believed that large eddies, mainly in the outer layer, break down and finally disappear in the inner layer [10]. One may assume that the wall is a momentum sink and the boundary layer takes the flow momentum from the main (external) stream and carries it down towards the wall.

With this physical picture of a turbulent boundary layer, the key issue is to determine the effects of the eddies on the boundary layer flow. Engineers and physicists have tried different ways to analyze the turbulence. Regardless of the analysis method, it is important to note that the turbulence is usually described by eddies and their dynamics. In the next sub-section the major turbulent flow analysis techniques are described briefly.

6.3.1 Data Correlation, Modeling and Simulation of The Turbulence

It was hoped that one could find some *universal laws* governing turbulent boundary layer flows. Motivated with that hope, experimental data were collected and correlated for many important engineering situations.

Velocity and friction laws [9], given for the turbulent flow over flat plates and in circular tubes, are the results of organizing and correlating such data. Further speculations suggested that for certain types of flows, called equilibrium flows, universal laws can be derived. The characteristic parameter of these equilibrium flows is the β parameter which remains constant in an equilibrium flow. β is defined as below:

$$\beta \equiv \frac{\delta^*}{\tau_w}\frac{dP}{dx}. \tag{6.1}$$

In this definition δ^* is the displacement thickness of the boundary layer and τ_w is the shear stress at the wall. Obviously the flow over a flat plate ($\beta = 0$) and fully developed internal flows ($\beta = const.$) are both equilibrium flows.

Simple dimensional analysis, supported with order of magnitude analysis, shows that the scales of the eddies in the inner and outer layers of a turbulent boundary layer differ considerably [10].

The velocity scale of the turbulence in the outer layer is estimated to have an order of magnitude equal to the free-stream velocity (u_e). For the inner layer the velocity scale is rated as something proportional to u_τ, where u_τ is the shear velocity defined later in this chapter. Obviously, the velocity scale of the turbulence is smaller in the inner layer as compared to the outer layer.

Regarding the length scales, while the scales of the eddies in the outer layer are the same order of magnitude as the thickness of the boundary layer itself (δ), the scale of the inner layer eddies is estimated as ν/u_τ which is much less than the outer layer length scale.

One may develop time scales for the turbulence in the inner and outer layers as well. The time scale for the turbulence in the outer layer would be δ/u_e and for the inner layer ν/u_τ^2. In general the time scale of the turbulence in the inner layer is much smaller than the outer layer. This means that the outer layer cannot respond to a change in the flow condition as fast as the inner layer. This results in *relaxation* or *historical effects* in turbulent boundary layers. In other words, the state of a turbulent flow at a given position depends upon upstream history and cannot be uniquely specified in terms of the local strain-rate tensor as in laminar flows [10].

Roughly speaking, the ratio of the length and time scales of the turbulence in the outer layer to the inner layer scales is equal to δ^+ which, as will be explained later, is often a big number.

Because the inner layer rapidly responds to the variation of the flow condition, it can be analyzed based on the local flow conditions. The memory effects caused

by the large time scales of the outer layer means that analysis based on local flow conditions may be subject to large error. The failure to obtain a universal velocity law for non-equilibrium flows (flows with variable β) can, for example, be attributed mainly to this physical effect.

The need for robust computational tools has motivated the researchers to propose universal laws (although not quite accurate) for turbulent boundary layer flows under variable pressure gradients. Need dictates that the information obtained for many equilibrium flows be used to roughly predict a non-equilibrium flow. It is this approach which will be explained further and used in this thesis to design efficient short ducts. It should be expected that the results will be quantitatively correct in some cases, but only show reasonable trends in other situations.

There is a pressing need for more powerful analysis techniques, which would allow the engineers to cope with arbitrary equilibrium or non-equilibrium turbulent boundary layer flows.

In turbulence modeling, which is the most popular approach in today's **CFD** technology, the required scales are calculated by solving some transport equations. The turbulent quantities are actually modeled and related to mean quantities. The $k-\epsilon$ model, which uses two **PDE**'s for the production and destruction of the turbulent energy has been very successful in many industrial applications.

In large eddy simulation, only small eddies are modeled and the large ones are directly simulated and solved. The argument is that small eddies (concentrated near the wall or in the so called inner layer of the boundary layer) behave in a predictable way and can be accurately modeled. There are hopes that this approach may be a good compromise between the complete modeling and the direct simulation approach.

Finally, direct numerical simulation is used to accurately simulate and resolve all scales of the eddies. This approach will not, it seems, be a practical computational tool for the engineering analysis applications in the near future.

6.3.2 Integral Boundary Layer Analysis

The effects of an incompressible turbulent boundary layer on the flow field can be modeled in terms of some integral parameters. The most important ones are the coefficient of friction (C_F), the displacement thickness (δ^*) and the momentum thickness

(θ) defined as follows (u_e is the velocity at the outer edge of the boundary layer):

$$C_F \equiv \frac{\tau_w}{\frac{1}{2}\rho u_e^2}. \tag{6.2}$$

$$\delta^* \equiv \int_0^\infty (1 - \frac{u}{u_e})dy. \tag{6.3}$$

$$\theta \equiv \int_0^\infty \frac{u}{u_e}(1 - \frac{u}{u_e})dy. \tag{6.4}$$

In integral boundary layer analysis the governing equations are integrated across the boundary layer and transformed to another form in which the unknowns are these boundary layer integral quantities. Velocity and friction laws, mentioned previously, are used in the integral analysis methods.

For a steady two-dimensional incompressible turbulent boundary layer flow, the governing equations (the mass and momentum constraints) can be written in the following forms [9]:

$$\frac{\partial u}{\partial x} + \frac{\partial v}{\partial y} = 0. \tag{6.5}$$

$$u\frac{\partial u}{\partial x} + v\frac{\partial u}{\partial y} = -\frac{\partial \tilde{P}}{\partial x} + \nu\frac{\partial^2 u}{\partial y^2} - \frac{\partial}{\partial y}(\overline{u'v'}) - \frac{\partial}{\partial x}(\overline{u'^2}). \tag{6.6}$$

$$0 = -\frac{\partial \tilde{P}}{\partial y} - \frac{\partial}{\partial y}(\overline{v'^2}). \tag{6.7}$$

The integrated form of Eq. 6.7 is:

$$\tilde{P}(x,y) = \tilde{P}_e - \overline{v'^2}. \tag{6.8}$$

In the inviscid (external) flow field, the Bernoulli equation relates the pressure and the velocity as follows:

$$\frac{\partial \tilde{P}_e}{\partial x} = -u_e\frac{du_e}{dx}. \tag{6.9}$$

The total shear stress is defined as below:

$$\tilde{\tau} = \mu\frac{\partial u}{\partial y} - \rho\overline{u'v'}. \tag{6.10}$$

After integrating Eq. 6.5 to find an expression for the cross-wise velocity component v and using Eq. 6.8, 6.9 and 6.10, Eq. 6.6 can be written in the following form:

$$[u]\frac{\partial u}{\partial x}+\left[-\int_0^y \frac{\partial u}{\partial x}dy\right]\frac{\partial u}{\partial y}=u_e\frac{du_e}{dx}+\frac{1}{\rho}\frac{\partial \tilde{\tau}}{\partial y}+\frac{\partial}{\partial x}\left(\overline{v'^2}-\overline{u'^2}\right). \tag{6.11}$$

Experiments show that the last term is negligible, in many applications, compared to the other terms [9]:

$$\frac{\partial}{\partial x}\left(\overline{v'^2}-\overline{u'^2}\right)\approx 0. \tag{6.12}$$

Therefore, the governing equation for incompressible turbulent boundary layer flow is:

$$[u]\frac{\partial u}{\partial x}+\left[-\int_0^y \frac{\partial u}{\partial x}dy\right]\frac{\partial u}{\partial y}=u_e\frac{du_e}{dx}+\frac{1}{\rho}\frac{\partial \tilde{\tau}}{\partial y}. \tag{6.13}$$

This equation clearly shows that if the external flow field (u_e) is known, there are two unknowns in this equation: u and $\tilde{\tau}$. In fact, velocity and friction laws, which are obtained from the correlated data, can be used in this equation. Integration of Eq. 6.13 across the boundary layer and using Eq. 6.2, 6.3 and 6.4 results in the following nonlinear first order ordinary differential equation [9]:

$$\frac{d\theta}{dx}+\left(\frac{\delta^*+2\theta}{u_e}\right)\frac{du_e}{dx}=\frac{\tau_w}{\rho u_e^2}=2C_F. \tag{6.14}$$

In this equation, as was expected, integral parameters of the boundary layer (θ, δ^*, C_f) appear. Rewriting Eq. 6.14 in the following form clearly shows that the wall force balances the momentum change and the pressure change.

$$\tau_w dx=d\left(\rho u_e^2\theta\right)-\left(\delta^* d\tilde{P}\right). \tag{6.15}$$

Now the question is how one can obtain all the required information from this equation (Eq. 6.14). As will be explained, there are two family of methods: the classical (Von Karman-type) integral boundary layer analysis techniques and the inner variable-based methods.

6.3.3 Von-Karman-Type Approaches

The basic philosophy of Karman-type integral boundary layer analysis methods is explained comprehensively in [111]. These methods are well known by the shape

parameters which are defined and used by them. Particularly the shape parameter H ($H \equiv \delta^*/\theta$) is important because of its application in the correlation of data and prediction of separation. It is meaningful to call these methods outer variable methods because mainly the outer layer variables are used.

The velocity profiles used in this family of methods are categorized into two families [111]. The *one-parameter family* can be generally shown as below:

$$\frac{u}{u_e} = \mathcal{F}\left(\frac{y}{\theta}, H\right). \tag{6.16}$$

The *two-parameter family* is:

$$\frac{u}{u_e} = \mathcal{F}\left(\frac{y}{\theta}, H, Re_\theta\right). \tag{6.17}$$

The Re_θ is the momentum thickness Reynolds number defined as $Re_\theta \equiv \theta u_e/\nu$. As an example, the famous *power law velocity profile* is a member of the one-parameter family and has the following form:

$$\frac{u}{u_e} = \left(\frac{y}{\delta}\right)^n = \left[\frac{y}{\theta} \cdot \frac{H-1}{H(H+1)}\right]^{\frac{H-1}{2}}. \tag{6.18}$$

Note that the velocity law, given in Eq. 6.18, introduces two unknowns θ and H. Now, using the definition of H, the governing equation (Eq. 6.14) can be written in the following form:

$$\frac{d\theta}{dx} + \left[\left(\frac{H+2}{u_e}\right)\frac{du_e}{dx}\right]\theta = \frac{\tau_w}{\rho u_e^2}. \tag{6.19}$$

This equation is considered as the required equation for the unknown θ and, assuming u_e is known, two other equations are required for H and τ_w (or C_f). One of the required equations comes from a friction law which has the following general format:

$$\frac{\tau_w}{\rho u_e^2} = \mathcal{F}(H, Re_\theta). \tag{6.20}$$

The other required equation, which is an equation for the unknown H, can be obtained from many different equations like the energy equation, the moment of momentum equation or an entrainment equation. The general format, however, has been proposed as [111]:

$$\frac{dH}{dx} = -\left(\frac{M}{u_e}\right)\frac{du_e}{dx} - \left(\frac{N}{\theta}\right)\frac{\tau_w}{\rho u_e^2}. \tag{6.21}$$

M and N in this equation are, in general, functions of H and Re_θ.

Therefore, the classical integral boundary layer analysis methods need, in general, three auxiliary equations (a velocity law, a friction law and a shape factor law) to solve the boundary layer integral governing equation (Eq. 6.19). Experimental data are used in these auxiliary equations to close the system of equations.

6.3.4 Inner Variable-Type Approaches

The use of boundary layer inner variables (to be defined in this section) in integral boundary layer analysis does not seem, at first glance, to be a new strategy. In fact when the first paper about the inner variable theory was published in 1969 [112], and it was introduced as a new method, some researchers strongly objected, claiming it to be the classical Von-Karman approach. But, as will be explained here, although the method can be implemented exactly like the conventional Karman-type methods, it has new features and deserves to be considered as a new approach. In fact, a generalized formulation for the integral inner variable theory is presented here as a contribution of this thesis, and the philosophy behind this family of methods is explained.

While there is a well established agreement about the mathematical description of the inner layer of turbulent boundary layers, the appropriate way of correlating the available experimental information in the outer layer has been a matter of debate for a long time. Interestingly, this debate still has not been resolved and there are two different lines of thought [113]. Let's return back to the *velocity law* concept and see how a turbulent boundary layer is described.

For the region close to the wall, here called the inner layer, the *law of the wall* is applicable. According to this law, a universal velocity distribution exists near the wall which can be written as follow:

$$u^+ = \mathcal{F}\left(y^+\right). \tag{6.22}$$

It can be shown (analytically) that quite close to the wall, in the so called *viscous sub-layer*, the velocity law takes the following amazingly simple form:

$$u^+ = y^+. \tag{6.23}$$

This simple equation uses the so called inner variables y^+ and u^+. In fact the inner layer velocity and length scales are used to non-dimensionalize the velocity and length

near the wall. Formal definitions of y^+ and u^+ are as follows:

$$y^+ \equiv \frac{y}{(\frac{\nu}{u_\tau})} = \frac{yu_\tau}{\nu}. \tag{6.24}$$

$$u^+ = \frac{u}{u_\tau}. \tag{6.25}$$

In these definitions, ν is the fluid kinematic viscosity and u_τ, the shear velocity, is defined as below:

$$u_\tau \equiv \sqrt{\frac{\tau_w}{\rho}}. \tag{6.26}$$

The data available for the outer layer can be correlated by the *defect law*:

$$\frac{u - u_e}{u_\tau} = \mathcal{G}\left(\frac{y}{\delta}, \frac{\delta}{\tau_w}\frac{dP}{dx}\right). \tag{6.27}$$

The inner and outer layers meet in an overlap region which can be described by either of the following logarithmic expressions (hence called the *logarithmic region* or *log layer*):

$$\frac{u - u_e}{u_\tau} = -\frac{1}{k}\ln y^+ + A \tag{6.28}$$

$$u^+ = \frac{1}{k}\ln y^+ + B \tag{6.29}$$

The linear part of the inner layer merges to the logarithmic region through a smooth curve. This part of the turbulent boundary layer, described mathematically by Spalding [9], is called the *buffer layer* and extends from $y^+ \approx 5$ (the edge of the viscous sub-layer) to $y^+ \approx 30$ (the inner edge of the log layer).

Coles [114] noted that the deviations or excess velocity of the outer layer above the log layer in turbulent boundary layers have a wake-like shape. By adding the wake to the log-law, the following composite velocity law, which is valid from the outer edge of the buffer layer to the edge of the boundary layer, is obtained (this is called the *wake law*[1]):

$$u^+ = \frac{1}{k}\ln y^+ + B + \left(\frac{2\Pi}{k}\right)\mathcal{F}\left(\frac{y}{\delta}\right). \tag{6.30}$$

1. In [115] it has been called *the law of the wall and wake.*

In Eq. 6.30, B and k are experimental constants ($k = 0.41, B = 5.0$) and Π is the wake parameter. In fact the wake law is based on the notion that the boundary layer can be modeled as a wake flow constrained by a wall. One interesting fact about the wake law, which is used as the standard velocity law in inner variable theory, is that it contains both the velocity u and the shear stress τ_w and therefore both of these quantities (u and τ_w) in Eq. 6.13 are represented by inner variables and a separate friction law is no longer necessary. Also, there is no shape parameter involved[2].

Clauser [116] noticed that if the pressure gradient parameter (β) is kept constant in a flow, then the wake parameter (Π) will also remain constant. Therefore a universal velocity law (the law of the wake) governs all equilibrium turbulent boundary layer flows in which β (and Π) remains constant. Normally β is variable and the flow is called a non-equilibrium flow. In an attempt to extend the wake law to non-equilibrium flows as well, the wake parameter in Eq. 6.30 is considered as a variable and the equation is called *the extended law of the wake*. It has been observed that if the flow is not severely non-equilibrium, the extended law of the wake works well and can be used in engineering applications [10]. Obviously a $\Pi - \beta$ correlation is required as an auxiliary equation for the extended law of the wake.

In this thesis the inner variable theory is chosen for the integral boundary layer analysis. This theory has been used by White [9] and Das [115, 117] for solving ordinary and inverse boundary layer problems. Here, the main ideas are borrowed from the Das' method of solving inverse boundary layer problems. However, the governing equations are derived and formulated to be applicable for calculating boundary layer thicknesses and predicting separation. The generalized set of ordinary differential equations, previously obtained by Das in a different form, is obtained first and then simplified for the particular application in this thesis.

The wake law which provides the velocity law in the integral inner variable theory can be written as:

$$u = u_{wall} + u_{wake} = u_\tau \left[\frac{1}{k} \ln y^+ + B\right] + u_\tau \left[\frac{2\Pi}{k} \mathcal{F}(\eta)\,.\right] \qquad (6.31)$$

This velocity law states that if the wall shear stress (or the shear velocity) and the adverse pressure gradient (or the wake parameter) are known, the velocity profile in terms of the η coordinate is known. Here, the algebraic form of $\mathcal{F}(\eta)$, proposed by Moses [118], is used. Using the proposed function for $\mathcal{F}(\eta)$ ($\eta \equiv y^+/\delta^+$), the velocity

2. Some researchers strongly believe in shape parameters and have tried to define many different shape parameters [111].

law is obtained as:

$$u^+ = \left\{\frac{1}{k}\ln y^+ + B\right\} + \left\{\frac{2\Pi}{k}\left[3\left(\frac{y^+}{\delta^+}\right)^2 - 2\left(\frac{y^+}{\delta^+}\right)^3\right]\right\}. \tag{6.32}$$

One can use Eq. 6.32 as the velocity law and use it in equations 6.3 and 6.4 to obtain the following [115]:

$$\delta^* = \frac{\nu\delta^+}{ku_e}(1+\Pi) \tag{6.33}$$

$$\theta = \delta^* - \left(\frac{\nu\delta^+ u_\tau}{k^2 u_\tau^2}\right)\left(\frac{52}{35}\Pi^2 + \frac{19}{6}\Pi + 2\right) \tag{6.34}$$

Noting that $\tau_w = \rho u_\tau^2$ and using equations 6.33 and 6.34, the boundary layer governing equation (Eq. 6.14) can be written as:

$$[M_1]\frac{du_\tau}{dx} + [M_2]\frac{d\Pi}{dx} + [M_3]\frac{d\delta^+}{dx} + [M_4]\frac{d\delta^*}{dx} = [M_5]. \tag{6.35}$$

Parameters M_1 to M_5 are functions of $u_e, u_\tau, \delta^+, \delta^*, \Pi$. This equation is the most general form of the inner variable theory, as used for the analysis of boundary layer flows and contains all the information hidden in the momentum and continuity equation and also the velocity law. If parameters u_τ, Π, δ^+, δ^* and u_e satisfy Eq. 6.35, mass and momentum constraints are satisfied. In inverse boundary layer problems, another form of Eq. 6.35 is used in which u_e is unknown and δ^* is considered as a known quantity [115]. In the analysis of boundary layers, as is the case here, u_e is known and Eq. 6.35 introduces 4 unknowns.

To close the system of equations (solving the turbulence closure problem) three extra equations are required. Assuming that Eq. 6.35 is an equation for u_τ, two equations are readily obtained from the velocity law itself.

The equation for δ^* has been already obtained (Eq. 6.33) and applying the velocity law at the edge of the boundary layer (where $u = .99u_e$) results in the following equation for δ^+:

$$\frac{u_e}{u_\tau} = \frac{1}{k}\ln\delta^+ + B + \frac{2\Pi}{k}. \tag{6.36}$$

Now, an equation for Π is required. A correlation, in the form of a $\Pi - \beta$ relation, is an input which is needed in the inner variable theory. Here a correlation proposed

by Das [115] is used:

$$\beta = C_0 + C_1\Pi + C_2\Pi^2. \tag{6.37}$$

In this correlation, $C_0 = -0.4$, $C_1 = 0.76$ and $C_2 = 0.42$. These are obtained by fitting Eq. 6.37 to 15 sets of data.

The form of Das' correlation, given by Eq. 6.37, is open to question. Also, it is not necessary to use a $\Pi - \beta$ correlation in the inner variable theory. In fact Ferziger [119] used the wake law at the edge of the boundary layer to obtain an equation for the friction coefficient. An entrainment correlation was used in [119] to allow the experimental data, required in turbulent boundary layer analysis methods, to be used. Use of the correlations, such as Eq. 6.37, limits the range of application of the method (assuming that the velocity law is more or less universal). If it is applied to cases where the pressure gradient is outside the range of data used to obtain the correlation, large errors should be expected. Besides, it can be shown that the correlation given by Eq. 6.37 does not have any mathematical limitation for adverse pressure gradients but does have such a limitation for favorable pressure gradients. In fact this correlation predicts negative wake strength for highly accelerating flows. It can be shown that the logical range of the application of the Das' correlation is as below:

$$\frac{du_e}{dx} \leq \frac{-C_0 u_\tau^2}{u_e \delta^*}. \tag{6.38}$$

Let's assume that u_τ is known at a point along the boundary layer. Given that the external velocity field u_e is also known, the quantities Π, δ^+ and δ^* can be obtained as[3]:

$$\exp\left(k\frac{u_e}{u_\tau} - 2\Pi - Bk\right) = \left[-ku_\tau^2\left(C_0 + C_1\Pi + C_2\Pi^2\right)\right]\left[\nu\frac{du_e}{dx}(1+\Pi)\right]^{-1}. \tag{6.39}$$

$$\delta^* = \left[-u_\tau^2\left(C_0 + C_1\Pi + C_2\Pi^2\right)\right]\left[u_e\frac{du_e}{dx}\right]^{-1}. \tag{6.40}$$

$$\delta^+ = \left[u_e k\delta^*\right]\left[\nu(1+\Pi)\right]^{-1}. \tag{6.41}$$

As Eq. 6.39 shows, the calculation of Π requires solving an implicit nonlinear equation. Using Eq. 6.35 and differentiating equations 6.39, 6.40 and 6.41, results in the

3. Details of the derivation of equations in this section is given in Appendix B.

following system of Ordinary Differential Equations (**ODE**'s):

$$\begin{bmatrix} M_1 & M_2 & M_3 & M_4 \\ N_1 & N_2 & N_3 & N_4 \\ P_1 & P_2 & P_3 & P_4 \\ Q_1 & Q_2 & Q_3 & Q_4 \end{bmatrix} \begin{Bmatrix} du_\tau/dx \\ d\Pi/dx \\ d\delta^+/dx \\ d\delta^*/dx \end{Bmatrix} = \begin{Bmatrix} M_5 \\ N_5 \\ P_5 \\ Q_5 \end{Bmatrix}. \tag{6.42}$$

Parameters M_i, N_i, P_i and Q_i are functions of $u_e, u_\tau, \delta^+, \delta^*, \Pi$ and are defined in Appendix B. This system of **ODE**'s may be considered as the 4-equation model of the integral inner variable theory appropriate for turbulent boundary layer analysis. A similar generalized 4-equation model could be obtained for the inverse boundary layer problems.

White [9] has formulated a one-equation model in which only one differential equation is used for calculating u_τ and other unknowns are obtained through some algebraic equations. Das and White [115] have proposed a three equation model applicable in inverse boundary layer problems and have called that *inverse inner variable theory*. A four-equation model of the inverse inner variable theory has been also introduced in [9]. Here, based on the type of the information which are needed in the design problem, a three equation model is developed and used. To do so the wake parameter Π is eliminated from the set of equations to obtain the following set of nonlinear **ODE**'s:

$$\begin{bmatrix} C_{11} & C_{12} & C_{13} \\ C_{21} & C_{22} & C_{23} \\ C_{31} & C_{32} & C_{33} \end{bmatrix} \begin{Bmatrix} du_\tau/dx \\ d\delta^+/dx \\ d\delta^*/dx \end{Bmatrix} = \begin{Bmatrix} C_{14} \\ C_{24} \\ C_{34} \end{Bmatrix}. \tag{6.43}$$

The coefficients C_{ij} are defined as below:

$$C_{11} \equiv N_1 M_2 - N_2 M_1. \tag{6.44}$$

$$C_{12} \equiv N_3 M_2 - N_2 M_3, \tag{6.45}$$

$$C_{13} \equiv N_4 M_2 - N_2 M_4. \tag{6.46}$$

$$C_{14} \equiv N_5 M_2 - N_2 M_5. \tag{6.47}$$

$$C_{21} \equiv P_1 M_2 - P_2 M_1. \tag{6.48}$$

$$C_{22} \equiv P_3 M_2 - P_2 M_3. \tag{6.49}$$

$$C_{23} \equiv P_4 M_2 - P_2 M_4, \tag{6.50}$$

$$C_{24} \equiv P_5 M_2 - P_2 M_5, \tag{6.51}$$

$$C_{31} \equiv Q_1 M_2 - Q_2 M_1, \tag{6.52}$$

$$C_{32} \equiv Q_3 M_2 - Q_2 M_3, \tag{6.53}$$

$$C_{33} \equiv Q_4 M_2 - Q_2 M_4, \tag{6.54}$$

$$C_{34} \equiv Q_5 M_2 - Q_2 M_5. \tag{6.55}$$

Note that the solution of this system of nonlinear first order **ODE**'s requires three initial conditions. These initial conditions are not independent and actually just one initial value (for example u_τ) is required. The other two initial conditions can be obtained through the algebraic equations, i.e. equations 6.39, 6.40 and 6.41. However, if initial conditions are available for all of the unknowns (u_τ, δ^+ and δ^*), they can be used as the correct (experimental) initial conditions in the set of **ODE**'s. In other words the integral mass and momentum constraints are always explicitly enforced and satisfied but if three required initial conditions are specified independently, the velocity law and the experimental $\Pi - \beta$ correlation are not necessarily satisfied at the initial point.

It is beneficial to non-dimensionalize the above system of equations and obtain the following form:

$$\begin{bmatrix} C_{11}^* & C_{12}^* & C_{13}^* \\ C_{21}^* & C_{22}^* & C_{23}^* \\ C_{31}^* & C_{32}^* & C_{33}^* \end{bmatrix} \begin{Bmatrix} X^* \\ Y^* \\ Z^* \end{Bmatrix} = \begin{bmatrix} C_{14}^* \\ C_{24}^* \\ C_{34}^* \end{bmatrix}. \tag{6.56}$$

The non-dimensional parameters are defined as follows:

$$X^* \equiv \left(\frac{L}{U}\right) \frac{du_\tau}{dx}, \tag{6.57}$$

$$Y^* \equiv (L) \frac{d\delta^+}{dx}, \tag{6.58}$$

$$Z^* \equiv \frac{d\delta^*}{dx}. \tag{6.59}$$

$$C_{11}^{*} \equiv (\frac{1}{L})C_{11}, \tag{6.60}$$

$$C_{12}^{*} \equiv (\frac{1}{LU})C_{12}, \tag{6.61}$$

$$C_{13}^{*} \equiv (\frac{1}{U})C_{13}. \tag{6.62}$$

$$C_{14}^{*} \equiv (\frac{1}{U})C_{14}, \tag{6.63}$$

$$C_{21}^{*} \equiv (\frac{U}{L})C_{21}. \tag{6.64}$$

$$C_{22}^{*} \equiv (\frac{1}{L})C_{22}, \tag{6.65}$$

$$C_{23}^{*} \equiv C_{23}. \tag{6.66}$$

$$C_{24}^{*} \equiv C_{24}. \tag{6.67}$$

$$C_{31}^{*} \equiv (\frac{U}{L})C_{31}. \tag{6.68}$$

$$C_{32}^{*} \equiv (\frac{1}{L})C_{32}. \tag{6.69}$$

$$C_{33}^{*} \equiv C_{33}. \tag{6.70}$$

$$C_{34}^{*} \equiv C_{34}. \tag{6.71}$$

U and L in these definitions are two appropriate reference quantities. In duct problems U is generally chosen as the inlet velocity and L is the wall length.

6.4 Prediction of Separation

Separation is a phenomenon which may be observed in real (viscous) fluid flows under adverse pressure gradients. If one of these two factors (viscosity or the adverse pressure gradient) is missing, then the flow will not separate [120]. In other words, the flow separation occurs under an adverse pressure gradient and with laminar or turbulent viscosity effects.

In practice, depending on the separation driving force, two types of separation can be defined (Figure 6.2). In *geometry-driven separation* there is a sharp turning point and the detachment (separation) point is fixed and nearly independent of the Reynolds number. In contrast, in *pressure-driven separation* the separation point is strongly affected by the Reynolds number. While the analysis of the separated flow field is a difficult task in both types of separation, the prediction of the separation point in pressure-driven separation is a further complication.

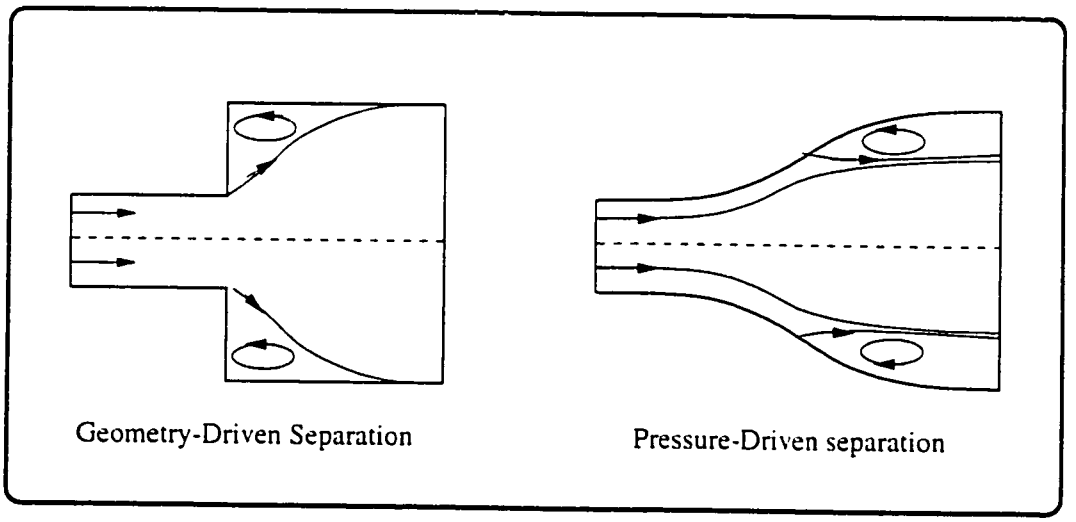

Figure 6.2: Two types of separation.

Kline studied the phenomenon of stall in internal flows and concluded that it is not just a single phenomenon but in fact a spectrum of states [121]. Based on the physical model proposed by Kline, stall may already be present at very low values of adverse pressure gradient, and the amount of stall produced then grows in a relatively continuous fashion with increased adverse pressure gradient until finally

a fully developed stall corresponding to the classical picture (bulk separation of the flow from the wall) occurs. According to the Kline physical model, in an apparently un-stalled turbulent boundary layer flow, "streaks of stall" occur regularly very near the wall. The streaks form part of a regular but transient three-dimensional pattern that is repeated over the entire wall. In an attached turbulent boundary layer flow, these streaks are caught up by the main stream, and are swept away immediately. When the adverse pressure gradient is strong enough, the streaks are no longer swept away immediately, and they begin to accumulate into large areas of stall. These large areas of stall create different flow regimes in confined (internal) flows. Kline discovered four different flow regimes in a straight flat plate diffuser and showed that the separation can be a transitory or steady and stable phenomenon depending on the flow condition and the duct geometry [122, 123]. Kline suggested that the relevant question regarding stall is not, as previously believed, is the flow stalled? On the contrary, the relevant questions are how fast is stall fluid produced by the action of the pressure forces on the fluid layers very near the wall and how fast is this stalled fluid carried away by mixing with the faster moving layers of fluid? It would appear that the amount of stall actually present is determined by the balance between these two rates. In the flat plate diffuser flow studied by Kline [121], the balance appears to be a relatively delicate one, and a small alteration in either of these rates will frequently cause a large change in the flow pattern over a period of time.

In spite of the known physical complications of separation, engineering needs motivated researchers to provide computational tools for the prediction of separation. These tools have been used mostly in external flows but they can also be used in flows in short ducts in which there are thin attached boundary layers. In [124] it is explained that, while the analysis of a separated flow needs at least a form of differential formulation, the prediction of the separation can be done by shortcut or integral methods with close to acceptable accuracy in many cases. In Appendix C, some simple shortcut methods are briefly explained and references are introduced for further information. These shortcut methods have been useful for the prediction of flow separation over airfoils. One of the successful shortcut methods for the prediction of separation, has been the Stratford method. This method is based on the two layer model of turbulent boundary layers, used in this study, and is described in some detail in Appendix *C*.

In internal attached flows, pressure gradients, in general, are quite different compared to flow over airfoils. In spite of successful applications of the shortcut methods in some short duct design problems, none of the shortcut methods were found by

the author to provide results satisfactory enough to be eligible for a general design algorithm. The Stratford method, however, gives satisfactory results in straight short nozzles and will be used in some straight nozzle design problems in this thesis. Therefore, it was decided to use the integral boundary layer, theory already described, for the prediction of the separation.

It is well known that the boundary layer equations fail to simulate the flow just ahead of the separation point. If there is an appropriate index which shows the failure of the equations upstream of the separation point, it can be used as the symptom of separation. In the Karman-type integral boundary layer methods, shape factors are used for the prediction of the separation. In general, the prediction of separation point is not accurate in these methods but is always conservative. In this thesis, the integral inner variable theory is used and ahead of the separation point the friction coefficient sharply (and unexpectedly) increases (while expected to go towards zero), the boundary layer thicknesses suddenly increase and the wake parameter increases sharply. These symptoms may be used as the separation criterion. Comparison with the available data shows that in straight diffuser problems the ratio of δ^*/δ can also be used as the separation criterion. When this ratio gets close to 0.41, separation occurs. In this thesis if one of these symptoms is observed during the solution, it is interpreted as separation. This will not be an accurate method for the prediction of separation but it works well as a conservative prediction method applicable in preliminary design studies. It will be shown that this prediction method gives satisfactory results in some of the situations for which there are experimental results.

6.5 Validation of the Boundary Layer Analysis Method

One of the best available resources for the validation of turbulent boundary layer analysis methods is the experimental results published in [118]. As a matter of fact Das' correlation [115] was obtained from some of these experimental results. To validate the proposed method in this thesis, a few test cases from the Stanford conference proceedings [118] were chosen and analyzed by the proposed method. In each case the initial values for C_F, δ^* and δ and the measured free stream velocity along the boundary layer were taken from the data and the integral inner variable theory was used to predict the variations. The experimentally determined free stream velocity has to be approximated with an appropriately smooth mathematical function because the first

and second velocity derivatives are required. Here, polynomials are used for fitting appropriate curves to the data and, as will be shown, the degree of the polynomial affects the computational results. Note that in all of the diagrams the experimental results have been shown by circles and the computational results are designated by solid lines. In each diagram the normalized velocity at the edge of the boundary layer (U/V_1), the friction coefficient (C_F), the normalized displacement thickness (δ^*/δ_1^*) and the normalized boundary layer thickness (δ/δ_1) are shown. The corresponding initial value is used for the normalization in each case.

Figure 6.3 compares the predictions of the proposed method with the experimental data for the turbulent boundary layer flow over flat plates (flow 1400 in [118]). Clearly the integral analysis works well for this standard test case.

Figure 6.4 shows the results obtained for an attached decelerated flow (called flow 4400 in [118]). The results are in good agreement with the data and the calculated displacement thickness, which is particularly important here, matches the data quite well. Note that for low values of C_F, the calculated values diverge from the experimental data.

Figure 6.5 shows the results obtained for the flow 2100 test case [118]. This example is particularly important because it includes different pressure gradients and also a flow separation. A polynomial of degree 9 was used to fitting a curve to the experimentally determined free stream velocity. The computational results are in good agreement with the data except for low values of C_F. Close to the separation point, the calculated C_F rises up unexpectedly. Also, the rate of growth of both δ^* and δ increase dramatically close to the separation point. The computational results are sensitive to the mathematical modeling of the free stream velocity (the degree of the polynomial used) particularly close to the separation point. Figures 6.6 and 6.7 were obtained with different polynomials (degrees 7 and 5) for the same flow (flow 2100). In spite of the fact that all the polynomials fit the data in the deceleration part of the free stream velocity quite well, it is seen that when a polynomial of degree 5 is used (Figure 6.7), the separation point is predicted accurately while in the other two cases C_F rises up before the separation point. In short duct design, in which the **TVD** is often a complicated mathematical function, this sensitivity is problematic. It happens that for a very minor change in the **TVD**, a flow which was considered to be separated, is predicted as attached flow. The only way to make sure that the predicted attached flow is really attached, is to consider a safety margin for the calculations. This means that the already conservative method for the prediction of the separation, should also be used conservatively by the designer.

Finally, Figure 6.8 compares the computational results with an accelerating flow test case (flow 1300 [118]). The results are not as good as the previous ones and the predicted boundary layer thicknesses are poor. In fact, computational results for different accelerating flows show that the Das correlation is not appropriate for such flows.

To validate the prediction of separation in internal flows, the experimental results for the attached flow regime in flat plate straight diffusers [123, 125, 126] were used. The diffusers had a length L along the axis, and had inlet and outlet areas of W_1 and W_2 respectively. Figure 6.9 shows Kline's "$a-a$" line, the experimentally determined limit of the attached flow regime: the flow was always attached for geometries below this curve[4]. Shown for comparison is the limit of attached flow predicted by the proposed boundary layer method. The agreement is seen to be very good, especially considering the fact that experimental curve is conservative (i.e. there were points above the line for which the flow was attached in a time-averaged sense, but there was unsteady local separation.)

6.6 Limitations of the Boundary Layer Analysis Method

The proposed integral boundary layer analysis method works well for problems in which the pressure gradients are not too far from the correlated data. In general, for highly accelerating flows, no prediction can be made by the method. Therefore, one cannot design efficient short nozzles of small size or, for example, wind tunnel contractions with severe rate of area reduction. For the nozzle problems, only when the acceleration is not severe and the actual sizes are not too small, the integral boundary layer method can be used. For efficient short straight nozzles (aerodynamic contractions) the method of Stratford (see Appendix C) is used for the prediction of separation because it has been used successfully for this type of problems.

In diffusers and spacers, if there is no severe local acceleration zones, the integral boundary layer method can be used. Again, the actual size of the duct should not be too small. Application of the integral boundary layer method in two diffuser design problems for which experimental data is available will be discussed in the next chapter.

4. According to Kline's experiments, line $a-a$ was very weakly dependent on Reynolds number over the range from 6000 to 300000 based on the throat width and mean throat velocity [122].

6.7 Summary

In this chapter short and efficient short ducts were introduced (defined). It was explained that to design an efficient short duct, the designer should be able to predict separation and analyze turbulent boundary layers under various pressure gradients.

Therefore, the available integral turbulent boundary layer analysis methods were reviewed, and a generalized formulation, based on the inner variable theory, was proposed and tested.

The issue of the separation was also briefly discussed. While different short-cut methods were addressed in this chapter (and Appendix C), no single method was found appropriate for use as a general method for predicting the separation in efficient short duct design problems. The integral boundary layer method, introduced in the first part of the chapter, was proposed to be used for the prediction of separation as well. It was shown that it could predict the separation in a straight two-dimensional diffuser quite well, and will be applicable for decelerating flows.

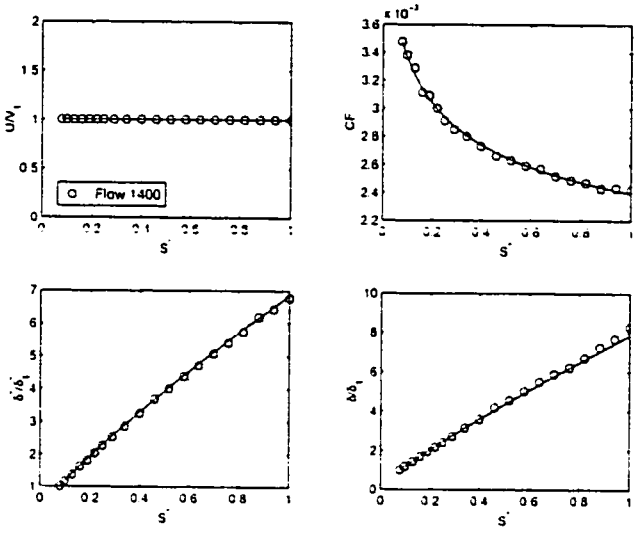

Figure 6.3: Comparison of the computational results with the flow 1400 data [118].

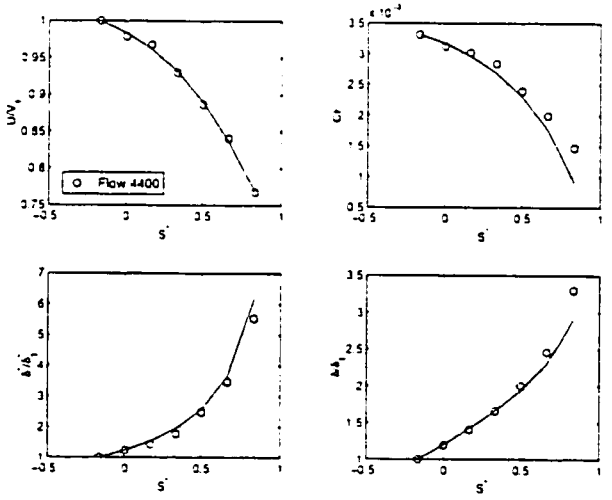

Figure 6.4: Comparison of the computational results with the flow 4400 data [118].

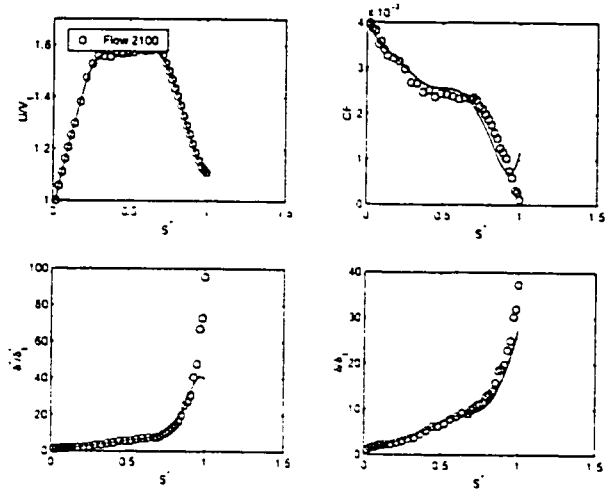

Figure 6.5: Comparison of the computational results with the flow 2100 data (polynomial of degree 9) [118].

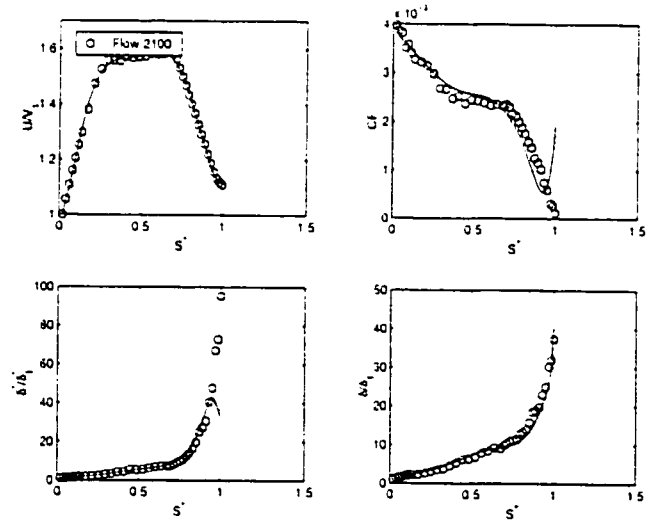

Figure 6.6: Comparison of the computational results with the flow 2100 data (polynomial of degree 7) [118].

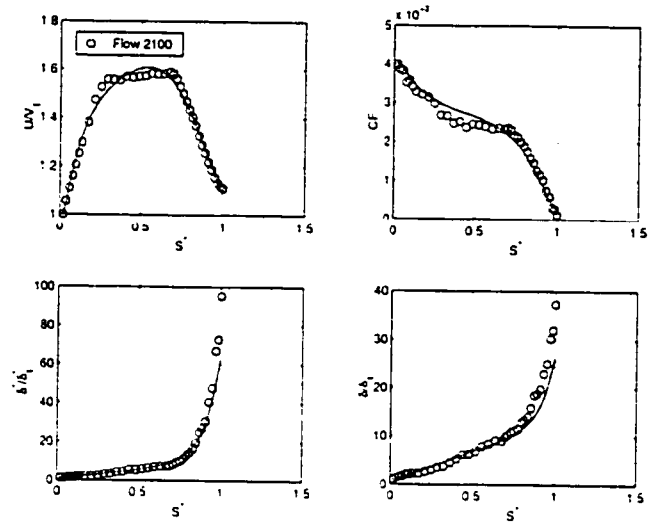

Figure 6.7: Comparison of the computational results with the flow 2100 data (polynomial of degree 5) [118].

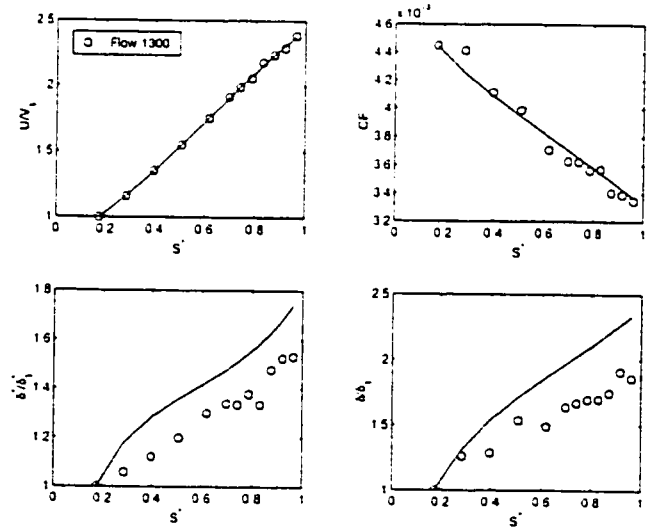

Figure 6.8: Comparison of the computational results with the flow 1300 data [118].

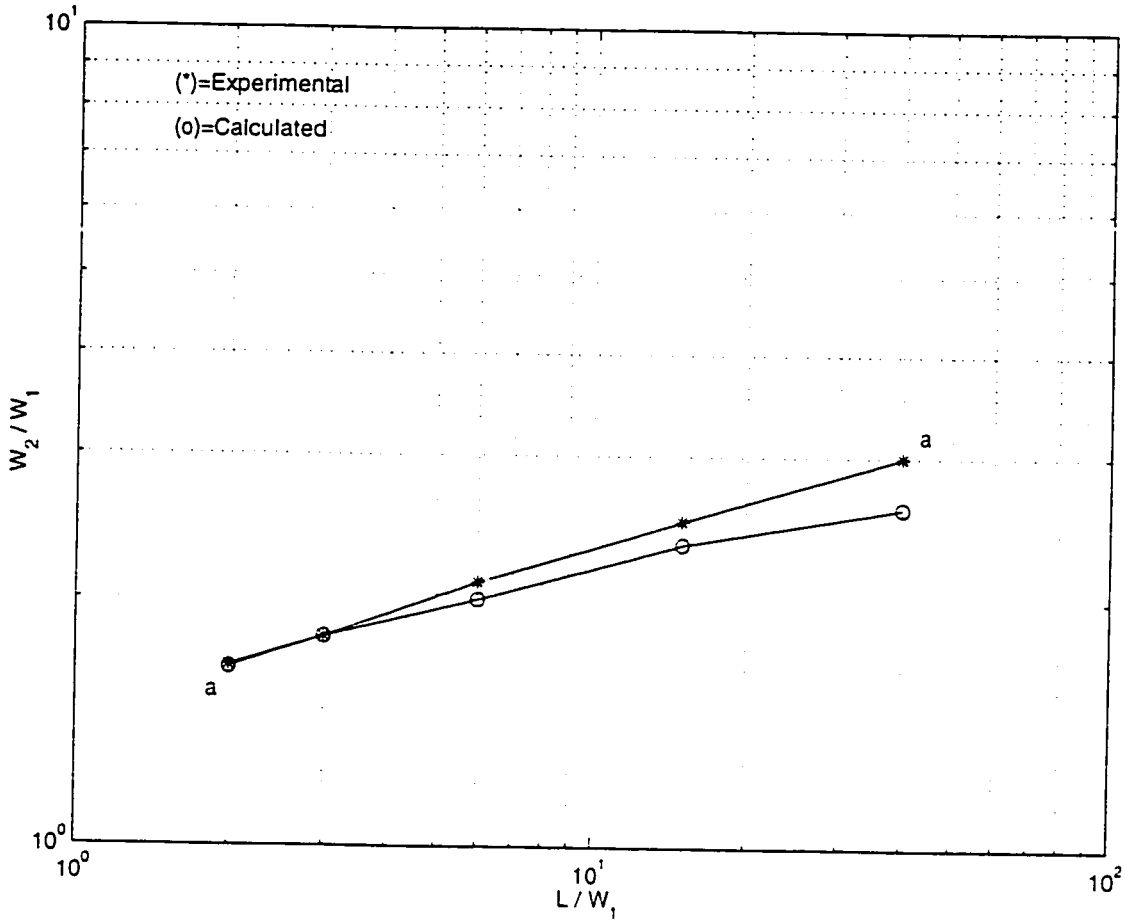

Figure 6.9: Comparison of the computational results with the Kline $a - a$ line [123].

Chapter 7

Direct Design: Applications

7.1 Introduction

In this chapter some applications of the proposed direct shape design method, at its current stage of development, are presented.

After this introduction, in Section 2, three families of duct shapes (duct families D_I , D_{II} and D_{III}) are introduced and the efficient duct design algorithm is described. Also, general guidelines relating to the specification of the **TVD** in different short duct design problems are explained. Then, a number of practically important short duct design problems are discussed and solved. Particular attention is devoted to the specification of the **TVD** in each case and a brief literature survey is provided in each relevant sub-section.

Finally, in Section 3, shape design of some heat conducting bodies is discussed. Two families of heat conductors (families H_I and H_{II}), each of which has two adiabatic surfaces, are introduced and the corresponding **SSD** problems are solved. The design goal, in this case, is to achieve a specified uniform heat flux at the outer boundary.

Examples are limited to steady, two-dimensional problems.

7.2 Shape Design: Flow In Short Ducts

In this section, design of efficient short diffusers, spacers and nozzles, is discussed. Before the design of these short ducts is discussed, some general remarks are in order. These introductory remarks are presented in three sub-sections:

- In Sub-section 1, a number of practically important short ducts are introduced and categorized as members of duct shape families D_I, D_{II} and D_{III}.

- In Sub-section 2. an efficient short duct design algorithm is described. Even though the potential core of a short duct can be designed directly to achieve a specified **TVD**, the design of efficient short ducts is inevitably iterative. An iterative algorithm which is used to find the actual duct shape as the solution of the **SSD** problem is discussed in this sub-section.
- Finally, in Sub-section 3. general guide lines for the specification of the **TVD** and its modifications (if necessary) in short duct design problems are discussed.

7.2.1 Introductory Remarks

7.2.1.1 The Duct Shape Families

Figure 7.1 shows different configurations often used as short ducts in engineering applications. The categorization provided in Figure 7.1 makes sense if one considers these ducts as flow control devices and compares the output of the device ($\vec{V}_2$ or the uniform flow at the outlet) to the input ($\vec{V}_1$ or the uniform inlet flow).

Diffusers decelerate the flow and nozzles accelerate the flow. Spacers just guide the flow in the desired direction and do not accelerate or decelerate the flow[1]. Defining the duct area ratio as the outlet area divided by the inlet area ($AR \equiv W_2/W_1$), diffusers are characterized by $AR > 1$, spacers are characterized by $AR = 1$ and finally nozzles are characterized by $AR < 1$. For incompressible two-dimensional flow in ducts with uniform inlet and outlet velocities, the area ratio is also equal to V_1/V_2.

The direction and lateral displacement of the inflow can also be controlled by the duct shape. Straight ducts do not change the direction of the flow and do not displace it laterally. Offsets are defined here as flow passages which only displace the flow laterally without changing the mean flow direction and curved ducts cause lateral displacement and flow turning. Different duct shapes, as shown in Figure 7.1, provide means to control the flow as required by the application.

When the proposed design method is used to solve shape design problems, it is beneficial to define some families of shapes. The members of each family are characterized by some *family characteristic parameters*. Even though the concept of shape families can be used to provide a framework for a general shape design package (software), for example for the design of two-dimensional ducts, no attempt is made here to provide such a general framework. Instead, shape families D_I, D_{II}

1. Note that only the flow at the duct outlet is compared with the flow at the duct inlet. Each duct, in fact, is considered as a flow control device whose input is $\vec{V}_1$ and its output is $\vec{V}_2$.

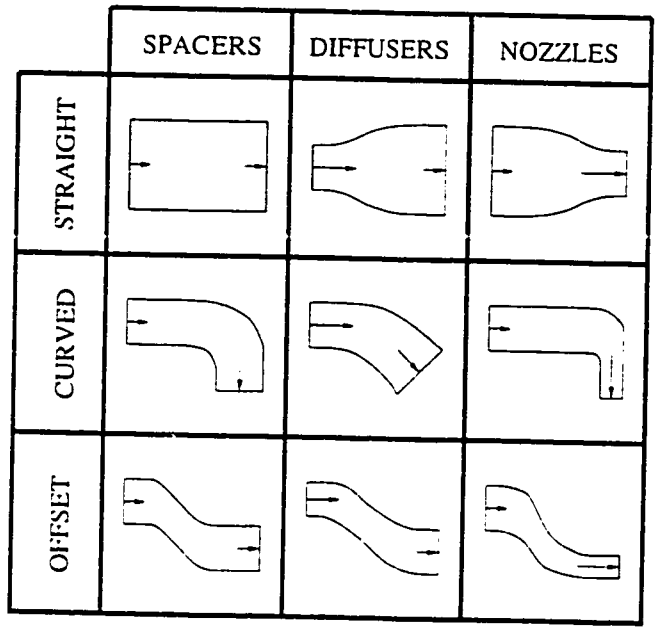

Figure 7.1: Classification of short ducts.

and D_{III} are introduced to facilitate the design procedure which will be used to solve the **SSD** problem for different ducts shown in Figure 7.1. Members of each duct shape family, which are characterized by their *family characteristic parameters*, are also constrained by some geometrical constraints. Table 7.1 shows the characteristic parameters and constraints for the families D_I, D_{II} and D_{III} as defined and used in this thesis. Parameters θ and Δ in this table are defined and shown in Figure 7.2).

The designer starts the design procedure with the following given information:

- information at the inlet: inlet uniform velocity (V_1), inlet width (W_1), inlet

Family	Characteristic Parameters	Constraints
D_I (Straight)	AR	$\theta = 0$ and $\Delta = 0$
D_{II} (Offset)	AR and $\Delta \neq 0$	$\theta = 0$
D_{III} (Curved)	AR and $\theta \neq 0$	$\Delta \neq 0$

Table 7.1: Characteristic parameters and constraints in duct shape families.

boundary layer information (as discussed in Chapter 6).

- the family of the duct and the associated characteristic parameters.
- the **TVD**.

The given geometrical information, however, does not fully specify the duct shape. In fact, the actual size and the wall profile remain unknown and are considered shape design variables. In Figure 7.2, a member of the family D_{III} is shown as an example. Note that Δ_1, Δ_2 (hereafter called the *size variables*) and the actual shape of the upper and lower boundaries (hereafter called the *profile*) are not fixed by the design input information. The designer has to specify the *size variables* and the *profile* to completely define the *duct shape*.

The following section explains how the size and profile of the duct are designed in the context of efficient short duct design problems.

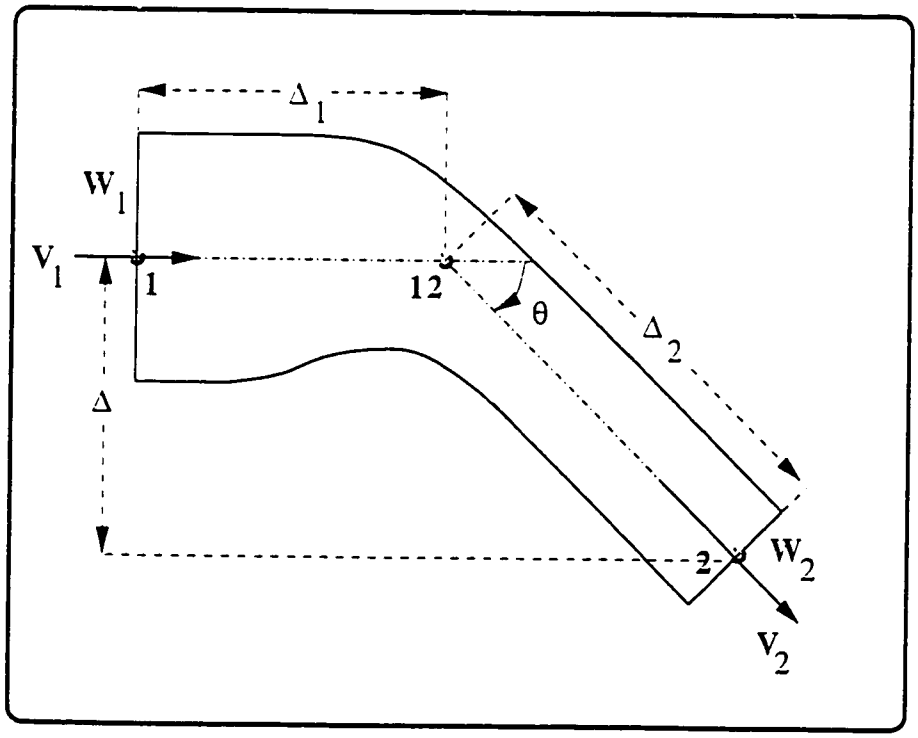

Figure 7.2: Duct geometrical characteristics.

7.2.1.2 Efficient Short Duct Design Algorithm

As was mentioned in the previous sub-section, the duct *shape* is specified when not only its family is known, but also the *size variables* and the *profile* are known. Given the required input data, the efficient short duct designer has to start with an initial guess. The initial guess generator, introduced in Chapter 3, provides appropriate initial shapes for the members of different shape families. The initial shape is always much bigger than that which is required. Let's assume that the curved nozzle shown in Figure 7.3A is the initial guess in an efficient shape design problem. Note that in this case W_1, W_2 and θ are fixed. The size variables (Δ_1, Δ_2) have been chosen longer than required in this initial guess.

The designer starts the design procedure by iteratively reducing the size variables. For each modified shape, the separation and uniformity of the flow at the inlet and outlet are checked. During these trials, no attention is drawn towards the duct profile. Only the size variables are changed and a reasonable smooth profile is used (see Figure 7.3C). The idea is that the size affects the separation more than the wall profile[2]. In other words, if the size is very big, any reasonable profile works well and results in no separation. Conversely, if the size is too small, separation cannot be prevented even when the best profile is used. The size iterations are stopped when the designer finds a critical duct size (with smooth profile) for which the flow is attached but any further size reduction results in separation. The designer, then, deliberately reduces the size and fixes the minimum or critical size (Δ_{1C}, Δ_{2C}) shown in Figure 7.3D. The surface velocity distribution associated with this shape should be reasonably close to the **TVD**.

The shape with the critical size, which was obtained iteratively, is now used as the initial guess for the direct shape design method. The concern in the proposed shape design method is the duct profile as was discussed previously. The **TVD** is imposed and the associated **SSD** problem is (directly) solved to find the appropriate duct shape which prevents separation (Figure 7.3B). Slight modification in the **TVD** might be needed at this stage of the design. Note that in the designed efficient short duct there are parallel sections near the inlet and outlet. This is necessary to make sure that the uniform inlet and outlet velocity assumptions are justified.

Strictly speaking, only the profile design part of the algorithm is relevant to the direct shape design concept proposed in this research. Therefore, in most of the short

2. Of course it is assumed that the designer has no difficulty in providing smooth and reasonable profiles for different duct sizes.

duct design examples provided in the next section, a duct with critical size is used as the initial guess and the emphasis will be on the profile design. It is assumed that an optimized (minimum or critical) size has been obtained (iteratively) and an appropriate **TVD** is used to obtain an efficient short duct. The guide lines for providing an appropriate **TVD** are presented in the next sub-section.

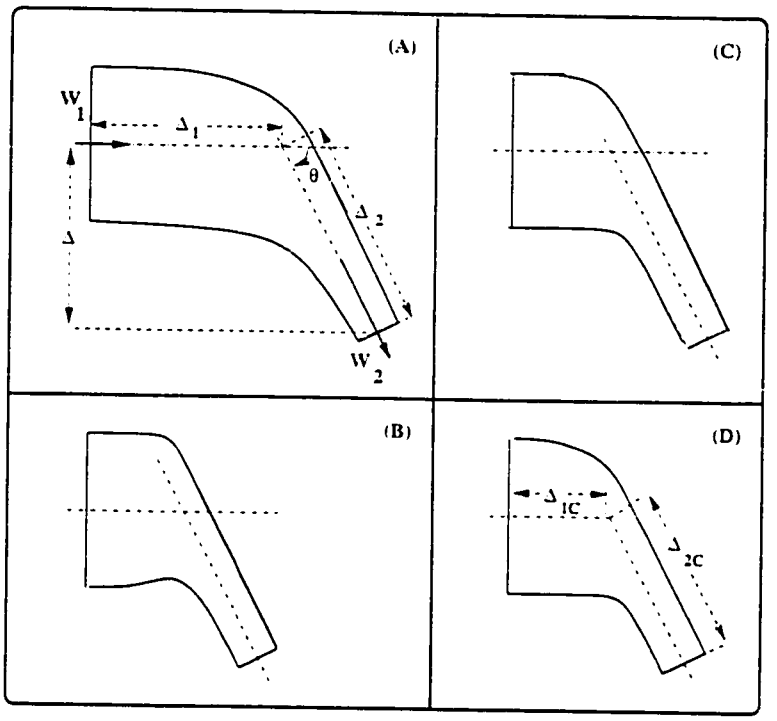

Figure 7.3: Duct size variables and profile.

After the shape (i.e. size and the profile) of the potential core of the efficient short duct is obtained, the boundary layer displacement thickness distribution along the duct is calculated and added to the potential core to obtain the actual shape of the duct.

For all the numerical computations regarding duct design problems in this chapter, a 65×15 computational grid is used. While coarser grids could be used to do the computations in some cases, this grid, which was used by Stanitz in his benchmark elbow design, was found appropriate and is used in all duct design examples. Grid refinement, for the examples provided in this chapter, did not result in any changes

in the shapes to an extent observable with the eye. Although it was possible to decrease the residual to the machine zero level for each example. The uniformity of the flow at inlet and outlet cross sections is assumed to be achieved when the difference between the minimum and maximum stream-wise velocities, normalized with the average velocity at the section, is less than 0.05.

7.2.1.3 Target Velocity Distribution

The objective in **SSD** problems, in the context of ideal fluid flow, is to approach a specified **TVD** by changing the shape. In this sub-section, general guidelines regarding the specification of the **TVD** in short duct design problems are presented.

One of the useful concepts related to the specification of the **TVD** is the concept of flow backlash in a duct flow. For the sake of clarification, consider a two-dimensional potential flow in a straight nozzle shown in Figure 7.4A. The stream and cross-stream coordinates are non-dimensionalized by the inlet width (W_1). The one-dimensional velocity distribution, normalized with the inlet velocity and shown by dashed line in Figure 7.4B, is basically due to the area ratio[3] which is a global geometrical characteristic of the nozzle. If this global effect were the only way that the duct geometry could affect the flow, the flow would be monotonically accelerating along the duct. However, due to local (profile) effects, induced by changes in the curvature of the duct walls, the surface flow (flow near the boundaries) experiences some local adverse pressure gradients. The surface velocity distribution, obtained from the two-dimensional potential flow analysis and shown with the solid line in Figure 7.4B, shows these curvature-induced deceleration and acceleration regions[4]. The surface velocity undershoot and overshoot, as shown in Figure 7.4B for example, are called *flow backlash* in this thesis. The flow backlash represents how the surface flow responds to the changes in the duct wall curvature. Note that whenever there is a flow backlash, regardless of the global flow, there is a locally induced (or intensified) deceleration region which may cause separation. If the designer wants to design a short duct which is not prone to separation and does not create or intensify the adverse pressure gradient regions along the boundaries, the flow backlash must be tailored appropriately. In other words, the designer should specify a **TVD** which does not have any backlash or is carefully tailored to not have dangerous backlash which causes separation. The concept of flow backlash, as defined here, is very helpful in

3. It is recalled that area ratio is defined here as the outlet area divided by the inlet area.
4. In each overshoot or undershoot region both flow acceleration and deceleration occur. However, it is the deceleration of the flow which is important in the **SSD** problems defined in this thesis.

duct shape design problems. In all short duct design examples given in this section, the boundary velocity distribution associated with the initial guess is also shown to emphasize that the **TVD** is actually a modified form of the initial boundary velocity distribution in which the flow backlash is treated appropriately. Therefore, the first physical-based rule for the specification of the **TVD** is that the flow backlash, observed in the initial guess, has to be tailored appropriately to make sure that the deceleration regions do not result in separation.

Another physical-based rule, which is used in the specification of the **TVD**, is that an attached flow can accelerate very sharply but, it cannot decelerate rapidly. Therefore, the general trend is that the slope of the **TVD** in deceleration regions is kept low but the slope in the acceleration regions can be very high.

Finally, it has to be noted that, in general, the specified target velocities for the upper and lower walls of a two-dimensional curved duct are different. This difference is necessary to allow the duct to turn. In fact, the difference between the specified velocities at upper and lower walls dictates the turning angle. Therefore, in straight symmetrical ducts, the **TVD**'s for the upper and lower walls are the same and in other duct configurations the difference between the specified target velocities at the upper and lower walls determines the duct turning angle or offset.

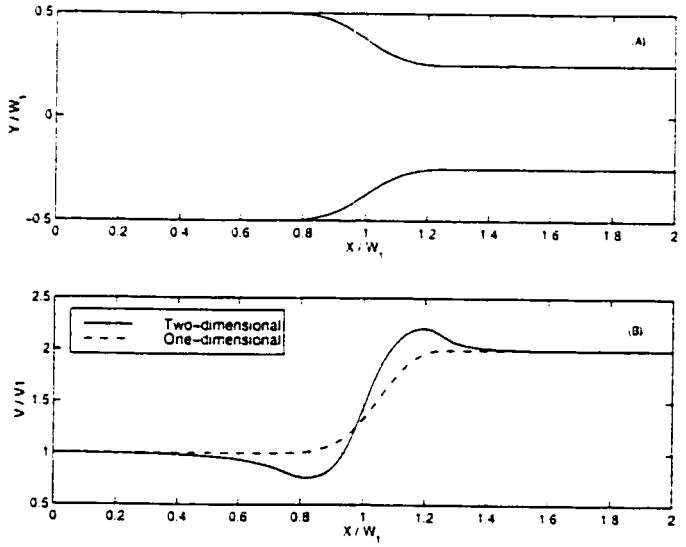

Figure 7.4: Flow backlash in a duct flow.

7.2.2 Design of Short Diffusers

In a diffuser, the flow is globally decelerating. The global deceleration is determined by the area ratio of the diffuser. However, different diffusers with the same area ratio and different wall profile, will experience different flow decelerations near the boundaries. An efficient short diffuser does not intensify the adverse pressure gradients along the boundaries. The following examples show how the **TVD** should be specified to eliminate or control the flow backlash and end up with an efficient shape. In cases where experimental data are available, computational results are compared to the experimental data.

7.2.2.1 Straight Diffusers

The flow phenomenon in straight diffusers, in particular, has been studied extensively and addressed in many publications e.g. [125-142]. In most of these references, boundary layer theory is used to take into account the viscous effects. Traditionally, straight diffusers were designed based on experimental data. Experimental data, obtained from many tests, have been collected in some references (e.g. [123]) and are used in the design of straight diffusers. Kline [128] discovered four flow regimes in straight flat plate diffusers. Considering the fact that the best performance (in terms of the pressure recovery) is obtained in the large transitory stall regime [128], most recent diffuser design techniques are able to analyze and design straight diffusers working in different flow regimes. In [126] a one dimensional potential flow model combined with a boundary layer technique is used to design the diffuser for a given performance. The objective of the design in most of the two-dimensional methods is to find appropriate length or area ratio for the diffuser which results in the best performance corresponding to the given inlet flow.

It has been found experimentally that in the straight diffuser flow, the wall profile is not as important as the gross geometrical parameters (such as the area ratio) and inlet boundary layer characteristics[5]. That is why, in practice, straight flat plate diffusers are used and design of the wall profile has not been a major issue in the design of straight diffusers. However, in [129] three different types of straight diffusers have been studied experimentally and it was concluded that the bell type (see Figure 7.5) was the best design in a sense that it keeps the wall boundary layers thin and

5. The inlet blockage (defined as $2\delta^*/W_1$) is the most important inlet boundary layer parameter in straight diffusers [123] and has an important effect on the performance and the flow regime of the diffuser.

lends itself to separation later than the corresponding flat plate and trumpet diffusers. If one constrains the flow to be parallel and uniform at both inlet and outlet, as is the case here, the wall profile will be more important.

Here, an efficient short straight diffuser which has parallel and uniform flow at the inlet and exit is designed. Figure 7.6 shows a design example. The initial guess and the tangential velocity distribution associated with it are given in Figures 7.6A and 7.6B. Separation is predicted for the diffuser shown in Figure 7.6A when the proposed integral boundary layer theory is used for the prediction of separation (some iterations are required to find this minimum size). The designer specifies a **TVD** as shown in Figure 7.6D to provide a duct profile which prevents separation. Note that a small overshoot in velocity is required at the inlet to allow rapid turning of the wall close to the inlet. If the designer does not allow such an overshoot in velocity, it will take a long upstream section to achieve uniform flow there. The major difference between the **TVD** and the initial boundary or surface velocity (Figure 7.6B) is in the deceleration policy imposed to achieve an efficient shape. While for the initial shape the adverse pressure gradient along the boundary is more or less the same along the diffuser, in the proposed **TVD** the boundary layer near the inlet is heavily loaded (sharp adverse pressure gradient) and the adverse pressure gradient is gradually relaxed towards the outlet.

Winter and East [140] have proposed power function **TVD**'s ($V = cx^{-m}$) in straight diffuser design. Greywall [143] also presented a design method for the design of the potential core in straight diffusers and suggested a similar power function as the **TVD**. The **TVD** proposed here is consistent with the power function idea however, as was explained previously, the designer is not required to use a simple mathematical function. Bezier curves are flexible enough to impose any **TVD**, as required. In fact, the deceleration is tuned with the ability of the boundary layer to remain attached to the wall. Near the inlet the boundary layer is fresh and energetic and close to the outlet of an efficient diffuser, the flow cannot tolerate any adverse pressure gradient.

The inlet boundary layer information in this design example was taken similar to the initial data in the flow 2100 [118] and the diffuser inlet width (W_1) was chosen equal to $0.4m$. Inlet blockage is equal to 0.005 which is small enough to assure that the diffuser works in the attached flow regime.

Figure 7.7 shows the designed diffuser again and provides more information regarding the wall profile and the distribution of the displacement thickness along the walls. Figure 7.7C shows the wall turning angles for the designed (optimized) diffuser. As this Figure shows, in an efficient short straight diffuser, much of the turning, re-

quired for the area change, takes place near the inlet. In other words, much of the pressure recovery is gained near the inlet and the rest of the duct is mainly responsible to return the flow back to the main stream direction safely. Figure 7.7D shows the distribution of the boundary layer displacement thickness along the duct (normalized with the inlet value) calculated by the integral boundary layer theory. The actual size of the viscous layer is much less than the width of the duct. Therefore, Figure 7.7A which shows the potential core shape, is practically quite close to the actual duct shape and the viscous corrected shape is not distinguishable from the potential core when both are drawn with the same scale.

It is interesting to see how the flow responds to a trumpet profile for a diffuser with same dimensions as the designed diffuser shown in Figure 7.7A. A trumpet-type diffuser is shown in Figure 7.8A and its corresponding boundary tangential velocity distribution is shown in Figure 7.8B. Note that the slope of the deceleration (the adverse pressure gradient) increases towards the exit. This, does not comply with the boundary layer demands for this particular design (the boundary flow is highly decelerated near the end where the boundary layer flow is tired). As Figure 7.8C shows, much of the wall turning is close to the exit. As is expected, the flow separates from the wall due to the wrong policy imposed by the **TVD**. The very sharp increase in the displacement thickness near the exit (at $s^* \approx 0.7$ in Figure 7.8D) is the sign of separation. Further information about the viscous flow in this trumpet-type diffuser, obtained from the integral boundary layer method, is shown in Figure 7.9. It is seen that C_F and the normalized wall shear stress (τ_w/τ_{w1}) go towards zero and then rise up rapidly. The results shown after the separation point ($s^* = 0.73$) have no value and actually the parameters behave wildly (see for example the displacement thickness, Figure 7.8D, or the shape factor H shown in Figure 7.9). Even though no quantitative measure can be attributed to the shape factor H at the separation point , it is seen that H rises very sharply near the separation point and can be used as a separation symptom. These boundary layer analysis results on bell and trumpet-type straight diffusers agree well with the observations reported in [129].

7.2.2.2 Curved Diffusers

Combined effects of global deceleration, local curvature-induced adverse pressure gradients, and the flow turning makes the curved diffuser design problem a very difficult one. In three-dimensional cases, the secondary flow also affects the flow field and the boundary pressure gradients. In three-dimensional curved diffusers, the secondary flow provides a mechanism for the exchange of mass between low pressure and high

pressure regions along the duct wall. From this point of view, the secondary flow is a helpful phenomenon and it is expected that if a short two-dimensional curved duct is designed to prevent separation, a three dimensional duct with same area ratio, turning angle and wall curvature will have attached flow with a broader margin of safety. In other words two dimensional design results can be conservatively used in the design of three-dimensional ducts. However, the secondary flow makes the flow non-uniform and if the flow has to be uniform at the outlet of a short duct, the secondary flow has to be suppressed or controlled somehow. Here, two-dimensional flow is considered and the issue of secondary flow is not the concern.

To get an idea about the flow phenomena in a curved diffuser, a potential flow 90°-curved diffuser is considered first. Figure 7.10A shows the initial guess made for the design of a 90°-curved diffuser with area ratio equal to 2. The tangential velocities along the upper and lower boundaries, calculated after solving the analysis problem associated with the initial guess, show the undesirable flow backlash on both upper and lower boundaries (Figure 7.10B). Note that the tangential velocity along the upper wall for the initial guess is everywhere less than the tangential velocity along the lower wall. This means that the pressure along the upper wall is everywhere higher than the pressure along the lower wall and this is consistent with the fact that the duct turns towards its lower wall.

The flow backlash regions intensify the adverse pressure gradients along the walls and the shape designer has to propose an optimized **TVD** to obtain a shape that better controls the flow (not creating backlash). Based on the guidelines explained previously in this chapter, the **TVD** is proposed as shown in Figure 7.10D. The direct shape design method uses the initial guess and the **TVD**, and returns the shape shown in Figure 7.10C. This shape may be considered as an optimum shape in a sense that the shape does not intensify the global deceleration dictated by the diffuser area ratio. It is seen that the deceleration at the upper boundary starts sooner than the lower wall. It takes a few iterations for the designer to determine the distance between the velocity distributions at the upper and lower walls which results in 90° turning.

Design of an efficient short curved diffuser with a high area ratio is difficult and often the flow separates because of the sharp deceleration, dictated by the area ratio. Often, to design a short high area ratio diffuser with attached flow, other methods such as suction, blowing or using guide vanes, should be considered.

In the context of the boundary layer theory (combined with the potential flow analysis), the curved diffuser flow has been studied by some researchers, e.g. [144–147]. Also there are many experimental results on the curved diffuser flow mainly for the

purpose of the validation of **CFD** codes; e.g. [148]. Most of the published results consider, unfortunately, three-dimensional flows in curved diffusers.

Parsons [146] designed and built a two-dimensional curved diffuser with an area ratio equal to 1.34 and a turning angle equal to 45°. Parsons used the Stanitz method to design the potential core and used an integral boundary layer method proposed by Moses [146] to correct the shape for viscous effects. In Figure 7.11A the shape of the potential core calculated by Parsons (dashed lines) and the actual duct which was built and tested (solid lines) are shown. Figure 7.11B shows the **TVD** specified by Parsons. In this figure the velocity data (calculated from the measured pressures) is also shown[6]. It is seen that the agreement between the expected (specified) boundary velocities and the actual velocities near the boundary is good.

The **TVD** used by Parsons was applied in the proposed shape design method. The potential core obtained agreed exactly with that of Parsons. In Figures 7.12A and 7.12B the initial guess and its associated boundary velocity are shown. The imposed **TVD**, which was the same as the parsons **TVD**, is shown in 7.12D. The designed potential core, which is the same as the Parsons potential core, is shown in Figure 7.12C. The integral boundary layer theory, proposed in this thesis, was used to correct the Parsons potential core shape for the viscous effects. This boundary layer method predicts separation on the lower wall and does not provide realistic results in this case. The boundary layer calculations on the upper wall stall close to the acceleration region shown in the **TVD** (Figure 7.12D). This, seems to be related to the weakness of the boundary layer method in dealing with highly accelerating flows.

The Parsons duct can be redesigned with another **TVD** in which no flow backlash is allowed (Figure 7.13D). The initial guess and its calculated boundary velocity are shown in Figures 7.13A and 7.13B. Figure 7.13C shows the potential core obtained for the modified **TVD** shown in Figure 7.13D. Note that the elimination of the flow backlash results in an initially sharper deceleration on the outer wall. Even though the initial surface velocity (Figures 7.12B) is drastically changed in Figures 7.12D and 7.13D, the designed shape does not seem to change considerably with respect to the initial guess. In Figures 7.14, 7.15 and 7.16 important parts of the initial and final shapes are magnified and shown. These figures show that the wall curvatures are quite different, indeed, in the initial and designed shapes.

Figure 7.17 compares the modified potential core, shown in Figure 7.13D, with

6. In this Figure, VL and VU refer to the tangential velocities at lower and upper boundaries respectively.

the Parsons potential core. The viscous corrections corresponding to this modified TVD, predicted by the integral boundary layer, are shown in Figure 7.18. For the purpose of comparison, the Parsons duct is also shown in this Figure[7]. It is seen that the predictions of the present proposed integral boundary layer theory is poor on the lower wall near the exit.

7.2.2.3 Offset Diffusers

S-shaped diffusers play an important role as inlets to the air-breathing propulsion engines that are installed at offset locations in aircraft. The performance of the engine depends on the flow condition at the engine face, which in turn depends on the inlet design. It is desirable that an engine inlet provides a uniform flow at the engine face with as high a total pressure as possible. This is generally the task in designing offset diffusers. There are few publications which address this problem in the context of boundary layer flow [149, 150]. Also, there are some published experimental results which include three-dimensional phenomena as well [151–153].

S-shaped diffusers may be considered as a combination of two 45°-curved diffusers. As mentioned previously, the global geometrical parameters of a diffuser are often more important than the details of the wall profile. In s-shaped diffusers, a double turning of the flow is required. In an efficient short s-shaped diffuser, the first turn should be accomplished in a shorter length compared to the second turn. This design philosophy is consistent with the design philosophy stated for the straight diffusers, i.e. the deceleration near the inlet is relatively sharp and diminishes gradually towards the exit.

Figure 7.19 shows the design of a s-shaped diffuser. In Figure 7.19B the TVD is shown. Note that the cross-over point, between the two serial curved diffusers, is closer to the inlet and the deceleration in the first turn is steeper than the second turn. Figure 7.19A shows the designed potential core of the efficient short offset diffuser for the given offset and area ratio. As is expected, the designed potential core has unequal deceleration ratio in the two turns. The first turn is accomplished in a shorter length as compared to the second turn. This asymmetrical diffuser is much superior to the diffuser with symmetric turns in terms of susceptibility to flow separation and boundary layer displacement thickness distribution. Figure 7.19C shows the flow angles at the upper and lower boundaries of the potential core and Figure 7.19D shows the predicted boundary layer displacement thicknesses for upper

7. Note that different TVD's were used to design these ducts.

and lower boundaries. The inlet width in this case was equal to $3.8cm$ and the inlet blockage was equal to 0.05.

Rehman and Bowyer [150] designed and built a two-dimensional s-shape diffuser with area ratio equal to 2 as shown with the solid lines in Figure 7.20A. To design the duct, they specified a **TVD** as shown with the solid and dashed lines in Figure 7.20B. Then the Stanitz method was used to obtain the potential core shape (dashed lines in Figure 7.20A). Finally an integral boundary layer analysis technique, proposed by Truckenbrodt (see [150]), was used to correct the potential core for the viscous effects. The actual velocity distribution along the duct walls, obtained from the measured pressures along the boundaries of the built diffuser, is close to the specified **TVD** shown in Figure 7.20B.

To compare the results obtained from the proposed method with the data provided by Rehman and Bowyer [150], the proposed design method in this thesis was used and the **TVD** for the design problem was chosen exactly as was proposed in [150] and shown in Figure 7.20B (solid and dashed lines). The designed inviscid core was the same as the one obtained in [150] by Stanitz' method. For the given inlet information (the inlet blockage was equal to 0.05), the potential core was corrected for the viscous effects. The final designed duct shape was practically the same as the duct tested by Rehman and Bowyer (indistinguishable from the duct shape shown with the solid lines in Figure 7.20A). Therefore, the integral boundary layer theory, used in this thesis, provides realistic viscous corrections for this example.

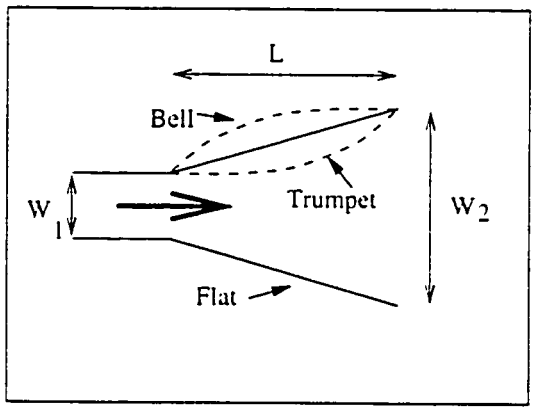

Figure 7.5: Experimentally studied straight diffusers [129].

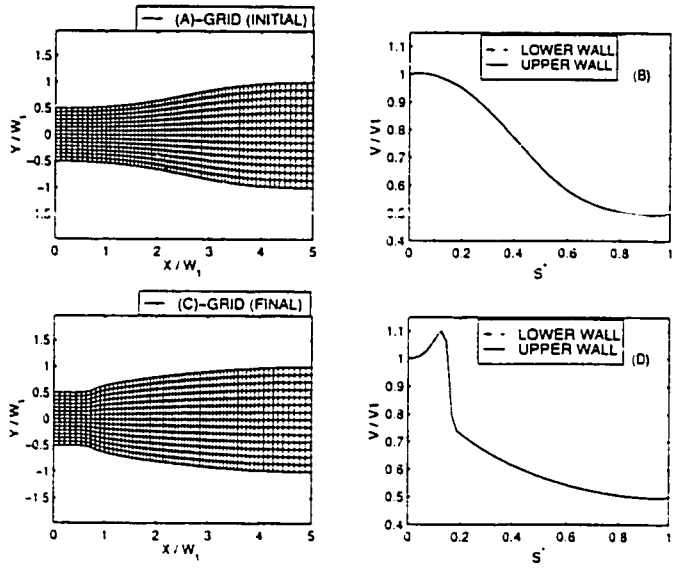

Figure 7.6: Design of a straight diffuser.

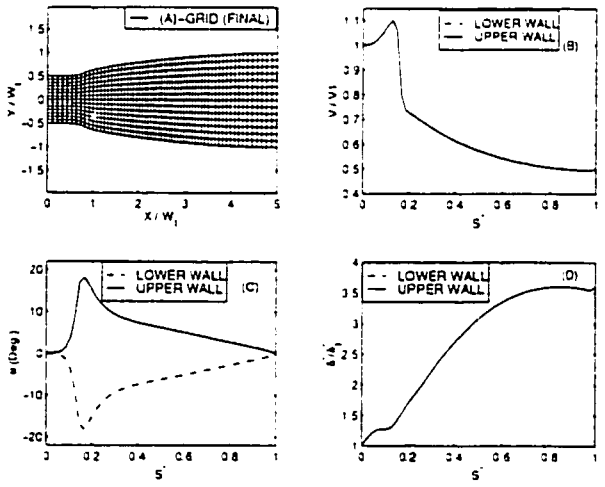

Figure 7.7: Displacement thickness distribution for a straight diffuser.

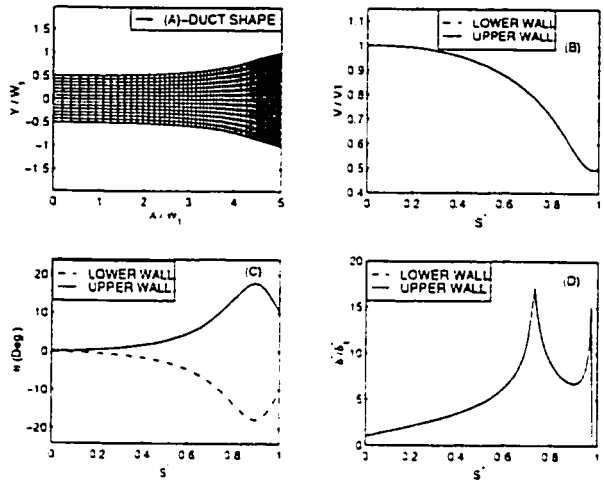

Figure 7.8: A straight diffuser with a trumpet-type profile.

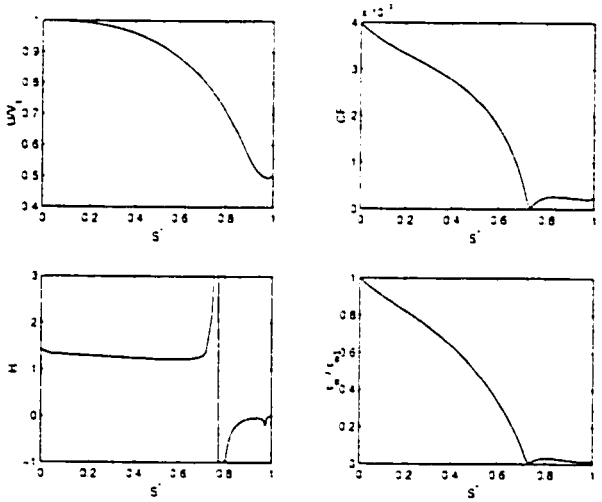

Figure 7.9: Boundary layer results for the diffuser shown in Figure 7.8.

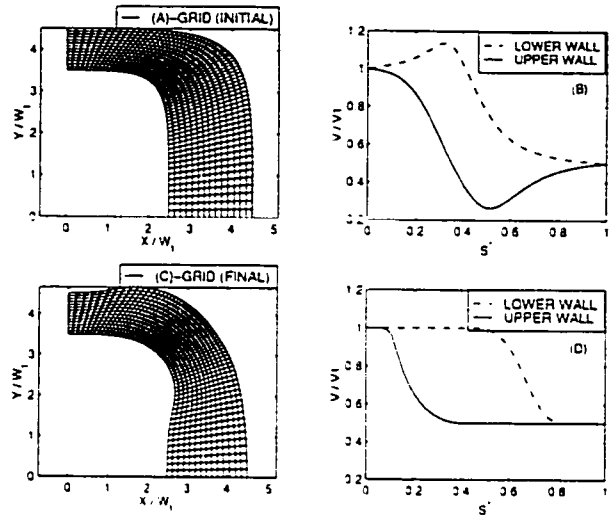

Figure 7.10: Design of a potential flow 90°-curved diffuser.

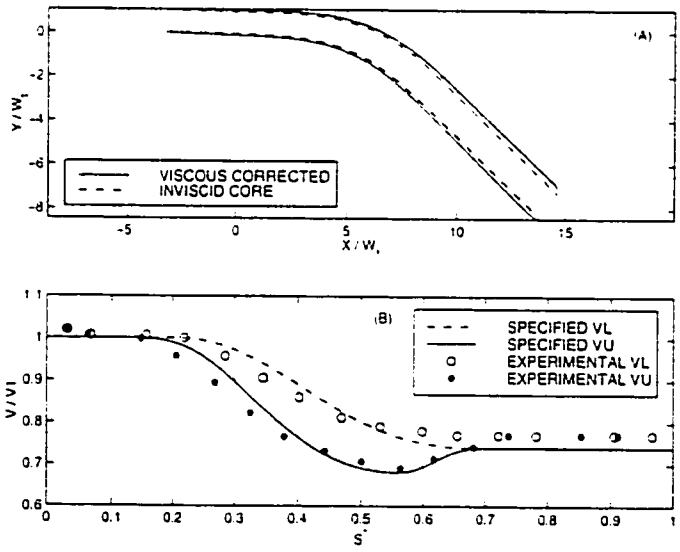

Figure 7.11: Parsons' curved diffuser [146].

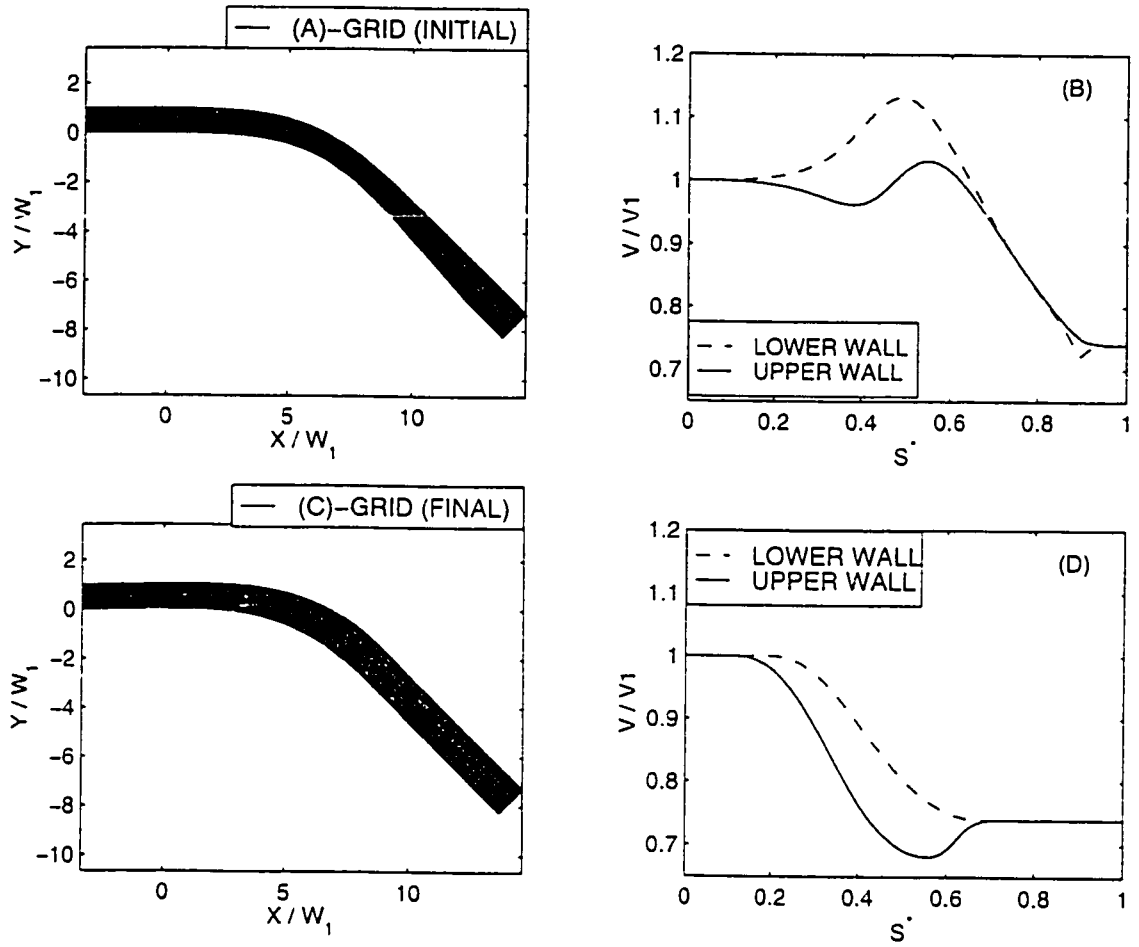

Figure 7.12: Design of Parsons' potential core [146].

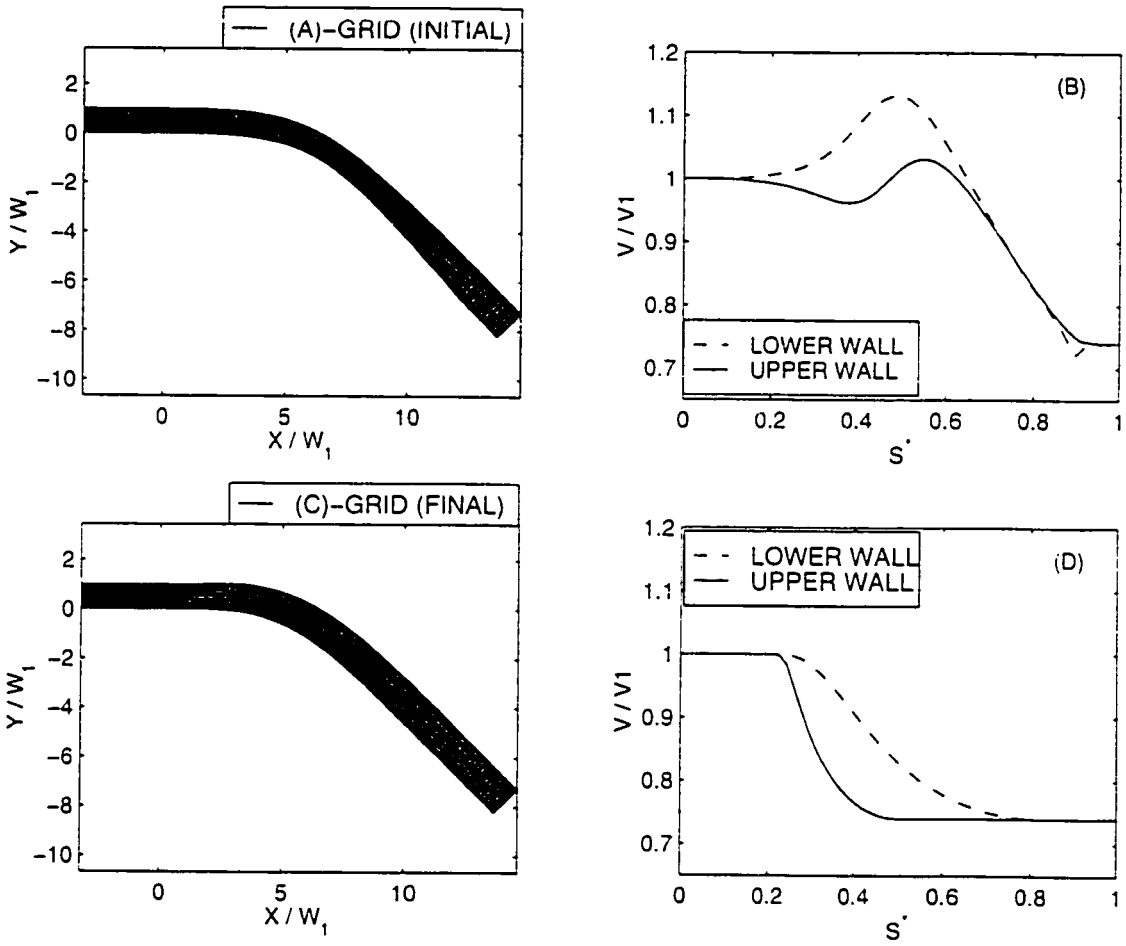

Figure 7.13: Modified design of Parsons' potential core [146].

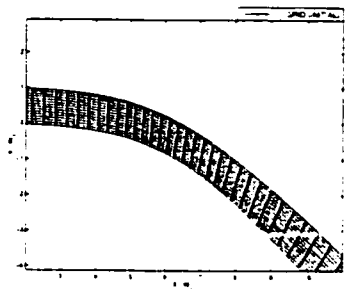

Figure 7.14: Magnified shape of the duct shown in Figure 7.12A.

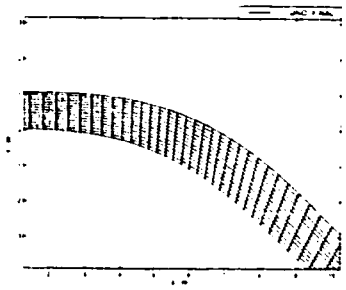

Figure 7.15: Magnified shape of the duct shown in Figure 7.12C.

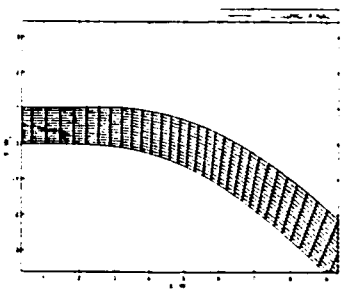

Figure 7.16: Magnified shape of the duct shown in Figure 7.13C.

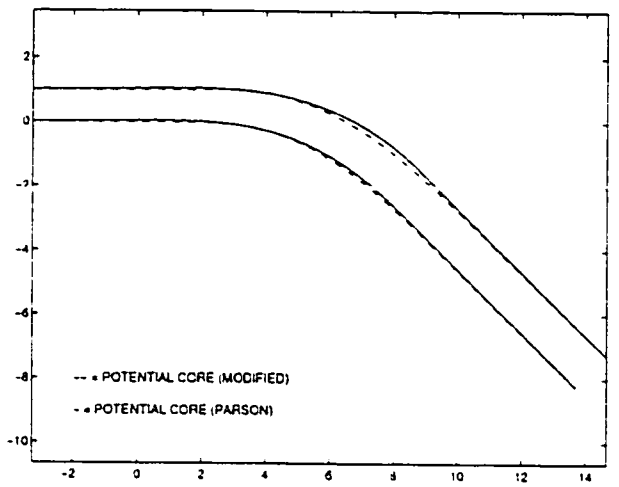

Figure 7.17: Comparison of the modified potential core and the Parsons potential core [146].

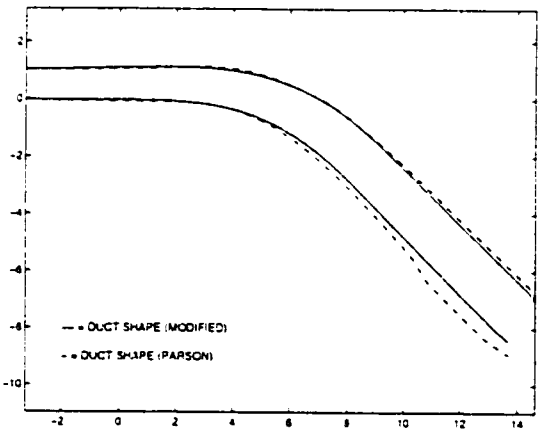

Figure 7.18: Comparison of the modified duct shape and the Parsons' duct shape [146].

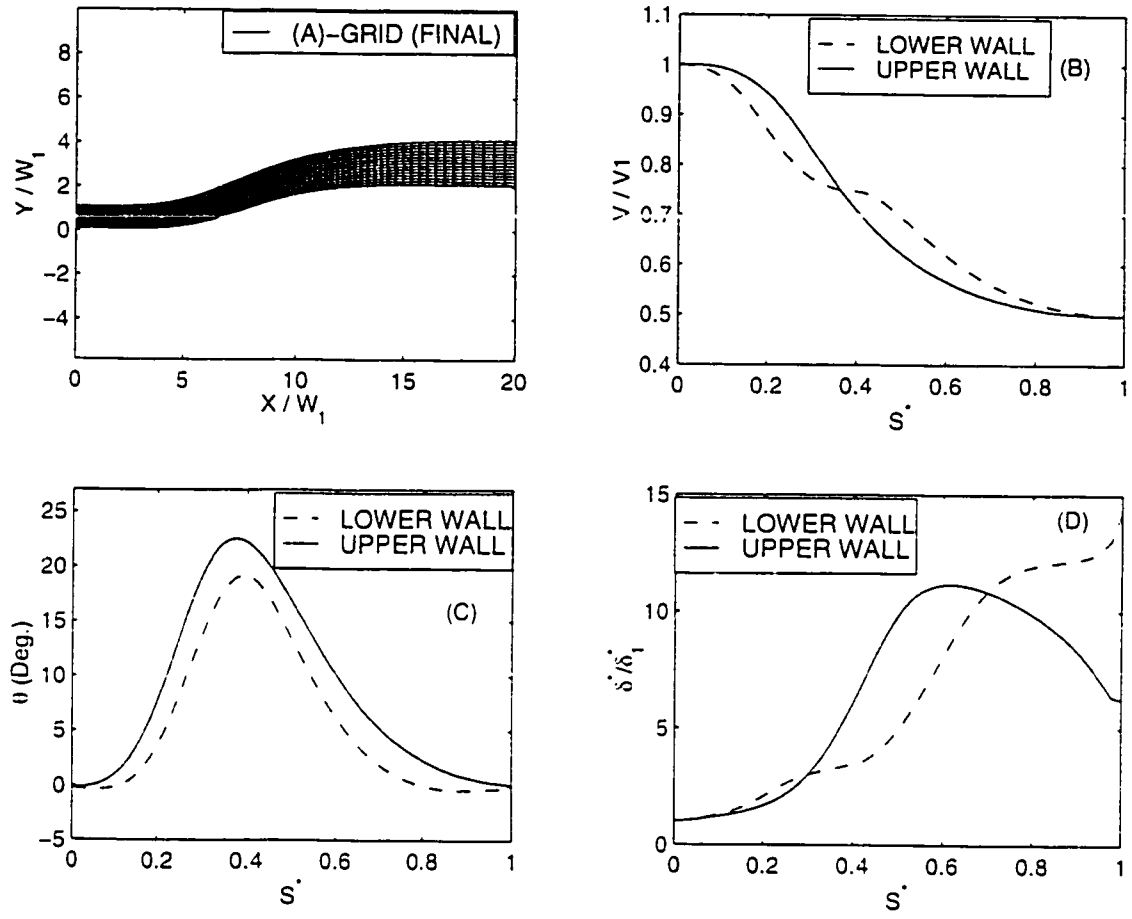

Figure 7.19: Design of a s-shaped diffuser.

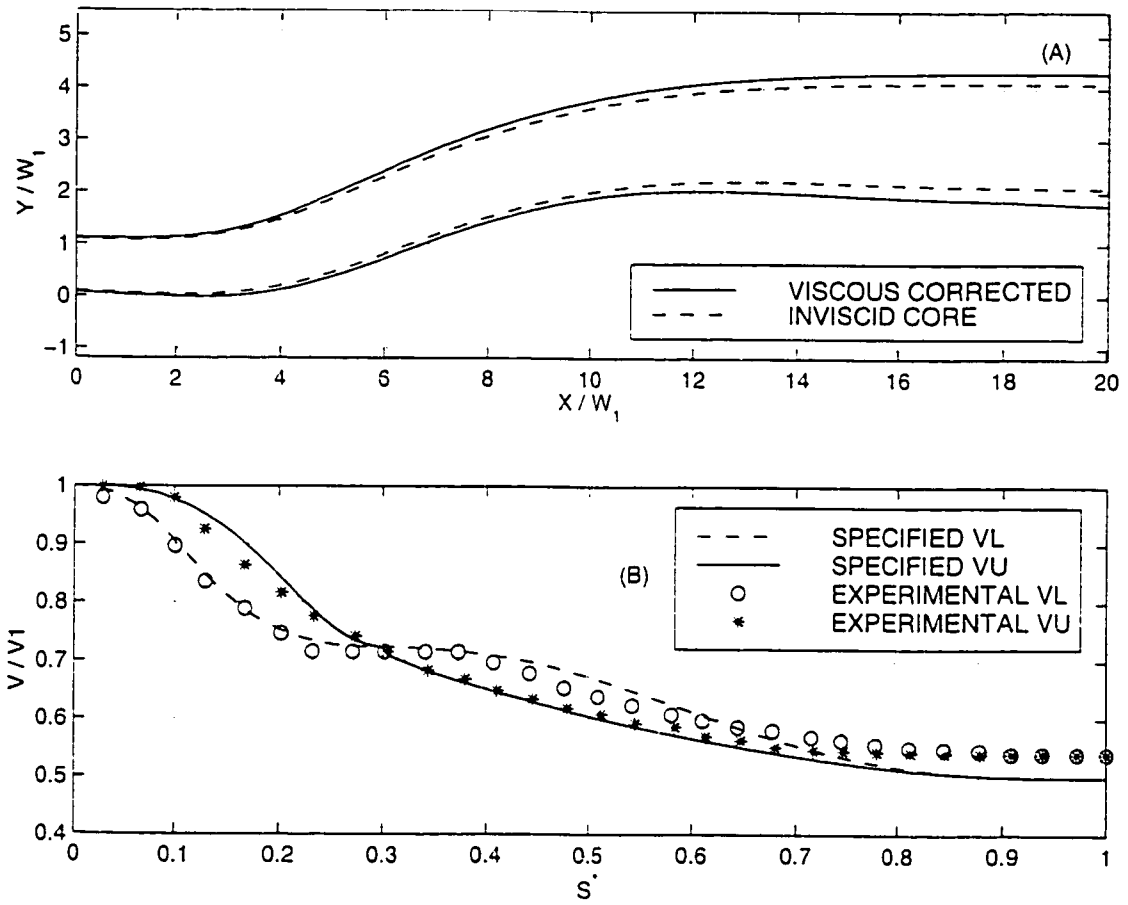

Figure 7.20: An experimentally studied s-shaped diffuser [150].

7.2.3 Design of Short Spacers

In this section design of efficient short spacers is discussed. The area ratio of a spacer is equal to one and there is no global deceleration or acceleration associated with the gross area change. Therefore, a straight spacer is simply a straight duct with uniform cross-sectional area and there is not any flow backlash in such a duct. In curved and offset spacers, however, there are undershoot and overshoot regions along the duct walls due to turning and profile effects. The flow backlash cannot be eliminated in these spacers[8], but the designer can propose an optimized **TVD** in a sense that the boundary flow decelerates gradually and accelerates sharply. In the following two sub-sections, examples are provided to show how the method works in this type of short duct design problems.

7.2.3.1 Curved Spacers

Curved spacers (simple bends) are an integral part of any piping system, and are also frequently encountered in heat exchangers, chemical reactors, and other apparatus. Many researchers have studied the distortion of the flow field due to the centrifugal force produced by the wall curvature and in particular the effects of secondary flows. The number of publications in this regard is countless (references [154-157] were consulted in this study). Two-dimensional studies have also been carried out by some researchers [158, 159]. Figure 7.21A shows an initial guess for a 90°-curved spacer. The calculated tangential velocity along the boundaries is shown in Figure 7.21B. It is seen that there is a big velocity overshoot at the lower boundary and a big velocity undershoot at the upper boundary. Knowing that the difference between the upper and lower boundary velocities is necessary for the flow to turn, the designer can only reduce the slope of the initial surface velocity in the deceleration zones and increase the slope in the acceleration regions. The proposed **TVD** in this case is shown in Figure 7.21D and the designed potential flow duct is shown in Figure 7.21C. Again the designer only tries to suppress the intensification of the adverse pressure gradients caused by the duct shape. Whether the flow separates or not depends on the inlet flow condition and actual size of the duct.

In Figure 7.22, viscous corrections made for the designed potential core shown in Figure 7.21C, are shown. The inlet boundary layer information in this design example were taken similar to the initial data in the flow 2100 [118] and the spacer inlet width

8. If there is not any flow backlash in a spacer, the surface tangential velocities at the upper and lower walls are the same and there can not be any flow turning. This occurs in straight spacers.

(W_1) was chosen equal to $2.0m$.

7.2.3.2 Offset Spacers

Design of offset spacers can be done using the same arguments which have already been explained. An offset spacer is considered essentially as a combination of two curved spacers. The designer should propose a **TVD** with appropriate slopes in the deceleration as well as acceleration zones and also an appropriate location for the cross-over point between two serial curved spacers.

Figure 7.23 shows an example with a very low offset. The initial guess is shown in Figure 7.23A and its associated surface velocity distribution is shown in Figure 7.23B. The designer modifies the initial surface velocity and proposes a **TVD** as shown in Figure 7.23D. Note that in the proposed **TVD**, acceleration regions are sharp and the deceleration regions are tailored to be very mild. The optimum shape in this case, which is associated with the optimized **TVD** shown in Figure 7.23D, is shown in Figure 7.23C.

Design of non-diffusing two-dimensional s-shaped ducts has been studied by Kitchen and Bowyer [160]. They studied s-shaped spacers with circular arc walls and considered the duct offset-to-length ratio and width-to-length ratio as the design parameters. The optimal duct was defined as that duct which was least prone to separation. Kitchen and Bowyer did not tailor the **TVD** to obtain an optimized shape. They, instead, specified a desirable normal acceleration function and determined the corresponding center-line path of the duct. They actually modified, with their design method, an initial shape with two 45° turns and circular walls which was experimentally studied by Butz [161]. The conclusion was that the first turn in an optimized s-shaped spacer should be appreciably sharper than the second reverse turn. They proposed that the initial turn should be completed in approximately 37% of the overall horizontal duct length.

In Figure 7.24, the initial guess is chosen with the same dimensions as the Butz' duct (Figure 7.24A)[9]. The **TVD** (Figure 7.24D) is proposed to modify the surface velocity calculated for the initial guess (Figure 7.24B) based on the general guidelines proposed in this thesis. Note that the deceleration on the lower wall is improved considerably and on the upper surface also, the two deceleration zones are milder than the initial shape. The designed shape has two unequal turns and is in qualitative agreement with the optimized shape proposed in [160].

9. The wall profiles in Figure 7.24 are not circular though. They are created with Bezier curves.

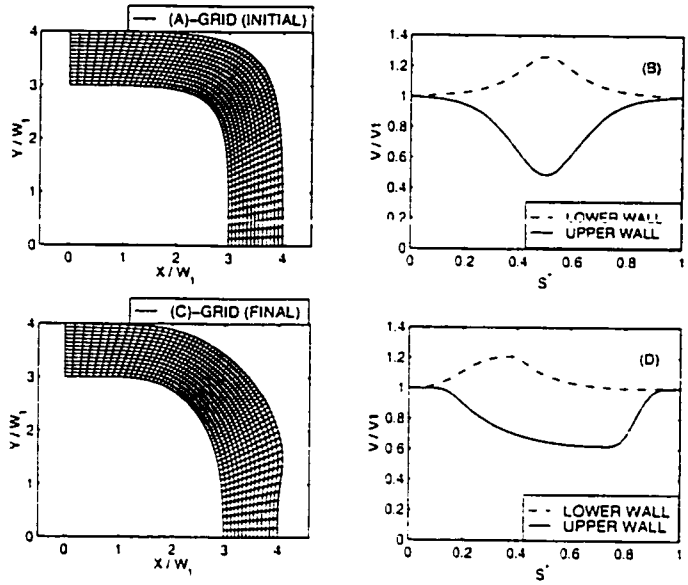

Figure 7.21: Design of a curved spacer.

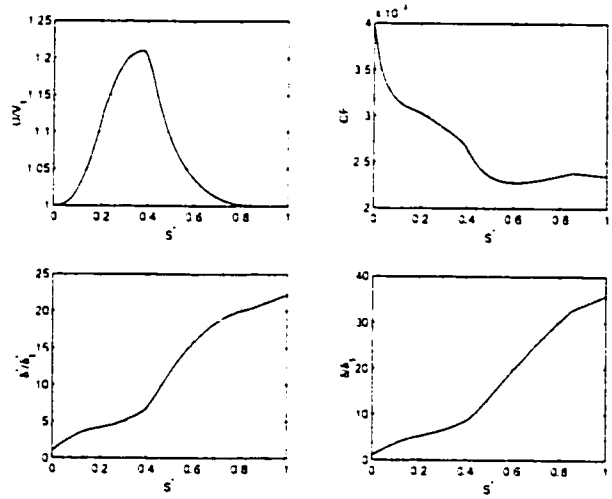

Figure 7.22: Boundary layer analysis results (lower wall) for duct shown in Figure 7.21C.

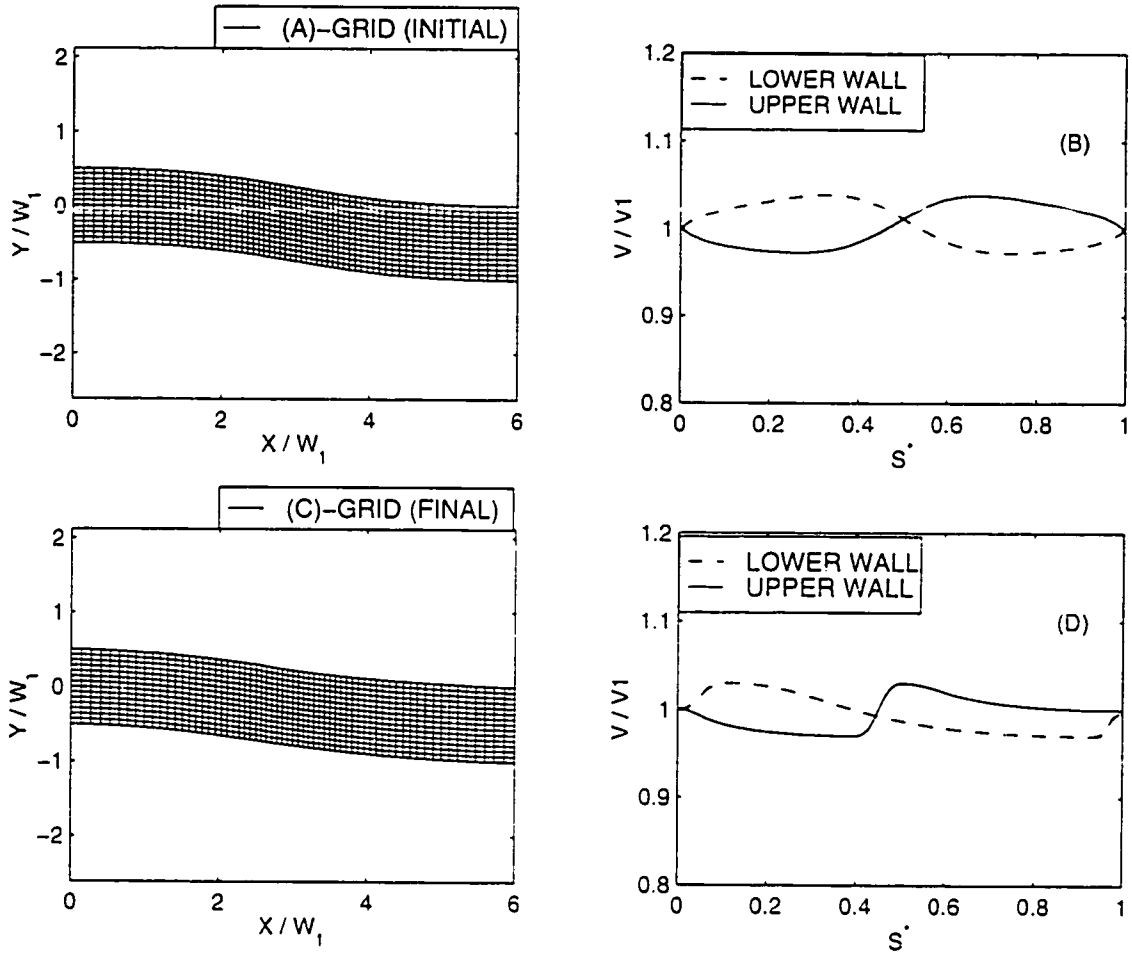

Figure 7.23: Design of a s-shaped spacer (low offset).

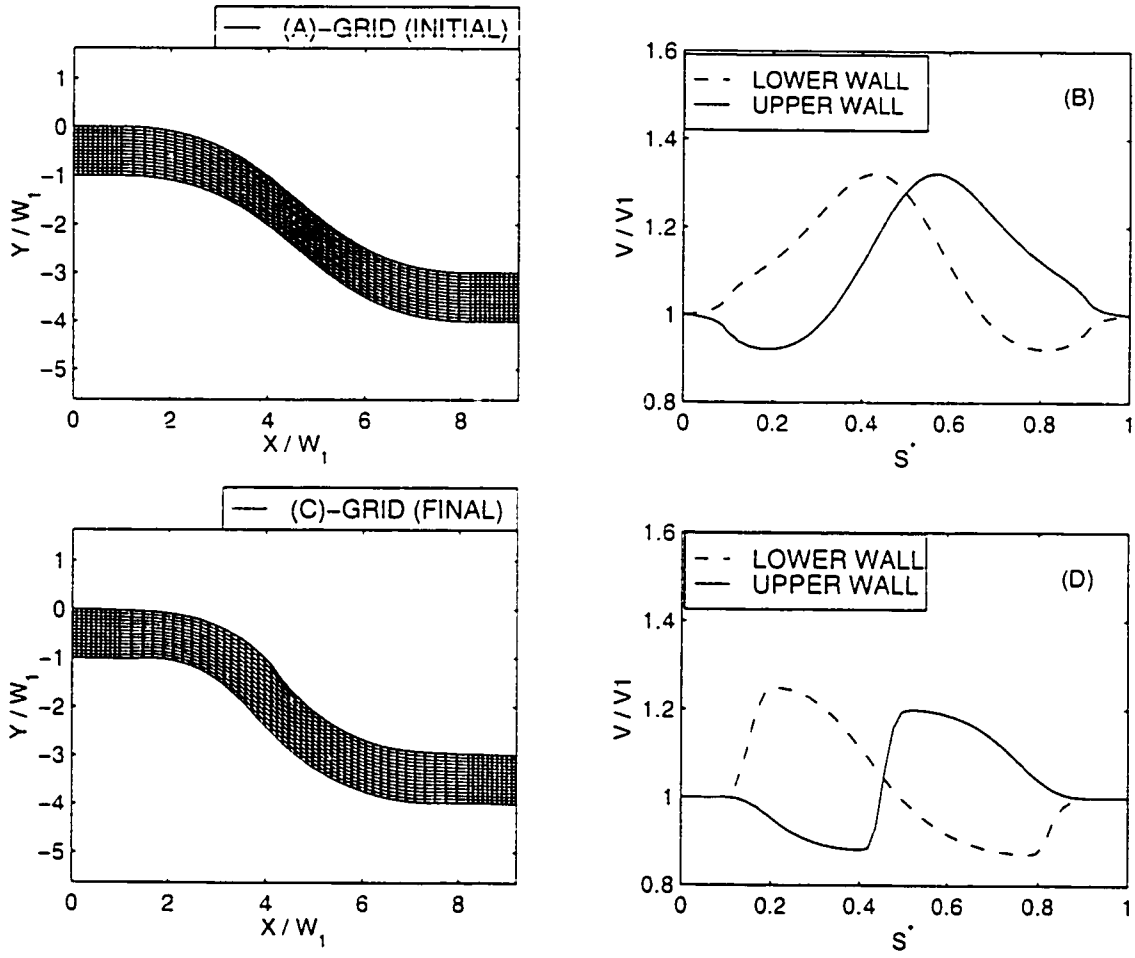

Figure 7.24: Design of a s-shaped spacer (high offset).

7.2.4 Design of Short Nozzles

In this section design of efficient short nozzles is discussed. While the bulk flow is accelerating, there are local adverse pressure gradient regions due to the curvature effects. If there is enough global acceleration, the designer can use these conflicting effects and eliminate the flow backlash completely in curved and offset nozzles. In straight short nozzles, however, one cannot eliminate the flow backlash completely and keep the flow at the inlet and exit parallel and uniform. The reason will be explained in the next sub-section. In spite of the fact that the flow backlash can be eliminated in curved nozzles, efficient short nozzles have controlled flow backlash regions. The reason will be discussed in the sub-section devoted to curved nozzles.

7.2.4.1 Straight Nozzles

Straight nozzles are used in many applications. A particularly important application is the aerodynamic contraction used in wind tunnels. The contraction is necessary because the cross sections of the return ducts are made much larger than the test section in order to reduce the losses, particularly those through corners, vanes and screens. Additionally, a contraction has the desirable effect of reducing the fluctuating components of the velocity.

Changing the cross sectional area requires turning of the walls and this causes flow backlash. In aerodynamic contractions the flow backlash, particularly near the inlet, should be controlled to prevent separation. In fact the whole purpose of the aerodynamic design of contractions is to make sure that the flow at the test section entrance is nearly parallel and uniform. This means that the boundary layer at the exit of the contraction should be very thin and the flow has to be uniform and parallel and nearly free of turbulence there. An efficient short straight nozzle is the shortest contraction which meets all these requirements.

As Figure 7.25 shows, if the designer tries to eliminate the adverse pressure gradients along a short straight nozzle, it will not be possible to keep the flow parallel and uniform at the inlet and outlet. The initial guess and its surface velocity distribution are shown in Figures 7.25A and 7.25B. If the **TVD** is chosen as shown in Figure 7.25D, the designed shape will be as shown in Figure 7.25C. Note that the sharp acceleration imposed by the **TVD**, has upstream and downstream effects on the duct shape. However, the upstream geometrical effect is more severe as compared to the downstream effect.

For the initial guess, shown in Figure 7.25A, the wall curvature at the inlet

and outlet is zero. Rapid change of the wall curvature from zero to a finite value results in some flow backlash upstream and downstream as shown in Figure 7.25B. Therefore, to prevent dangerous flow backlash near the inlet[10], the cross sectional area should be decreased very slowly. For low area ratio nozzles, which are often used as aerodynamic contractions, the downstream geometrical effect due to sudden acceleration is less important as compared to the upstream effect.

A comprehensive evaluation of the state of the art regarding the design of aerodynamic contractions has been given in [162]. Here the contraction design problem is approached in the context of efficient short duct design. The main concern is to control the flow backlash by appropriately profiling the duct walls when the duct length is reduced. In practical contraction design, the problems of laminar to turbulent transition near the inlet and the possibility of relaminarization near the exit have to be studied as well. Whitehead [163], Bloomer [164], Bossel [165], Chmielewski [166], Morel [167] and Mikhail [168] have had major contributions in the design of aerodynamic contractions. Most of the published contraction design examples are for two-dimensional axisymmetric geometries. Often, mathematical expressions with some unknown parameters are used to describe the contraction shape. The unknown parameters are then found by trial and error such that attached flow is guaranteed according to the Stratford criterion which is well suited for this type of boundary layer flows (see Appendix *C*). Mikhail [168] have proposed another approach in which the wall curvature is optimized iteratively to make sure that the adverse gradient regions are tolerable.

To obtain a better sense about the effects of the wall profile on the flow near the boundaries in straight nozzles, the potential flow was solved for different two-dimensional straight nozzles (Figure 7.26). Bezier curves were used to provide shapes with extreme scenarios for the wall profiles. One may gradually accelerate the flow and basically distribute the acceleration all along the duct (Figure 7.26A), rapidly accelerate the flow near the exit (Figure 7.26B) or decrease the cross sectional area sharply near the inlet (Figure 7.26C). The calculated surface velocity distributions are also shown, for these cases, in Figure 7.26. Note that the nozzle shown in Figure 7.26B provides the best surface velocity distribution in terms of the boundary layer considerations, i.e. the deceleration is gradual near the inlet where the boundary layer is thick and more sensitive to adverse pressure gradients and the flow experiences a sharp deceleration near the exit where the boundary layer is energized. The conclusion

10. Note that the flow backlash near the inlet is the major concern in nozzles. The flow is accelerating along a nozzle and the boundary layer is energized along the duct. That is why the emphasis is on the flow backlash near the inlet.

is that the flow turning should be gradually increased as the velocity increases along the duct. In other words, the surface flow deceleration should be chosen according to the ability of the boundary layer to remain attached under the adverse pressure gradient induced by the flow turning. Based on this design philosophy the boundary layer near the exit has more ability to accept rapid turning and one should design the nozzle so that much of the turning and acceleration occurs near the exit.

Bradshaw [169, 170] has introduced an efficient two dimensional aerodynamic contraction[11] and showed part of the shape of that aerodynamic contraction. The duct shape as provided in [170] is shown in Figure 7.27. It is seen that the cross sectional area gradually reduces near the inlet and rapidly decreases near the exit. Unfortunately, the detailed flow information is not available for this aerodynamic contraction.

The area ratio of the contraction shown in [170], is close to 0.1. In Figure 7.28 the potential flow design of an aerodynamic contraction with an area ratio equal to 0.1 is shown. The initial guess and the associated surface velocity distribution are shown in Figures 7.28A and 7.28B. Note that the **TVD** (Figure 7.28D) proposes a gradual deceleration near the inlet and rapid acceleration near the exit. In the **TVD**, no overshoot is allowed near the exit. This causes some downstream effects on the geometry but, as is seen in Figure 7.28C, the downstream effect on the geometry is negligible. Due to the sharp acceleration, the proposed boundary layer analysis method in this thesis fails to predict the separation or calculate the boundary layer parameters for this case. The final length of the duct, shown in Figure 7.28, was obtained based on the Stratford separation criterion when the inlet boundary layers were considered similar to the flow 1300 [118].

The proposed integral boundary layer method in this thesis works well for accelerating flows when the acceleration is slow. In Figure 7.29, a **TVD** (Figure 7.29B) is specified for the design of a nozzle with area ratio equal to 0.5 (Figure 7.29A). The overshoot near the exit is necessary to return the flow back to the straight and parallel position rapidly. The actual dimensions of the duct are large ($W_1 = 4m$) and the actual acceleration is in fact very slow. The distribution of the boundary flow angles (Figure 7.29C) and the displacement thickness (Figure 7.29D) are also shown[12]. Note that the flow turning is more gradual near the inlet as compared to the flow near the exit even for this case in which the area ratio is moderate.

11. Bradshaw [170] introduces this shape as a very short two-dimensional contraction that provides a uniform turbulence free flow at the exit.
12. The inlet boundary layers were considered similar to the flow 1300 [118].

To conclude this sub-section, it is instructive to compare the shape of efficient short straight nozzles and diffusers. As Figures 7.7A and 7.29A suggest, the wall profile for an optimum nozzle is very similar to an optimum diffuser in which the direction of the flow is reversed (outlet of the diffuser should be considered as the inlet for the nozzle). In other words, in spite of the similarity of the profile, the inflection point of an efficient short straight diffuser is close to the inlet (Figure 7.7A) in contrast to the nozzle for which the inflection point is near the exit (Figure 7.29A). It is important to note that while an efficient straight nozzle was designed for which the length of the duct was less than the inlet width (Figure 7.29A), the length of an optimum efficient straight diffuser with the same inlet and outlet area is at least five times greater than the inlet width (Figure 7.7A).

7.2.4.2 Curved Nozzles

Previously, in Chapter 3, the Stanitz 90°-elbow (nozzle) was considered for the purpose of the validation of the proposed method. In this section again 90°-curved nozzles are considered. Even though it is possible to consider lower turning angles, a 90° turning angle is chosen to be able to show the physical phenomena associated with simultaneous turning and acceleration more clearly. 90°-Curved nozzles have been studied by some researchers and the benchmark solution of Stanitz has been used for the purpose of validation (e.g. [171, 172]).

Figure 7.30A shows the initial guess made to design a 90°-curved nozzle ($AR = 0.5$). The calculated surface tangential velocity is shown in Figure 7.30B. The **TVD** is proposed by the designer as shown in Figure 7.30D. Note that the flow backlash is eliminated and there is not any deceleration region along the duct. The designed shape, corresponding to this **TVD**, is shown in Figure 7.30C. The shape suggests that in a backlash-free curved nozzle, the inner wall turns inward before the turn to prevent adverse pressure gradient being developed on the upper wall and the upper wall turns inward after the turn to prevent adverse pressure gradient being developed on the lower wall. The turn itself is a circular turn for which constant pressure, or in this case velocity, difference is maintained along the turn. For this nearly optimum shape, surface flow angles at the upper and lower walls are shown in Figure 7.31B. Figure 7.31A shows the wall turning angles for the initial guess for the purpose of comparison. Note that in contrast to the backlash-free **TVD**, proposed for a 90°-curved diffuser (Figure 7.10D), the slope of acceleration in the backlash-free curved nozzle has been chosen quite high.

A backlash-free curved nozzle is not efficient in a sense that the duct can be made

shorter without causing separation. Figure 7.32D shows a typical **TVD** specified to design an efficient 90°-curved nozzle. Again the initial guess and its associated surface velocity distribution are shown in Figures 7.32A and 7.32B and the designed shape is shown in Figure 7.32C. Note that some controlled velocity undershoot and overshoot are allowed to occur (Figure 7.32D). This means that the upstream and downstream flow are made parallel and uniform more rapidly in Figure 7.32C as compared to 7.30C. In other words, the **TVD** shown in Figure 7.32D results in a shorter duct.

If the inlet boundary layers at the upper and lower walls are not the same, the designer may specify surface velocities along the upper and lower walls differently (in the proposed **TVD**). Two examples, in which the upper and lower boundary layers are treated quite differently, are shown in Figures 7.33 and 7.34. In Figure 7.33, only the lower wall is intended to be backlash-free (note the specified **TVD** in Figure 7.33D) and the initial guess and its associated surface velocity are shown in Figures 7.33A and 7.33B. It is seen that the upper wall, in the designed shape, adapts itself after the turn to prevent any backlash on the lower wall. In Figure 7.34, only the upper wall is intended to be free of backlash (see Figure 7.34D) and again the initial guess and its associated surface velocity are shown in Figures 7.34A and 7.34B. It is seen that in the designed shape (Figure 7.34C), the lower wall adapts itself before the turn to control the flow on the upper wall. The viscous corrections can be made for lower and upper walls by the proposed integral boundary layer method as before if the actual size of the duct is chosen big enough.

7.2.4.3 Offset Nozzles

Offset nozzles accelerate the flow and laterally displace the duct axis. This requires a double turning of the flow. The designer may consider the offset as a combination of two curved nozzles and propose the **TVD** accordingly. All the previous discussions about the selection of the **TVD** for curved nozzles can be applied here as well. One further point is the selection of the cross-over point between the two nozzles. The designer may use two different turning angles for the first and second turns. Having in mind that the flow is globally accelerating in an offset nozzle, the boundary layer is energized along the duct and the second turn can handle more rapid turning. Therefore, in contrast to offset diffusers, the inflection point in the wall profile of an efficient offset nozzle is closer to the exit.

Figure 7.35C shows an offset nozzle designed to achieve the backlash-free **TVD** shown in Figure 7.35D. The initial guess and its associated surface velocity distribution are shown in Figures 7.35A and 7.35B respectively. Note that much of the

acceleration and turning occur near the inlet or in the first turn.

Figure 7.36C shows another designed offset nozzle (with the same initial guess gross dimensions as the previous one shown in Figure 7.35) in which much of the acceleration occurs in the second turn. Note that this policy has been implemented in the **TVD** shown in Figure 7.36D. In Figures 7.37, 7.38, 7.39 and 7.40 offset nozzles shown in Figures 7.35 and 7.36 are magnified (for further clarity) and the surface flow angles are also shown.

Typical distributions of the wall shear stress and displacement thickness for both potential flow designs shown in Figures 7.37 and 7.39 are shown in Figures 7.41 and 7.42. The boundary layer results, shown in Figures 7.41C, 7.41D, 7.42C and 7.42D, are, qualitatively, as expected. It is seen that in offset nozzles the shear stress at the beginning of the second turn (see Figures 7.41C and 7.42C) is higher than the inlet shear stress. Also it is seen that the slope of the decreasing shear stress along the upper wall near the inlet is higher in Figure 7.42C as compared to the one shown in Figure 7.41C. Therefore, the design strategy implemented by the **TVD** (Figure 7.41B), which considers more acceleration (and turning) in the second turn, is a better policy from the flow separation point of view. For efficient short offset nozzles, which work close to the separation limit and have decelerated flow regions along the wall, this design policy should be followed. In Figures 7.41 and 7.42, inlet boundary layer information were chosen the same as the boundary layer initial condition given for flow 2100 [118]. Again, actual dimensions are large enough ($W_1 = 4m$) to make sure that the boundary flow accelerations are not sharp and the proposed integral boundary layer method is applicable.

To achieve an efficient short offset nozzle, the length is reduced until separation is predicted. Figure 7.43A shows the initial guess for which the flow is predicted to separate from the walls. The designer tries to decrease the slope of the deceleration regions and increase the slope of the acceleration regions. The **TVD** is chosen as shown in Figure 7.43D and the potential duct shape is designed as shown in Figure 7.43C. Note that the contribution of the first turn in the global acceleration in this efficient shape is less than the second turn as shown in the **TVD** (Figure 7.43D). The flow does not separate in the designed duct, shown in Figure 7.43C, according to the integral boundary layer analysis method used in this thesis.

In Figure 7.44C another potential flow core is shown which was designed based on an inappropriate **TVD** shown in Figure 7.44D. The initial guess and its surface velocity distribution are shown in Figures 7.44A and 7.44B. As it is seen, if the designer considers much of the acceleration in the first turn, severe deceleration near the

inlet is inevitable. The integral boundary layer analysis method predicts separation for the duct shown in Figure 7.44C as is expected.

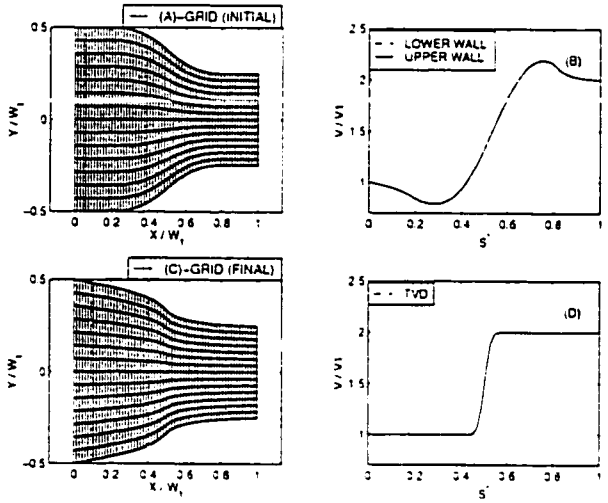

Figure 7.25: Effect of sharp acceleration on the geometry.

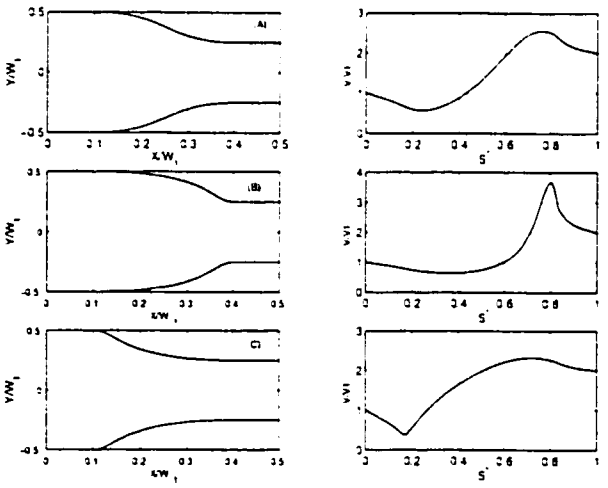

Figure 7.26: Effect of the straight nozzle shape on the surface flow.

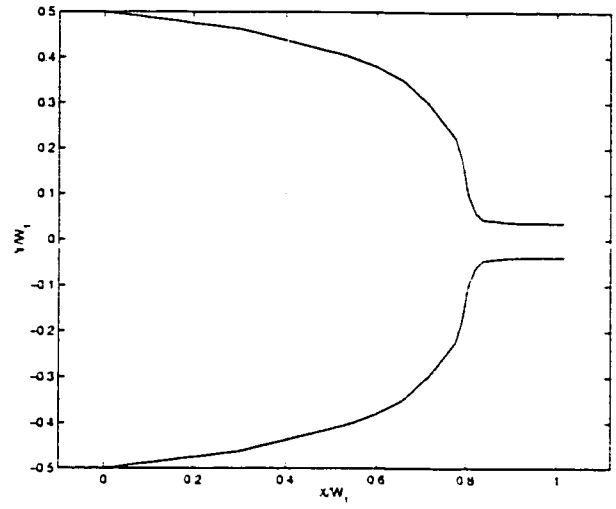

Figure 7.27: An efficient two-dimensional contraction [170].

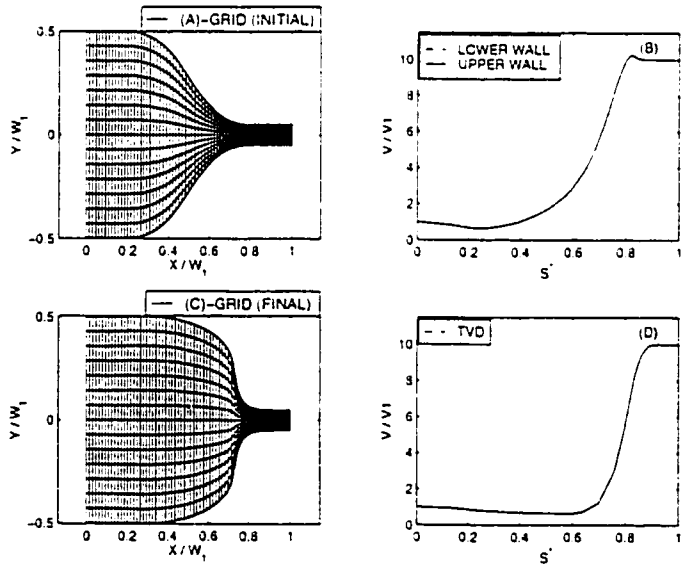

Figure 7.28: Potential design of a low area ratio straight nozzle.

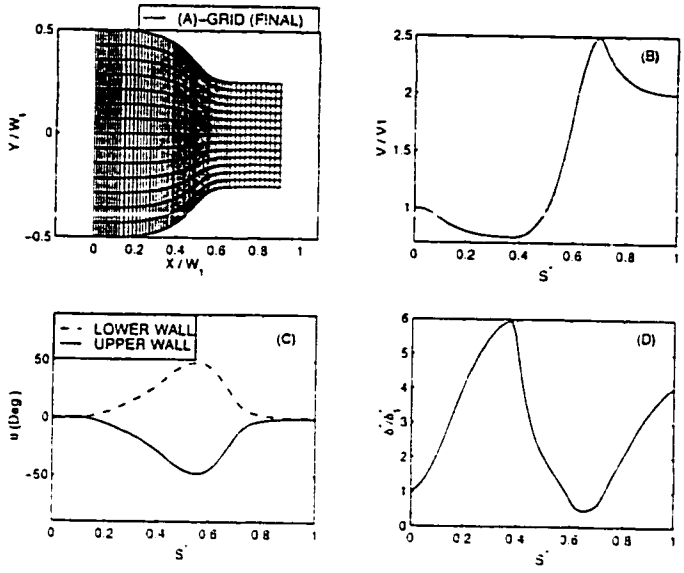

Figure 7.29: Design of a straight nozzle with small area reduction.

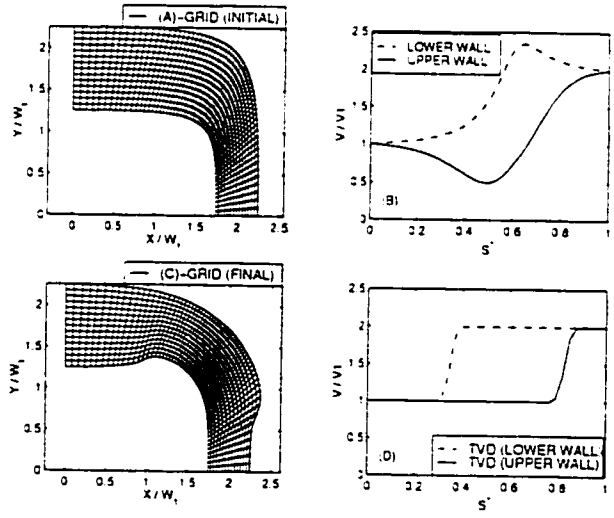

Figure 7.30: Design of a 90°-curved nozzle.

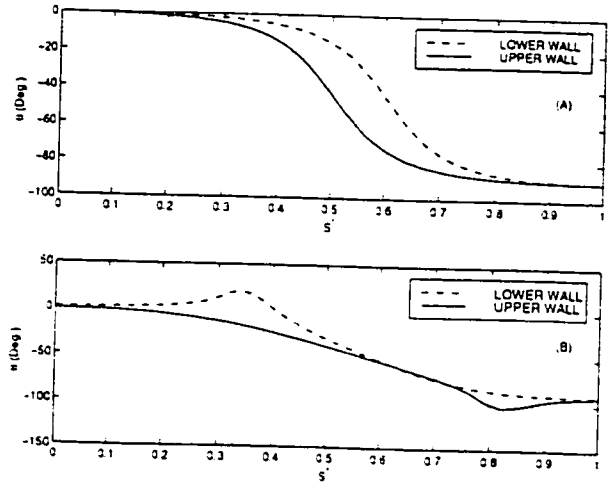

Figure 7.31: Surface flow angles for the ducts shown in Figure 7.30.

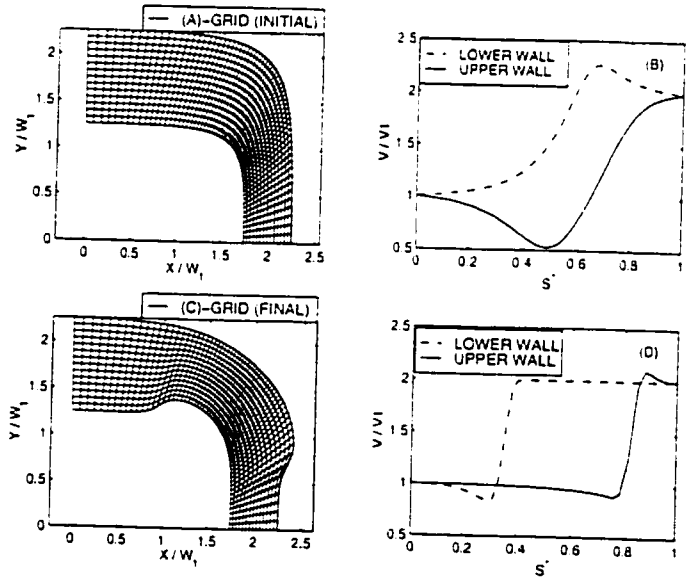

Figure 7.32: Design of a 90°-curved nozzle.

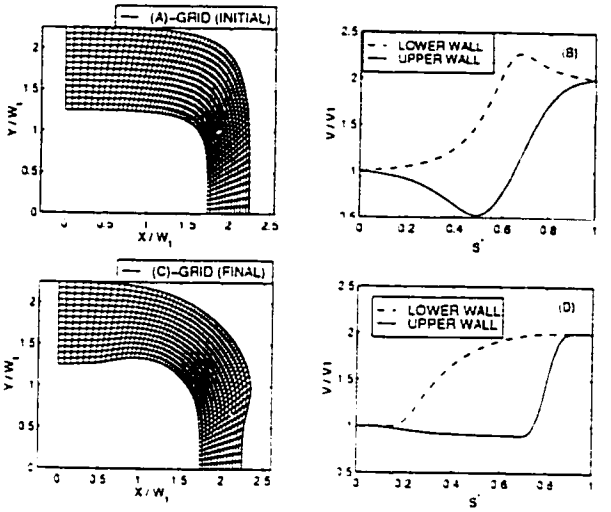

Figure 7.33: Design of a 90°-curved nozzle with a backlash-free lower wall.

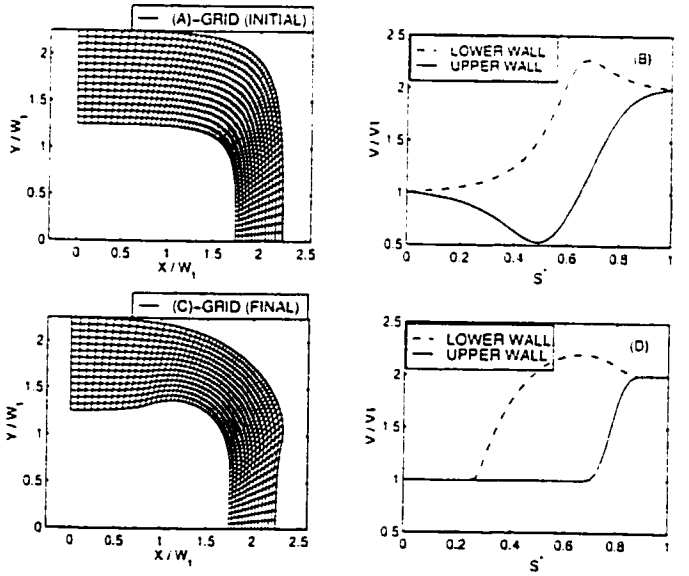

Figure 7.34: Design of a 90°-curved nozzle with a backlash-free upper wall.

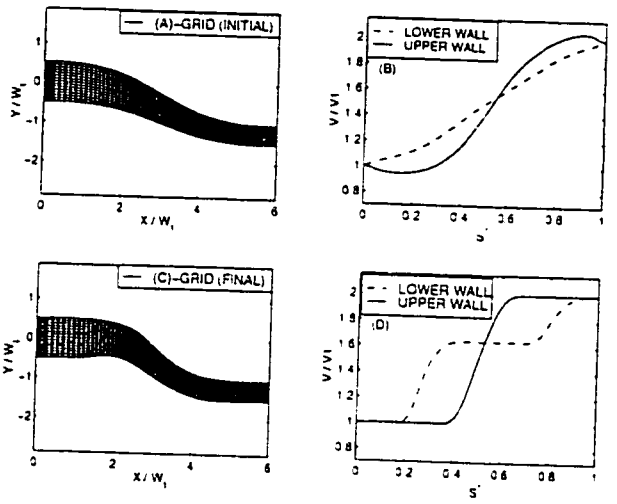

Figure 7.35: Design of an offset nozzle.

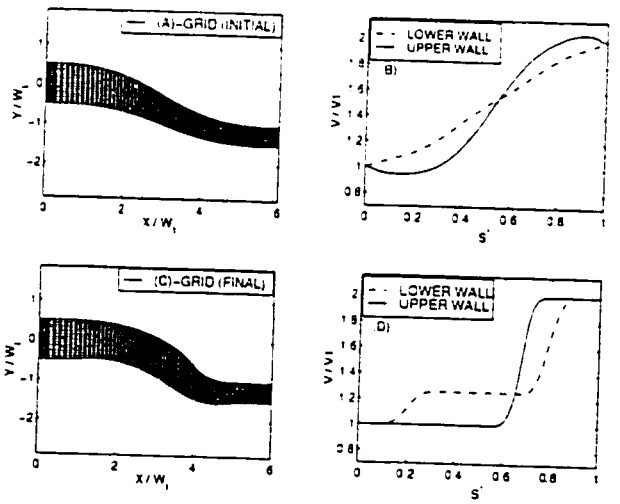

Figure 7.36: Design of an optimized offset nozzle.

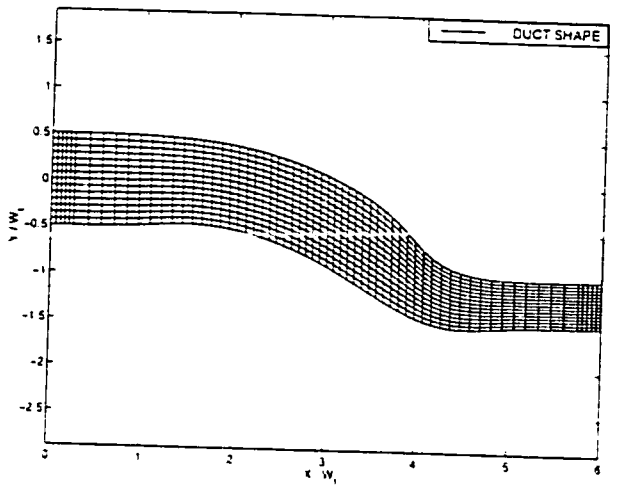

Figure 7.37: An offset nozzle in which much of the acceleration occurs in the second turn.

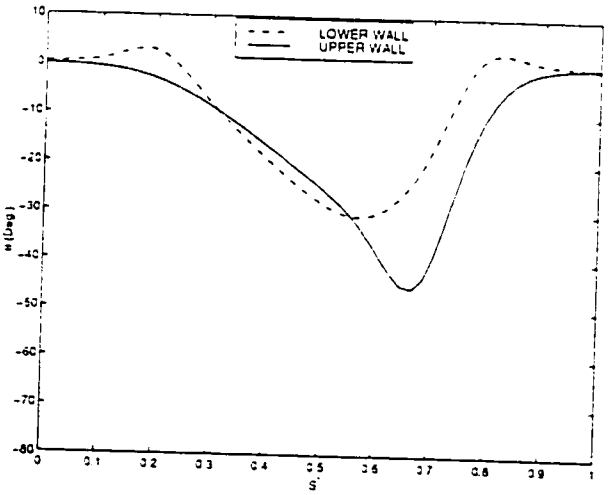

Figure 7.38: Surface flow angles for the nozzle shown in Figure 7.37.

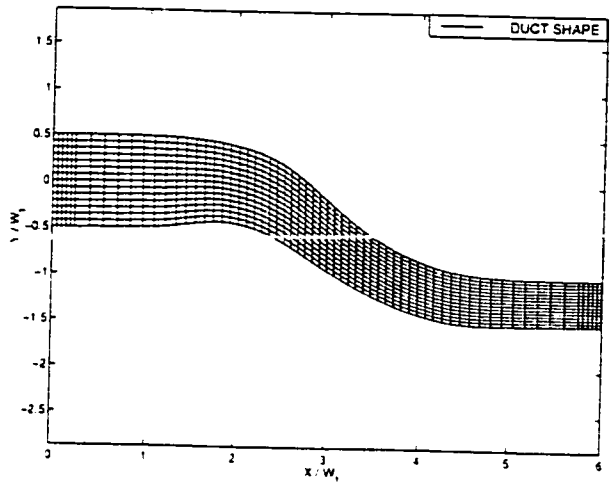

Figure 7.39: An offset nozzle in which much of the acceleration occurs in the first turn.

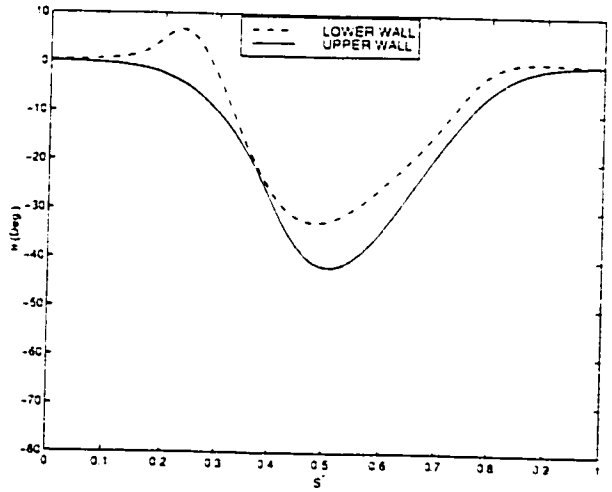

Figure 7.40: Surface flow angles for the nozzle shown in Figure 7.39.

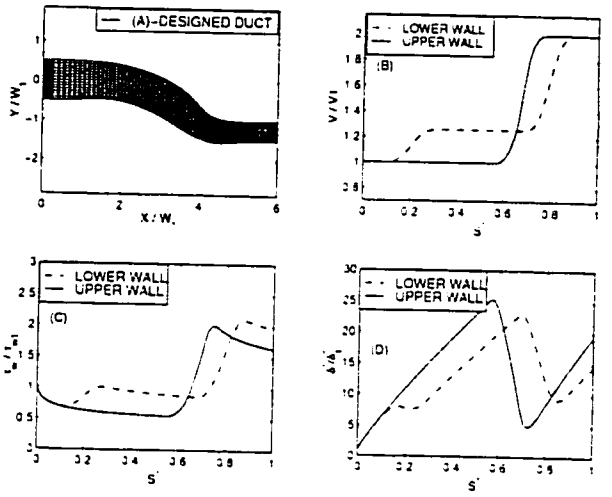

Figure 7.41: Boundary layer results for the nozzle shown in Figure 7.37.

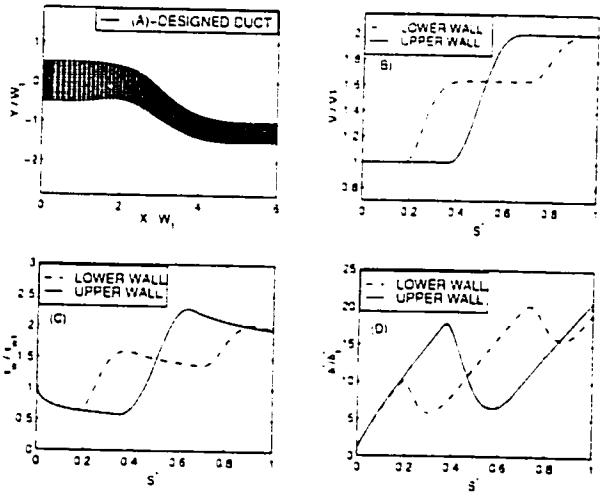

Figure 7.42: Boundary layer results for the nozzle shown in Figure 7.39.

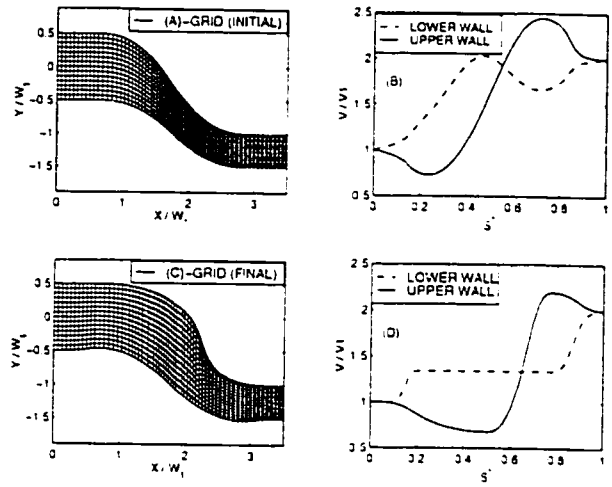

Figure 7.43: An efficient short offset nozzle.

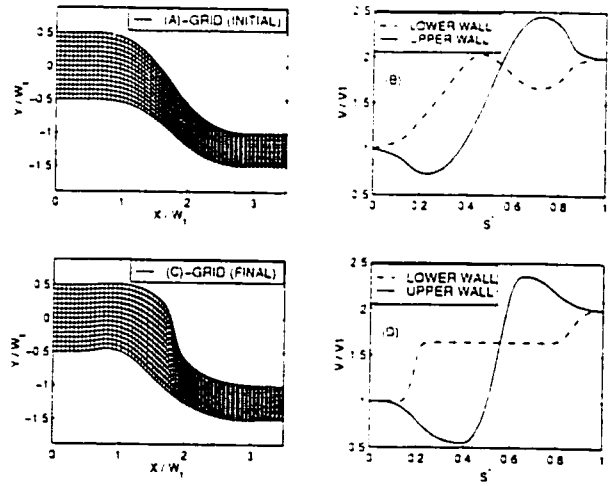

Figure 7.44: An offset nozzle designed based on an unsuitable TVD.

7.3 Shape Design: Conduction Heat Transfer

Recently, inverse problems of heat transfer have attracted lots of attention [4]. In general a well-posed heat transfer problem requires either temperature, heat flux, or convection heat transfer coefficients specified over the entire (known) boundary of the region. Well-posed Poisson problems also require the specification of heat source intensities throughout the domain. These regular types of thermal problems, which are basically analysis problems, have been called the *rating problems* [54]. Other possible thermal problems, based on our categorization in Chapter 2, fall into one of the categories of design problems and are often known as inverse heat transfer problems. Those inverse heat transfer problems in which part of the shape of the solution domain is not known in advance, are often called thermal *sizing problems* in heat transfer text books and references [54]. Steady two-dimensional sizing problems, in the context of conduction heat transfer, are governed by the Laplace equation and can be solved by the proposed direct shape design method in this research.

Figure 7.45 shows a heat conducting body with thermal conductivity K which covers a substrate material. The substrate is hot (T_W) and transfers heat to the ambient fluid (T_a). The heat is convected from the outer boundary of the heat conductor (T_s) to the ambient fluid. The convection heat transfer coefficient for the convection of heat is assumed uniform (h). Such a physical situation occurs quite frequently in micro-electronic cooling. If the substrate is considered as a heat source and the ambient fluid as the heat sink, the conductor shape controls the rate of heat transfer from the heat source to the heat sink. Therefore, the heat conductor is, in fact, a heat flow control device.

Because of the symmetry of the heat conductor shown in Figure 7.45, only half of the given geometry needs to be considered. Therefore, the conduction of heat in the conductor can be modeled as steady two-dimensional conduction heat transfer in a solution domain with four boundary surfaces. The surfaces on the symmetry line are adiabatic (Neumann boundary condition) and Dirichlet boundary conditions are given on the hot and cold sides of the model (T_W and T_s). If T_s, T_a and h are uniform, the heat flux at the outer boundary of the heat conductor (hereafter called the surface heat flux) will be uniform. These thermal constraints, in particular the uniformity of the surface temperature and heat flux, are proposed and used in a conduction **SSD** problem defined in [54] and are appropriate to test the proposed direct shape design method in the context of thermal problems. Here, no attempt is made to explore more practical thermal boundary conditions and the physical model proposed in [54]

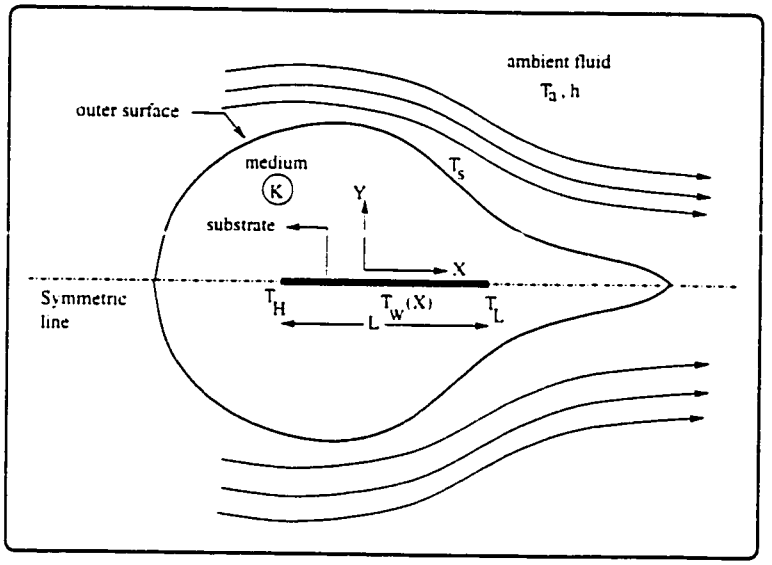

Figure 7.45: A typical **SSD** problem in conduction heat transfer.

is used in all conduction **SSD** examples.

To generalize the idea, and show how geometrical constraints can be implemented in this thermal **SSD** problem, two families of heat conductors (families H_I and H_{II}) are introduced and shown in Figure 7.46. The adiabatic surfaces of these families of heat conductors might be physically insulated or simply correspond to symmetry surfaces.

Family H_I, shown in Figure 7.46, is considered here because it degenerates to a simple one-dimensional problem when the temperatures of both hot and cold surfaces (T_W and T_s) are uniform. Family H_{II}, also considered here, has been studied in [54] in which a combination of the body-fitted grid generation scheme and the conjugate gradient optimization method have been used to solve the conduction shape design problem for this family of shapes. Family H_{II} is also the physical model associated with the problem shown in Figure 7.45.

If the shape of the heat conductor is known (the so called rating problem), the heat transfer rate, the temperature distribution inside the conductor and the surface heat flux can be calculated. The unified discrete formulation, obtained for the Laplace equation in this thesis, can be used to solve this analysis problem.

If the shape of the conductor is not known (the sizing problem), extra bound-

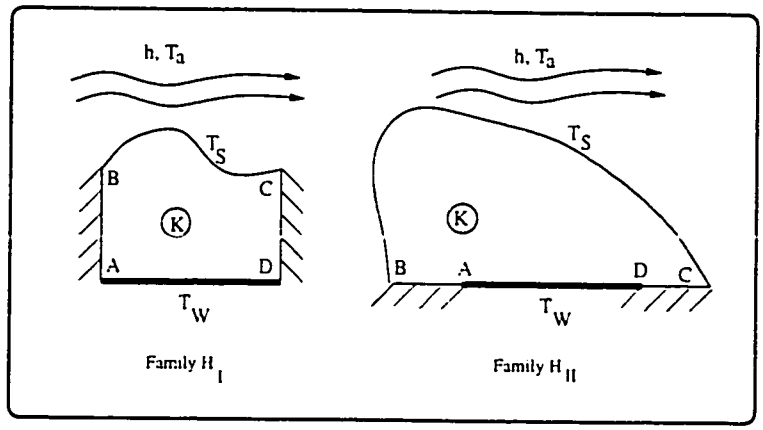

Figure 7.46: Two particular shape families of heat conductors.

ary information is required. This extra boundary condition, i.e. a specified surface (target) heat flux, renders the problem as a well-posed surface shape design problem. For different specified uniform surface heat fluxes, different conductor shapes are obtained. Figure 7.47 shows how the specified target heat flux at the outer boundary affects the shape of the conductor and the outer boundary (surface) profile. Note that it is assumed that the surface temperature (T_s) is fixed and given and the surface heat flux (or the convection heat transfer h) has to be specified by the designer. For each specified surface heat flux, the shape and size of the conductor (and the isothermal surface profile of it) is different. One may also keep the convection heat transfer fixed and change the surface temperature to generate different conductor shapes. The important point is that the total heat transfer rates corresponding to different shapes specified by $S1$, $S2$..... in Figure 7.47, are not the same. If total heat transfer rate (Q) is specified, as the design target, a number of **SSD** problems should be solved to obtain different shapes ($S1$, $S2$, $S3$ and.....) corresponding to different surface heat fluxes (q_1, q_2, q_3 and....). These shapes provide different heat transfer rates (Q_1, Q_2, Q_3 and.....)[13]. After a sequence of **SSD** problems are solved, interpolation between the results (calculated shapes: $S1$, $S2$, $S3$ and.....) will provide a shape with the outer boundary at T_s which corresponds to the desired Q.

When the substrate temperature is also constrained to be uniform ($T_W(X) = T_W = const.$), the heat conductor has two isothermal and two adiabatic surfaces. This

13. Note that $Q = \int q_s dA$.

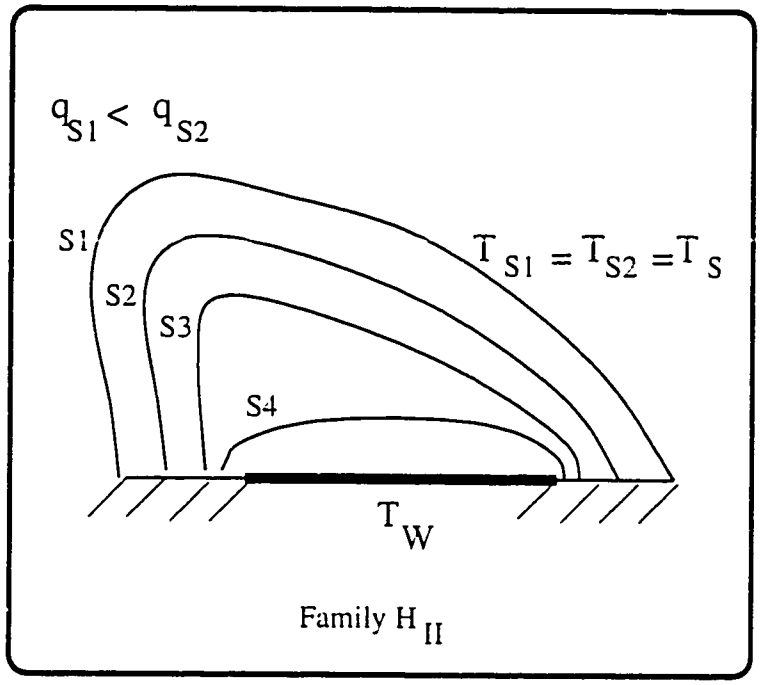

Figure 7.47: Variation of the conductor shape with the specified surface heat flux in the thermal **SSD** example.

physical model is used extensively in steady two-dimensional conduction problems and the shape factor, defined as $S \equiv (Q/K\Delta T)$, is used to calculate the conduction heat transfer rate. The unified discrete form of the Laplace equation, proposed in this thesis, can be used to numerically solve these types of problems when analytic formulas for the conduction shape factor are not available. The corresponding shape design problem in this case may be considered as the problem of finding a shape which provides a specified conduction shape factor for the given physical situation. Solution of this design problem is similar to the case that the total heat transfer rate is given as the design objective. Again a series of **SSD** problems have to be solved to achieve the desired shape with the given conduction shape factor and boundary information.

To evaluate the performance of the proposed direct design method in solving thermal **SSD** problems, 4 different test cases are considered in this section for the shape families H_I and H_{II} shown in Figure 7.46. Thermal constraints (boundary conditions), used in the problem definition, have already been explained. In Figure 7.48

these test cases are shown. In all cases the non-dimensional boundary temperature of the cold surface (θ_s) is considered to be uniform[14]. The normalized hot surface temperature (θ_W) is different for each of the test cases. In Case 1 it is uniform, in Case 2 it varies linearly and in Cases 3 and 4 the substrate temperature is a non-linear function of the normalized distance along the substrate. The X coordinate along the substrate and the reference length L were shown and defined in Figure 7.45.

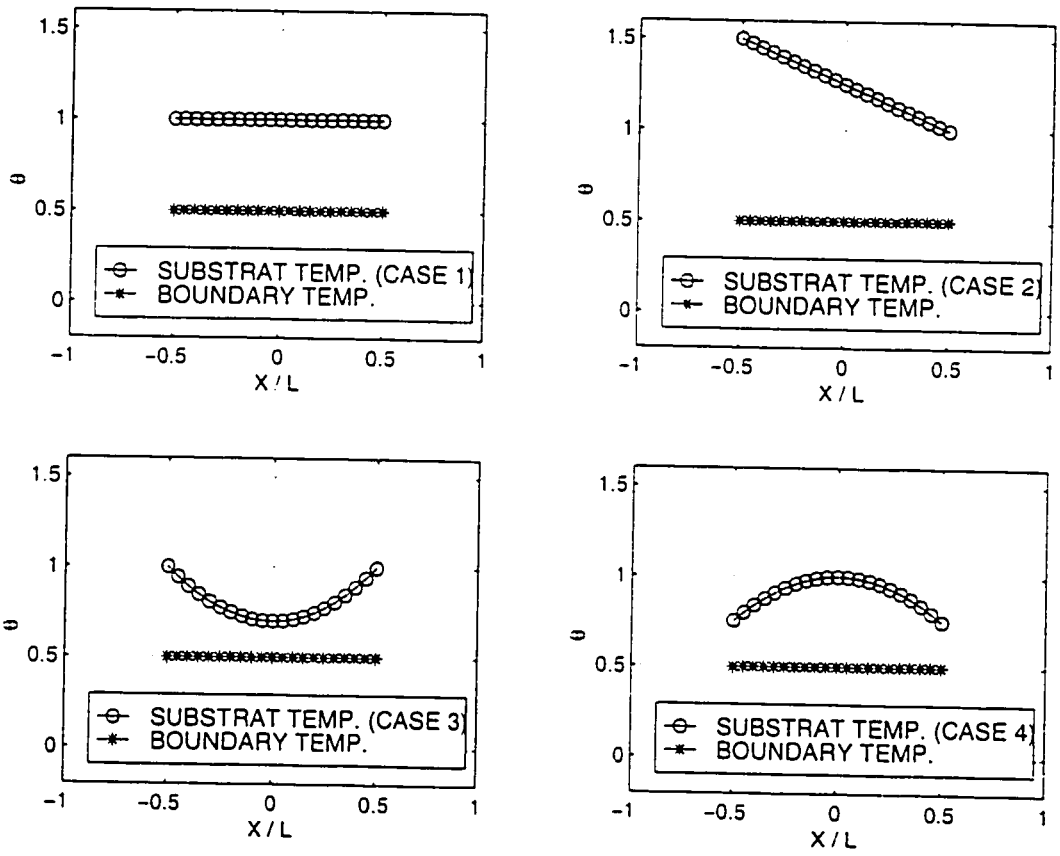

Figure 7.48: Hot and cold surface temperature distributions in conduction test cases.

Figures 7.49 to 7.52 show the solution of the thermal **SSD** problem when the shape is constrained to remain a member of the family H_I. The computational grid

14. The normalized temperature is defined as $\theta \equiv (T - T_a)/(T_L - T_a)$. T_L is the substrate minimum temperature (see Figure 7.45).

is (11 × 11) in all of these examples. In Figure 7.49 test Case 1 is used. Figure 7.49A shows the normalized hot and cold surface temperatures used in the problem. For the initial guess (grid) shown in Figure 7.49C, the conduction heat transfer problem can be solved and the surface heat flux can be calculated ($q_{initial}$). Now, if a higher surface heat flux is specified as the target (in this case $q_{target} = 4q_{initial}$), the conductor shape should change to accommodate this new (target) surface heat flux. When q_{target} was imposed as the target surface heat flux and the proposed direct shape design method was used to solve this **SSD** problem, the conductor shape was obtained as shown in Figure 7.49D. Figure 7.49B shows the position of the hot surface as well as the initial and final (designed) positions of the cold surface. The diagrams which show the initial and final computational grids (Figures 7.49C and 7.49D) are particularly important and show the robustness of the method in making drastic change in the initial guess. This particular format will be used to show the computational results in all conduction design problems discussed in this section.

The problem shown in Figure 7.49 is a one-dimensional conduction heat transfer problem for which the analytical solution is available. The calculated height of the conductor, normalized with the substrate length (Y/L), is equal to the analytically calculated height for the specified surface heat flux.

Figures 7.50, 7.51 and 7.52 show similar results for different substrate temperatures. In Figure 7.50, the temperature along the substrate varies linearly (test Case 2). Note that in the designed conductor shape (Figures 7.50D) the conducting material is accumulated near the hot side of the substrate and the conductor is thinner near the cold side of the substrate to provide a uniform surface heat flux as dictated by the target surface condition (q_{target}).

In Figures 7.51 and 7.52, the substrate temperature varies nonlinearly (test Cases 3 and 4). Again, when a uniform surface heat flux, higher than the initially calculated surface heat flux in each case, was specified as the design objective and the corresponding **SSD** problem was solved, a physically expected shape was obtained (Figures 7.51D and 7.52D). It is seen that the designed shape, and in fact the conduction resistance of the final shape, changes appropriately in each case to comply with the prescribed uniform surface heat flux. The flexibility and robustness of the proposed method in starting with an initial shape too far from the desired one and converging to the final shape in just few iterations is very desirable. For the results shown here, 7 intermediate target heat fluxes have been used and each intermediate stage of the design takes only three iterations to make the maximum absolute residual lower than .001. Most of the examples need only 3 or 4 intermediate stages to

converge but obviously the required number of iterations in each intermediate stage then increases correspondingly.

Figures 7.53 to 7.56 show the results obtained when the heat conductor is constrained to remain a member of the family H_{II}. The computational grid, used in these cases, is (21×21) as was used in reference [54]. The initial guess in these design examples is a semi-circular shape whose radius is equal to the substrate length. The initial surface heat flux, $q_{initial} = h(T_s - T_a)$, was used to choose a target surface heat flux ($q_{target} > q_{initial}$). In all cases the designed shapes are consistent with the physical expectations and also comply with the results presented in [54].

The method works well regardless of the resolution of the grid or the initial guess. However, to obtain a grid independent solution, the grid should be chosen fine enough. In Figure 7.57 a (6×6) computational grid is used for the test Case 3 applied to a family H_{II} member. The boundary nodes move correctly to produce the required shape but due to the coarseness of the grid the surface shape is not smooth. The vertical scale in Figure 7.57D was changed to clearly show how the elements were deformed in the final shape. In Figure 7.58 a fine (41×41) grid is used. It is seen that the (41×41) grid practically produces the same result obtained by the (21×21) grid.

7.4 Summary

In this chapter the proposed direct shape design method was used to solve some engineering design problems.

First, the potential flow duct design concept was aided by the integral boundary layer analysis method (introduced in Chapter 6) to modify initially guessed shapes and design efficient short ducts. The required characteristics for the **TVD**'s in different duct design problems, which allow the designer to control the flow backlash and obtain efficient shapes, were discussed and the following simple, physical based, guidelines were proposed:

- Deceleration should be tailored conservatively along the walls and much of it should be near the places where the boundary layer is thin and fresh.
- Acceleration can be very high but care must be taken to prevent deterioration of the uniformity of the flow far upstream and downstream. Small controlled undershoot and overshoot regions near the sharp pressure gradient regions are helpful to assist the flow to become uniform in a short distance.

- Turning of the flow requires pressure (or velocity) difference between the upper and lower walls. In short duct design problems, this is the mechanism which allows the designer to tune the **TVD** and obtain the required turning.

Second, the application of the method in the context of conduction shape design problems was discussed. The computational results clearly show the applicability and robustness of the method for solving this group of engineering shape design problems.

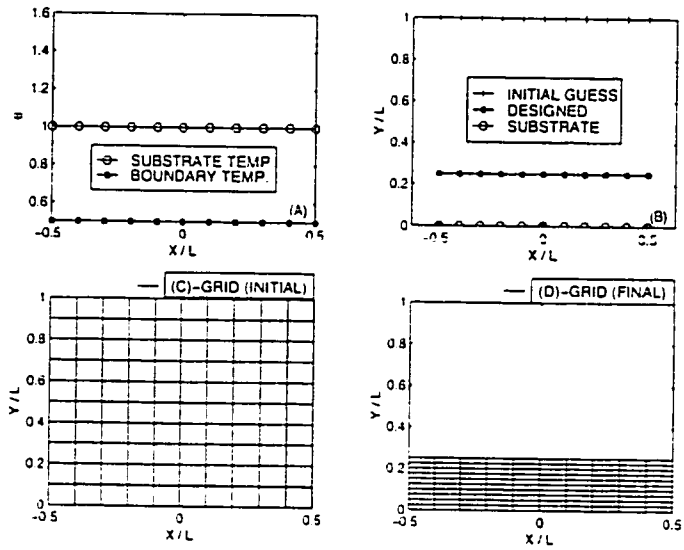

Figure 7.49: Conduction shape design for family H_I, test case 1.

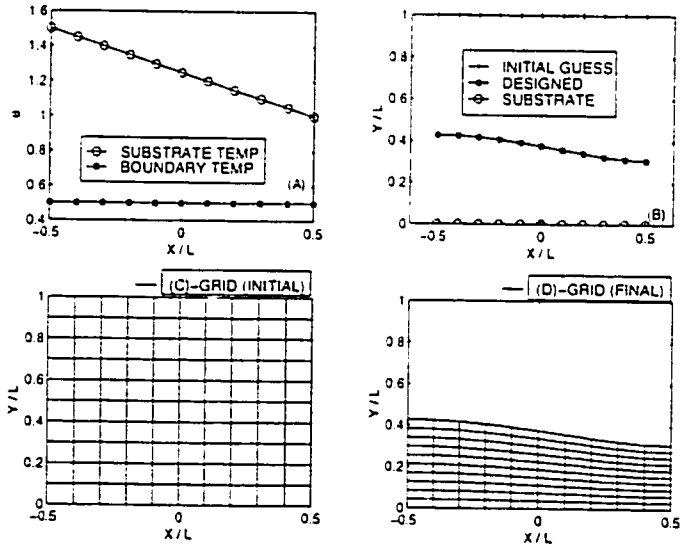

Figure 7.50: Conduction shape design for family H_I, test case 2.

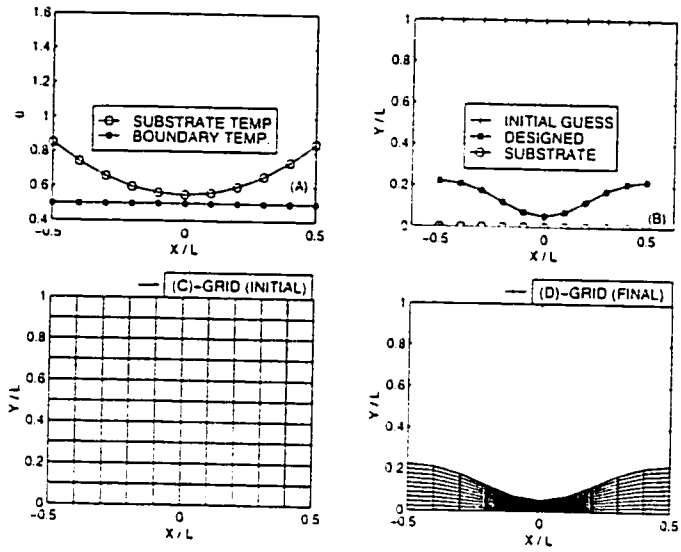

Figure 7.51: Conduction shape design for family H_I, test case 3.

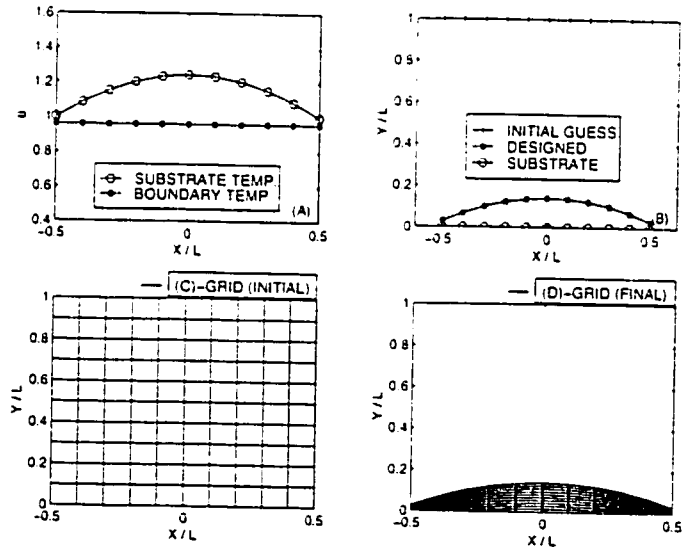

Figure 7.52: Conduction shape design for family H_I, test case 4.

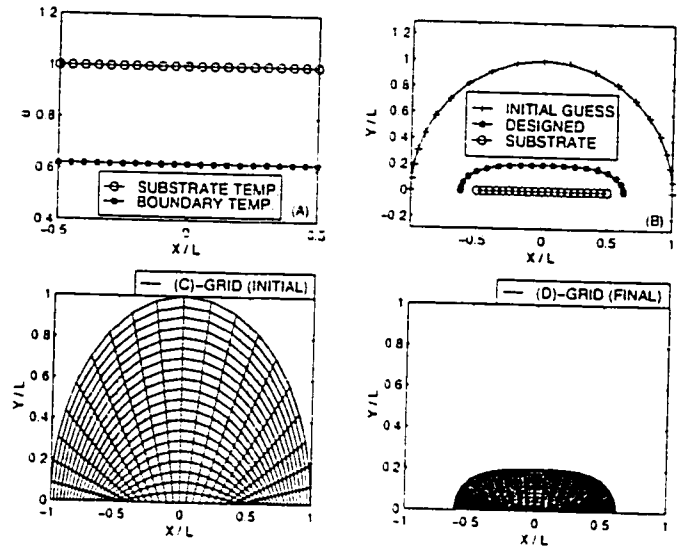

Figure 7.53: Conduction shape design for family H_{II}, test case 1.

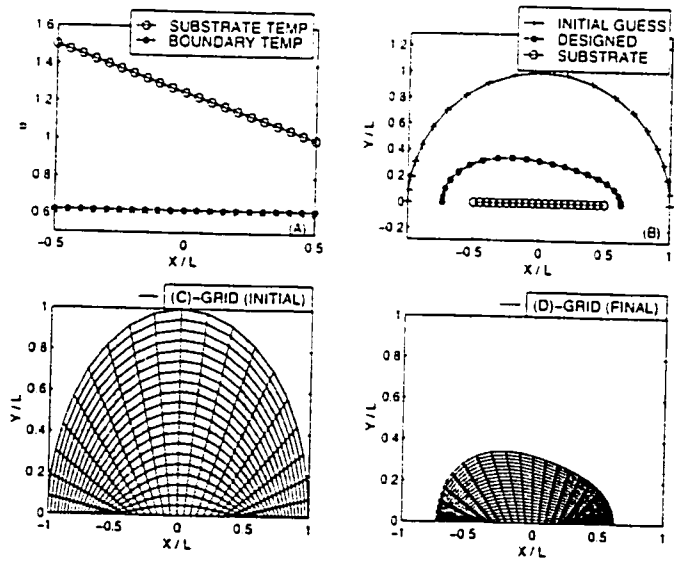

Figure 7.54: Conduction shape design for family H_{II}, test case 2.

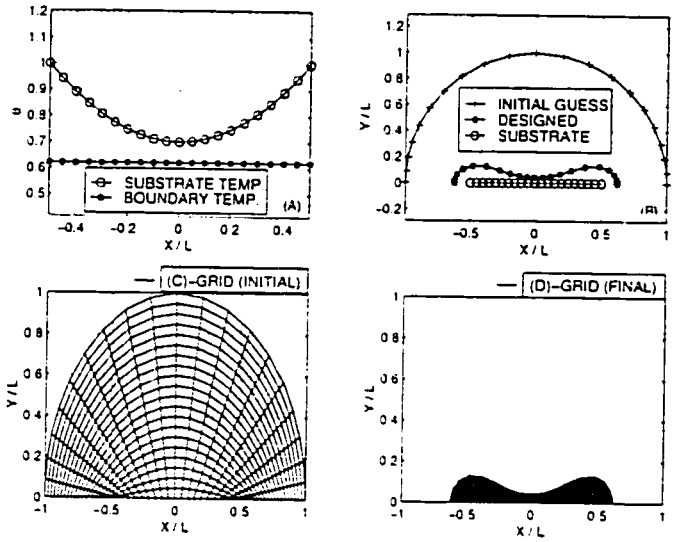

Figure 7.55: Conduction shape design for family H_{II}, test case 3.

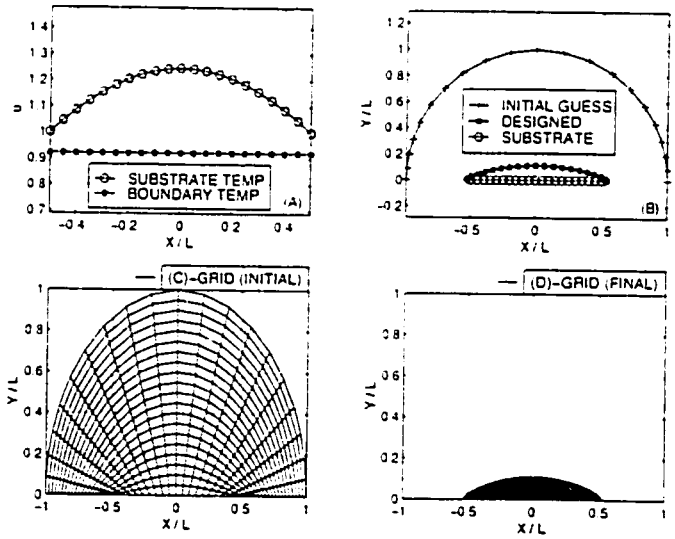

Figure 7.56: Conduction shape design for family H_{II}, test case 4.

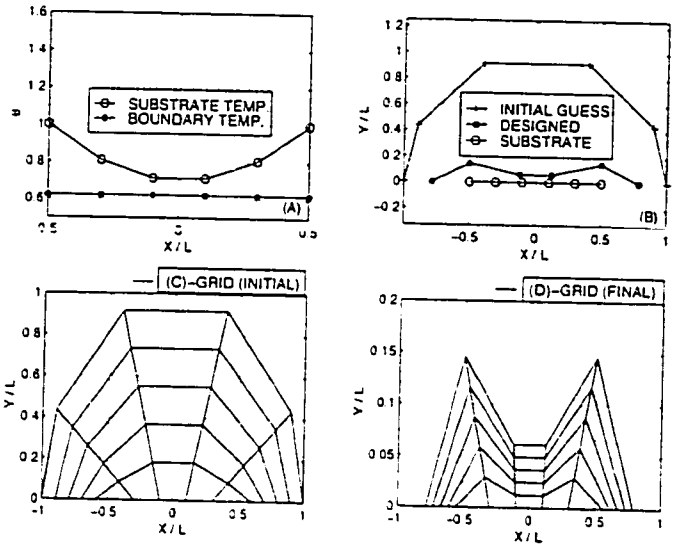

Figure 7.57: Conduction shape design for family H_{II}, test case 3 (coarse grid).

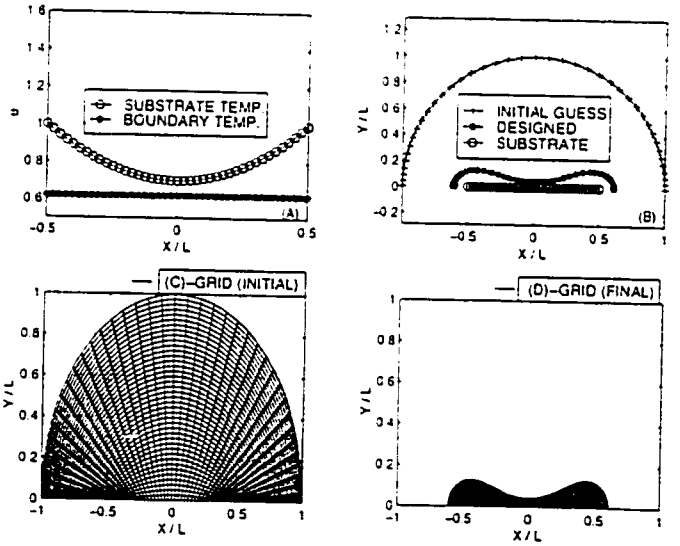

Figure 7.58: Conduction shape design for family H_{II}, test case 3 (fine grid).

Chapter 8

Direct Design: Primitive Variable Formulation

8.1 Introduction

In previous chapters the secondary variable formulation was used and the application of the proposed direct design method in the context of potential flow was discussed. From the CFD point of view, it was shown how the method handled the diffusion term in a general transport equation.

The primitive variable formulation has been successfully applied for solving different flow analysis problems, but there is not such a generality for the secondary variable formulations at the present time. Therefore, the proposed direct shape design method has to be applied in the context of the primitive variable formulation if it is intended to be a general shape design method.

In this chapter a steady ideal one-dimensional flow problem is considered using the pressure and velocity as the flow variables. This simple problem provides a basis for discussing some fundamental issues and paves the way towards multi-dimensional complex cases. The algorithm which is used to obtain the final discretized form of the governing equations and the method used to enforce the pressure-velocity coupling in the numerical simulation step, are the most important contributions of this chapter to the thesis. Also the content of this chapter can be considered as a complement for the previous chapters in another sense: while in the previous chapters diffusion modeling was discussed, the test cases in this chapter deal with the issues of convection and source term modeling. Section 2 introduces the problem (physical model) and its mathematical model. Section 3, provides a semi-discretized mathematical model for

the flow phenomenon followed by a section about the linearization of the equations. The issues of pressure-velocity coupling, convection modeling and interpolation formulas are discussed in Section 5 which provides the final working equations for the numerical solution. Sections 6 and 7 provide some test cases and show how the unified governing equations, obtained from the adopted numerical simulation technique, successfully solve the analysis and shape design problems.

8.2 Level *C* Mathematical Model

It was shown in Chapter 2 that the conservative mathematical model for the momentum constraint in steady inviscid flows is as follows[1]:

$$\vec{\nabla} \cdot \vec{V}\vec{V} = -\vec{\nabla}P. \tag{8.1}$$

The **FVM** requires an exact integral formulation of the problem as the starting point. For the discretized solution domain shown in Figure 8.1, the required integral expression is written as follows:

$$\int_{\Omega_{cv}} \left(\vec{\nabla} \cdot \vec{V}\vec{V}\right) d\Omega + \int_{\Omega_{cv}} \left(\vec{\nabla}P\right) d\Omega = 0. \tag{8.2}$$

Using the divergence theorem and multiplying the terms by the unit vector in the direction of the flow ($\vec{i}$), the following integral equation is obtained:

$$\int_{\Gamma_{cv}} \left(\vec{V}\vec{V} \cdot \vec{n}\right) \cdot \vec{i} dA + \int_{\Omega_{cv}} \vec{\nabla} \cdot \left(P\vec{i}\right) d\Omega = 0. \tag{8.3}$$

The final form of the exact integral momentum equation is:

$$\int_{\Gamma_{cv}} uu \left(\vec{n} \cdot \vec{i}\right) dA + \int_{\Gamma_{cv}} P \left(\vec{n} \cdot \vec{i}\right) dA = 0. \tag{8.4}$$

In this integral equation, u stands for the stream-wise velocity component.

An exact integral expression for the mass constraint can be obtained by a similar approach:

$$\int_{\Gamma_{cv}} u \left(\vec{n} \cdot \vec{i}\right) dA = 0. \tag{8.5}$$

1. For the sake of simplicity, the superscript $\tilde{}$ is dropped and P is used instead of $\tilde{P}$ in this chapter.

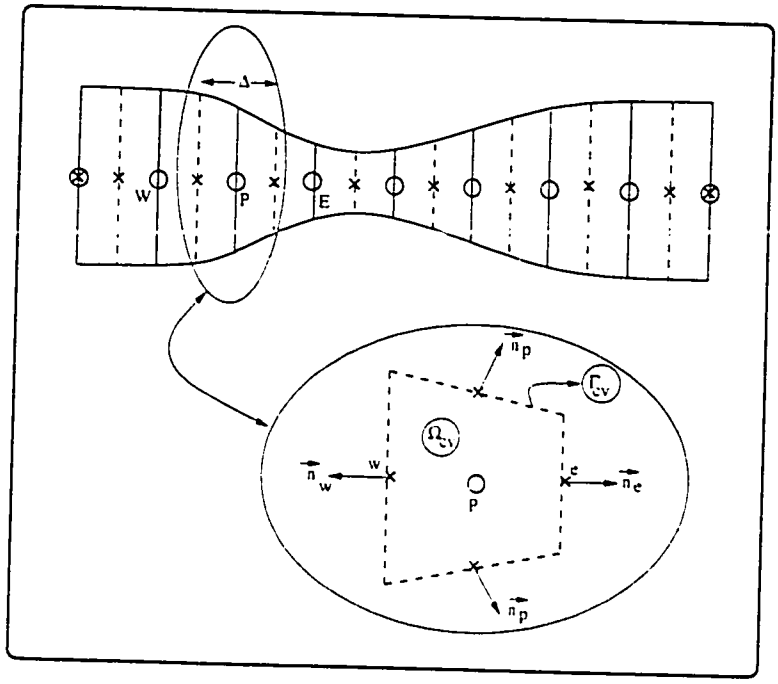

Figure 8.1: Discretization of the flow domain.

8.3 Level D_0 Mathematical Model

It is common in **CFD** to approximately calculate the surface integrals, given in Eq. 8.4 and 8.5, with the mid-point rule. Applying this approximation, the exact integral governing equations are approximately represented by the following algebraic equations[2]):

$$u_e a_e - u_w a_w = 0 \tag{8.6}$$

$$u_e u_e a_e - u_w u_w a_w + p_e a_e - p_w a_w = P_P(a_e - a_w) \tag{8.7}$$

The governing equations in the above form, which contain the integration point quantities, have been named the level one approximation in the **FVM** [173]. Here these equations, which are the earliest results of the discretization, are called the level D_0 mathematical model of the problem. To emphasize the physical meaning of different

2. In this chapter, capital letters are used for nodal point quantities and small letters are used to denote the integration point quantities. Also, the summation rule is not applied to the subscripts.

terms, as is desirable in the **FVM**, Eq. 8.6 and 8.7 are expressed as below:

$$\mathcal{F}_e^m - \mathcal{F}_w^m = 0 \tag{8.8}$$

$$\mathcal{F}_e^u - \mathcal{F}_w^u = \mathcal{S}^P \tag{8.9}$$

The source, mass flow and momentum flow terms[3] are:

$$S^P \equiv a_e(P_P - p_e) + a_w(p_w - P_P) \tag{8.10}$$

$$\mathcal{F}_e^u \equiv u_e u_e a_e \tag{8.11}$$

$$\mathcal{F}_w^u \equiv u_w u_w a_w \tag{8.12}$$

$$\mathcal{F}_e^m \equiv u_e a_e \tag{8.13}$$

$$\mathcal{F}_w^m \equiv u_w a_w \tag{8.14}$$

8.4 Level D_{0L} Mathematical Model

Equations 8.8 and 8.9, the approximate governing equations of the flow problem, are not appropriate for numerical solution. These equations contain all the relevant physics and could be used in solving both analysis and shape design problems. However, there are three major problems which prevent these equations from being the discrete mathematical model of the physical phenomenon appropriate for numerical solution. The first issue is the non-linearity. The second issue is the appearance of some quantities at the integration points which are not known in the discretized domain[4]. The last problem is related to an interesting (and challenging) problem in the Navier-Stokes equations, which is the absence of pressure in the mass constraint. The first problem is discussed in this section and two others will be discussed in the next section.

Recalling that the final (new) shape in shape design problems may be considered as a *perturbed shape*, the source and flow terms are perturbed and linearized as below:

$$\mathcal{F}^m = \mathcal{F}^{m0} + \delta\mathcal{F}^m. \tag{8.15}$$

3. $\mathcal{F}^m$ and $\mathcal{F}^u$ are not strictly mass and momentum flows. Only when the density is equal to one, this terminology is correct. However for the sake of simplicity and to avoid new terminologies, $\mathcal{F}^m$ and $\mathcal{F}^u$ will be called mass and momentum flows in this chapter.
4. The discretized domain just recognizes the nodal points.

$$\mathcal{F}^u = \mathcal{F}^{u0} + \delta\mathcal{F}^u, \tag{8.16}$$

$$\mathcal{S}^p = \mathcal{S}^{p0} + \delta\mathcal{S}^p. \tag{8.17}$$

The 0 superscript designates old values here and δ stands for a variation (or disturbance) in the relevant quantity. The perturbation terms are approximated as follows:

$$\delta\mathcal{F}^m \approx \left(\frac{\partial\mathcal{F}^m}{\partial u}\right)^0 (u - u^0) + \left(\frac{\partial\mathcal{F}^m}{\partial a}\right)^0 (a - a^0). \tag{8.18}$$

$$\delta\mathcal{F}^u \approx \left(\frac{\partial\mathcal{F}^u}{\partial u}\right)^0 (u - u^0) + \left(\frac{\partial\mathcal{F}^u}{\partial a}\right)^0 (a - a^0). \tag{8.19}$$

$$\begin{aligned}\delta\mathcal{S}^p \approx &\left(\frac{\partial\mathcal{S}^P}{\partial p_w}\right)^0 (p_w - p_w^0) + \left(\frac{\partial\mathcal{S}^P}{\partial p_e}\right)^0 (p_e - p_e^0) + \\ &\left(\frac{\partial\mathcal{S}^P}{\partial a_w}\right)^0 (a_w - a_w^0) + \left(\frac{\partial\mathcal{S}^P}{\partial a_e}\right)^0 (a_e - a_e^0) + \\ &\left(\frac{\partial\mathcal{S}^P}{\partial P_P}\right)^0 (P_P - P_P^0).\end{aligned} \tag{8.20}$$

Using the above approximations, the mass and momentum constraints at the *level* D_{0L} (the discretized linear version of the level D_0 equations) will be obtained as:

$$(L_1^m)\, a_e + (L_2^m)\, a_w + (L_3^m)\, u_e + (L_4^m)\, u_w = \mathcal{R}^m, \tag{8.21}$$

$$(L_1^u)\, a_e + (L_2^u)\, a_w + (L_3^u)\, u_e + (L_4^u)\, u_w + (L_5^u)\, p_e + (L_6^u)\, p_w + (L_7^u)\, P_P = \mathcal{R}^u. \tag{8.22}$$

The coefficients L_i^m, L_i^u, R^m and R^u are functions of old geometrical and physical quantities.

8.5 Level D Mathematical Model

It was explained in Chapter 2 that interpolation is required to relate the integration point quantities to the nodal point quantities. Many different interpolation schemes have been proposed. Schemes that appear to have only minor differences can result in major changes in the numerical properties of the discrete equations. The goal is to choose the best method. As discussed previously, the interpolation should be both

accurate and have transport properties that agree with those of the governing equations. Some interpolation schemes like **CDS**, i.e. $u_e \approx 0.5(U_p + U_E)$, do not satisfy the transportive properties of the flow and therefore it is not surprising that they fail to provide a good discretized mathematical model for the problem. Others, like the very elegant proposal of Raw and Schneider [30], more fully meet the requirements. Sometimes the requirements for interpolation are counter-intuitive. For example, in co-located methods, the velocity at the integration point apparently must be obtained by two different interpolations: one for the velocity used to compute the mass flow, and one for the convected momentum. Traditionally, failure to use different interpolations leads to pressure-velocity decoupling [174].

While the use of two different velocity interpolations for mass and momentum is almost universally accepted and used in co-located schemes to get the pressure-velocity coupling, the author considers this to be inconsistent or at least unnecessary. A goal of this thesis was to lay the groundwork (in $1D$) for a consistent formulation in which the pressure-velocity coupling issue is treated independently and the interpolation formulas for the flow field quantities, including the velocity, are obtained based on some relevant governing equations.

The new scheme is essentially based on two concepts which will be explained in what follows. Even though it is not claimed at this stage that the proposed scheme will successfully cope with multi-dimensional problems, it appears to be the first time that a co-located scheme has been successfully tested that does not use different interpolations for the convecting and convected velocities to provide the necessary coupling between the pressure and the velocity in the numerical model.

The first basic concept in developing the new scheme is the fact that in Eq. 8.20 and 8.21 six integration point quantities (a_e, a_w, u_e, u_w, p_e and p_w) appear and therefore six interpolation formulas have to be specified. The interpolation formulas for the geometrical parameters a_e and a_w are obtained by noting that the wall is piecewise linear in the discretized space:

$$a_e \approx \frac{A_P + A_E}{2}. \tag{8.23}$$

$$a_w \approx \frac{A_P + A_W}{2}. \tag{8.24}$$

The physics of the flow provides the required constraints for finding appropriate interpolations for the pressure and velocity at the integration points. The mass and the momentum equations are used in their non-conservative forms as follows

(conceptually this is based on the idea developed in [30]):

$$\left[\frac{\partial(ua)}{\partial x}\right]_{ip} = 0. \tag{8.25}$$

$$\left[u\frac{\partial u}{\partial x} + \frac{\partial p}{\partial x}\right]_{ip} = 0. \tag{8.26}$$

These constraints have to be linearized and the derivatives have to be discretized. To make sure that the velocity component, obtained from the momentum constraint, satisfies the mass constraint, a factor of the mass equation is subtracted from the momentum equation [173, 175]. Therefore, the following equations are used as the required physical constraints at the integration point *ip*:

$$\left[a^0\frac{\partial u}{\partial x} + u^0\frac{\partial a}{\partial x}\right]_{ip} = 0. \tag{8.27}$$

$$\left[u^0\frac{\partial u}{\partial x} + \frac{\partial p}{\partial x} - \left(\frac{u^0}{a^0}\right)\left(a^0\frac{\partial u}{\partial x} + u^0\frac{\partial a}{\partial x}\right)\right]_{ip} = 0. \tag{8.28}$$

Now, the derivatives in the equations have to be discretized. Following the general policy in the **FVM**, the transportive properties of different terms are taken into the consideration. In the present problem, only the convected velocity (specific momentum) behaves parabolically. Therefore, the derivatives at the integration point e (for example) are discretized as follows:

$$\left(\frac{\partial u}{\partial x}\right)_e^{convecting} \approx \frac{U_E - U_P}{\Delta}. \tag{8.29}$$

$$\left(\frac{\partial u}{\partial x}\right)_e^{convected} \approx \frac{u_e - U_P}{(\Delta/2)}. \tag{8.30}$$

$$\left(\frac{\partial p}{\partial x}\right)_e \approx \frac{P_E - P_P}{\Delta}. \tag{8.31}$$

$$\left(\frac{\partial a}{\partial x}\right)_e \approx \frac{A_E - A_P}{\Delta}. \tag{8.32}$$

Following the above discretization scheme, the following equations are obtained:

$$a_e^0(U_E - U_P) + u_e^0(A_E - A_P) = 0. \tag{8.33}$$

$$u_e = \frac{U_P + U_E}{2} + \frac{1}{2u_e^0}(P_P - P_E) + \frac{u_e^0}{2a_e^0}(A_E - A_P). \tag{8.34}$$

It is seen that the integration point pressure does not appear in the above equations. The modified momentum equation (Eq. 8.28) provides an interpolation formula for the integration point velocity (u_e) such that both momentum and mass constraints have been considered to obtain an interpolation formula for u_e. Considering the role of the pressure in the incompressible flow, it is expected that a modified form of the continuity equation provides the required interpolation formula for the integration point pressure (p_e). The momentum equation, in some form, has to be used in this modification such that both mass and momentum constraints are also being considered in providing an interpolation formula for p_e.

The second basic concept in the new scheme is, indeed, the concept of *a correct second order constraint on the pressure field* which is used to modify the continuity equation to make it ready to provide an appropriate interpolation formula for the integration point pressure. It is important to note that **CDS** has been used to discretize the pressure gradient and it is expected that the predicted pressure field will have non-physical numerical oscillations. In other words, as beautifully explained in [176], there is an unconstrained mode of oscillation for the pressure in the discretized equations[5].

In the new scheme, to introduce the pressure in the mass equation and also prevent the modal oscillations in the pressure field, a *correct second order constraint on the pressure field* is added to the continuity equation (Eq. 8.33). If the constraint on the pressure field is *correct*, it is practically a zero term and the calculated velocity field will satisfy the continuity equation. In other words, the conservation of mass, as one of the governing equations, is enforced in the solution procedure. Furthermore, if the constraint on the pressure field is *second order*, it will allow the integration point pressure to appear in the discretization while the **CDS**, which models the elliptic behavior of the pressure, is used. This also provides the required pressure-velocity coupling in the interpolation formula for the integration point pressure.

5. The non-physical oscillations in the numerical solution have been called modal oscillations in [176] and that terminology is used here as well.

A correct second order constraint on the pressure field can be obtained by taking the divergence of the momentum equation. The result is the following Poisson equation for the pressure:

$$\left[\frac{\partial^2 p}{\partial x^2} = -u^0 \frac{\partial^2 u}{\partial x^2}\right]_{ip}. \tag{8.35}$$

The second derivative of the velocity in Eq. 8.35 is also constrained by the divergence of the continuity equation. Taking the divergence of Eq. 8.25 and noting that the second derivative of the cross-sectional area is zero[6], reveals that the required second order constraint on the pressure field can be used as:

$$\left[\frac{\partial^2 p}{\partial x^2}\right]_{ip} = 0. \tag{8.36}$$

Equation 8.36 has to be discretized, made dimensionally consistent with the other terms in the mass equation (Eq. 8.33) and used in that equation. For the integration point e, it follows that:

$$a_e^0(U_E - U_P) + u_e^0(A_E - A_P) \approx \left(\frac{\Delta^2 a_e^0}{4u_e^0}\right)\left(\frac{P_E - 2p_e + P_P}{(\Delta^2/4)}\right). \tag{8.37}$$

Now, it is easy to re-arrange the above equation and obtain an explicit formula for p_e:

$$p_e = \frac{P_E + P_P}{2} + \frac{u_e^0}{2}(U_P - U_E) + \frac{u_e^{0^2}}{2a_e^0}(A_P - A_E). \tag{8.38}$$

Similar expressions can be easily obtained for u_w and p_w.

Having all these, the unified final (level D) mathematical model of the problem is obtained as:

$$\begin{aligned}\left(C_W^{mP}\right) P_W + \left(C_P^{mP}\right) P_P + \left(C_E^{mP}\right) P_E + \\ \left(C_W^{mA}\right) A_W + \left(C_P^{mA}\right) A_P + \left(C_E^{mA}\right) A_E + \\ \left(C_W^{mU}\right) U_W + \left(C_P^{mU}\right) U_P + \left(C_E^{mU}\right) U_E = \\ \left(C^{mR}\right).\end{aligned} \tag{8.39}$$

6. The cross-sectional area is a linear function of x in each element.

$$\begin{aligned}&\left(C_W^{uP}\right) P_W + \left(C_P^{uP}\right) P_P + \left(C_E^{uP}\right) P_E + \\ &\left(C_W^{uA}\right) A_W + \left(C_P^{uA}\right) A_P + \left(C_E^{uA}\right) A_E + \\ &\left(C_W^{uU}\right) U_W + \left(C_P^{uU}\right) U_P + \left(C_E^{uU}\right) U_E = \\ &\left(C^{uR}\right).\end{aligned} \tag{8.40}$$

The first superscript in the C factors points to the relevant equation and the second one represents the dependent variable which the factor multiplies. The subscripts specify the node location in the computational molecule. The C factors in Eq. 8.39 and 8.40 are introduced in Appendix D.

Two boundary conditions for the pressure and velocity are required to render the problem as a well-posed mathematical problem. Here, the velocity at the inlet and the outlet pressure are specified. Note that the final (discretized) mathematical model can be used in both analysis and shape design problems. In analysis problems the geometry is known and pressure and velocity have to be calculated. In shape design problems, the (target) pressure is specified and the velocity and the shape of the duct (the wall profile) are calculated throughout the solution domain.

8.6 Validation

The proposed scheme has to be checked and validated. In particular, it is important to check the scheme and determine whether it allows modal oscillations to appear or not.

An interesting one-dimensional modal oscillation test method was introduced and used by Karimian and Schneider [175]. Yin [176] used the same idea to test one-dimensional computational molecules for the modal oscillations. The basic idea in this test is to impose a local disturbance on the pressure and/or velocity fields and see how these fields respond to the applied disturbance. In general, both the velocity and pressure fields have to be checked because, due to the lack of the appropriate pressure-velocity coupling in a scheme, modal oscillations in one field may not be detected in the other one.

Figure 8.2 introduces one-dimensional modal oscillation test cases, some of which were used in [175] and [176], and shows how the pressure, velocity or both can be stimulated to trigger modal oscillations in one-dimensional numerical schemes.

In the constant area duct, duct 1 in Figure 8.2, both the pressure and the velocity are constant and uniform along the duct and neither the pressure nor the velocity is stimulated. Such a one-dimensional test case cannot detect any *ill-posed* one-

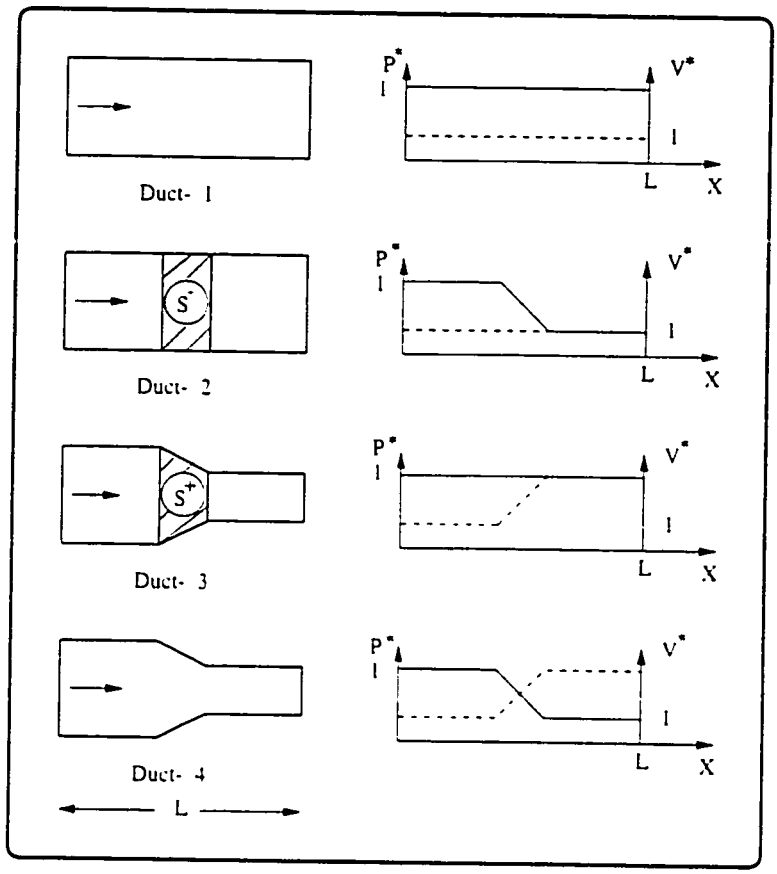

Figure 8.2: One-dimensional test cases.

dimensional computational molecule which accepts multiple oscillatory solutions. If a local momentum sink is located somewhere along the duct, the pressure drops and if the computational molecules allow it, modal oscillations will appear in the solution. Therefore, a duct with a momentum sink (or source) triggers the pressure oscillations and may be called the *pressure stimulation test case* (duct 2). If there is a local area change along the duct, the velocity as well as the pressure field will experience changes and such a test simultaneously triggers both the velocity and pressure oscillations. Therefore, this test may be called the *pressure-velocity stimulation test case* (duct 4). It is possible to put a *tuned* local momentum source or sink in a variable area duct to compensate the pressure change and just trigger the oscillations in the velocity (duct

3). Such a duct would trigger only the velocity modal oscillations and may be used as a *velocity stimulation test case*. P^* and V^* in the diagrams shown in Figure 8.2 are non-dimensionalized pressure and velocity normalized with P_2 and V_1 respectively.

To check the proposed scheme in this chapter, only the pressure stimulation case is used to determine whether the proposed scheme accepts modal oscillations or not. The pressure-velocity coupling is checked simply by algebraic manipulations of the interpolation formulas for the pressure and velocity (Eq. 8.34 and 8.38) to make sure that the pressure and velocity are mathematically tied together and neither one can be eliminated from the interpolation formulas. Because of the strong coupling, a modal oscillation in the pressure field can cause constrained oscillations in the velocity field and therefore if the scheme passes the pressure stimulation test case, it is concluded that it does not accept modal oscillations. It should be mentioned that the test cases shown in Figure 8.2 just detect any modal oscillations in the pressure or velocity fields. A rigorous mathematical technique, for one-dimensional problems, has been proposed by Yin [176] which can predict the possibility and the shape of the modal oscillations in a numerical scheme.

To not only check the proposed scheme but also give an idea that why and how the modal oscillations appear in the numerical solutions, two *ill-posed* numerical schemes (called Schemes 1 and 2 in this chapter) are also developed and introduced. These schemes use different interpolation formulas compared to the proposed scheme. It has to be emphasized that proposing *ill-posed* interpolation schemes is easy and there are many examples of such schemes. The interpolation Schemes 1 and 2, introduced here, are just developed and used to show the importance of a logical and carefully designed procedure in the process of developing a numerical scheme.

Scheme 1 uses Eq. 8.26 to provide an interpolation formula for the unknown u_e. An upstream difference scheme is used to discretize the velocity derivative and **CDS** is used for the pressure gradient. The resulted interpolation formula is:

$$u_e = U_P + \left(\frac{1}{2u_e^0}\right)(P_P - P_E). \tag{8.41}$$

The interpolation formula for the pressure in the Scheme 1 is proposed based on the *elliptic behavior* of the pressure in incompressible flows:

$$p_e = \frac{P_P + P_E}{2}. \tag{8.42}$$

Scheme 2 follows the same approach as was explained for the *proposed scheme* except that the following equations are used as the governing equations at the inte-

gration points:

$$\left[a^0\frac{\partial u}{\partial x}+u^0\frac{\partial a}{\partial x}\right]_{ip}=0. \tag{8.43}$$

$$\left[u^0\frac{\partial u}{\partial x}+\frac{\partial p}{\partial x}\right]_{ip}=0. \tag{8.44}$$

Now, a pressure stimulation test duct which is discretized by 11 elements and a momentum sink is located in the middle of it, is used to test the proposed scheme as well as Schemes 1 and 2.

Figure 8.3 shows the result of the pressure stimulation test for Scheme 1. Note that the pressure lends itself to modal oscillations and transfers the oscillations to the velocity field. The problem with this scheme is that mass conservation was not enforced to develop an interpolation formula for the integration point pressure. In fact, Eq. 8.42 was not obtained from an appropriate form of the continuity equation which relates the integration point pressure to other field variables.

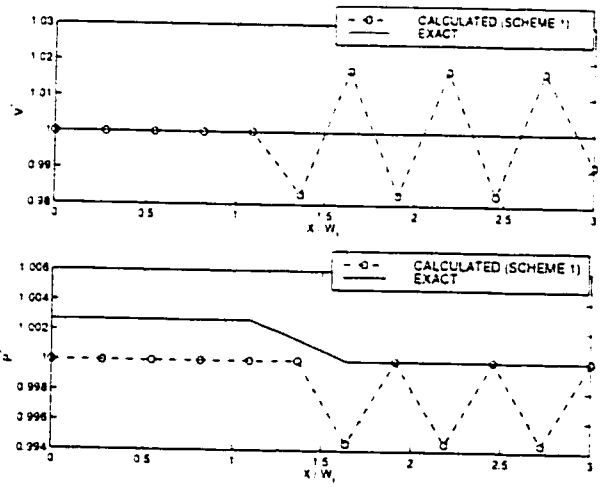

Figure 8.3: Pressure stimulation test for scheme 1.

In Figure 8.4 Scheme 2 is evaluated. Note that there are some local numerical oscillations which are damped eventually. In this case the problem with illness of

the computational molecules is more delicate. In fact the mass constraint is satisfied to provide an interpolation formula for the integration point pressure, but the scheme does not care about the mass constraint when an interpolation scheme for the integration point velocity is developed.

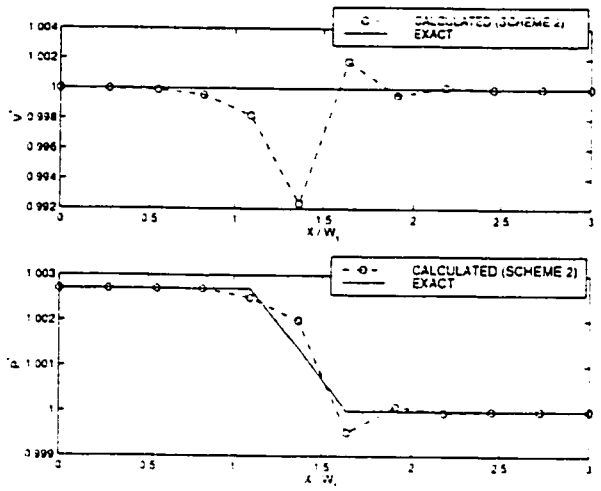

Figure 8.4: Pressure stimulation test for scheme 2.

The performance of the proposed scheme, when the pressure-stimulation test is applied, is shown in Figure 8.5. It is seen that the proposed computational molecules do a great job and can be trusted as the discretized mathematical model for the problem.

Figure 8.6 shows the results obtained when the pressure-velocity stimulation test was used to check the proposed scheme. As is expected, the predictions, even for this coarse grid, are in excellent agreement with the analytic solution and there are no modal oscillations in the numerical solution.

8.7 One-Dimensional Duct Design

The unified formulation of the one-dimensional ideal flow, Eq. 8.39 and 8.40, is now used to solve **SSD** problems. The pressure distribution along the duct is specified, and the (symmetrical) distribution of the cross sectional area along the duct is directly calculated.

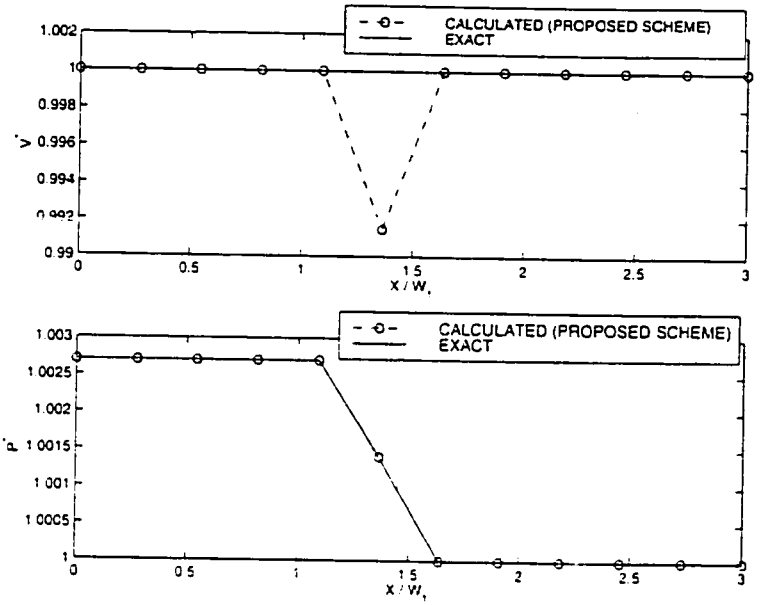

Figure 8.5: Pressure stimulation test for the proposed scheme.

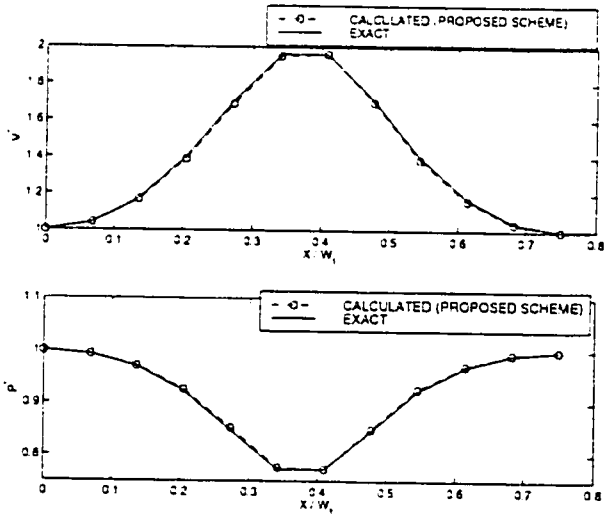

Figure 8.6: Pressure-velocity stimulation test for the proposed scheme.

Figure 8.7 shows a trivial test case. An initial guess is provided by the designer for which the calculated pressure distribution is shown as the initial pressure distribution. The target pressure is a constant pressure along the duct, shown in Figure 8.7. The code returns the expected shape, a constant area duct.

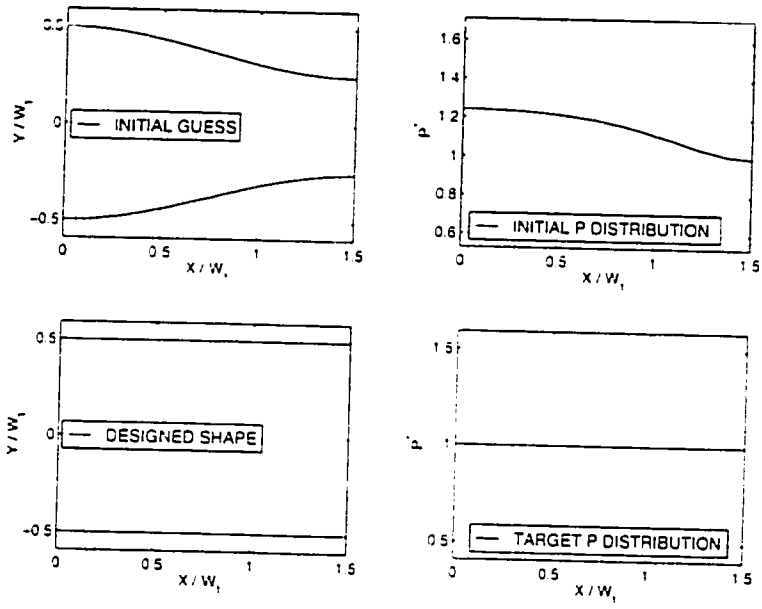

Figure 8.7: Design of a constant area duct.

Figure 8.8 shows another design example in which the initial guess is a constant area duct and the specified target pressure varies along the duct. It is seen that the designed shape complies with the expected duct shape for the given target pressure.

8.8 Summary

This chapter provided an application example for the direct design method in the context of primitive variable formulation. The selected problem was a steady one-dimensional ideal flow. A unified discretized mathematical model, appropriate for solving both analysis and design problems, was developed and tested. A physical-based approach was proposed and used for finding the required interpolation formulas and a technique was presented for introducing the role of the pressure in the continuity

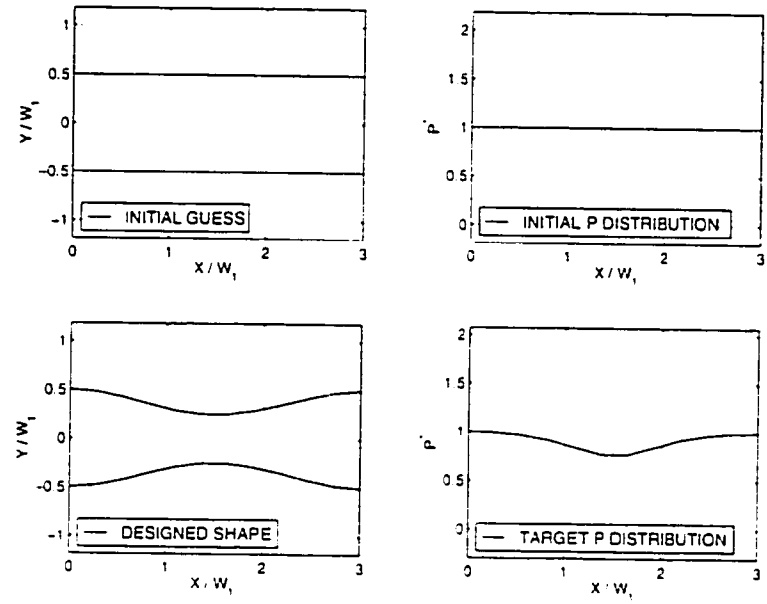

Figure 8.8: Design of a convergent-divergent duct.

equation and providing a good pressure-velocity coupling in the discretized mathematical model. Even though the concepts of advected and advecting velocities were used in the proposed numerical scheme, only one velocity interpolation formula was used and two concepts of velocity (i.e. convected and convecting velocities) were not used to solve the pressure-velocity coupling issue. The pressure-velocity coupling was obtained independently and two concepts of velocity in the discretized space were used just to correctly model the transportive properties of the mass-carrying velocity and the velocity carried by the momentum. All required interpolation formulas were *derived* from relevant governing equations and no ad-hoc interpolation formula was used to relate the integration point quantities to the nodal point quantities.

It is hoped that this numerical scheme, which provides an appropriate pressure-velocity coupling, and indeed the direct design procedure, can be extended to two and three-dimensional thermo-fluid problems.

Chapter 9

Closure

9.1 Summary and Discussion

This research has developed a new numerical direct shape design method for thermo-fluid engineering problems.

The fact that both the analysis and its associated shape design problem are governed by the same physical laws and governing equations, led to the concept of unified discrete formulation which can be used in the numerical simulation of both the analysis and its associated shape design problem. Application of this unified discrete formulation in solving engineering shape design problems shows that the primary objective of the research, i.e. developing a direct design method for solving **SSD** problems, have been realized.

Robustness and ease of the implementation and the physical clarity of the method in directly calculating the shape in the physical space, were beyond the initial expectations of the author at the beginning of this research. The method does not seem to have any inherent limitations and its future looks very promising. The author believes that the method, at its current stage of development, has distinguished features, compared to other available techniques, and can be used in a general shape design software for solving Laplacian-type problems (e.g. potential flow duct design). Extension of the method to provide a unified discrete mathematical model for the full Navier-Stokes equations seems a matter of implementation of the ideas already introduced in this research. Of course, taking into account the three dimensionality and physical complexities of the flow will be a major step forward and has its own difficulties. However, no inherent limitation was implied by the proposed method and considering the available **CFD** technology those difficulties can be resolved.

The important contributions of this research to the available computational methods in thermo-fluid mechanics may be summarized as below:

- A method was developed to obtain a unified formulation which governs both the analysis and surface shape design problems. Using the proposed method, the space coordinates of all the grid points in the discretized domain are considered as unknowns and directly solved for in shape design problems. An appropriate grid evolution policy, which allows control and tracking of the grid, and an appropriate linkage between the boundary points and internal ones, which allows to use the extra boundary information to close the system of equations, were used to obtain an appropriate unified formulation.

- A generalized inner variable theory was developed which allows the integral parameters in an arbitrary turbulent boundary layer flow be calculated. The theory is a modified form of the theory proposed by Das [115], but is superior and better formulated, in the belief of the author, for making viscous corrections in potential flow solutions. A three-equation version of the formulation was used to solve some practical design problems, i.e. design of efficient short ducts. The limitations of the integral boundary layer methods are well known and no claim is made that the proposed method is robust or accurate in general. The robustness and desired accuracy can be obtained, however, if a set of correlations (not a single one) are available to choose from in different applications.

- Guidelines for the specification of **TVD** in short duct design problems, in the context of **SSD** problems, were presented and used to design different efficient short ducts.

- A new interpolation scheme was developed, in the context of co-located primitive variable formulation, which provides a good coupling between the pressure and velocity fields and does not use two different interpolations for advecting and advected velocities. The proposed method has been only validated for one-dimensional applications, but it seems to be extensible to multidimensional complex problems as well. The general design method proposed in this thesis will, the author believes, be extended to apply to more complex flows, and the method will some day revolutionize the application of the **CFD** to the design of fluid and heat flow surfaces.

9.2 Recommendations For Future Research

The direct design concept is very attractive in many engineering applications. The proposed direct surface shape design method in this thesis, at its current stage of development, is comparable or superior to other available methods that have been specifically developed for the design of two-dimensional potential flow ducts as well as the algorithms for designing two-dimensional heat conductors. The present method appears, however, to be directly applicable for the design of complex three-dimensional problems that involve viscous flow. To advance the capabilities of this method will require further research on the topics briefly discussed below:

- Extension of the applications: secondary variable formulation.
  - Physically simple $3-D$ problems.

    Extension of the proposed method to three-dimensional applications is an area which was not considered in this research. It seemed appropriate in this thesis to neglect the physical complexities like the viscosity effects, turbulence and discontinuities in the flow field and just concentrate on the geometrical complexities first. The next goal is to provide engineers with a direct shape design tool capable of modeling and solving both analysis and shape design problems which are governed by the three-dimensional Laplace equation. A robust three-dimensional potential flow design method is very useful, and perhaps necessary, for attacking three-dimensional viscous flow design problems.
  - Physically complex $2-$ and $3-D$ problems

    The application of the method for solving complex two and three-dimensional problems in the context of secondary variable formulation could be a logical extension of the method. Considering the current state of the art of the secondary variable formulations, it does not seem that there is too much interest in this regard. However, from an academic point of view there are lots of challenging problems when one tries to use dependent variables such as vorticity and stream vector to attack complex three-dimensional problems.
- Extension of the applications: primitive variable formulation.

  A similar research topic may be conducted to apply the method for solving complex multi-dimensional problems in the context of primitive variable formulation. It is now generally accepted that the primitive variable formulation is a better candidate for solving complex problems and solving simple and complex

two and three-dimensional shape design problems in the context of primitive variable formulation would be highly welcomed by the engineering community.

- Extension of the applications: external flow problems.
  In this thesis the direct design method was used for solving some internal flow problems. Applicability of the method in solving external flow problems has to be studied.

- Extension of the applications: value design problems.
  The concept of direct design may be applied in other design problems, defined in Chapter 2. Many different design problems are now considered as inverse heat transfer problems and are solved by different techniques. It would be interesting to see how useful the idea of direct design might be in those applications.

- Implementation of the method: linearization.
  In this research work, it was intended to show that the Newton linearization was the most natural and best approach to linearize the governing equations particularly in the context of (shape) design problems. However, when the primitive variable formulation is used, different linearization scenarios deserve to be considered. For example, in Chapter 8, the Newton linearization was not used in the non-conservative form of the momentum equation used for developing an interpolation scheme.

- Implementation of the method: solver technology.
  Even though the direct design approach should not be blamed even if it uses direct solvers for ever, it would be interesting to study the structure of the final coefficient matrix in different applications, obtained in shape design problems, and see how the iterative solvers deal with them.

- Implementation of the method: side constraints.
  One of the attractive features of some of the optimization methods is the fact that they can handle design constraints. Of course it is not a necessary condition for a design algorithm to be able to handle the side constraints, but it is clearly a very desirable feature. It will be a revolutionary design concept if a multidisciplinary direct design is offered to the engineering community.

- Implementation of the method: grid related policies.
  The adopted grid-related policies in this research were sufficiently good to not impose any harm on the numerical solution procedure. However, it is not certain

that these policies will be adequate in dealing with the complex problems in which the quality of the grid is much more important. This is a vast area of research and will be an important issue in later developments of the method.

- Implementation of the method: prediction of separation.

  The engineering community eagerly looks for simple, robust and accurate methods for the prediction of separation in preliminary design applications. The hope for the existence of such a thing is still alive and further research is welcomed in this area.

- Optimized target pressure distribution.

  As was previously explained, in surface shape design problems it is assumed that the designer is able to provide a good (optimized) target pressure distribution. In the literature it is quite common to assume this and nearly always this ability is attributed to designer's experience. This is generally speaking true. In this thesis some guidelines, in the context of internal flow shape design problems, were provided. It would be helpful, however, to provide some general guidelines for proposing *good* target pressure distributions in different flow problems or surface heat flux distributions in thermal problems.

  It is ironic that this very last recommended research topic was the first question which was asked when this research started four years ago! Chapter 7 tried to shed some light on this issue when the design of different diffusers, spacers and nozzles was discussed. However, those explanations do not provide an exhaustive answer for this question. Therefore, the question is offered to the future researchers as the last recommended research topic in this thesis.

Appendix A

Addendum to Chapters 3 and 4

In this appendix, the required information regarding to some mathematical expressions, used in Chapters 3 and 4, are provided.

In the first section an appropriate equation is developed for the (diffusion) flow term. It is shown that how different quantities in a shape design problem can be described by expressions consisted of two, constant and variable, parts in the context of EB-FVM.

In the second section, it will be shown that how the length of a boundary element face can be described in terms of the spine coordinates of the neighbor nodes.

A.1 An Appropriate Mathematical Form For the Flow Term

It was shown in Chapter 3 that the flow term, at an arbitrary integration point, can be mathematically described as below:

$$[\mathcal{F}_\Theta]_{ip} \equiv \left[\frac{\partial \Theta}{\partial x}\Delta y - \frac{\partial \Theta}{\partial y}\Delta x\right]_{ip}. \tag{A.1}$$

As this equation shows, two different types of quantities need to be modeled and calculated: a purely geometrical quantity (e.g. Δx) and a gradient term (e.g. $\frac{\partial \Theta}{\partial x}$). In the following sub-sections appropriate mathematical expressions are obtained for Δx, Δy, $\frac{\partial \Theta}{\partial x}$, $\frac{\partial \Theta}{\partial y}$ and the flow term itself ($\mathcal{F}_\Theta$).

A.1.1 An Expression For Δx

In Chapter 3, the following differential equation was obtained for an infinitesimal length (in an element) in the x direction:

$$dx = \frac{\partial x}{\partial s}ds + \frac{\partial x}{\partial t}dt. \tag{A.2}$$

Considering the fact that the quadrilateral elements are bi-linear, one can write:

$$\Delta x = \frac{\partial x}{\partial s}\Delta s + \frac{\partial x}{\partial t}\Delta t. \tag{A.3}$$

Using Eq. 3.19 and 3.20, Δx can be written as below:

$$\Delta x = \left[(x_1 - x_2)\frac{\partial N_1}{\partial s} + (x_4 - x_3)\frac{\partial N_4}{\partial s}\right]\Delta s + \left[(x_1 - x_4)\frac{\partial N_1}{\partial t} + (x_2 - x_3)\frac{\partial N_2}{\partial t}\right]\Delta t. \tag{A.4}$$

The derivatives of the shape functions in terms of the local coordinates can be calculated with the aid of Eq. 3.5 to 3.8. It is easy to obtain:

$$\frac{\partial N_1}{\partial s} = -\frac{\partial N_2}{\partial s}. \tag{A.5}$$

$$\frac{\partial N_3}{\partial s} = -\frac{\partial N_4}{\partial s}. \tag{A.6}$$

$$\frac{\partial N_1}{\partial t} = -\frac{\partial N_4}{\partial t}. \tag{A.7}$$

$$\frac{\partial N_2}{\partial t} = -\frac{\partial N_3}{\partial t}. \tag{A.8}$$

Using Eq. A.5 to A.8 in Eq. A.4 and applying the Einstein summation rule results in:

$$\Delta x = \left[\frac{\partial N_i}{\partial s}\Delta s + \frac{\partial N_i}{\partial t}\Delta t\right]x_i. \tag{A.9}$$

Therefore, Δx can be mathematically described as:

$$\Delta x = \alpha_i x_i. \tag{A.10}$$

in which:

$$\alpha_i \equiv \frac{\partial N_i}{\partial s}\Delta s + \frac{\partial N_i}{\partial t}\Delta t. \tag{A.11}$$

Note that α_i is a constant quantity in both analysis and shape design problems which depends only on the local coordinates. Therefore Δx is a linear function of the x coordinates of the neighbor nodes. A similar expression can be obtained for Δy:

$$\Delta y = \alpha_i y_i. \tag{A.12}$$

A.1.2 An Expression For $\partial\Theta/\partial x$

The assumed bi-linear variation of the unknown Θ in an element implies that:

$$\frac{\partial \Theta}{\partial x} = \frac{\partial N_m}{\partial x}\Theta_m. \tag{A.13}$$

In [108] it is shown that:

$$\frac{\partial N_m}{\partial x} = \frac{1}{J}\left(\frac{\partial y}{\partial t}\frac{\partial N_m}{\partial s} - \frac{\partial y}{\partial s}\frac{\partial N_m}{\partial t}\right). \tag{A.14}$$

Using Eq. A.14. 3.21 and 3.22. one obtains:

$$\begin{aligned}\frac{\partial N_m}{\partial x} = &\frac{1}{J}\left[\frac{\partial N_m}{\partial s}\frac{\partial N_1}{\partial t}(y_1 - y_4) + \frac{\partial N_m}{\partial s}\frac{\partial N_2}{\partial t}(y_2 - y_3)\right] - \\ &\frac{1}{J}\left[\frac{\partial N_m}{\partial t}\frac{\partial N_1}{\partial s}(y_1 - y_2) + \frac{\partial N_m}{\partial t}\frac{\partial N_4}{\partial s}(y_4 - y_3)\right].\end{aligned} \tag{A.15}$$

This equation can also be written as below:

$$\begin{aligned}\frac{\partial N_m}{\partial x} = &\frac{1}{J}\left[\left(\frac{\partial N_m}{\partial s}\frac{\partial N_1}{\partial t} - \frac{\partial N_m}{\partial t}\frac{\partial N_1}{\partial s}\right)y_1\right] + \\ &\frac{1}{J}\left[\left(\frac{\partial N_m}{\partial s}\frac{\partial N_2}{\partial t} + \frac{\partial N_m}{\partial t}\frac{\partial N_1}{\partial s}\right)y_2\right] + \\ &\frac{1}{J}\left[\left(-\frac{\partial N_m}{\partial s}\frac{\partial N_2}{\partial t} + \frac{\partial N_m}{\partial t}\frac{\partial N_4}{\partial s}\right)y_3\right] + \\ &\frac{1}{J}\left[\left(-\frac{\partial N_m}{\partial s}\frac{\partial N_1}{\partial t} - \frac{\partial N_m}{\partial t}\frac{\partial N_4}{\partial s}\right)y_4\right].\end{aligned} \tag{A.16}$$

Using the quantity γ_{mn} as defined in Chapter 3 (Eq. 3.48), Eq. A.16 is written in the following compact form:

$$\frac{\partial N_m}{\partial x} = \left(\frac{\gamma_{mn} - \gamma_{nm}}{J}\right) y_n. \tag{A.17}$$

Therefore, the gradient of Θ in the x direction can be expressed as:

$$\frac{\partial \Theta}{\partial x} = \left(\frac{\gamma_{mn} - \gamma_{nm}}{J}\right) y_n \Theta_m. \tag{A.18}$$

Similarly one can show:

$$\frac{\partial \Theta}{\partial y} = -\left(\frac{\gamma_{mn} - \gamma_{nm}}{J}\right) x_n \Theta_m. \tag{A.19}$$

The Jacobian J in the above equations depends on both local and global coordinates and therefore in the next sub-section an appropriate expression for the Jacobian is obtained.

A.1.3 An Expression For the Jacobian (J)

The Jacobian is defined as below ([108]):

$$J = \frac{\partial x}{\partial s}\frac{\partial y}{\partial t} - \frac{\partial y}{\partial s}\frac{\partial x}{\partial t}. \tag{A.20}$$

Using Eq. 3.19, 3.20, 3.21, 3.22 and A.5 to A.8, one can obtain:

$$J = \frac{\partial N_p}{\partial s} x_p \cdot \frac{\partial N_n}{\partial t} y_n - \frac{\partial N_p}{\partial s} y_p \cdot \frac{\partial N_n}{\partial t} x_n. \tag{A.21}$$

This equation can be written in the following compact form in which the quantities related to the local and global coordinates are separated:

$$J = \gamma_{pn} \left(x_p y_n - x_n y_p\right). \tag{A.22}$$

A.1.4 An Expression For $\mathcal{F}_\Theta$

Now that appropriate expressions have been obtained for all the terms in Eq. A.1, it is easy to obtain:

$$\mathcal{F}_\Theta = \left(\frac{\gamma_{mn} - \gamma_{nm}}{\gamma_{pn}}\right)\left(\frac{x_p x_n + y_p y_n}{x_p y_n - y_p x_n}\right)\Theta_m. \tag{A.23}$$

In this equation the contributions of local coordinates, global coordinates and the physical unknowns at the neighbor nodes are separated and one can clearly see the true mathematical form of the approximate flow term in the discretized form of the Laplace equation in the context of the **EB-FVM**.

It is beneficial to define the parameter λ_m as below:

$$\lambda_m \equiv (\gamma_{mn} - \gamma_{nm})(x_p x_n + y_p y_n). \tag{A.24}$$

Therefore the flow term can be written in the following compact form:

$$\mathcal{F}_\Theta = \left(\frac{\lambda_m}{J}\right)\Theta_m. \tag{A.25}$$

A.1.5 Linearized Form of $\mathcal{F}_\Theta$

It was shown in Chapter 3 that:

$$\mathcal{F}_\Theta = \left[B_i^\Theta\right]\Theta_i + \left[B_i^x\right]x_i + \left[B_i^y\right]y_i + \left[B^{xy\Theta}\right]. \tag{A.26}$$

The coefficients B in this equation are defined as below:

$$B_i^\Theta \equiv \frac{\lambda_i^0}{J^0}. \tag{A.27}$$

$$B_i^x \equiv \frac{x_n^0\Theta_p^0}{J^0}\left[\alpha_i(\gamma_{pn} - \gamma_{np}) + \alpha_n(\gamma_{pi} - \gamma_{ip})\right] + \frac{y_n^0\Theta_p^0\lambda_p^0}{J^{0^2}}(\gamma_{ni} - \gamma_{in}). \tag{A.28}$$

$$B_i^y \equiv \frac{y_n^0\Theta_p^0}{J^0}\left[\alpha_i(\gamma_{pn} - \gamma_{np}) + \alpha_n(\gamma_{pi} - \gamma_{ip})\right] - \frac{x_n^0\Theta_p^0\lambda_p^0}{J^{0^2}}(\gamma_{ni} - \gamma_{in}). \tag{A.29}$$

$$B^{xy\Theta} \equiv -\left(B_i^x x_i^0 + B_i^y y_i^0\right) = 0. \tag{A.30}$$

A.2 An Expression For the Boundary Element Face Length

The length of the boundary element face L_{PW}, shown in Figure 4.4, is equal to:

$$L_{PW} = \left[(x_P - x_W)^2 + (y_P - y_W)^2\right]^{\frac{1}{2}}. \tag{A.31}$$

The Cartesian coordinates of points P and W are related to their spine coordinates as below:

$$x_P = \bar{x_P} + R_P \cos\theta^P, \tag{A.32}$$

$$x_W = \bar{x_W} + R_W \cos\theta^W, \tag{A.33}$$

$$y_P = \bar{y_P} + R_P \sin\theta^P, \tag{A.34}$$

$$y_W = \bar{y_W} + R_W \sin\theta^W. \tag{A.35}$$

Therefore, one can write:

$$L_{PW} = \frac{1}{2}\left[R_P^2 + A_P^{LPW} R_P + R_W^2 + A_W^{LPW} R_W - A_{PW}^{LPW} R_P R_W + A^{LPW}\right]^{\frac{1}{2}}. \tag{A.36}$$

Coefficients A in Eq. A.36 are functions of the reference point coordinates and the angles of spines associated with nodes P and W as below:

$$A_P^{LPW} \equiv 2\left[\cos\theta^P(\bar{x_P} - \bar{x_W}) + \sin\theta^P(\bar{y_P} - \bar{y_W})\right]. \tag{A.37}$$

$$A_W^{LPW} \equiv 2\left[\cos\theta^P(\bar{x_W} - \bar{x_P}) + \sin\theta^W(\bar{y_W} - \bar{y_P})\right]. \tag{A.38}$$

$$A_{PW}^{LPW} \equiv 2\left(\cos\theta^W \cos\theta^P + \sin\theta^W \sin\theta^P\right). \tag{A.39}$$

$$A^{LPW} \equiv \bar{x_P^2} + \bar{x_W^2} + \bar{y_P^2} + \bar{y_W^2} - 2(\bar{x_P}\bar{x_W} + \bar{y_P}\bar{y_W}). \tag{A.40}$$

The boundary line segment L_{PW} changes from the initial (old) value L_{PW}^0 to the new value L_{PW} in shape design problems. One can estimate the new length based on the old value as below:

$$L_{PW} \approx L_{PW}^0 + \left(\frac{\partial L_{PW}}{\partial R_P}\right)^0 (R_P - R_P^0) + \left(\frac{\partial L_{PW}}{\partial R_W}\right)^0 (R_W - R_W^0). \tag{A.41}$$

This results in:

$$L_{PW} \approx (C_L^{L_{PW}}) R_W + (C_C^{L_{PW}}) R_P + (D^{L_{PW}}), \tag{A.42}$$

in which:

$$C_L^{L_{PW}} \equiv \frac{2R_W^0 + A_W^{L_{PW}} - \left(A_{PW}^{L_{PW}}\right) R_P^0}{2L_{PW}^0}. \tag{A.43}$$

$$C_C^{L_{PW}} \equiv \frac{2R_P^0 + A_P^{L_{PW}} - \left(A_{PW}^{L_{PW}}\right) R_W^0}{2L_{PW}^0}. \tag{A.44}$$

$$D^{L_{PW}} \equiv L_{PW}^0 - \left(C_L^{L_{PW}}\right) R_W^0 - \left(C_C^{L_{PW}}\right) R_P^0. \tag{A.45}$$

Similarly, the line segment L_{PE} (see Figure 4.4) can be estimated as below:

$$L_{PE} \approx (C_R^{L_{PE}})R_E + (C_C^{L_{PE}})R_P + (D^{L_{PE}}). \tag{A.46}$$

in which:

$$C_R^{L_{PE}} \equiv \frac{2R_E^0 + A_E^{L_{PE}} - \left(A_{PE}^{L_{PE}}\right) R_P^0}{2L_{PE}^0}. \tag{A.47}$$

$$C_C^{L_{PE}} \equiv \frac{2R_P^0 + A_P^{L_{PE}} - \left(A_{PE}^{L_{PE}}\right) R_E^0}{2L_{PE}^0}. \tag{A.48}$$

$$D^{L_{PE}} \equiv L_{PE}^0 - \left(C_R^{L_{PE}}\right) R_E^0 - \left(C_C^{L_{PE}}\right) R_P^0. \tag{A.49}$$

The coefficients A in Eq. A.47 to A.49 are defined as below:

$$A_P^{LPE} \equiv 2\left[\cos\theta^P(\dot{x_P} - \dot{x_E}) + \sin\theta^P(\dot{y_P} - \dot{y_E})\right]. \tag{A.50}$$

$$A_E^{LPE} \equiv 2\left[\cos\theta^E(\dot{x_E} - \dot{x_P}) + \sin\theta^E(\dot{y_E} - \dot{y_P})\right]. \tag{A.51}$$

$$A_{PE}^{LPE} \equiv 2\left(\cos\theta^E\cos\theta^P + \sin\theta^E\sin\theta^P\right). \tag{A.52}$$

$$A^{LPE} \equiv \dot{x_P}^2 + \dot{x_E}^2 + \dot{y_P}^2 + \dot{y_E}^2 - 2(\dot{x_P}\dot{x_E} + \dot{y_P}\dot{y_E}). \tag{A.53}$$

Appendix B

Addendum to Chapter 6: Inner-Variable Theory

In Chapter 6, the general theory for obtaining the required equations in the inner-variable approach was discussed. It was explained that if the mass and momentum equations provide an equation for the unknown u_τ, three auxiliary equations are required for Π, δ^* and δ^+.

The equation for δ^+ can be obtained by using the velocity law at the edge of the boundary layer. The result is:

$$\delta^+ = \exp\left[k\frac{u_e}{u_\tau} - 2\Pi - Bk\right]. \tag{B.1}$$

The required δ^* equation is obtained from the velocity law and the definition of the displacement thickness:

$$\delta^* = \frac{\nu\delta^+}{ku_e}(1+\Pi). \tag{B.2}$$

An experimental correlation provides the required equation for Π:

$$\beta = C_0 + C_1\Pi + C_2\Pi^2. \tag{B.3}$$

Using the definition of β and the Bernoulli equation, Eq. B.3 can be written as:

$$\delta^* = \left[-u_\tau^2\left(C_0 + C_1\Pi + C_2\Pi^2\right)\right]\left[u_e\frac{du_e}{dx}\right]^{-1}. \tag{B.4}$$

If one eliminates the parameter δ^* from Eq. B.2 and B.4, the following equation is

obtained for δ^+:

$$\delta^+ = \frac{-k}{\nu} u_\tau^2 \left[u_e \frac{du_e}{dx} \right]^{-1} \left[\frac{C_0 + C_1\Pi + C_2\Pi^2}{1+\Pi} \right]. \tag{B.5}$$

Now, cancelation of δ^+ between Eq. B.1 and B.5 results in:

$$\exp\left(k\frac{u_e}{u_\tau} - 2\Pi - Bk \right) = \left[-ku_\tau^2 \left(C_0 + C_1\Pi + C_2\Pi^2 \right) \right] \left[\nu \frac{du_e}{dx} (1+\Pi) \right]^{-1}. \tag{B.6}$$

This equation can be solved for Π, when u_e and u_τ are known. Equation B.4 then can be used for calculating δ^*. Finally, Eq. B.2 can be used to find δ^+:

$$\delta^+ = \left[u_e k \delta^* \right] \left[\nu (1+\Pi) \right]^{-1}. \tag{B.7}$$

Now, let's derive four differential equations for the dependent variables in the four-equation model of the inner variable theory.

B.1 Differential Equation For u_τ

The starting point for deriving a differential equation for u_τ is the combined (integrated) mass and momentum equation:

$$\frac{d\theta}{dx} + \left[\left(\frac{H+2}{u_e} \right) \frac{du_e}{dx} \right] \theta = \frac{\tau_w}{\rho u_e^2}. \tag{B.8}$$

Using the equation obtained for θ (Eq. 6.34) one can show:

$$\frac{d\theta}{dx} = \frac{d\delta^*}{dx} - \frac{\nu}{k^2} A. \tag{B.9}$$

In this equation, A is defined as:

$$A = \frac{\beta u_\tau}{u_e^2}\frac{d\delta^+}{dx} + \frac{\beta\delta^+}{u_e^2}\frac{du_\tau}{dx} - \frac{2\delta^+\beta u_\tau}{u_e^3}\frac{du_e}{dx} + \frac{\delta^+ u_\tau}{u_e^2}\frac{d}{dx}\left(\frac{52}{35}\Pi^2 + \frac{19}{6}\Pi + 2 \right). \tag{B.10}$$

Using Eq. B.10 in B.9 and organizing the terms results in:

$$[M_1]\frac{du_\tau}{dx} + [M_2]\frac{d\Pi}{dx} + [M_3]\frac{d\delta^+}{dx} + [M_4]\frac{d\delta^*}{dx} = [M_5]. \tag{B.11}$$

In Eq. B.11 coefficients M are defined as:

$$M_1 \equiv -\frac{\nu\delta^+}{k^2 u_e^2}\beta_1. \tag{B.12}$$

$$M_2 \equiv -\frac{\nu\delta^+ u_\tau}{k^2 u_e^2}\beta_2. \tag{B.13}$$

$$M_3 \equiv -\frac{\nu u_\tau}{k^2 u_e^2}\beta_1. \tag{B.14}$$

$$M_4 \equiv 1. \tag{B.15}$$

$$M_5 \equiv \left(\frac{u_\tau}{u_e}\right)^2 - \left(\frac{3\delta^*}{u_e} - \frac{4\nu\delta^+ u_\tau \beta_1}{k^2 u_e^3}\right)\frac{du_e}{dx}. \tag{B.16}$$

Parameters β_1 and β_2 are defined as below:

$$\beta_1 \equiv \frac{52}{35}\Pi^2 + \frac{19}{6}\Pi + 2. \tag{B.17}$$

$$\beta_2 \equiv \frac{104}{35}\Pi + \frac{19}{6}. \tag{B.18}$$

B.2 Differential Equation For Π

From Eq. B.1 one can obtain the following equation:

$$u_e = u_\tau\left(\frac{1}{k}\ln\delta^+ + B\right) + \frac{2\Pi}{k}u_\tau. \tag{B.19}$$

Differentiating this equation results in:

$$[N_1]\frac{du_\tau}{dx} + [N_2]\frac{d\Pi}{dx} + [N_3]\frac{d\delta^+}{dx} + [N_4]\frac{d\delta^*}{dx} = [N_5]. \tag{B.20}$$

In Eq. B.20 coefficients N are defined as:

$$N_1 \equiv \frac{1}{k}\ln\delta^+ + B + \frac{2\Pi}{k}. \tag{B.21}$$

$$N_2 \equiv \frac{2u_\tau}{k}. \tag{B.22}$$

$$N_3 \equiv \frac{u_\tau}{k\delta^+}. \tag{B.23}$$

$$N_4 \equiv 0. \tag{B.24}$$

$$N_5 \equiv \frac{du_e}{dx}. \tag{B.25}$$

B.3 Differential Equation For δ^+

Equation B.4 can be differentiated to give the following differential equation:

$$[P_1]\frac{du_\tau}{dx} + [P_2]\frac{d\Pi}{dx} + [P_3]\frac{d\delta^+}{dx} + [P_4]\frac{d\delta^*}{dx} = [P_5]\,. \tag{B.26}$$

In Eq. B.26 coefficients P are defined as:

$$P_1 \equiv \frac{2}{u_\tau}\left(C_0 + C_1\Pi + C_2\Pi^2\right). \tag{B.27}$$

$$P_2 \equiv C_1 + 2C_2\Pi. \tag{B.28}$$

$$P_3 \equiv 0. \tag{B.29}$$

$$P_4 \equiv \frac{1}{u_\tau^2}u_e\frac{du_e}{dx}. \tag{B.30}$$

$$P_5 \equiv -\frac{\delta^*}{u_\tau^2}\left[\left(\frac{du_e}{dx}\right)^2 + u_e\frac{d^2u_e}{dx^2}\right]. \tag{B.31}$$

B.4 Differential Equation For δ^*

Finally, differentiating Eq. B.2 results in:

$$[Q_1]\frac{du_\tau}{dx} + [Q_2]\frac{d\Pi}{dx} + [Q_3]\frac{d\delta^+}{dx} + [Q_4]\frac{d\delta^*}{dx} = [Q_5]\,. \tag{B.32}$$

In Eq. B.32 coefficients Q are defined as:

$$Q_1 \equiv 0. \tag{B.33}$$

$$Q_2 \equiv 1. \tag{B.34}$$

$$Q_3 \equiv \frac{u_e\delta^*k}{\nu\delta^{+2}}. \tag{B.35}$$

$$Q_4 \equiv -\frac{ku_e}{\nu\delta^+}. \tag{B.36}$$

$$Q_5 \equiv \frac{\delta^*k}{\nu\delta^+}\frac{du_e}{dx}. \tag{B.37}$$

Appendix C

Addendum to Chapter 6: Prediction of Separation

In this appendix some short-cut methods appropriate for predicting the separation in preliminary designs will be described. These methods have been used in the context of external flows (mostly flow over airfoils).

C.1 Method of Stratford

The Stratford method [177,178] is based upon the equations of motion and the analysis of the turbulence utilizing either dimensional analysis or mixing length theory. Moreover, a closed physical picture is attempted for the flow. The method postulates that the turbulent layer in a pressure rise may be divided into two distinct regions.

The outer layer is a historical region in which the pressure rise just causes a lowering of the dynamic head profile, the losses due to the shear stresses being almost the same as for the flow on a flat plate.

In the inner layer, on the other hand, the inertia forces are so small that the velocity profile is distorted by the pressure gradient until the latter is largely balanced by the transverse gradient of shear stress.

A summary of the treatment is sketched in Figures C.1 and C.2.

C.1.1 The Outer Layer

For the outer layer, downstream of x_o, the shear forces are supposed zero and in such a flow the total pressure will remain constant along a stream line and Bernoulli's

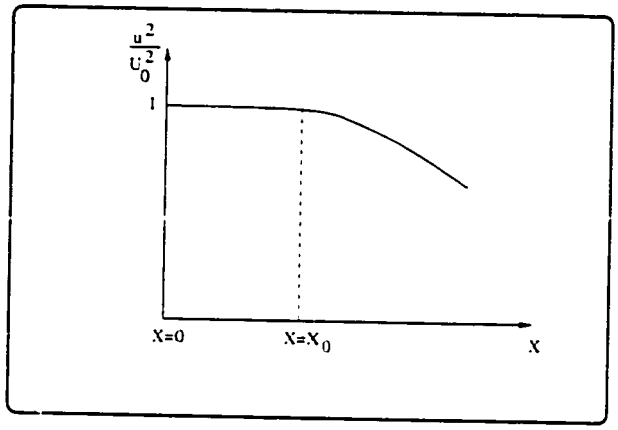

Figure C.1: Drop of the mainstream dynamic head for $\frac{dp}{dx} \geq 0$.

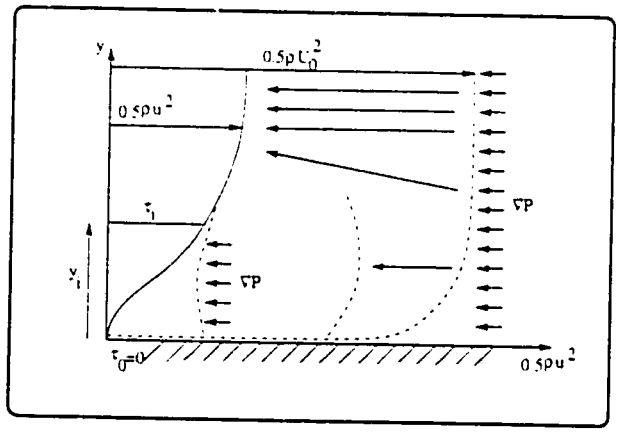

Figure C.2: Effect of the sudden pressure rise on the boundary layer velocity profile.

equation holds along the streamline S:

$$\frac{\partial P_{tot}}{\partial S} = 0. \tag{C.1}$$

This means that the dynamic head at any point is equal to the dynamic head on the same stream line at x_o minus the rise in static pressure. For the real flow the

Bernoulli equation being replaced by:

$$\frac{\partial P_{tot}}{\partial S} = \frac{\partial \tau}{\partial S}. \tag{C.2}$$

It may be assumed that the distribution of $\frac{\partial \tau}{\partial S}$ is similar to a second flow which has identical conditions as far as $x = x_o$, but which continues at constant static pressure there after, because the effect of the pressure rise in the outer part of the boundary layer in this region is to cause a general lowering of the velocity profile rather than a change in shape.

If we denote the comparison profile by a dash, and ψ_i is the value of ψ at the edge of the inner layer it may be shown that for the outer layer ($\psi \geq \psi_i$) we have:

$$\frac{1}{2}\rho u^2(x,\psi) = \frac{1}{2}\rho u'^2(x,\psi) - (p_x - p_{x_o}). \tag{C.3}$$

This means that the dynamic head at any point is therefore equal to the dynamic head at the corresponding point in the comparison flow minus the rise in static pressure. Equation C.3 represents for the outer part of the boundary layer a solution which is almost exact at positions a short distance downstream of x_o, and which would be expected to indicate at least the main behavior for large distances downstream of x_o.

For an alternative assessment, the reduction in the value of the local dynamic head from its initial value may be divided into three parts, these being due respectively to the rise in static pressure, to the viscosity between $x = 0$ and $x = x_o$ and to the viscosity downstream of x_o. Of these three effects, the first two have been included exactly in equation C.3 and the third effect which is likely to be relatively small for the outer part of a boundary layer at separation, has been allowed for approximately.

The standard solution required for u', the velocity in the boundary layer without pressure rise, may be taken as the following semi-empirical form:

$$\frac{u'}{U_o} = (\frac{y'}{\delta'})^{\frac{1}{n}}, \tag{C.4}$$

$$\delta' = \frac{(n+1)(n+2)}{n}\theta', \tag{C.5}$$

$$\theta' = 0.036x\mathcal{R}e^{-0.2}. \tag{C.6}$$

n varies slightly with the Reynolds number but is usually close to 7.

Summing up, the action of the pressure rise in the outer layer has been interpreted as a direct reduction in the dynamic head along each stream line, the only effect of the shear forces being to cause a superposed loss. It can be said that in the outer layer the back pressure force is balanced by the fluid inertia forces.

C.1.2 The Inner Layer

In the inner layer the inertia forces at the wall are zero, so that the pressure forces must be balanced entirely by the gradient of the shear force. This means that for $y = 0$:

$$\frac{\partial p}{\partial x} = \frac{\partial \tau}{\partial y}. \tag{C.7}$$

as follows from the equation of motion. Such a balance at the wall can occur only after there has been a change in the profile shape.

In the inner layer there is a transition between fluid at the wall, for which the pressure force is balanced entirely by the shear force gradient, and fluid in the outer layer, where the pressure force causes simply a direct reduction of dynamic head.

It may be shown that close to the wall the asymptotic form of the separation profile is as follows:

$$u = \sqrt{\frac{4}{\rho k^2}(\frac{\partial p}{\partial x})y}. \tag{C.8}$$

in which k is the Karman constant. This equation could be regarded as the first term of a series expansion representing the whole inner layer profile. To account for the effects of higher terms, regardless of their sources, a simple empirical factor β has been proposed by Stratford. The modified form of the equation C.8 becomes:

$$u = \sqrt{\frac{4}{\rho(k\beta)^2}(\frac{\partial p}{\partial x})y}. \tag{C.9}$$

Thus close to the wall the asymptotic form of the separation profile is that the velocity is proportional to $\sqrt{y}$.

C.1.3 Separation Criterion

At the joining between the inner and outer layers, continuity is specified in ψ, u and $\frac{\partial u}{\partial y}$ and this results in the following equations:

$$\mathcal{F}(n)C_p^{\frac{n-2}{4}}\sqrt{x\frac{dC_p}{dx}}(10^{-6}\mathcal{R}e_x)^{-0.1} = 11.342\beta. \tag{C.10}$$

$$\mathcal{F}(n) \equiv \frac{(n+1)^{\frac{n+1}{4}}(n+2)^{\frac{1}{2}}}{(n-2)^{\frac{n-2}{4}}}. \tag{C.11}$$

$$n = \log \mathcal{R}e_x. \tag{C.12}$$

$$C_p \equiv \frac{p_x - p_{x_\circ}}{\frac{1}{2}\rho\, U_\circ^2} = 1 - (\frac{u}{U_\circ})^2. \tag{C.13}$$

$\mathcal{R}e_x$ being the Reynolds number based on the local value of the distance x and the peak value $U_\circ$ and $\beta = 0.66$ or 0.73 for $\frac{d^2C_p}{dx^2} < 0$ or $\frac{d^2C_p}{dx^2} \geq 0$.

Based on the Stratford criterion, separation occurs when the left hand side of equation C.10 exceeds the right hand side. So the margin of safety is defined as the difference between the right and left hand side of the equation C.10.

Experiments have shown that for a separating turbulent boundary layer the value of $(x\frac{dC_p}{dx})$ is in the neighborhood of unity and so the value of C_p at separation would be between 0.3 and 0.5.

For pressure distributions having an initial region of favorable pressure gradient, the value of x to be used in the above equation has to be an equivalent value, the flow with favorable gradient being replaced by one at constant pressure and with a main stream velocity equal to the peak main stream velocity. The criterion of equivalence is the value of the boundary layer momentum thickness θ at the point of peak velocity:

$$x_\circ = \int_0^{X_\circ} (\frac{u}{U_\circ})^3 dX. \tag{C.14}$$

If the initial boundary layer is laminar also, using the standard assumption of sudden transition, one can obtain an equivalent condition:

$$x_\circ = 38.2(\frac{\nu}{X_t u_t})^{\frac{3}{8}}(\frac{U_\circ}{u_t})^{\frac{1}{8}}[\int_0^{X_t}(\frac{u}{U_\circ})^5 d(\frac{X}{X_t})]^{\frac{5}{8}}X_t + \int_{X_t}^{X_\circ}(\frac{u}{U_\circ})^3 dX. \tag{C.15}$$

where X and x are the distances from the actual and the equivalent leading edge, suffix (t) indicates values at transition and suffix (o) refers to conditions at the position of peak velocity or at transition whichever is later.

C.1.4 Modification of the Stratford Criterion

For a fully developed velocity distribution inside a duct which faces a sudden adverse pressure gradient, it may be assumed that the displacement thickness of the boundary layer at the starting point of the adverse pressure gradient can be used for finding the equivalent leading edge which is required in the Stratford method. This matter should be further investigated and the validity of the Stratford method for duct flow problems has not been proven yet.

C.2 Method of Dulikravich

The criterion for separation in this method has been obtained based on the similarity between this phenomenon and a similar process in fracture mechanics [179]. Based on this criterion, the separation occurs in a point at the vicinity of the boundary layer which the rate of decrease of the kinetic energy of the main stream is the minimum. For a steady incompressible flow, this criterion results in the following expression:

$$2\left(\frac{\partial V_s}{\partial S}\right)^2 + V_s\left(\frac{\partial^2 V_s}{\partial S^2}\right) = 0. \qquad \text{(C.16)}$$

V_s is the tangential component of the velocity at the wall. As an example of the application of this criterion, it has been used quite successfully in predicting the separation point of the flow over a two-dimensional cylinder. For such a flow, V_s is equal to $V_\infty\sqrt{2-2\cos(2\theta)}$ and one can obtain $\theta_s = 54.73°$, where θ is measured from the trailing edge. Various experiments have reported the separation point for this situation as $52° \leq \theta_s \leq 58°$ for flows with Reynolds numbers above 10^6. Better agreement between this theory and experiment is expected for higher Reynolds numbers [179].

C.3 Method of Page

Page has presented an approximate theory for flow separation which does not go into great detail for any single class of flows, such as incompressible flows, but applies over a large range of conditions in a unifying manner [180]. Figure C.3 shows the phenomenological model of a steady separated flow as provided by Page.

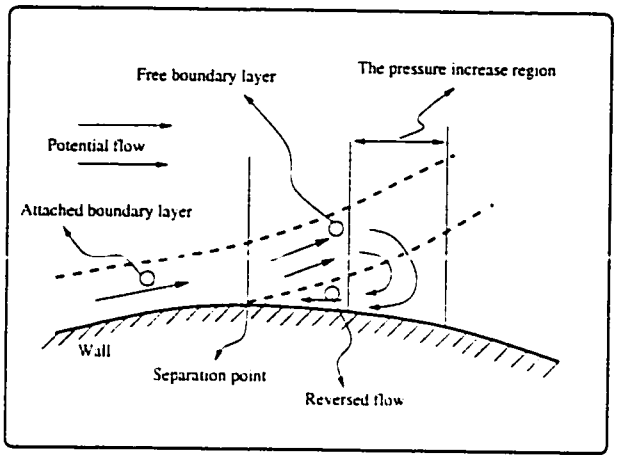

Figure C.3: A phenomenological model of a steady separated flow.

The model portrays six entities in a separated flow. They are:

- The attached boundary layer.
- The free boundary layer.
- The reversed flow.
- The wall.
- The potential flow.
- The pressure increase region.

All of these interact with one another. Page acknowledges that each flow region is influenced by its boundary conditions and the boundary conditions, themselves, interact with each other. Nevertheless, he tries to analyze each component or entity of the model separately. He argues that after the analysis of each component is completed, the results may be merged to give the simultaneous solution. Page provides a criterion for the prediction of the incipient separation [180] which correctly models the variation of the separation point with the flow condition but fails to provide acceptable quantitative results.

C.4 Method of Head

Head's method is an integral method that can be used both for calculating the boundary layer parameters, as well as for predicting the position of separation in turbulent flows [181]. It uses the momentum integral equation and two auxiliary equations, namely, the Ludwieg-Tillman expression for the skin-friction coefficient and a shape factor $G(H)$ relationship obtained from the entrainment properties of the turbulent boundary layer.

Head's method, like most integral methods, uses the shape factor H as the criterion for separation. Although it is not possible to give an exact value of H corresponding to separation, when H is between 1.8 and 2.4, separation is assumed to exist. It has to be noted that close to separation the shape factor increases quickly and the difference between the lower and upper limits of H makes very little difference in locating the separation point.

C.5 Method of Goldschmied

Goldschmied's separation criterion, like Stratford's method, is based on the existence of inner and outer regions in the turbulent boundary layer. The Goldschmied separation criterion has been obtained as below [182]:

$$(C_P)_{sep.} = 200 C_F. \tag{C.17}$$

Appendix D

Addendum to Chapter 8

The unified governing equations, appropriate for solving both analysis and shape design problems, were derived in Chapter 7 in the context of primitive-variable ($P-\vec{V}$) formulation. The final set of algebraic equations (the level D mathematical model) was obtained as:

$$\begin{aligned}(C_W^{mP})\,P_W + (C_P^{mP})\,P_P + (C_E^{mP})\,P_E + \\ (C_W^{mA})\,A_W + (C_P^{mA})\,A_P + (C_E^{mA})\,A_E + \\ (C_W^{mU})\,U_W + (C_P^{mU})\,U_P + (C_E^{mU})\,U_E = \\ (C^{mR})\,.\end{aligned} \tag{D.1}$$

$$\begin{aligned}(C_W^{uP})\,P_W + (C_P^{uP})\,P_P + (C_E^{uP})\,P_E + \\ (C_W^{uA})\,A_W + (C_P^{uA})\,A_P + (C_E^{uA})\,A_E + \\ (C_W^{uU})\,U_W + (C_P^{uU})\,U_P + (C_E^{uU})\,U_E = \\ (C^{uR})\,.\end{aligned} \tag{D.2}$$

The coefficients used in these equations are defined as:

$$C_W^{mP} \equiv -\left(\frac{a_w^0}{2u_w^0}\right). \tag{D.3}$$

$$C_P^{mP} \equiv \left(\frac{a_e^0}{2u_e^0} + \frac{a_w^0}{2u_w^0}\right). \tag{D.4}$$

$$C_E^{mP} \equiv -\left(\frac{a_e^0}{2u_e^0}\right). \tag{D.5}$$

$$C_W^{mA} \equiv 0. \tag{D.6}$$

$$C_P^{mA} \equiv -u_w^0. \tag{D.7}$$

$$C_E^{mA} \equiv u_e^0. \tag{D.8}$$

$$C_W^{mU} \equiv -\left(\frac{a_w^0}{2}\right). \tag{D.9}$$

$$C_P^{mU} \equiv \frac{1}{2}\left(a_e^0 - a_w^0\right). \tag{D.10}$$

$$C_E^{mU} \equiv \left(\frac{a_e^0}{2}\right). \tag{D.11}$$

$$C^{mR} \equiv \left(a_e^0 u_e^0 - a_w^0 u_w^0\right). \tag{D.12}$$

$$C_W^{uP} \equiv -\frac{3}{2}\left(a_w^0\right). \tag{D.13}$$

$$C_P^{uP} \equiv \left(\frac{1}{2}a_e^0 + \frac{3}{2}a_w^0\right). \tag{D.14}$$

$$C_E^{uP} \equiv -\frac{1}{2}\left(a_e^0\right). \tag{D.15}$$

$$C_W^{uA} \equiv \frac{1}{2}\left(P_P^0 - p_w^0\right). \tag{D.16}$$

$$C_P^{uA} \equiv \frac{1}{2}\left(p_e^0 - p_w^0 - 2u_w^{0^2}\right). \tag{D.17}$$

$$C_E^{uA} \equiv u_e^{0^2} + \frac{1}{2}\left(p_e^0 - P_P^0\right). \tag{D.18}$$

$$C_W^{uU} \equiv -\frac{3}{2}\left(u_w^0 a_w^0\right). \tag{D.19}$$

$$C_P^{uU} \equiv \left(\frac{3}{2}u_e^0 a_e^0 - \frac{1}{2}u_w^0 a_w^0\right). \tag{D.20}$$

$$C_E^{uU} \equiv \frac{1}{2}\left(u_e^0 a_e^0\right). \tag{D.21}$$

$$C^{u\tilde{n}} \equiv a_e^0\left(p_e^0 - P_P^0 + 2u_e^{0^2}\right) + a_w^0\left(P_P^0 - p_w^0 - 2u_w^{0^2}\right). \tag{D.22}$$

Bibliography

[1] K. Kurpisz and A. J. Nowak. *Inverse Thermal Problems*. Computational Mechanics Publication, 1995.

[2] Max D. Gunzburger (editor). *Flow Control*. Springer-Verlag, 1995.

[3] M. D. Gunzburger. Introduction Into Mathematical Aspects Of Flow Control And Optimization. In *Inverse Design And Optimization Methods*. Lecture Series 1997-05. Von Karman Institute For Fluid Dynamics, 1997.

[4] G. S. Dulikravich and T. J. Martin. Inverse Shape And Boundary Condition Problems And Optimization In Heat Conduction. In W. J. Minkowycz and E. M. Sparrow, editors, *Advances in Numerical Heat Transfer*, volume 1, chapter 10, pages 381–426. Taylor & Francis, 1997.

[5] G. S. Dulikravich. Aerodynamic Shape Design. In *Special Course on Inverse Methods for Airfoil Design for Aeronautical and Turbomachinary Applications*, number 780. AGARD, 1990.

[6] A. Van der Velden. Aerodynamic Shape Optimization. In *Optimum Design Methods for Aerodynamics*, pages 10.1–10.13. AGARD, 1994.

[7] O. Pironneau. On Optimum Design in Fluid Mechanics. *Journal of Fluid Mechanics*, 64:97–110, 1974.

[8] G. Volpe. *Inverse Airfoil Design: A Classical Approach Updated for Transonic Applications*, volume 125 of *Progress in Astronautics and Aeronautics*, chapter 7, pages 191–220. AIAA Journal, 1990.

[9] F. M. White. *Viscous Fluid Flow.* McGraw-Hill, 1991.

[10] D. C. Wilcox. *Turbulence Modeling for CFD.* DCW Industries, second edition, 1998.

[11] TASCflow, Theory Documentation, Version 2.3. Advanced Scientific Computing Ltd, 1994.

[12] R. A. Adams. *Calculus of Several Variables.* Addison-Wesley, 1987.

[13] C. Hirsch. *Numerical Computation of Internal and External Flows,* volume 1. John Wiley & Sons, 1990.

[14] L. Quartapelle. *Numerical Solution of the Incompressible Navier-Stokes Equations,* volume 113 of *ISNM.* Birkhauser Verlag, 1993.

[15] Jr G. S. Patterson. Prospects for Computational Fluid Mechanics. *Annual Review in Fluid Mechanics,* 10:289-300, 1978.

[16] D. R. Chapman. Computational Aerodynamics Development and Outlook. *AIAA Journal,* 17(12):1293-1313, Dec. 1979.

[17] W. D. McNally and P. M. Sockol. Review-Computational Methods for Internal Flows with Emphasis on Turbomachinery. *Journal of Fluids Engineering,* 107(6):7-22, March 1985.

[18] G. J. Hancock. Aerodynamics-The Role of the Computer. *Aeronautical Journal,* 89-(887):269-279, 1985.

[19] P. Kutler. A Perspective of Theoretical and Applied Computational Fluid Dynamics. *AIAA Journal,* 23:328-341, Mar. 1985.

[20] J. P. Boris. New Directions in Computational Fluid Dynamics. *Annual Review in Fluid Mechanics,* 21:345-385, 1989.

[21] J. L. Steger. A Viewpoint on Discretization Schemes for Applied Aerodynamic Algorithms for Complex Configurations. In A. Kumar M. Y. Hussaini and M. D. Salas, editors, *Algorithmic Trends in Computational Fluid Dynamics,* ICASE/NASA LaRC Series, pages 3-15. Springer-Verlag, 1990.

[22] H. O. Kreiss. Some Remarks About Computational Fluid Dynamics. In M. Y. Hussaini, A. Kumar, and M. D. Salas, editors, *Algorithmic Trends in Computational Fluid Dynamics,* ICASE/NASA LaRC Series, pages 17-20. Springer-Verlag, 1990.

[23] R. W. MacCormack. Algorithmic Trends in CFD in the 1990's for Aerospace Flow Field Calculations. In M. Y. Hussaini, A. Kumar, and M. D. Salas, editors, *Algorithmic Trends in Computational Fluid Dynamics*, ICASE/NASA LaRC Series, pages 21–32. Springer-Verlag, 1990.

[24] B. Lakshminarayana. An Assessment of Computational Fluid Dynamic Techniques in the Analysis and Design of Turbomachinary-The 1990 Freeman Scholar Lecture. *Journal of Fluids Engineering*, 113:315–352, Sept. 1991.

[25] A. Jameson. The Present Status, Challenges and Future Developments in Computational Fluid Dynamics. Presented at CFD 96 Ottawa, 1996.

[26] P. J. Zwart, G. D. Raithby, and M. J. Raw. An Integrated Space-Time Finite-Volume Method For Moving-Boundary Problems. *Numerical Heat Transfer*, 34:257–270, 1998.

[27] S. V. Patankar. *Numerical Heat Transfer and Fluid Flow*. Hemisphere Pub. Corp., 1980.

[28] B. R. Baliga and S. V. Patankar. A New Finite-Element Formulation for Convection-Diffusion Problems. *Numerical Heat Transfer*, 3:393–409, 1980.

[29] G. E. Schneider and M. Zedan. Control-Volume-Based Finite-Element Formulation of the Heat Conduction Equation. In H. E. Collicott and P. E. Bauer, editors, *Spacecraft Thermal Control, Design, And Operation*, volume 86 of *Progress in Astronautics and Aeronautics*, pages 305–327. AIAA, 1982.

[30] G. E. Schneider and M. J. Raw. Control Volume Finite-Element Method For Heat Transfer And Fluid Flow Using Colocated Variables-1.Computational Procedure. *Numerical Heat Transfer*, 11:363-390, 1987.

[31] G. D. Raithby and P. F. Galpin. The Practical Application of Computational Fluid Mechanics. June 1991. Presented at the Canadian Congress of Applied Mechanics (CANCAM), Winnipeg.

[32] E. Onate and S. R. Idelsohn. A Comparison Between Finite Element And Finite Volume Methods In CFD. In Ch. Hirsch *et al.*, editor, *Computational Fluid Dynamics* '92, volume 1. Elsevier Science Publishers, 1992.

[33] G. D. Stubley, G. D. Raithby, and A. B. Strong. Proposal For a New Discrete Method Based on an Assessment of Discretization Errors. *Numerical Heat Transfer*, 3:411–428, 1980.

[34] J. H. Ferziger and M. Perić. *Computational Methods for Fluid Dynamics.* Springer, 1992.

[35] B. P. Leonard. Bounded Higher-Order Upwind Multidimensional Finite-Volume Convection-Diffusion Algorithms. In W. J. Minkowycz and E. M. Sparrow, editors, *Advances in Numerical Heat Transfer*, volume 1, pages 1–54. Taylor & Francis, 1997.

[36] P. F. Galpin, G. D. Raithby, and J. P. Van Doormaal. Discussion of Upstream-Weighted Advection Approximations for Curved Grids. *Numerical Heat Transfer*, 9:241–246, 1986.

[37] P. F. Galpin, R. G. Huget, and G. D. Raithby. Fluid Flow Simulations in Complex Geometries. Paper Presented at the CNS/ANS Conference on Simulation Methods in Nuclear Engineering, Montreal, October 1986.

[38] J. A. George, J. W. H. Liu, and E. G. Y. Ng. *User's Guide for SPARSPAK: Waterloo Sparse Linear Equations Package.* Dept. of Computer Science, University of Waterloo, 1980. Research Report CS-78-30 (revised).

[39] A. Ashrafizaadeh and G. D. Raithby. Prediction of Efficient Shapes for Nozzles and Diffusers. In *46th CASI Annual Conference Proceedings.* Canadian Aeronautics and Space Institute, May 1999.

[40] S. S. Rao. *Engineering optimization, theory and practice.* John wiley & sons, 1996.

[41] J. R. Appel, A. G. Godfrey, and M. Cliff. Optimization-Based Design in High-Speed Flows. In *CFD for Design and Optimization*, volume 232, pages 61–68. ASME, 1995.

[42] M. E. Eleshaky and O. Baysal. Airfoil Shape Optimization Using Sensitivity Analysis on Viscous Flow Equations. In *Multidisciplinary Applications of CFD*, volume 129, pages 27–37. ASME, 1991.

[43] M. H. Rizk. Optimization by Updating Design Parameters as CFD Iterative Flow Solutions Evolve. In *Multidisciplinary Applications of CFD*, volume 129, pages 51–62. ASME, 1991.

[44] G. Kuruvila, S. Táasan, and M. D. Salas. Airfoil Optimization by the One-Shot Method. In *Optimum Design Methods for Aerodynamics*, pages 7.1–7.21. AGARD, 1994.

[45] O. Baysal and M. E. Eleshaky. Aerodynamic Design Optimization Using Sensitivity Analysis and Computational Fluid Dynamics. *AIAA Journal*, 30(3):718–725, March 1992.

[46] H. Cabuk and V. Modi. Shape Optimization Analysis: First and Second Order Necessary Conditions. *Optimal Control Applications and Methods*, 11:173–190, 1990.

[47] G. N. Vanderplaats. Multidiscipline Design Optimization. *Applied Mechanics Review*, 41(6):257–262, June 1988.

[48] R. M. Hicks and P. A.Henne. Wing Design by Numerical Optimization. *Journal of Aircraft*, 15(7):407–412, July 1978.

[49] N. Hirose, S. Takanashi, and N. Kawai. Transonic Airfoil Design Procedure Utilizing a Navier-Stokes Analysis Code. *AIAA Journal*, 25(3):353–359, March 1987.

[50] R. H. Liebeck and A. I. Ormsbee. Optimization of Airfoils for Maximum Lift. *Journal of Aircraft*, 7(5):409–415, Sept.-Oct. 1970.

[51] M. H. Rizk. The Single-Cycle Scheme: A New Approach to Numerical Optimization. *AIAA Journal*, 21(12):1640–1647, December 1983.

[52] M. H. Rizk. A New Approach to Optimization for Aerodynamic Applications. *Journal of Aircraft*, 20(1):94–96, Jan. 1983.

[53] M. H. Rizk. Application of the Single-Cycle Optimization Approach to Aerodynamic Design. *Journal of Aircraft*, 22(6):509–515, June 1985.

[54] Chin-Hsiang Cheng and Chun-Yin Wu. An Approach Combining Body-Fitted Grid Generation And Conjugate Gradient Methods For Shape Design in Heat Conduction Problems. *Numerical Heat Transfer*, 37-B:69–83, 2000.

[55] R. Alsan Meric. Shape Design Sensitivity Analysis And Optimization For Nonlinear Heat And Electric Conduction Problems. *Numerical Heat Transfer*, 34-A:185–203, 1998.

[56] K. Laor and H. Kalman. Performance And Optimum Dimensions Of Different Cooling Fins With A Temperature-Dependent Heat Transfer Coefficient. *International Journal of Heat and Mass Transfer*, 39(9):1993–2003, 1997.

[57] S. Obayashi. Aerodynamic Optimization With Evolutionary Algorithms. In *Inverse Design And Optimization Methods*. Lecture Series 1997-05. Von Karman Institute For Fluid Dynamics. 1997.

[58] I. DeFalco. An Introduction To Evolutionary Algorithms And Application To The Airfoil Design Problem. Part 1: The Algorithms. In *Inverse Design And Optimization Methods*. Lecture Series 1997-05. Von Karman Institute For Fluid Dynamics. 1997.

[59] I. DeFalco. An Introduction To Evolutionary Algorithms And Application To The Airfoil Design Problem. Part 2: The Results. In *Inverse Design And Optimization Methods*. Lecture Series 1997-05. Von Karman Institute For Fluid Dynamics. 1997.

[60] Giampietro Fabbri. A Genetic Algorithm For Fin Profile Optimization. *International Journal of Heat and Mass Transfer*. 40(9):2165–2172. 1997.

[61] A. Jameson. Aerodynamic Design Methods. In W. G. Habashi. editor. *Proceedings of the International Workshop on Solution Techniques for Large-Scale CFD Problems*. Cerca. Sept. 1994.

[62] P. D. Frank and G. R. Shubin. A Comparison of Optimization-Based Approach for a Model Computational Aerodynamics Design Problem. *Journal of Computational Physics*. 98:74–89. 1992.

[63] J. C. Lewis and R. K. Agarwal. Airfoil Design via Control Theory Using Full-Potential and Euler Equations. In *CFD for Design and Optimization*. volume 232. pages 53–60. CFD. 1995.

[64] J. Reuther and A. Jameson. Supersonic Wing and Wing-Body Shape Optimization Using an Adjoint Formulation. In *CFD for design and optimization*. volume 232. pages 45–52. ASME. 1995.

[65] A. Jameson. Optimum Aerodynamic Design via Boundary Control. In *Optimum Design Methods for Aerodynamics*. pages 3.1–3.33. AGARD. 1994.

[66] P. K. Lamm. Inverse Problems and Ill-Posedness. Inverse Problems in Engineering: Theory and Practice. ASME. 1993.

[67] J. D. Stanitz. Design of Two-Dimensional Channels with Prescribed Velocity Distributions along the Channel Walls. Technical Report 1115. Lewis Flight Propulsion Laboratory. 1953.

[68] S. D. McMillan. Stanitz Grid Generator. Technical Report 95-002, Advanced Scientific Computing ltd., 1995.

[69] C. D. Nelson and T. Yang. Design of Branched and Unbranched Axially Symmetrical Ducts with Specified Pressure Distribution. *AIAA Journal*, 15(9):1272–1277, September 1977.

[70] John. D. Stanitz. General Design Method for Three-Dimensional, Potential Flow Fields. I-Theory. Technical Report -3288, NASA, 1980.

[71] J. D. Stanitz. A Review of Certain Inverse Methods for the Design of Ducts with 2- or 3-Dimensional Potential Flow. *Applied Mechanics Review*, 41(6):217–238, June 1988.

[72] J. D. Stanitz. Aerodynamic Design of Efficient Two-Dimentional Channels. *Transaction of the ASME*, pages 1241–1255, October 1953.

[73] J. D. Stanitz and L. J. Sheldrake. Application of a Channel Design Method to High Solidity Cascades and Tests of an Impulse Cascade With 90 deg. of Turning. Technical Report 2652, NACA, 1952.

[74] P. Chaviaropoulos, V. Dedoussis, and K. D. Papailiou. On The 3-D Inverse Potential Target Pressure Problem. Part I: Theoretical Aspects And Method Formulation. *Journal of Fluid Mechanics*, 282:131–146, 1995.

[75] P. Chaviaropoulos, V. Dedoussis, and K. D. Papailiou. On The 3-D Inverse Potential Target Pressure Problem. Part II: Numerical Aspects And Application To Duct Design. *Journal of Fluid Mechanics*, 282:147–162, 1995.

[76] P. Chaviaropoulos, V. Dedoussis, and K. D. Papailiou. A Robust Inverse Inviscid Method For Airfoil Design. In Ch. Hiirsch et al., editor, *Computational Fluid Dynamics 92*, volume 2, pages 581–588. Elsevier, 1992.

[77] P. Chaviaropoulos, V. Dedoussis, and K. D. Papailiou. Compressible Flow Airfoil Design Using Natural Coordinates. *Computer Methods In Applied Mechanics And Engineering*, 110:131–142, 1993.

[78] V. Dedoussis, P. Chaviaropoulos, and K. D. Papailiou. Rotational Compressible Inverse Design Method For Two-Dimensional, Internal Flow Configurations. *AIAA Journal*, 31(3):551–558, 1993.

[79] G. S. Dulikravich. A Stream Function Coordinate (SFC) Concept in Aerodynamic Shape Design. In *Special Course on Inverse Methods for Airfoil Design for Aeronautical and Turbomachinary Applications*, number 780. AGARD, 1990.

[80] M. S. Greywall. Streamwise Computation of Three-Dimensional Parabolic Flows. *Computer Methods In Applied Mechanics And Engineering*, 36:71–93, 1983.

[81] M. S. Greywall. Streamwise Computation of Two-Dimensional Incompressible Potential Flows. *Journal of Computational Physics*, 59:224–231, 1985.

[82] M. S. Greywall. Streamwise Computation of Three-Dimensional Incompressible Potential Flows. *Journal of Computational Physics*, 78:178–193, 1988.

[83] R. A. Novak. Streamline Curvature Computing Procedures for Fluid-Flow Problems. *Journal of Engineering for Power*, pages 478–490, October 1967.

[84] C. E. Pearson. Use of Streamline Coordinates in the Numerical Solution of Compressible Flow Problems. *Journal of Computational Physics*, 42:257–265, 1981.

[85] L. Zannetti, F. Larocca, and R. Marsilio. Euler Solver for 3D Inverse Problems. In *Advances And Applications In Computational Fluid Dynamics*, volume 66 of *FED*, pages 71–79. ASME, 1988.

[86] L. Zannetti. A Natural Formulation for the Solution of 2-D or Axisymmetric Inverse Problems. *International Journal for Numerical Methods in Engineering*, 22:451–463, 1986.

[87] P. Laidler and D. F. Myring. The Inverse Problem for Incompressible Internal Flows. *Aeronautical Journal*, 88(872):38–45, February 1984.

[88] R. L. Barger. Streamline Curvature Design Procedure for Subsonic and Transonic Ducts. Technical Report TN D-7368, NASA, December 1973.

[89] R. L. Barger and C. W. Brooks Jr. A Streamline Curvature Method for Design of Supercritical and Subcritical Airfoils. Technical Report TN D-7770, NASA, September 1974.

[90] A. K. Agrawal, S. Krishnan, and Tah teh Yang. Use of Subdomains for Inverse Problems in Branching Flow Passages. *Journal of Fluids Engineering*, 115:227–232, June 1993.

[91] K. Aziz and J. D. Hellums. Numerical Solution of the Three-Dimensional Equations of Motion for Laminar Natural Convection. *The Physics of Fluids*, 10(2):314–324, February 1967.

[92] G. J. Hirasaki and J. D. Hellums. A General Formulation of the Boundary Conditions on the Vector Potential in Three-Dimensional Hydrodynamics. *Quarterly of Applied Mathematics*, 26:331–342, 1968.

[93] G. J. Hirasaki and J. D. Hellums. Boundary Conditions on the Vector and Scalar Potentials in Viscous Three-Dimensional Hydrodynamics. *Quarterly of Applied Mathematics*, 28:293–296, 1970.

[94] G. D. Mallinson and G. D. Vahl Davis. The Method of the False Transient for the Solution of Coupled Elliptic Equations. *Journal of Computational Physics*, 12:435–461, 1973.

[95] G. D. Mallinson and G. De. Vahl Davis. Three-Dimensional Natural Convection in a Box: A Numerical Study. *Journal of Fluid Mechanics*, 83:1–33, 1977.

[96] Y. A. S. Aregbesola and D. M. Burley. The Vector and Scalar Potential Method for the Numerical Solution of Two- and Three-Dimensional Navier-Stokes Equations. *Journal of Computational Physics*, 24:398–415, 1977.

[97] S. M. Richardson and A. R. H. Cornish. Solution of Three-Dimensional Incompressible Flow Problems. *Journal of Fluid Mechanics*, 82:309–319, 1977.

[98] A. K. Wong and J. A. Reizes. An Effective Vorticity-Vector Potential Formulation for the Numerical Solution of Three-Dimensional Duct Flow Problems. *Journal of Computational Physics*, 55:98–114, 1984.

[99] H. Yang and R. Camarero. An Improved Vorticity-Potential Method for Three-Dimensional Duct Flow Simulations. *International Journal for Numerical Methods in Fluids*, 6:35–45, 1986.

[100] R. W. MacCormac. On the Development of Efficient Algorithms for Three Dimensional Fluid Flow. In T. E. Tezduyar and T. J. R. Hughes, editors, *Recent Developments in Computational Fluid Dynamics*, volume 95 of *AMD*, pages 117–137. ASME, 1988.

[101] R. L. Davis and J. E. Carter. Three-Dimensional Viscous Flow Solutions With a Vorticity-Stream Function Formulation. *AIAA Journal*, 27(7):892–900, 1989.

[102] S. B. Beale. Recent Advances in the Use of Stream Functions for Flow Visualisation. In *Proceedings of the six annual conference of the Computational Fluid Dynamics Society of Canada*, pages 109–116, 1998.

[103] E. E. Litvai. On the Boundary Conditions for the Vector Potential in Three Dimensional Duct Flows. In K. N. Ghia, U. Ghia, and D. Goldstein, editors, *Advances In Computational Methods In Fluid Dynamics*, volume 196, pages 197–207. ASME, 1994.

[104] W. X. Xu, G. D. Raithby, and G. D. Stubley. Prediction of Compliant-Surface Flows. In *Proceedings of 4th Annual Conference of CFD Society of Canada*, 1996.

[105] G. D. Raithby, W. X. Xu, and G. D. Stubley. Prediction of Incompressible Free Surface Flows with an Element-Based Finite Volume Method. *Computational Fluid Dynamics Journal*, 4(3):353–371, Oct. 1995.

[106] Gerald Farin. *Curves And Surfaces For Computer Aided Geometric Design, A Practical Guide*. Academic Press, 1997.

[107] S. F. Kistler and L. E. Scriven. Coating Flow Theory by Finite Element and Asymptotic Analysis of the Navier Stokes System. *International Journal for Numerical Methods in Fluids*, 4:207–229, 1984.

[108] G. E. Schneider. Elliptic Systems: Finite-Element Method I. In W. J. Minkowycz, E. M. sparrow, G. E. Schneider, and H. Pletcher R, editors, *Handbook of Numerical Heat Transfer*, pages 379–421. John Wiley & Sons, 1988.

[109] R. F. Van den Dam, J. A. Van Egmond, and J. W. Slooff. Optimization of Target Pressure Distribution. In *Special Course on Inverse Methods for Airfoil Design for Aeronautical and Turbomachinary Applications*, number 780. AGARD, 1990.

[110] S. D. McMillan. Stanitz Grid Generator. Technical Report 95-002, Advanced Scientific Computing Ltd., 1995.

[111] P. S. Granville. Integral Methods for Turbulent Boundary Layers in Pressure Gradients. *Journal of Ship Research*, pages 191–204, September 1972.

[112] F. M. White. A New Integral Method for Analyzing the Turbulent Boundary Layer With Arbitrary Pressure Gradient. *Journal of Basic Engineering*, pages 371–378, September 1969.

[113] W. S. Saric (editor). Turbulent Boundary Layers in Subsonic and Supersonic Flow. Technical Report AG-335. AGARD. 1996.

[114] D. Coles. The Law of the Wake in the Turbulent Boundary Layer. *Journal of Fluid Mechanics*, 1:191–226, 1956.

[115] D. K. Das. An Inverse Inner-Variable Theory for Separated Turbulent Boundary Layers. *Journal of Fluids Engineering*. 114:543–553. December 1992.

[116] F. H. Clauser. Turbulent Boundary Layers in Adverse Pressure Gradients. *Journal of the Aeronautical Sciences*. pages 91–108. 1954.

[117] D. K. Das. A Simple Theory for Calculating Turbulent Boundary Layers Under Arbitrary Pressure Gradients. *International Journal of Engineering Fluid Mechanics*. 1(1):83–99. Spring 1988.

[118] S. J. Kline. D. G. Cockrell. M. V. Morkovin. and G. Sovran. editors. *Computation of Turbulent Boundary Layers-1968 AFOSR-IFP-Stanford Conference*. volume 1. Stanford University. CA.. 1968.

[119] J. H. Ferziger. A. A. Lyrio. and J. G. Bardina. New Skin Friction and Entrainment Correlations for Turbulent Boundary Layers. *Journal of Fluids Engineering*. 104:537–540. December 1982.

[120] P. K. Chang. *Separation of Flow*. volume 3 of *International Series Of Monographs In Interdisciplinary And Advanced Topics In Science And Engineering*. Pergamon Press. 1970.

[121] S. J. Kline. Some New Conceptions Of the Mechanism of Stall in Turbulent Boundary Layers. *Journal of the Aeronautical Sciences*. 24:470–471. June 1957.

[122] S. J. Kline. On the Nature of Stall. *Journal of Basic Engineering*. 81:305–320. September 1959.

[123] Jr. P. W. Runstadler. F. X. Dolan. and Jr. R. C. Dean. Diffuser Data Book. Technical Report TN-186. Creare Inc.. 1975.

[124] A. Ashrafizadeh. Separation in Steady Two-Dimensional Incompressible Turbulent Flows. Technical report. University of Waterloo. Department of Mechanical Engineering. CFD Group. Unpublished. April 1998.

[125] L. R. Reneau, J. P. Johnston, and S. J. Kline. Performance and Design of Straight, Two-Dimensional Diffusers. *Journal of Basic Engineering*, pages 141–150, March 1967.

[126] J. P. Johnston. Review: Diffuser Design and Performance Analysis by a Unified Integral Method. *Journal of Fluids Engineering*, 120:6–18, March 1998.

[127] R. C. Binder. Calculation of Diffuser Efficiency for Two-Dimensional Flow. *Journal of Applied Mechanics*, pages 213–216, September 1947.

[128] S. J. Kline, D. E. Abbott, and R. W. Fox. Optimum Design of Straight-Walled Diffusers. *Journal of Basic Engineering*, 81:321–331, September 1959.

[129] J. J. Carlson, J. P. Johnston, and C. J. Sagi. Effects of Wall Shape on Flow Regimes and Performance in Straight, Two-Dimensional Diffusers. *Journal of Basic Engineering*, pages 151–160, March 1967.

[130] H. L. Moses and J. R. Chappell. Turbulent Boundary Layers in Diffusers Exhibiting Partial Stall. *Journal of Basic Engineering*, pages 655–665, September 1967.

[131] B. A. Waitmanand L. R. Reneau and S. J. Kline. Effects of Inlet Conditions on Performance of Two-Dimensional Subsonic Diffusers. *Journal of Basic Engineering*, pages 349–360, September 1961.

[132] S. Wolf and J. P. Johnston. Effects of Nonuniform Inlet Velocity Profiles on Flow Regimes and Performance in Two-Dimensional Diffusers. *Journal of Basic Engineering*, pages 462–474, September 1969.

[133] L. R. Reneau and J. P. Johnston. A Performance Prediction Method for Unstalled, Two-Dimensional Diffusers. *Journal of Basic Engineering*, pages 643–654, September 1967.

[134] O. J. McMillan and J. P. Johnston. Performance of Low-Aspect-Ratio Diffusers With Fully Developed Turbulent Inlet Flows, Part 1 - Some Experimental Results. *Journal of Fluids Engineering*, pages 385–392, September 1973.

[135] S. Ghose and S. J. Kline. The Computation of Optimum Pressure Recovery in Two-Dimensional Diffusers. *Journal of Fluids Engineering*, 100:419–426, Dec. 1978.

[136] G. Hokenson. Inverse Design of Optimal Diffusers With Experimental Corroboration. *Journal of Fluids Engineering*, 101:478–482, December 1979.

[137] J. Ashjaee and J. P. Johnston. Straight-Walled, Two-Dimensional Diffusers: Transitory Stall and Peak Pressure Recovery. *Journal of Fluids Engineering*, 102:275–282, September 1980.

[138] J. A. Hoffmann. Effects of Free-Stream Turbulence on Diffuser Performance. *Journal of Fluids Engineering*, 103:385–390, September 1981.

[139] J. Bardina, A. Lyrio, S. J. Kline, J. H. Ferziger, and J. P. Johnston. A Prediction Method for Planar Diffuser Flows. *Journal of Fluids Engineering*, 103:315–321, June 1981.

[140] K. G. Winter and L. F. East. The Design of Optimum Diffusers for Incompressible Flow. In W.Haase, editor, *Recent Contributions to Fluid Mechanics*, pages 312–320. Springer-Verlag, 1982.

[141] R. C. Strawn and S. J. Kline. A Stall Margin Design Method for Planar and Axisymmetric Diffusers. *Journal of Fluids Engineering*, 105(105):28–33, March 1983.

[142] N. M. A. Ahmed and D. F. Myring. An Inverse Method for the Design of Axi-Symmetric Optimal Diffusers. *International Journal for Numerical Methods in Engineering*, 22:377–394, 1986.

[143] M. S. Greywall. A New Algorithm for Solution of Inverse Problems in Internal Flows. *Inverse Problems in Mechanics(ASME)*, 186:67–70, 1994.

[144] R. W. Fox and S. J. Kline. Flow Regimes in Curved Subsonic Diffusers. *Journal of Basic Engineering*, pages 303–316, September 1962.

[145] C. J. Sagi and J. P. Johnston. The Design and Performance of Two-Dimensional, Curved Diffusers. *Journal of Basic Engineering*, pages 715–731, December 1967.

[146] D. J. Parsons and P. G. Hill. Effects of Curvature on Two-Dimensional Diffuser Flow. *Journal of Fluids Engineering*, pages 349–360, September 1973.

[147] G. J. Hokenson and F. Y. Su. Unified Inlet/Diffuser Design by an Inverse Method. *AIAA Journal*, 15(1):3–45, Jan. 1977.

[148] B. Majumdar, R. Mohan, S. N. Singh, and D. P. Agrawal. Experimental Study of Flow in a High Aspect Ratio 90 Deg Curved Diffuser. *Journal of Fluids Engineering*, 120:83–89, March 1998.

[149] J. L. Sproston. Design of S-Shaped Diffusers in Incompressible Flow, December 1982.

[150] F. Rehman and Jr. J. M. Bowyer. Turbulent Incompressible Air Flow Through S-Shaped Ducts With Cross-Sectional Area Change. In W.W. Bower and M. J. Morris, editors. *Forum On Turbulent Flows*, volume 76 of *FED*, pages 49–57. ASME, 1989.

[151] P. Bansod and P. Bradshaw. The Flow in S-Shaped Ducts. *The Aeronautical Quarterly*, 23:131–140, 1971.

[152] S. C. M. Yu and E. L. Goldsmith. Some Aspects of the Flow in S-Shaped Diffusing Ducts. *Aeronautical Journal*, 98(978):305–310, October 1994.

[153] S. C. M. Yu and W. K. Chan. Effects of a Central Straight on an S-Shaped Diffusing Duct. *Aeronautical Journal*, pages 351–354, October 1996.

[154] H. Z. Herzig and A. G. Hansen. Experimental and Analytical Investigation of Secondary Flows in Ducts. *Journal of the Aeronautical Sciences*, pages 217–231, March 1957.

[155] S. N. Barua. On Secondary Flow In Stationary Curved Pipes. *The Quarterly Journal Of Mechanics And Applied Mathematics*, 16:61–77, 1963.

[156] W. M. Collins and S. C. R. Dennis. The Steady Motion Of A Viscous Fluid In A Curved Tube. *The Quarterly Journal Of Mechanics And Applied Mathematics*, 28:133–156, 1963.

[157] Y. G. Lai, R. M. C. So, M. Anwer, and B. C. Hwang. Modelling of Turbulent Curved-Pipe Flows. In W. Rodi and E. N. Ganić, editors. *Engineering Turbulence, Modelling and Experiments*, pages 227–236. Elsevier, 1990.

[158] R. M. C. So. Entry Flow in Curved Channels. *Journal of Fluids Engineering*, 58(2):305–310, June 1976.

[159] P. Orlandi and D. Cunsolo. Two-Dimensional Laminar Flow in Elbows. *Journal of Fluids Engineering*, 101:276–283, June 1979.

[160] B. J. Kitchen and Jr. J. M. Bowyer. Toward the Optimization of a Non-Diffusing, Two-Dimensional, S-Shaped Duct. In W.W. Bower and M. J. Morris, editors, *Forum On Turbulent Flows*, volume 76 of *FED*, pages 85–92. ASME, 1989.

[161] L. A. Butz. Turbulent Flow in S-Shaped Ducts. Master's thesis, Purdue University, May 1980.

[162] J. C. Gibbings. Incompressible Flow in Contracting Ducts. *Aeronautical Journal*, 97(967):230–246, 1993.

[163] L. G. Whitehead and L. Y. Wu. Contracting Ducts of Finite Length. *The Aeronautical Quarterly*, 2:254–271, Feb. 1951.

[164] N. T. Bloomer. Notes on the Mathematical Design of Nozzles and Wind Tunnel Contractions. *The Aeronautical Quarterly*, 8:279–290, 1957.

[165] H. H. Bossel. Computation of Axisymmetric Contractions. *AIAA Journal*, 7(10):2017–2020, October 1969.

[166] G. E. Chmielewski. Boundary-Layer Considerations in the Design of Aerodynamic Contractions. *Journal of Aircraft*, 11(8):435–438, August 1974.

[167] T. Morel. Comprehensive Design of Axisymmetric Wind Tunnel Contractions. *Journal of Fluids Engineering*, pages 225–233, June 1975.

[168] M. N. Mikhail. Optimum Design of Wind Tunnel Contractions. *AIAA Journal*, 17(5):471–477, May 1979.

[169] P. Bradshaw and R. C. Pankhurst. *The Design of Low-Speed Wind Tunnels*, volume 5 of *Progress in Aeronautical Sciences*. Pergamon Press, 1964.

[170] P. Bradshaw. *Experimental Fluid Mechanics*. Pergamon Press, second edition, 1970.

[171] J. Moore and J. G. Moore. A Calculation Procedure for Three-Dimensional, Viscous, Compressible Duct Flow. Part *i*–Inviscid Flow Considerations. *Journal of Fluids Engineering*, 101:415–422, December 1979.

[172] J. Moore and J. G. Moore. A Calculation Procedure for Three-Dimensional, Viscous, Compressible Duct Flow. Part *ii*–Stagnation Pressure Losses in a Rectangular Elbow. *Journal of Fluids Engineering*, 101:423–428, December 1979.

[173] G. D. Raithby and G. E. Schneider. Elliptic Systems: Finite-Difference Method II. In W. J. Minkowycz, E. M. Sparrow, G. E. Schneider, and H. Pletcher R, editors, *Handbook of Numerical Heat Transfer*, pages 241–291. John Wiley & Sons, 1988.

[174] D. Yin, M. J. Raw, and G. D. Raithby. An Analysis of Velocity and Pressure Discretizations in Colocated-Grid Finite Volume Methods. In *Procceding of CFD Conference in Canada*, 1996.

[175] S. M. H. Karimian and G. E. Schneider. Pressure-Based Computational Method For Compressible and Incompressible Flows. *Journal of Thermophysics and Heat Transfer*, 8(2):267–274, 1994.

[176] De-Wei Yin. Pressure and Velocity Interpolations and Modal Oscillations in Colocated-Grid Fluid Flow Calculations. Master's thesis, University of Waterloo, 1997.

[177] B. S. Stratford. The Prediction of Separation of the Turbulent Boundary Layer. *Journal of Fluid Mechanics*, pages 1–16, 1958.

[178] B. S. Stratford. An Experimental Flow With Zero Skin Friction Throughout Its Region of Pressure Rise. *Journal of Fluid Mechanics*, pages 17–35, 1958.

[179] G. S. Dulikravich. A Criteria for Surface Pressure Specification in Aerodynamic Shape Design. AIAA paper-90-0124, 1990.

[180] R. H. Page. A Theory For Incipient Separation. *Developments in Mechanics*, 1:563–577, 1961.

[181] T. Cebeci, G. J. Mosinskis, and A. M. O. Smith. Calculation of Separation Points in Incompressible Turbulent Flows. *Journal of Aircraft*, 9(9):618–624, September 1972.

[182] F. R. Goldschmied. An Approach to Turbulent Incompressible Separation under Adverse Pressure Gradients. *Journal of Aircraft*, pages 108–115, March-April 1965.